Production of pairs of mesons, leptons and quarks in ultraperipheral ultrarelativistic heavy ion collisions

Mariola Kłusek-Gawenda

A Thesis presented for the degree of

Doctor of Philosophy

Thesis Supervisor
Professor Dr Hab. Antoni Szczurek

The Henryk Niewodniczański
Institute of Nuclear Physics
Polish Academy of Sciences
Kraków, Poland

2014

Produkcja par mezonów, leptonów oraz kwarków w ultraperyferycznych zderzeniach ultrarelatywistycznych ciężkich jonów

Mariola Kłusek-Gawenda

Praca na stopień doktora nauk fizycznych

wykonana pod kierunkiem

Promotora
Prof. Dr Hab. Antoniego Szczurka

Instytut Fizyki Jądrowej
im. Henryka Niewodniczańskiego
Polskiej Akademii Nauk
Kraków, Polska

2014

Abstract

The main goal of the dissertation is theoretical determination of the total and differential cross sections for the production of pairs of mesons, leptons and quarks in ultraperipheral ultrarelativistic heavy ion collisions. The Equivalent Photon Approximation (EPA) in the impact parameter space has been used as a theoretical tool for calculation of the reaction mechanism in the electromagnetic processes. We have presented the predictions in a reference to STAR, PHENIX and ALICE experimental data. We have focused on the calculations with inclusion of the realistic charge distribution in nucleus and we have shown the difference between results for the realistic nucleus charge form factor and that for the monopole form factor often used in the literature. We have studied several elementary cross sections for $\gamma\gamma$ fusion and we have compared our parametrizations of $\gamma\gamma \to X_1X_2$ processes to existing word experimental data. Furthermore, we have calculated the cross section for photoproduction of single and double ρ^0 mesons, the latter due to a double-scattering mechanism. Additionally, we have studied the $\rho^0 \to \pi^+\pi^-$ and $\rho^0\rho^0 \to \pi^+\pi^-\pi^+\pi^-$ decays. Finally, we have discussed in detail electromagnetic excitation of gold and lead nuclei by soft photons and as well as the emission of neutrons from decays of the excited nuclear system.

Streszczenie

Głównym celem niniejszej rozprawy jest teoretyczne wyznaczenie całkowitych i różniczkowych przekrojów czynnych na produkcję par mezonów, leptonów i kwarków w ultraperyferycznych ultrarelatywistycznych zderzeniach ciężkich jonów. Przybliżenie Równoważnych Fotonów w przestrzeni parametru zderzenia zostało użyte jako teoretyczne narzędzie do obliczeń przekrojów czynnych w tych procesach elektromagnetycznych. Zaprezentowaliśmy przewidywania odnosząc się do danych eksperymentalnych grup badawczych STAR, PHENIX i ALICE. Skupiliśmy się na obliczeniach z uwzględnieniem realistycznych formfaktorów jąder, które są otrzymane w oparciu o realistyczny rozkład ładunku w jądrze i pokazaliśmy różnicę pomiędzy wynikami dla realistycznego i monopolowego czynnika kształtu często używanego w literaturze. Przeanalizowaliśmy elementarne przekroje czynne dla fuzji $\gamma\gamma \to X_1X_2$ i porównaliśmy nasze wyniki z istniejącymi światowymi danymi eksperymentalnymi. Ponadto wykonaliśmy obliczenia przekrojów czynnych na fotoprodukcję pojedynczych mezonów ρ^0 i na produkcję dwóch mezonów ρ^0, ten drugi w procesie dwukrotnego rozpraszania. Dodatkowo rozpatrzyliśmy rozpady $\rho^0 \to \pi^+\pi^-$ i $\rho^0\rho^0 \to \pi^+\pi^-\pi^+\pi^-$. Na końcu szczegółowo przedyskutowaliśmy elektromagnetyczne wzbudzenie jądra złota i ołowiu oraz emisję neutronów z rozpadów wzbudzonego systemu jądrowego.

Dedicated to

my parents,

husband and daughter

Acknowledgements

I would like to express my deepest thanks to my supervisor Prof. Antoni Szczurek for his help, patience and kindness. I am grateful for passing to me his knowledge and very valuable guideline.

Furthermore I would like to thank Assoc. Prof. Wolfgang Schäfer and Assoc. Prof. Andrzej Rybicki for valuable discussions and all other friendly people in the Division of Nuclear Physics and Strong Interactions (NO2) for a nice atmosphere in the work. I would like to express my gratitude to those who supported me during my traineeship stay at CERN, especially to Prof. Marek Kowalski, Dr Rainer Schicker and Bartłomiej Żabiński. Additionally, I would like to thank Prof. Valeriy Serbo and Prof. Magno Machado for nice collaboration during our common work on heavy quark-antiquark production.

I am very grateful to my parents and sisters for their support throughout the period of my PhD studies. Last but not least, I would like to express my particular acknowledgement to my husband and daughter. They are my biggest motivation.

I am grateful for financial support for the preparation of the doctoral dissertation from the Polish National Science Centre in the framework of a doctoral scholarship financing based on the decisions number

- 2013/08/T/ST/00669 (ETIUDA 1),
- 2011/03/B/ST2/02634 (OPUS),
- 2366/B/H03/2011/40 (promoter's grant no. N N202 236640).

Contents

Preface

Ultrarelativistic heavy ion collisions provide a nice opportunity to study $\gamma\gamma$ collisions which are not available otherwise. One can expect an enhancement of the rate of the reactions of this type compared to proton-proton or e^+e^- collisions which is due to large charges of the colliding ions. In this type of reactions almost real photons couple to the nucleus (nuclei) as a whole. Naively the enhancement of the cross section is proportional to $Z_1^2 Z_2^2$ which is a huge factor. We discuss that the inclusion of realistic nucleus charge form factor, which is equivalent to the inclusion of realistic charge distributions in nuclei, makes the cross section smaller than the cross section for the case when using the monopole form factor often used in the literature. We study many processes that lead to exclusive production of particle pairs.

The main goal of the dissertation is theoretical determination of the total and differential cross sections for the production of particle pairs that are created in ultraperipheral heavy ion collisions. These ions move with ultrarelativistic velocity. Measurements of ultrarelativistic nuclei and particles are performed with the help of detection system of the RHIC and LHC accelerators. The Relativistic Heavy-Ion Collider (RHIC) at BNL and the Large Hadron Collider (LHC) at CERN produce Au+Au and Pb+Pb collisions at energies 200 GeV/nucleon and 2.76 or 5.5 TeV/nucleon, respectively.

The outline of this Thesis:

Chapter 1 focuses on the discussion of the main theoretical tool of our analysis: the Equivalent Photon Approximation (EPA). The pioneer of this method was Enrico Fermi (1924). Some corrections and extensions were proposed later

by C. von Weizsäcker and E. J. Williams (1934). EPA is a standard semi-classical alternative to the Feynman rules for calculation of the electromagnetic interaction cross sections. This Chapter contains derivation of the EPA and a notation which is used in this dissertation and in our calculations. Next we discuss the size and shape of the heavy nuclei. This is connected with correct description of the charge density distribution using two-parameter Fermi model.
In order to derive a formula for the nucleus charge form factor, which is equivalent to introducing realistic charge distribution in the nucleus, it is useful to know the Rutherford and Mott cross section and corresponding matrix element for the process. We show results for both realistic and monopole form factors.

Chapter 2 describes one of the most important ingredient of the EPA, elementary cross sections for $\gamma\gamma$ fusion. Each section in this chapter is devoted to other subprocess:

- dimuon production,
- ρ^0 mesons production,
- quark-antiquark production,
- two-pion production.

A second category of the underlying reaction mechanisms for the exclusive production of simple final state is presented in Chapter 3. This is a vector meson photoproduction. We show the difference between results when taking into account a fixed (sharp) and smeared mass of the ρ^0 meson. One of main goals of this chapter is the presentation of the differential cross section for the production of four charged pions in ultraperipheral ultrarelativistic heavy ion collisions.

Chapter 4 includes theoretical predictions for the production of pairs of mesons, leptons and quarks in ultraperipheral ultrarelativistic heavy ion collisions. The nuclear cross section is calculated with the help of EPA in the impact parameter space. We present our predictions in a reference to STAR, PHENIX and ALICE experimental data. The possibility of exclusive measurements of $\mu^+\mu^-$, $\rho^0\rho^0$, $c\bar{c}$, $b\bar{b}$, $\pi^+\pi^-$

and $\pi^0\pi^0$ pairs is discussed. We focus on the calculation with inclusion of the realistic charge distribution and we show the difference between results for the realistic nucleus charge form factor and that for the monopole form factor.

In Chapter 5 we study a new approach for calculating the electromagnetic excitation of nuclei as well as differential and total cross section for emission of neutrons from decays of excited nuclear systems for ultraperipheral ultrarelativistic Au-Au and Pb-Pb collisions. Both single-photon, double-photon and mutual excitation processes are included and discussed. We compare our results with results of other theoretical approaches and with recent experimental data of PHENIX, PHOBOS, BRAHMS and ALICE Collaborations.

Chapter 6 closes the dissertation. It also discusses possibilities to study the exclusive production of meson, lepton and quark pairs in ultraperipheral ultrarelativistic heavy ion collisions. The importance of the realistic charge distribution in the nucleus is presented and discussed. Outlook of future phenomenological and experimental studies is presented.

Appendices include some useful formulae concerning details of the calculations presented in different sections.

Scientific achievements of the PhD student

Publications:

[1] M. Kłusek, W. Schäfer and A. Szczurek,

Exclusive production of $\rho^0\rho^0$ pairs in $\gamma\gamma$ collisions at RHIC,

Phys. Lett. **B674** (2009) 92-97,

[2] M. Kłusek, A. Szczurek and W. Schäfer,

Realistic cross sections for exclusive $\rho^0\rho^0$ production in ultrarelativistic heavy-ion collisions,

PoS EPS-HEP2009 (2009) 458,

[3] M. Kłusek-Gawenda, and A. Szczurek,
Exclusive muon-pair productions in ultrarelativistic heavy-ion collisions – realistic nucleus charge form factor and differential distributions,
Phys. Rev. **C82** (2010) 014904,
[4] M. Kłusek-Gawenda, A. Szczurek, M.V.T. Machado and V.G. Serbo,
Double – photon exclusive processes with heavy quark – heavy antiquark pairs in high-energy Pb-Pb collisions at LHC,
Phys. Rev. **C83** (2011) 024903,
[5] M. Kłusek-Gawenda and A. Szczurek,
Exclusive production of pion pairs with large invariant mass in nucleus-nucleus collisions,
arXiv [nucl-th] 1110.6378 (2011),
[6] A. Szczurek and M. Kłusek-Gawenda,
Photon-photon production of lepton, quark and meson pairs in peripheral heavy ion collisions,
arXiv [nucl-th] 1110.4741 (2011),
[7] M. Kłusek-Gawenda and A. Szczurek,
Exclusive production of $\rho^0\rho^0$ pairs in ultrarelativistic heavy ion collisions,
Int. J. Mod. Phys. **A26** (2011) 741-743,
[8] M. Kłusek-Gawenda and A. Szczurek,
Exclusive production of large invariant mass pion pairs in ultraperipheral ultrarelativistic heavy ion collisions,
Phys. Lett. **B700** (2011) 322-330,
[9] M. Kłusek-Gawenda and A. Szczurek,
Exclusive production of $\pi^+\pi^-$ and $\pi^0\pi^0$ pairs in photon-photon and in ultrarelativistic heavy ion collisions,
EPJ Web Conf. **37** (2012) 06006,
[10] S. Baranov, A. Cisek, M. Kłusek-Gawenda, W. Schäfer and A. Szczurek,
The $\gamma\gamma \to J/\psi J/\psi$ reaction and the $J/\psi J/\psi$ pair production in exclusive ultraperipheral ultrarelativistic heavy ion collisions,
Eur. Phys. J. **C73** (2013) 2335,

[11] M. Kłusek-Gawenda and A. Szczurek,
$\pi^+\pi^-$ and $\pi^0\pi^0$ pair production in photon-photon and in ultraperipheral ultrarelativistic heavy ion collisions,
Phys. Rev. **C87** (2013) 054908,
[12] M. Kłusek-Gawenda and A. Szczurek,
Exclusive production of two and four pions in ultraperipheral, ultrarelativistic collisions,
PoS EPS-HEP2013 (2013) 020,
[13] M. Kłusek-Gawenda, E. Kozik, A. Rybicki, I. Sputowska, and A. Szczurek,
Strong and Electromagnetic Forces in Heavy Ion Collisions,
Acta Phys. Polon. Supp **6** (2013) 451-456,
[14] A. Rybicki, A. Szczurek, M. Kłusek-Gawenda and I. Sputowska,
Studying the Interplay of Strong and Electromagnetic Forces in Heavy Ion Collisions with NICA,
arXiv [nucl-th] 1301.5210 (2013),
[15] M. Kłusek-Gawenda, M. Ciemała, W. Schäfer and A. Szczurek,
Electromagnetic excitation of nuclei and neutron evaporation in ultrarelativistic ultraperipheral heavy ion collisions,
Phys. Rev. **C89** (2014) 054907,
[16] M. Kłusek-Gawenda and A. Szczurek,
Double-scattering mechanism in the exclusive $AA \to AA\rho^0\rho^0$ reaction in ultrarelativistic collisions,
Phys. Rev. **C89** (2014) 024912,
[17] A. Szczurek and M. Kłusek-Gawenda,
Ultraperipheral production of very small number of particles in ultrarelativistic heavy ion collisions,
EPJ Web Conf. **66** (2014) 04028,
[18] M. Kłusek-Gawenda and A. Szczurek,
Exclusive electromagnetic production of pion pairs in lead-lead collisions at LHC,
EPJ Web Conf. **66** (2014) 04014.

Talks/posters:

[1] 3-7.11.2014 (Kraków), 6^{th} International Workshop on Multiple Partonic Interactions at the LHC,

Double scattering production of two ρ^0 mesons and four pions in heavy ion UPCs,

[2] 14.01.2014 (CERN), LHC Working Group on Forward Physics and Diffraction,

Pions and ρ^0 mesons production in UPC for the ALICE Collaboration,

[3] 2-6.09.2013 (Germany - Heidelberg), WE-Heraeus-Summerschool; Diffractive and electromagnetic processes at high energies,

Production of two pions and two ρ^0 mesons in peripheral ultrarelativistic heavy-ion collisions, [4] 2-7.06.2013 (Italy - Florence), INPC 2013; International Nuclear Physics Conference,

Exclusive electromagnetic production of pion pairs in lead-lead collisions at LHC,

[5] 26.03.2013 (Rzeszów), VIII Rzeszowska Konferencja Młodych Fizyków,

Produkcja par pionów vs eksperyment,

[6] 31.05 - 5.06.2012 (Kraków), Meson 2012; 12th International Workshop on Meson Production, Properties and Interaction,

Exclusive production of $\pi^+\pi^-$ and $\pi^0\pi^0$ pairs in photon-photon and in ultrarelativistic heavy ion collisions,

[7] 3-7.06.2011 (Spain - Santiago de Compostela), Low-x,

Exclusive production of pion pairs with large invariant mass in nucleus-nucleus collisions,

[8] 26.05.2011 (Rzeszów), VI Rzeszowska Konferencja Młodych Fizyków,

Ekskluzywna produkcja pary pionów i ciężkich kwarków w wysokoenergetycznych zderzeniach jonów ołowiu,

[9] 30.08 - 5.09.2010 (Zakopane), Zakopane Conference of Nuclear Physics 2010,

Exclusive production of $\rho^0\rho^0$ and $\mu^+\mu^-$ pairs in ultrarelativistic heavy ion collisions,

[10] 10-15.06.2010 (Kraków), Meson 2010; 11th International Workshop on Meson Production, Properties and Interaction,

Exclusive production of $\rho^0\rho^0$ pairs in ultrarelativistic heavy ion collisions,

[11] 27.05.2010 (Rzeszów), V Rzeszowska Konferencja Młodych Fizyków,
Realistyczny i monopolowy formfaktor; przekrój czynny dla ekskluzywnej elektromagnetycznej produkcji $\mu^+\mu^-$,
[12] 4-8.01.2010 (Italy - Trento), Workshop at ECT* TRENTO; Diffractive and electromagnetic processes at the LHC,
Exclusive electromagnetic production of $\rho^0\rho^0$ *and* $\mu^+\mu^-$ *charge density in the nucleus*,
[13] 16-22.07.2009 (Kraków), The 2009 Europhysics Conference on High Energy Physics,
Realistic cross section for exclusive $\rho^0\rho^0$ *production in ultrarelativistic heavy-ion collisions*,
[14] 7-15.07.2009 (Zakopane), Trans-European School of High Energy Physics,
Exclusive production of $\rho^0\rho^0$ *in peripheral nuclear collisions at RHIC and LHC*,
[15] 5.06.2009 (Rzeszów), IV Rzeszowska Konferencja Młodych Fizyków,
Ekskluzywna produkcja mezonów $\rho^0\rho^0$ *w zderzeniach gamma-gamma przy ultrarelatywistycznych energiach.*

Chapter 1

Equivalent photon approximation

This chapter is devoted to the introduction of the Weizsäcker-Williams method which is a useful tool for calculating cross sections for the reactions considered in this thesis. Here some history of the equivalent photon approximation, its derivation, and the notation which is used in the current dissertation will be presented. In general, the equivalent photon approximation is a standard semi-classical alternative to the Feynman rules for calculation of the electromagnetic interaction cross sections. In this approach the strong electromagnetic field is a source of photons that can induce electromagnetic reactions in ion-ion collisions.

Next I will discuss how the size and shape of a heavy nucleus can be (and was) studied in other processes. This information can be used then to extract the basic ingredient of the approach - the electromagnetic form factor of a nucleus. The parametrization of the charge density and the nuclear form factor used in this dissertation is obtained from electron scattering experiments.

1.1 A short history

In 1924 Enrico Fermi wrote a paper with the title "On the Theory of the impact between atoms and electrically charged particles". He introduced the correspondence between the electric field of light and that of a charged particle. E. J. Williams [19] found some corrections and extension of the theory proposed by E. Fermi [20].

The generalization of Fermi's method to the relativistic case was independently determined by C. von Weizsäcker [21] and E. J. Williams [22] in 1934. The method rests on the similarity of the fields of a fast moving charged particle and the fields of a radiation pulse. The electromagnetic field surrounding the heavy ions is very strong. This is due to the coherent action of all the protons in the nucleus. The action of the field takes place in a very short time. The basic idea was described by Fermi [20]: "this time-dependent electromagnetic field can be replaced by the field of radiation with a corresponding frequency distribution". Following up this suggestion, Weizsäcker and Williams demonstrated how to replace the electromagnetic field of the fast moving nucleus by a spectrum of photons. These photons can be considered as real or quasi-real.

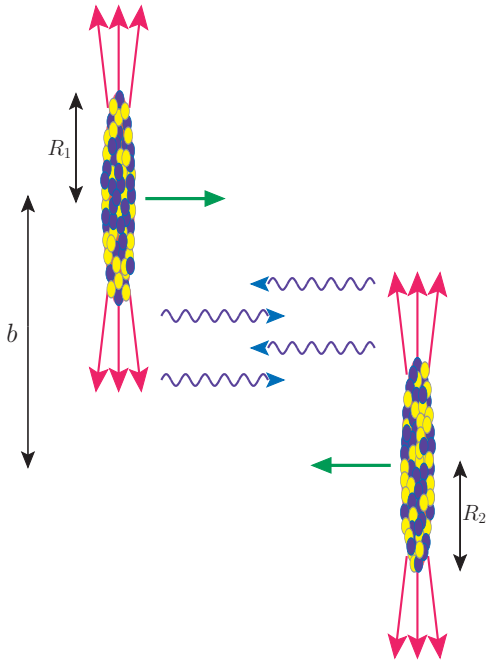

Figure 1.1: Schematic diagram illustrating EPA / Weizsäcker-Williams method which is used for description of electromagnetic processes in heavy-ion collisions.

A schematic view of two highly relativistic colliding ions is depicted in Fig. 1.1. The figure shows two fast moving nuclei with the charge Ze. These nuclei are contracted by relativistic Lorentz-FitzGerald contraction. Assuming that the nuclear radius R_0 is equal about 7 fm, and using the formula: $R = R_0/\gamma$ (where

$\gamma = 1/\sqrt{1-\beta^2}$ is the Lorentz factor and $\beta = p/E$ - the velocity of the particle with the energy E and momentum p) one can calculate that for RHIC energy ($\sqrt{s_{NN}} = 200$ GeV, $\gamma \approx 107$) the nuclear radius observed by an observer in the laboratory frame is equal about 0.13 fm.

Returning to Fig. 1.1, the strong electromagnetic field is viewed as a cloud of photons which can be called "equivalent". During collision of two ions, these photons can collide with each other or with the other nucleus.

The above physical picture introduces the so-called Equivalent Photon Approximation (EPA). Very often in the literature it is known as Weizsäcker-Williams method. Sometimes the procedure is referred to as a Method of Virtual Quanta. At present, one can find a lot of review works as well as shorter publications on the subject, e.g. [23–26].

The impact parameter space is the best suited for application to the nuclear collisions. The impact parameter is the distance between centers of nuclei (a letter b in Fig. 1.1) in the plane transverse to the collision axis. The aim of this dissertation is the description of ultraperipheral collisions (UPC) of heavy ions using explicitly this variable. For the processes of interest in this thesis it is necessary, that the transverse distance between the two nuclei is bigger than the sum of their radii ($b > R_{min} = R_1 + R_2$). This condition must be imposed in order to exclude the breakup of colliding nuclei.

1.2 A derivation of the Weizsäcker - Williams method

The Weizsäcker-Williams method is based on both classical and quantum concepts. The main idea relies on determination of equivalent photon number $n(\omega)$. The equivalent photon number integrated over impact parameter is expressed through

$$n(\omega) = \int_{R_{min}}^{\infty} 2\pi b \mathrm{d}b \, N(\omega, b) \, . \tag{1.2.1}$$

where $N(\omega, b)$ denotes an equivalent photon flux differential in both photon energy ω and impact parameter b. The quantum part involves the description of the interaction between emitted photon and a target particle (or photon emitted from the second nucleus). The total cross section for an electromagnetic photon-induced subprocess is factorized into an equivalent photon spectrum and the photon-ion interaction cross section:

$$\sigma = \int \mathrm{d}\omega \, n(\omega) \sigma_{A\gamma}(\omega) \ , \tag{1.2.2}$$

where the integral runs over photon energies.

For the case of two-photon collisions in the reaction $\mathrm{A_1A_2} \to \mathrm{A_1A_2X}$ one would like to achieve an analogous factorization into the probability that first (or second) nucleus emits a photon at energy ω_1 (ω_2), and the probability that two photons collide with each other to produce some final state called here X for brevity. For this case, the total cross section would take the form:

$$\sigma_{A_1A_2 \to A_1A_2X} = \int \mathrm{d}\omega_1 \, \mathrm{d}\omega_2 \, n(\omega_1) n(\omega_2) \sigma_{\gamma\gamma \to X}(\omega_1, \omega_2) \ . \tag{1.2.3}$$

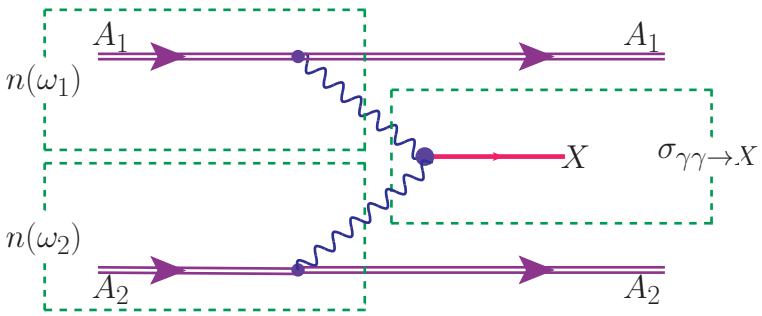

Figure 1.2: Schematic illustration of Eq. (1.2.3) - production of some final state (X) by two-photon-induced subprocess in heavy ion collision.

For the case of heavy nuclei, the constraint $b > R_1 + R_2$ strictly speaking breaks such a factorization (see the formulas in Appendix B). A schematic illustration of Eq. (1.2.3) is shown in Fig. 1.2. Let's start from a derivation of the equivalent photon fluxes $N(\omega, b)$ (see Eq. (1.2.1)). This formula depends on the impact parameter and energy of the photon. Firstly, one has to determine the frequency spectrum $I(\omega, b)$ (energy per unit area per unit frequency interval). A pedagogical discussion can be

found in the textbook of J.D. Jackson (Ref. [27]) for a fast moving point-like particle with the charge q. In what follows we take guidance from Jackson's discussion.

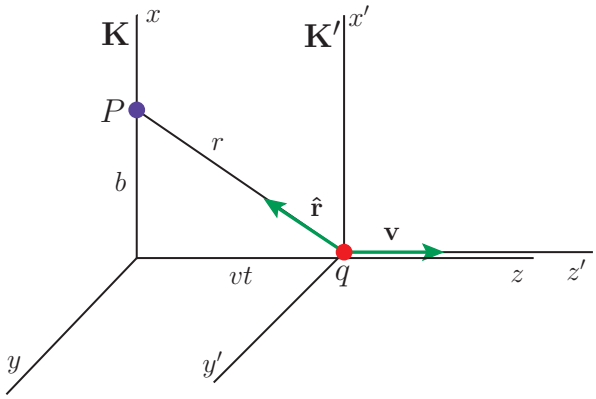

Figure 1.3: Particle with the point-like charge q moves with a constant velocity $v \approx c$. This particle passes an observation point P at impact parameter b.

In Fig. 1.3 one can see a particle of charge q, which when viewed from the frame K moves with a high velocity $v \sim c$ along the z-axis, and passes an observation point P in frame K with velocity $\mathbf{v} = \hat{\mathbf{z}}v$. In the frame K', the particle is at rest in the origin.

Here the target point P can be considered as an interaction point or another particle. Relative to the origin of K, point P is located at coordinates $(b, 0, 0)$ and the spatial coordinates of q as a function of time in K are $(0, 0, vt)$. The K and K' frames coincide at the time $t = t' = 0$. The impact parameter b is the distance of closest approach between q and P.

The electric $\mathbf{E}$ and magnetic $\mathbf{B}$ field strengths can then be obtained from the electromagnetic potentials as:

$$\begin{cases} \mathbf{E} &= -\nabla\Phi - \frac{1}{c}\frac{\partial \mathbf{A}}{\partial t}\,, \\ \mathbf{B} &= \nabla \times \mathbf{A}\,. \end{cases} \tag{1.2.4}$$

The form of (1.2.4) is the same for massive and massless fields but the explicit expression is different because Φ and $\mathbf{A}$ differ for the two cases. In the rest frame of the charge, its electromagnetic field is given by the electromagnetic potentials (we use primed quantities to denote that they belong to the frame K'):

$$\Phi'(\mathbf{r}', t') = \frac{1}{4\pi}\frac{q}{r'}e^{-mr'}\,, \qquad \mathbf{A}' = 0\,. \tag{1.2.5}$$

Here, to avoid possible subtleties due to the infinite range of the field, we introduced a "photon mass" m, which will be set to zero in the final results.

Clearly in its rest-frame K' the electromagnetic field of the charge is purely electric. It reads, in Heaviside-Lorentz units [28],

$$\begin{aligned} \mathbf{E}'(\mathbf{r}', t') &= -\nabla'\Phi' - \frac{\partial \mathbf{A}'}{\partial t'} \\ &= \frac{\mathbf{r}'}{r'} \frac{1}{4\pi} \frac{q}{r'^2} (1 + mr') e^{-mr'} . \end{aligned} \tag{1.2.6}$$

In the rest frame K' of the charge the electric field at point P (see Fig. 1.3) has the Cartesian components [29]:

$$\begin{cases} E'_x(\mathbf{r}', t') &= \frac{1}{4\pi} \frac{qb}{r'^3} (1 + mr') e^{-mr'} , \\ E'_y(\mathbf{r}', t') &= 0 , \\ E'_z(\mathbf{r}', t') &= \frac{1}{4\pi} \frac{-qvt'}{r'^3} (1 + mr') e^{-mr'} . \end{cases} \tag{1.2.7}$$

Here $r' = r'(t') = \sqrt{b^2 + (vt')^2}$. Because the frames K and K' differ only by a boost along the z-axis, the impact parameter b is the same in the frame K and K'. By the Lorentz boost, the time coordinates t and t' are related by:

$$t' = \gamma(t - vz) = \gamma t , \tag{1.2.8}$$

where in the last step z has been set to 0 because the evaluation point P has coordinates $(b, 0, 0)$ in the K frame.

The Lorentz transformation of electromagnetic fields is most easily derived by starting from the transformation properties of the field-strength tensor $F_{\mu\nu}$

$$F_{\mu\nu} = \frac{\partial A_\mu}{\partial x^\nu} - \frac{\partial A_\nu}{\partial x^\mu} . \tag{1.2.9}$$

Using the explicit transformation given in Ref. [27] one can obtain the fields transformed from frame K' to K

$$\begin{cases} E_x = \gamma(E'_x + \beta B'_y) , & B_x = \gamma(B'_x - \beta E'_y) , \\ E_y = \gamma(E'_y - \beta B'_x) , & B_y = \gamma(B'_y + \beta E'_x) , \\ E_z = E'_z , & B_z = B'_z . \end{cases} \tag{1.2.10}$$

Using the equation system (1.2.7) to (1.2.10), one can find the non-zero transformed fields at P in the K system [30]

$$\begin{cases} E_x(\mathbf{r},t) &= \frac{1}{4\pi}\frac{q\gamma b}{r^3}(1+mr)\,e^{-mr}\,, \\ E_z(\mathbf{r},t) &= \frac{1}{4\pi}\frac{q\gamma vt}{r^3}(1+mr)\,e^{-mr}\,, \\ B_y(\mathbf{r},t) &= \beta E_x\,. \end{cases} \tag{1.2.11}$$

Here $r = r(t) = \sqrt{b^2+(\gamma vt)^2}$ is expressed entirely in terms of coordinates of frame K.

Now, we see, that the boosted electromagnetic field contains besides the electric field component also a magnetic component. It is useful to check that the Lorentz-invariants $I_1 = \mathbf{E}\cdot\mathbf{B}$ and $I_2 = \mathbf{E}^2 - \mathbf{B}^2$ are indeed the same in both reference frames.

Our aim is to replace the electromagnetic field of Eq. (1.2.11) by an effective plane wave pulse of electromagnetic radiation. Such a pulse would have to fulfill $I_1 = I_2 = 0$, which by the Lorentz-invariance is not true for the field (1.2.11).

However, we can see, that for $\beta \to 1$ the magnitude of the magnetic field and the x-component of the electric field become equal: $|B_y| \to |E_x|$. Indeed, the fields $\mathbf{E}_1 = E_x\hat{\mathbf{x}}$, $\mathbf{B} = B_y\hat{\mathbf{y}}$ are orthogonal, $\mathbf{E}_1\cdot\mathbf{B} = 0$ and $\mathbf{E}_1^2 - \mathbf{B}^2 \to 0$ for $\beta \to 1$. Let us have a look at the Poynting vector, which is the energy flux density (the energy which flows through a surface perpendicular to $\mathbf{S}$ per unit area and unit time) associated with the electromagnetic field,

$$\mathbf{S} = \mathbf{E}\times\mathbf{B}\,. \tag{1.2.12}$$

The Poynting's theorem says that an energy lost by electromagnetic fields equals an energy gained by particles plus an energy flow out of the volume. Inserting the electric and magnetic fields in the rest frame K of the observer/target, we obtain for the Poynting vector

$$\begin{aligned} \mathbf{S} &= E_xB_y\hat{\mathbf{z}} + E_zB_y\hat{\mathbf{x}} = \\ &= \frac{q^2}{16\pi^2}\frac{\beta\gamma^2b^2}{\left[b^2+(\gamma vt)^2\right]^3}\left(1+m\sqrt{b^2+(\gamma vt)^2}\right)^2 e^{-2m\sqrt{b^2+(\gamma vt)^2}}\hat{\mathbf{z}} + \\ &+ \frac{q^2}{16\pi^2}\frac{\beta\gamma^2vtb}{\left[b^2+(\gamma vt)^2\right]^3}\left(1+m\sqrt{b^2+(\gamma vt)^2}\right)^2 e^{-2m\sqrt{b^2+(\gamma vt)^2}}\hat{\mathbf{x}}\,. \end{aligned} \tag{1.2.13}$$

We see that the component of the Poynting-vector along the z-axis (the direction of motion of the ultrarelativistic charge) corresponds to a sharp pulse of electromagnetic radiation at the observation point, which extends over a time $\Delta t \sim b/(\gamma v)$. Parametrically $\Delta t \propto 1/\gamma$ vanishes in the ultrarelativistic limit. The component of the Poynting vector parallel to the x-axis (i.e. parallel to the impact parameter) is linear in the field component E_z and would vanish when averaged over the time-interval $\left(\frac{-\Delta t}{2}, \frac{\Delta t}{2}\right)$. In the method of equivalent photons it is neglected, and we keep only the pulse

$$\mathbf{S}_1 = E_x B_y \hat{\mathbf{z}} = \mathbf{E}_1 \times \mathbf{B}\,. \tag{1.2.14}$$

Jackson (Ref. [27]) goes still further, and shows how to include effects quadratic in E_z, which would not vanish after averaging over the interval Δt. To this end he introduces an artificial magnetic field component

$$\mathbf{B}_{art.} = -\hat{\mathbf{x}} \times \mathbf{E} = -E_z \hat{\mathbf{y}}\,, \tag{1.2.15}$$

which gives rise to a second pulse

$$\mathbf{S}_2 = E_z \hat{\mathbf{z}} \times \mathbf{B}_{art.} = (E_z)^2\, \hat{\mathbf{x}}\,. \tag{1.2.16}$$

The validity of this method to account for the electric field component E_z rests on some additional assumptions. Jackson asserts that it is safe to introduce the artificial magnetic field $\mathbf{B}_{art.}$ so long as the system situated at point P is composed, in its rest frame, of nonrelativistic particles whose response to a magnetic field can be neglected. As we will see below, in the ultrarelativistic limit $\gamma \gg 1$ the effect of the second pulse is strongly suppressed. We do therefore not analyse the approximations any further, we wish to remark, however, that in a field-theoretic calculation of Feynman-diagrams, the second pulse naturally arises.

The derivation of $n(\omega)$ consists of an analysis of the $\mathbf{E}$ and $\mathbf{B}$ fields of an relativistic charged particle Ze. The equivalent photon number is a function of photon energy in the fields surrounding charge per unit photon energy.

To summarize, the core of the Weizsäcker-Williams method is to approximate the $\mathbf{B}$ and $\mathbf{E}$ fields of an relativistic charge as appropriate plane wave pulses of

electromagnetic radiation. These pulses are called as equivalent pulses. The chief assumption of the EPA is that the effects of the various frequency components of equivalent radiation add incoherently.

Using equations that define the relation between the Poynting vectors and each of the pulse frequency spectrum

$$\int_{-\infty}^{\infty} \mathrm{d}t \int \mathrm{d}^2 b \cdot S\left(t, b\right) = \int_{0}^{\infty} \mathrm{d}\omega \int \mathrm{d}^2 b \, I\left(\omega, b\right) \tag{1.2.17}$$

one can get the two frequency spectra

$$I_1\left(\omega, b\right) = 2\left|E_x\left(\omega, b\right)\right|^2 , \tag{1.2.18}$$

$$I_2\left(\omega, b\right) = 2\left|E_z\left(\omega, b\right)\right|^2 . \tag{1.2.19}$$

The details of the transformation $E(t) \rightarrow E(\omega)$ are given in Appendix A. Finally, the explicit form of the electric force as a function of photon energy ((A.0.17) and (A.0.24)) (in the Heaviside-Lorentz units) with the electromagnetic limit ($m \rightarrow 0$) and with the ultrarelativistic condition ($v = c\beta$) takes the form

$$E_{\perp}(\omega) \equiv E_x(\omega) = \frac{1}{4\pi}\frac{Ze}{b\beta}\sqrt{\frac{2}{\pi}}\frac{b\omega}{\gamma\beta}K_1\left(\frac{b\omega}{\gamma\beta}\right) , \tag{1.2.20}$$

$$E_{\parallel}(\omega) \equiv E_z(\omega) = -\frac{i}{4\pi}\frac{Ze}{b\gamma\beta}\sqrt{\frac{2}{\pi}}\frac{b\omega}{\gamma\beta}K_0\left(\frac{b\omega}{\gamma\beta}\right) . \tag{1.2.21}$$

One can mark the x component of electric field as $\perp$, because it is perpendicular to the particle motion. Similarly $E_{\parallel} = E_z$.

The equivalent pulse P_1 has a frequency spectrum given by

$$I_1(\omega, b) = \frac{1}{4\pi}\left(\frac{Ze}{\pi\beta}\right)^2 \frac{1}{b^2}\left(\frac{b\omega}{\gamma\beta}\right)^2 K_1^2\left(\frac{b\omega}{\gamma\beta}\right) . \tag{1.2.22}$$

Similarly the pulse P_2 has a frequency spectrum in the form

$$I_2(\omega, b) = \frac{1}{4\pi}\frac{1}{\gamma^2}\left(\frac{Ze}{\pi\beta}\right)^2 \frac{1}{b^2}\left(\frac{b\omega}{\gamma\beta}\right)^2 K_0^2\left(\frac{b\omega}{\gamma\beta}\right) . \tag{1.2.23}$$

The intensity of the pulse P_1 and P_2 is expressed by the modified Bessel functions (K_0 and K_1).

In Fig. 1.4 the intensity for first (left panel) and second (right panel) pulse as the function of the impact parameter (b) end photon energy (ω) is shown. The intensity

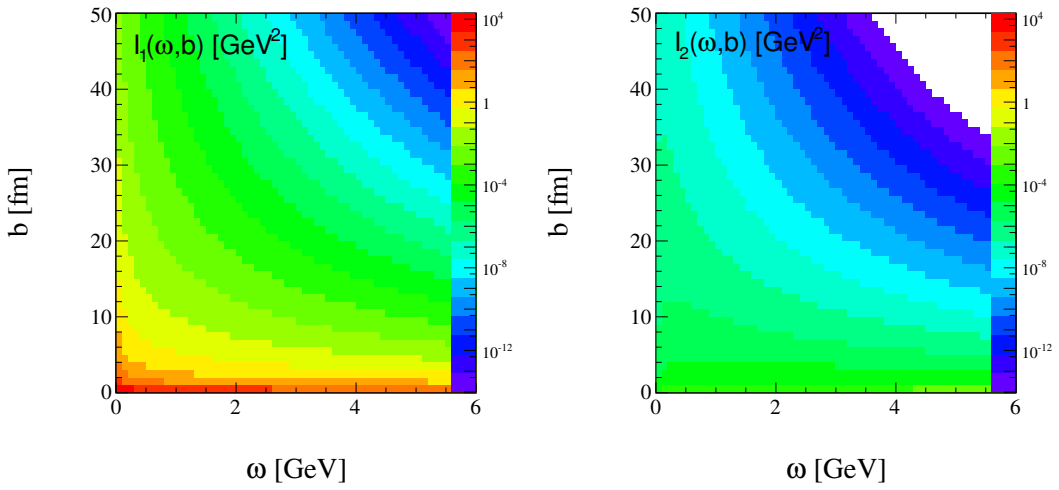

Figure 1.4: The frequency spectra for the equivalent pulse P_1 (left panel) and pulse P_2 (right panel) as a function of impact parameter and photon energy.

for both cases is shown in the same scale. Thus, one can observe that the result obtained from the equivalent pulse P_1 is more important than for the pulse P_2. The frequency spectra for the equivalent pulse P_1 has a maximum at the corner of very small values of the impact parameter and photon energy. The small intensity of the second pulse comes from the fact, that in comparison to the first pulse, the second one is divided by a square of γ factor (see Eq. (1.2.22) and (1.2.23)). Thus, the huge difference between $I_1(\omega, b)$ and $I_2(\omega, b)$ becomes important for ultrarelativistic particles. The above figures were calculated for $\gamma = 107$ ($\sqrt{s_{NN}} = 200$ GeV, RHIC energy).

In the next step one has to determine the equivalent photon number for a nucleus with the charge Ze. The dependence between calculated frequency spectra and the impact parameter-dependent equivalent photon spectra $N(\omega, b)$ is the following [27]

$$N(\omega, b) = \frac{1}{\omega} \left[I_1(\omega, b) + I_2(\omega, b) \right] . \tag{1.2.24}$$

Usually one uses a fine-structure constant $\alpha_{em} \simeq 1/137$ instead of an electron charge. Using the Heaviside-Lorentz units, we can write the well-known text-book relation $e^2 = 4\pi\alpha_{em}$. In addition defining

$$u = \frac{\omega b}{\gamma \beta} \tag{1.2.25}$$

one can write the final form of the flux of virtual photons (for point-like charge)

$$N(\omega, b) = \frac{Z^2 \alpha_{em}}{\pi^2 \beta^2} \frac{1}{\omega} \frac{1}{b^2} u^2 \left[K_1^2(u) + \frac{1}{\gamma^2} K_0^2(u) \right] . \tag{1.2.26}$$

The unit of the equivalent photon fluxes is $\mathrm{GeV}^{-1}\ \mathrm{fm}^{-2}$ or equivalently GeV.

The argument of the Bessel function is expressed through the impact parameter b, relativistic parameters γ, β and the energy of the photon ω. For ultrarelativistic case, using the uncertainty principle:

$$\Delta t \Delta E \simeq 1 \rightarrow \frac{b}{\gamma v} \omega \simeq 1 \xrightarrow{v \simeq c \rightarrow \beta \simeq 1} \omega_{max} \simeq \frac{\gamma \beta}{b} , \tag{1.2.27}$$

where Δt is the collision time, one can evaluate maximal value of the photon energy. This condition is called an adiabatic cutoff energy condition. This means that, for example, at RHIC energies ($\gamma = 107$, $\sqrt{s_{NN}} = 200$ GeV) in an electromagnetic collision of two gold (^{197}Au) nuclei the excitation of states with photon energies up to about 3 GeV can be reached.

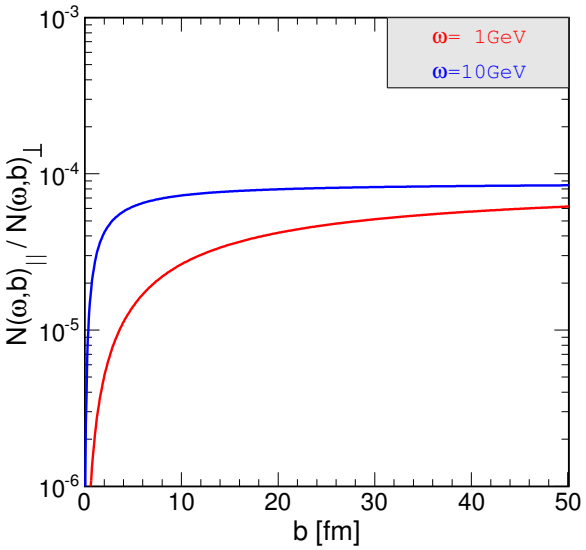

Figure 1.5: The ratio of longitudinal to transverse impact-parameter-dependent equivalent photon distributions (see Eq. (1.2.28) and (1.2.29)) for two different photon energies.

Fig. 1.5 presents the suppression of the longitudinal contribution in the equivalent photon contribution for a point-like charge. One can see the ratio of the longitudinal

$N(\omega, b)$ (in analogy to Eq. (1.2.21))

$$N_{\parallel}(\omega, b) = \frac{Z^2\alpha_{em}}{\pi^2\beta^2}\frac{1}{\omega}\frac{1}{b^2}u^2\frac{1}{\gamma^2}K_0^2(u) \tag{1.2.28}$$

to the perpendicular one (in analogy to Eq. (1.2.20))

$$N_{\perp}(\omega, b) = \frac{Z^2\alpha_{em}}{\pi^2\beta^2}\frac{1}{\omega}\frac{1}{b^2}u^2K_1^2(u) \tag{1.2.29}$$

for two values of photon energy (red line for $\omega = 1$ GeV, blue line for $\omega = 10$ GeV; the Lorentz factor $\gamma = 107$ ($\sqrt{s_{NN}} = 200$ GeV)). With larger value of the impact parameter this difference becomes smaller, however the longitudinal contribution is about four orders of magnitude smaller than the perpendicular one.

Since the nucleus is an extended object, it is more realistic to consider the charge distribution. Impact parameter-dependent equivalent photon spectra $N(\omega, b)$ for extended charge distribution were given e.g. by G. Baur and L. Ferreira (Ref. [31]), F. Krauss, M. Greiner and G. Soff (Ref. [32]). Following those suggestions, firstly one can write the 4-potential which is composed of functions describing the radiation fields Φ and $\mathbf{A}$

$$A^{\nu} = (\Phi, \mathbf{A}) \ . \tag{1.2.30}$$

In addition the 4-current is composed of the charge density ρ and current density $\mathbf{J}$

$$J^{\nu} = (\rho, \mathbf{J}) \ . \tag{1.2.31}$$

We consider here the case of massless photon. Thus, one can write one of the Maxwell equations in the gauge $\partial_{\nu}A^{\nu} = 0$

$$\Box A^{\nu}(r) = J^{\nu}(r) \ . \tag{1.2.32}$$

This is the inhomogeneous wave equation for the electromagnetic vector-potential in the Lorentz gauge in the frame K. In the reference system K' of the moving (with ultrarelativistic velocity) charge the current-density is expressed through

$$J'^{\nu}(r') = \rho(|\mathbf{r}'|)\, u'^{\nu} \tag{1.2.33}$$

with the four-velocity of the spherical symmetric charge distribution $u'^{\nu} = (1, 0, 0, 0)$. However, in the observer system $u^{\nu} = \gamma(1, 0, 0, \beta)$. Another 4-vector defining the

photon momentum in a respective frame of reference has the form: $k'^{\nu} = (\omega', \mathbf{k}')$ and $k^{\nu} = (\omega, \mathbf{k})$. Using the Fourier transform of the current-density from x variable to k one can get

$$\begin{aligned} J'^{\nu}(k') &= \int_{-\infty}^{\infty} \mathrm{d}^4 x' e^{ik'r'} J'^{\nu}(r') \\ &= 2\pi\delta(\omega')\,\rho(|\mathbf{k}'|)\,u'^{\nu} \\ &= 2\pi\delta(k'\cdot u')\,\rho\left(\sqrt{-k^2}\right)u'^{\nu}\ . \end{aligned} \tag{1.2.34}$$

Similarly using the Fourier transform of Eq. (1.2.32) and the solution of Eq. (1.2.34) one can obtain

$$\begin{aligned} A^{\nu}(k) &= -\frac{1}{k^2}J^{\nu}(k) \\ &= -2\pi\delta(k\cdot u)\,\frac{\rho\left(\sqrt{-k^2}\right)}{k^2}u^{\nu} \\ &= -2\pi\delta(k\cdot u)\,Ze\frac{F(-k^2)}{k^2}u^{\nu}\ . \end{aligned} \tag{1.2.35}$$

In this place the electromagnetic nuclear form factor of the nucleus with the nuclear charge number Z was introduced.

As was demonstrated for point-like charge (Fig. 1.5) also the second pulse can be neglected (Refs. [24, 27]). Thus, only the x component of the electric field is important for photon spectrum taking into account the realistic charge distribution.

The final form of the equivalent photon flux for realistic charge distribution is derived in Appendix A.1 (Eq. (A.1.42))

$$N(\omega, b) = \frac{Z^2\alpha_{em}}{\pi^2\beta^2}\frac{1}{\omega}\frac{1}{b^2}\left|\int \mathrm{d}\chi\,\chi^2\frac{F\left(\frac{\chi^2+u^2}{b^2}\right)}{\chi^2+u^2}J_1(\chi)\right|^2\ , \tag{1.2.36}$$

where J_1 is the Bessel function. In the above equation the scaling variable $u = \frac{\omega b}{\gamma\beta}$ was used which was defined in Eq. (1.2.25). In addition, a dimensionless auxiliary variable $\chi = k_{\perp}b$ was introduced.

It seems interesting in this context to calculate the form of the equivalent photon number for a point-like charge. This will be a check of the correctness of Eq. (1.2.36). In this case the value of the form factor is a constant $F(q^2) = 1$. Then

$$N(\omega, b) = \frac{Z^2\alpha_{em}}{\pi^2\beta^2}\frac{1}{\omega}\frac{1}{b^2}u^2K_1^2(u)\ . \tag{1.2.37}$$

In this place the result of the integral from the Abramowitz's & Stegun's handbook (Ref. [33]): $\int_0^\infty da\, a^2 J_1(a)/(a^2+b^2) = bK_1(b)$ was used. Eq. (1.2.37) is the same as that given by Eq. (1.2.29).

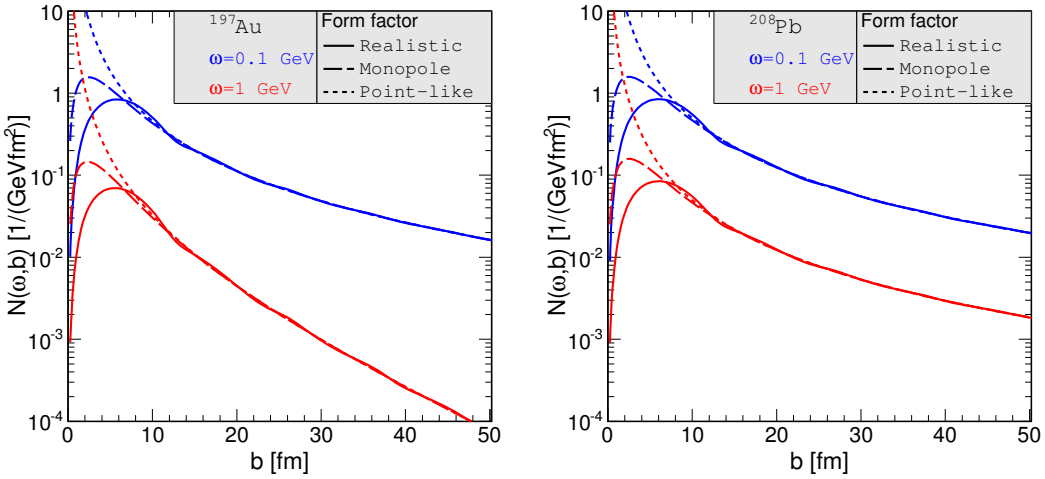

Figure 1.6: Equivalent photon fluxes as a function of the impact parameter for gold (left panel) and lead (right panel) nucleus for two different values of photon energy.

In Fig. 1.6 the equivalent photon fluxes as a function of the impact parameter is shown. The left panel is for gold nucleus and the right panel for lead nucleus. In practice for gold and lead different values of γ must be used adequate for appropriate experiments:

- ^{197}Au-^{197}Au collisions at $\sqrt{s_{NN}} = 200$ GeV (RHIC energy) $\rightarrow \gamma = 107$,
- ^{208}Pb-^{208}Pb collisions at $\sqrt{s_{NN}} = 2.76$ TeV (LHC energy) $\rightarrow \gamma = 1471$.

In addition here three different forms of the form factor are taken into account: solid lines - realistic form factor, dashed lines - monopole form factor, dotted lines - point-like form factor (the types of the form factors are presented in Chapter 1.4). One can see from the figure that the biggest differences for these three form factors occur for $b < 10$ fm. For larger value of the impact parameter, this difference becomes smaller. This is natural, as from very large distances $b \gg R_A$, the nucleus should "look like" a point-like charge. From the comparison of the result for two different values of γ, one can observe, that for more ultrarelativistic energies these distributions have larger tail in the impact parameter.

1.3 Nuclear cross section

In section 1.2 a general formula for the total cross section (see Eq. (1.2.3)) for the production of pairs of particle in heavy ion collision was written. In this section we will introduce this equation but in the exact form which will be used in the calculation of the nuclear distributions for the production of pairs of mesons, leptons or quarks in ultraperipheral ultrarelativistic heavy ion collisions. The main part of the following derivation can be found for example in Ref. [32].

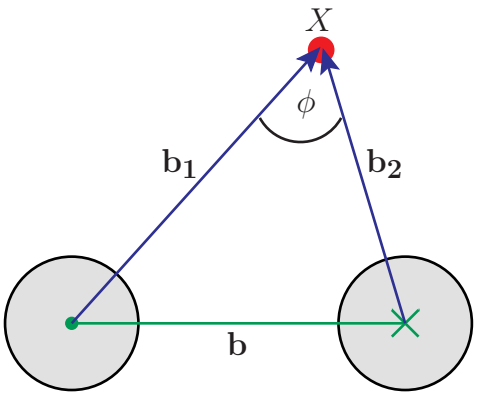

Figure 1.7: Diagram illustrates quantities in the impact parameter space. This is a view perpendicular to the direction of motion of two ions which have the same radius (R).

In the following the equivalent photon approximation will be considered in the impact parameter space. This choice gives the possibility to the exclude central collisions or the situation when the two ions overlap in the impact parameter space ($b < 2R$). In this dissertation, we will consider only ultraperipheral collisions. This means that the distance between two nuclei is larger than the sum of radii of these nuclei. The definition of the quantities in the impact parameter space is presented in Fig. 1.7. The value of the impact parameter can be written as $b = |\mathbf{b}| = \sqrt{|\mathbf{b_1}|^2 + |\mathbf{b_2}|^2 - 2|\mathbf{b_1}||\mathbf{b_2}|\cos\phi}$.

As was mentioned in the previous section, kinematic variables can be separated into components perpendicular and parallel to the direction of motion of the two colliding ions. Going by this line of thought, one can take into account a polarization-dependent cross section for $\gamma\gamma$ fusion. Additionally, connecting the relation (1.2.1)

with (1.2.3), one can write

$$\sigma_{A_1A_2\to A_1A_2X}\left(\sqrt{s_{A_1A_2}}\right) = \int \mathrm{d}^2\mathbf{b}\,\mathrm{d}\omega_1\,\mathrm{d}\omega_2\left[\sigma^{\perp}_{\gamma\gamma\to X_1X_2}\left(\omega_1,\omega_2\right)N_{\perp}\left(\omega_1,\omega_2,\mathbf{b}\right) + \sigma^{\parallel}_{\gamma\gamma\to X_1X_2}\left(\omega_1,\omega_2\right)N_{\parallel}\left(\omega_1,\omega_2,\mathbf{b}\right)\right] . \quad (1.3.38)$$

The details of this derivation can be found in Ref. [34]. The total two-photon fusion cross section is expressed through the polarized two-photon fusion cross section $\sigma_{\gamma\gamma\to X} = \left(\sigma^{\perp}_{\gamma\gamma\to X} + \sigma^{\parallel}_{\gamma\gamma\to X}\right)/2$. For these cross sections the polarisation vectors of the two photons are parallel and perpendicular to each other, respectively. The definition of fluxes for photons with parallel and perpendicular linear polarizations are presented in [1].

After introducing a few transformations (see Appendix B), the final form of the cross section in the equivalent photon approximation is expressed through the five-fold integral

$$\sigma_{A_1A_2\to A_1A_2X}\left(\sqrt{s_{A_1A_2}}\right) = \int \sigma_{\gamma\gamma\to X_1X_2}\left(\sqrt{s_{A_1A_2}}\right)N\left(\omega_1,\mathbf{b_1}\right)N\left(\omega_2,\mathbf{b_2}\right)S^2_{abs}\left(\mathbf{b}\right) \times 2\pi b\mathrm{d}b\,\mathrm{d}\bar{b}_x\,\mathrm{d}\bar{b}_y\,\frac{W_{\gamma\gamma}}{2}\mathrm{d}W_{\gamma\gamma}\,\mathrm{d}Y_{X_1X_2} , \quad (1.3.39)$$

where

$$Y_{X_1X_2} = \frac{1}{2}\left(y_{X_1} + y_{X_2}\right) \quad (1.3.40)$$

is a rapidity of the outgoing X_1X_2 system. The invariant mass of the $\gamma\gamma$ system is defined as

$$W_{\gamma\gamma} = \sqrt{4\omega_1\omega_2} . \quad (1.3.41)$$

The quantities $\bar{b}_x$, $\bar{b}_y$ are the components of the $\mathbf{b_1}$ and $\mathbf{b_2}$ vectors (see Fig. 1.7):

$$\mathbf{b_1} = \left[\bar{b}_x + \frac{b}{2}, \bar{b}_y\right] ,$$
$$\mathbf{b_2} = \left[\bar{b}_x - \frac{b}{2}, \bar{b}_y\right] . \quad (1.3.42)$$

Eq. (1.3.39) allows to calculate the value of the total cross section, distributions in the impact parameter (b), invariant mass ($W_{\gamma\gamma} = M_{X_1X_2}$) of the considered particles in the final state or rapidity of the pair ($Y_{X_1X_2}$) of these particles. The full derivation of this equation is given in Appendix B.

We wish to emphasize that very often experimental constraints cannot be easily imposed. If one wants to put some cuts on produced particles which come from experimental requirement or have the distribution in some helpful and interesting kinematical variables of an individual particle, more complicated calculations are required. A good idea is to use the elementary cross section not as one-dimensional quantity but differential in some variables. Then one has to replace $\sigma_{\gamma\gamma\to X_1X_2}(W_{\gamma\gamma})$ by two-dimensional quantity $\frac{\mathrm{d}\sigma_{\gamma\gamma\to X_1X_2}}{\mathrm{d}z}(W_{\gamma\gamma}, z)$, where $z = \cos\theta$. Then the calculation starts to be more complicated and labour-intensive, because Eq. (1.3.39) has one additional dimension.

Four-momenta (energy, transverse and longitudinal momentum) of one particle (X_i, $i = 1, 2$) in the X_1X_2 center of mass frame can be written as

$$E_{X_i} = \frac{\sqrt{\hat{s}}}{2} , \tag{1.3.43}$$

$$p_{X_i} = \sqrt{E_{X_i}^2 - m_{X_i}^2} , \tag{1.3.44}$$

$$p_{t,X_1} = \sqrt{1 - z^2} p_{X_1} , \tag{1.3.45}$$

$$p_{l,X_1} = z p_{X_1} . \tag{1.3.46}$$

In the equation above, $\hat{s} = W_{\gamma\gamma}^2$ is defined through the energy in the X_1X_2 center of mass frame (similarly like z).

The rapidity of each of the particles in the final state,

$$y_1 = Y_{X_1X_2} + y_{i/X_1X_2}(W_{\gamma\gamma}, z) , \tag{1.3.47}$$

where $y_{i/X_1X_2}(W_{\gamma\gamma}, z)$ expresses the rapidity of one of the particles (X_1 or X_2) in the recoil X_1X_2 system of reference. Other kinematical variables are calculated by adding relativistically velocities (Ref. [35])

$$\mathbf{v}_i = \frac{\mathbf{P}_{X_1X_2}}{E_{X_1X_2}} \oplus \mathbf{v}_{i/X_1X_2} , \tag{1.3.48}$$

where the first element in the above equation expresses the velocity vector ($\mathbf{v}_{X_1X_2}$) of the X_1X_2 system in the nucleus-nucleus center of mass ($\mathbf{P}_{X_1X_2}$ and $E_{X_1X_2}$ is momentum and energy of the X_1X_2 system, respectively) and $\mathbf{v}_{i/X_1X_2}$ is the velocity of one of the particles in the X_1X_2 system. Additionally, one can write the relations

which come from the energy-momentum conservation

$$E_{X_1X_2} = \omega_1 + \omega_2 \,, \tag{1.3.49}$$

$$P^z_{X_1X_2} = \omega_1 - \omega_2 \,. \tag{1.3.50}$$

Above a generic reaction $A_1A_2 \to A_1A_2X_1X_2$, where X_1 and X_2 can be mesons, leptons or quarks was considered. The most important physical quantity in Eq. (1.3.39) is the elementary cross section for the $\gamma\gamma \to X_1X_2$ process and the charge form factor of nucleus which is hidden in the equivalent photon spectra (Eq. (1.2.36)).

1.4 Nuclear form factor and charge density

In this section we will focus on our knowledge of the nuclear form factor which is the main ingredient of the photon fluxes discussed in the previous section.

To start let us introduce the cross section for scattering of a point-like and spinless projectile with the charge e (e.g. an electron) off a heavy, spinless, scattering centre with no inner structure and electric charge Ze.

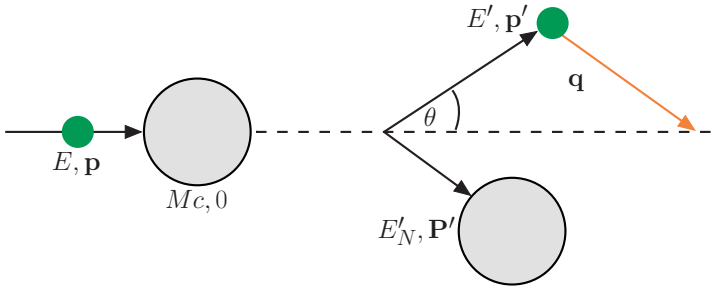

Figure 1.8: Kinematics of elastic electron-nucleus scattering.

Fig. 1.8 depicts the kinematics of the elastic electron-nucleus scattering. The electron moves with ultrarelativistic velocity, so its energy fulfills the dependences

$$E \gg m_e c^2 \,, \tag{1.4.51}$$

$$E \approx |\mathbf{p}|\, c \,. \tag{1.4.52}$$

Fixing that primes denote quantities after scattering, one can write four-momentum of the electron and nucleus in the laboratory frame

$$p = \left(\frac{E}{c}, \mathbf{p}\right) , \qquad p' = \left(\frac{E'}{c}, \mathbf{p}'\right) , \tag{1.4.53}$$

$$P = (Mc, 0) , \qquad P' = \left(\frac{E'_N}{c}, \mathbf{P}'\right) . \tag{1.4.54}$$

The Rutherford scattering formula can be calculated within both the non-relativistic [36] and relativistic approach [37]. The final form of the Rutherford cross section reads:

$$\left(\frac{\mathrm{d}\sigma}{\mathrm{d}\Omega}\right)_{\text{Rutherford}} = \frac{4Z^2\alpha^2 \left(\hbar c\right)^2 E'^2}{\left|\mathbf{q}c\right|^4} , \tag{1.4.55}$$

where the fine-structure constant equals $\alpha = e^2/\left(4\pi\epsilon_0\hbar c\right) \approx 1/137$ and $\mathbf{q} = \mathbf{p} - \mathbf{p}'$ is the momentum transfer (see Fig. 1.8). Eq. (1.4.55) can be interpreted in terms of the exchange of a virtual photon (factor $1/\left|\mathbf{q}\right|^2$) coupling to the charged particles with the strength proportional to their charges. In fact, the three-momentum transfer $\mathbf{q}$ is the momentum transferred by the exchanged photon.

One can assume that the electron energy and the magnitude of its momentum do not change in the interaction when recoil of the scattering center is neglected in the Rutherford scattering

$$E = E', \qquad \left|\mathbf{p}\right| = \left|\mathbf{p}'\right| . \tag{1.4.56}$$

The momentum transfer is given by

$$\left|\mathbf{q}\right| = 2\left|\mathbf{p}\right| \sin\frac{\theta}{2} , \tag{1.4.57}$$

where θ is a scattering angle (see Fig. 1.8). If we recall that Eq. (1.4.52) is a good approximation, replacing E' by Eq. (1.4.52) one can obtain the Rutherford differential cross section

$$\left(\frac{\mathrm{d}\sigma}{\mathrm{d}\Omega}\right)_{\text{Rutherford}} = \frac{Z^2\alpha^2 \left(\hbar c\right)^2}{4E^2 \sin^4\frac{\theta}{2}} . \tag{1.4.58}$$

In fact the Rutherford cross section should be modified by spin effects. Including the spin $\frac{1}{2}$ of the electron and neglecting nuclear recoil, one can write the formula for differential cross section which was obtained by Mott (Refs. [38, 39])

$$\left(\frac{\mathrm{d}\sigma}{\mathrm{d}\Omega}\right)_{\text{Mott}} = \left(\frac{\mathrm{d}\sigma}{\mathrm{d}\Omega}\right)_{\text{Rutherford}} \left(1 - \beta^2 \sin^2\frac{\theta}{2}\right) \tag{1.4.59}$$

with $\beta = v/c$. In the limiting case of $\beta \to 1$, the above equation takes a simpler form

$$\left(\frac{\mathrm{d}\sigma}{\mathrm{d}\Omega}\right)_{\mathrm{Mott}} = \left(\frac{\mathrm{d}\sigma}{\mathrm{d}\Omega}\right)_{\mathrm{Rutherford}} \cdot \cos^2\frac{\theta}{2}\,. \tag{1.4.60}$$

The expression shows that the Mott cross section drops faster at large scattering angle than the Rutherford cross section. The same situation can be seen in Fig. 1.9.

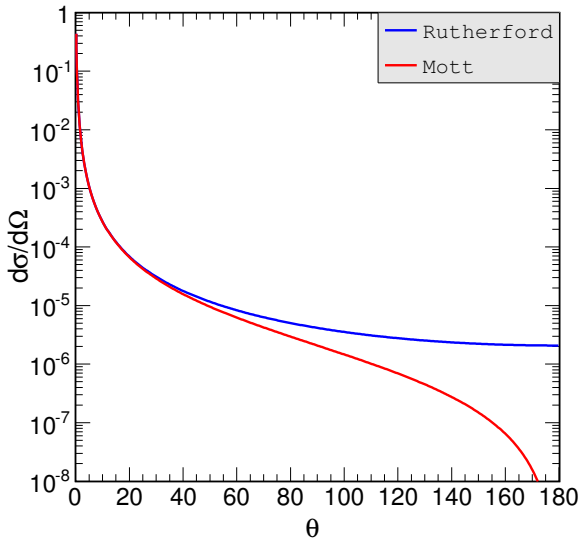

Figure 1.9: Comparison of the Rutherford and Mott cross section for scattering off a spinless target.

For larger values of a scattering angle ($\theta > 40°$) the difference becomes larger. Maximal deviation from the Rutherford formula appears at 180°. For a particle moving with relativistic velocity (the calculations presented in the figure are done for the case when $\beta = 1$), the projection of its spin $\mathbf{s}$ on the direction of its motion $\mathbf{p}/\left|\mathbf{p}\right|$ is a conserved quantity. This is called conservation of a helicity (in the $\beta \to 1$ limit) defined as

$$h = \frac{\mathbf{s}\cdot\mathbf{p}}{\left|\mathbf{s}\right|\left|\mathbf{p}\right|}\,. \tag{1.4.61}$$

The relativistic particles have either spin parallel to their momentum ($h = 1$) or spin pointing in the opposite direction of their motion ($h = -1$).

For a spinless target, at $\theta = \pi$, conservation of angular momentum would require that the helicity changes sign, in contradiction with its conservation. The orbital angular momentum l is perpendicular to the direction of motion. It therefore can not

cause any change in the direction of motion component of the angular momentum. Hence scattering at $\theta = 180°$ has to be completely lapsed.

If the target has spin, backscattering ($\theta = \pi$) of electrons is possible (non-zero cross section), because conservation of total angular momentum can be compensated by a change in the spin direction of the target. In this case, the above argumentation is not valid, and $\theta = \pi$ is possible.

Experimentally, the determination of a nuclear form factor involves some comparison of the experimental cross section with the Mott cross section for a nucleus without spin

$$\left(\frac{\mathrm{d}\sigma}{\mathrm{d}\Omega}\right)_{\text{exp.}} = \left(\frac{\mathrm{d}\sigma}{\mathrm{d}\Omega}\right)_{\text{Mott}} \cdot \left|F\left(\mathbf{q}^2\right)\right|^2 \ . \tag{1.4.62}$$

In practice, one therefore measures the cross section for fixed beam energy at various angles.

In order to derive the exact form of the form factor, one has to write the expression for the matrix element for $e + A \to e + A$ scattering. The incident and the outgoing electron (see Fig. 1.8) can be described by plane waves:

$$\psi_i = \frac{1}{\sqrt{V}} \exp\left(\frac{i\mathbf{p}\cdot\mathbf{r}}{\hbar}\right) \ , \tag{1.4.63}$$

$$\psi_f = \frac{1}{\sqrt{V}} \exp\left(\frac{i\mathbf{p}'\cdot\mathbf{r}'}{\hbar}\right) \ . \tag{1.4.64}$$

V is the normalization volume. The Hamiltonian of the Coulomb interaction for a charge e in an electric potential $\phi(\mathbf{r})$ generated by the nucleus is given by

$$\mathcal{H}_{int} = e\phi(\mathbf{r}) \ . \tag{1.4.65}$$

. Then the matrix element takes the form:

$$\langle \psi_i \left| \mathcal{H}_{int} \right| \psi_f \rangle = -\frac{e\hbar^2}{V\left|\mathbf{q}\right|^2} \int \exp\left(\frac{i\mathbf{q}\cdot\mathbf{r}}{\hbar}\right) \Delta\phi(\mathbf{r})\, \mathrm{d}^3 r \ . \tag{1.4.66}$$

Assuming that the charge density $\rho(\mathbf{r})$ is static, the electrostatic potential can be replaced by

$$\Delta\phi(\mathbf{r}) = -\frac{\rho(\mathbf{r})}{\epsilon_0} \ . \tag{1.4.67}$$

The charge density is normalized as

$$\int \rho(\mathbf{r})\, \mathrm{d}^3 r = Ze \ . \tag{1.4.68}$$

Defining a normalized charge distribution function which fulfills the relations

$$f(\mathbf{r}) = \frac{\rho(\mathbf{r})}{Ze}\,, \qquad \int f(\mathbf{r})\,\mathrm{d}^3r = 1 \tag{1.4.69}$$

one can finally rewrite

$$\langle \psi_i | \mathcal{H}_{int} | \psi_f \rangle = \frac{Ze^2\hbar^2}{\epsilon_0 V |\mathbf{q}|} \int f(\mathbf{r}) \exp\left(\frac{i\mathbf{q}\cdot\mathbf{r}}{\hbar}\right) \mathrm{d}^3r\,. \tag{1.4.70}$$

The integral

$$F(\mathbf{q}) = \int f(\mathbf{r}) \exp\left(\frac{i\mathbf{q}\cdot\mathbf{r}}{\hbar}\right) \mathrm{d}^3r \tag{1.4.71}$$

is the Fourier transform of the normalized charge distribution function $f(\mathbf{r})$. It is called the form factor of the charge distribution. This factor contains all information about the spatial distribution of electric charge in the studied object. The form factor fulfills the relations:

$$0 \leqslant \quad |F(\mathbf{q})| \quad \leqslant 1\,, \tag{1.4.72}$$

$$\text{for } |\mathbf{q}| \to 0\text{:} \qquad F(\mathbf{q}) \quad \to 1\,, \tag{1.4.73}$$

$$\text{for } |\mathbf{q}| \to \infty\text{:} \qquad F(\mathbf{q}) \quad \to 0\,. \tag{1.4.74}$$

One should explain here, that for a spherically symmetric scattering object, the form factor depends on the modulus of the momentum transfer and therefore is often written as $F(|\mathbf{q}|)$ or $F(\mathbf{q}^2)$. In the following we shall use the second notation.

Integration over the total solid angle (in polar coordinates) can be written

$$F\left(\mathbf{q}^2\right) = 4\pi \int f(r)\, \frac{\sin\left(\frac{|\mathbf{q}|r}{\hbar}\right)}{\frac{|\mathbf{q}|r}{\hbar}} r^2 \mathrm{d}r\,, \tag{1.4.75}$$

with the normalization condition

$$1 = \int f(\mathbf{r})\,\mathrm{d}^3r = \int_0^\infty \int_{-1}^1 \int_0^{2\pi} f(r)\, r^2 \mathrm{d}\phi\, \mathrm{d}\cos\vartheta\, \mathrm{d}r = 4\pi \int_0^\infty f(r)\, r^2 \mathrm{d}r \tag{1.4.76}$$

so that $F(\mathbf{0}) = 1$. In principle, according to Eq. (1.4.71), the radial charge distribution is determined from the inverse Fourier transform of the measured distribution $F(\mathbf{q}^2)$

$$f(\mathbf{r}) = \frac{1}{(2\pi)^3} \int F\left(\mathbf{q}^2\right) \exp\left(-\frac{i\mathbf{q}\cdot\mathbf{r}}{\hbar}\right) \mathrm{d}^3q\,. \tag{1.4.77}$$

The electron energy is finite and the cross section falls very quickly for larger momentum transfer, therefore in a given experiment, a very limited range of $\mathbf{q}$ is measurable. Information about radius of the nucleus can be obtained from the form factor behaviour for $\mathbf{q}^2 \to 0$. If the wavelength $\lambda = h/|\mathbf{q}|$ is considerably larger than the nuclear radius R then in the limit

$$|\mathbf{q}|\, R \ll \hbar \tag{1.4.78}$$

we can make a Taylor-expansion and keep only the lowest two terms (Refs. [40, 41])

$$\begin{aligned} F\left(\mathbf{q}^2\right) &= \int f(\mathbf{r}) \sum_{n=0}^{\infty} \frac{1}{n!} \left(\frac{i\,|\mathbf{q}|\,|\mathbf{r}| \cos\vartheta}{\hbar} \right)^n \mathrm{d}^3 r, \qquad \vartheta = \sphericalangle(\mathbf{r}, \mathbf{q}) \\ &= \int_0^{\infty} \int_{-1}^{1} \int_0^{2\pi} f(r) \left[1 - \frac{1}{2} \left(\frac{|\mathbf{q}|\, r}{\hbar} \right)^2 \cos^2\vartheta + \ldots \right] \mathrm{d}\phi\, \mathrm{d}\cos\vartheta\, r^2 \mathrm{d}r \\ &= 4\pi \int_0^{\infty} f(r)\, r^2 \mathrm{d}r - \frac{1}{2!\cdot 3} \frac{\mathbf{q}^2}{\hbar^2} 4\pi \int_0^{\infty} f(r)\, r^4 \mathrm{d}r + \ldots \\ &= 1 - \frac{1}{6} \frac{\mathbf{q}^2 \left\langle r^2 \right\rangle}{\hbar^2} + \ldots . \end{aligned} \tag{1.4.79}$$

In the above equation the normalization condition (Eq. (1.4.76)) was used and the mean square radius was defined as

$$\left\langle r^2 \right\rangle = 4\pi \int_0^{\infty} r^2 f(r)\, r^2 \mathrm{d}r \; . \tag{1.4.80}$$

Table 1.1: Relation between charge distributions and form factors for a few spherically symmetric charge distributions. This table is partially copied from Ref. [36].

Charge distribution $f(r) = \frac{\rho(r)}{Ze}$		Form factor $F(\mathbf{q}^2)$	
point	$\frac{\delta(r)}{4\pi}$	constant	1
exponential	$\frac{a^3}{8\pi} \exp(-ar)$	dipole	$\left(1 + \frac{\mathbf{q}^2}{a^2\hbar^2}\right)^{-2}$
Gaussian	$\left(\frac{a^2}{2\pi}\right)^{\frac{3}{2}} \exp\left(-\frac{a^2 r^2}{2}\right)$	Gaussian	$\exp\left(-\frac{\mathbf{q}^2}{2a^2\hbar^2}\right)$
hom. sphere	$r \leqslant R \Rightarrow \frac{3R^3}{4\pi}$, $r > R \Rightarrow 0$	oscillating	$\frac{3\hbar^3}{(\lvert\mathbf{q}\rvert R)^3} \left(\sin\frac{\lvert\mathbf{q}\rvert R}{\hbar} - \frac{\lvert\mathbf{q}\rvert R}{\hbar} \cos\frac{\lvert\mathbf{q}\rvert R}{\hbar} \right)$
Yukawa	$\frac{1}{4\pi r} \Lambda^2 \exp(-\Lambda r)$	monopole	$\frac{\Lambda^2}{\Lambda^2 + \lvert\mathbf{q}\rvert^2}$

Table 1.1 shows the relation between the normalized charge distribution $\rho(r)/(Ze)$ and the corresponding form factor in the Born approximation. $\rho(r)$ and $|F(\mathbf{q}^2)|$ are shown in Ref. [36] (see Fig. 5.6). If the object is larger then the form factor falls off faster. The analysis of electron scattering provides more information about charge distributions than any other technique. $F(\mathbf{q}^2)$ can be extracted from electron-nucleus scattering. Often one choose a reasonable parametrization of $f(\mathbf{r})$ which approximately describes experimental $F(\mathbf{q}^2)$. In principle $F(\mathbf{q}^2)$ can be used to reconstruct charge density in the nucleus. For heavy nuclei, these charge distributions [40] can be approximately described by the two-parameter Fermi distribution [42], called equivalently Woods-Saxon distribution

$$\rho(r) = \frac{\rho_0}{1 + \exp\left(\frac{r-c}{a}\right)} , \tag{1.4.81}$$

where the normalization constant ρ_0 is chosen so that the condition (1.4.68) is fulfilled. The parameters a and c determine the shape of the $\rho(r)$ distribution. The parameter c is the constant radius at which $\rho(r)$ has decreased by one half. The parameter a is usually related to the thickness of the edge of a nucleus t, defined as a distance in which the charge density drops from 0.9 to 0.1 of the density at the zero radius. When $a \ll c$ it can be written (Ref. [43])

$$t = r_{(\rho/\rho_0=0.1)} - r_{(\rho/\rho_0=0.9)} \approx 4.4a . \tag{1.4.82}$$

In practice, this value is almost the same for all heavy nuclei.

Table 1.2 and Table 1.3 contain a list of charge density distribution parameters which were used in Ref. [42]. It is very difficult to find in the literature the parameters of the two-parameter Fermi model for the charge distribution of the ^{208}Pb isotope. In Table 1.3, the parameters for the ^{207}Pb isotope are given. The arguments that it is reasonable to use the same parameters of c and a for the ^{207}Pb and ^{208}Pb isotopes are presented in Appendix C.

In Fig. 1.10 one can see the charge density distribution for gold and lead nucleus. The red line is related to the gold nucleus and the blue line is for the lead nucleus. The presented distribution for ^{208}Pb in Fig. 1.10 has similar values like those shown in Ref. [40]. The normalization of charge distribution to Ze leads to

Table 1.2: Charge density distribution parameters for ^{197}Au

$\sqrt{\langle r^2 \rangle}$ [fm]	c [fm]	a [fm]	Ref.
5.33	6.38	0.535	[44]
5.27			[45]

Table 1.3: Charge density distribution parameters for ^{207}Pb and ^{208}Pb.

^{207}Pb				^{208}Pb	
$\sqrt{\langle r^2 \rangle}$ [fm]	c [fm]	a [fm]	Ref.	$\sqrt{\langle r^2 \rangle}$ [fm]	Ref.
5.513	6.62	0.546	[46]	5.499	[47]
5.497			[48]	5.503	[48]

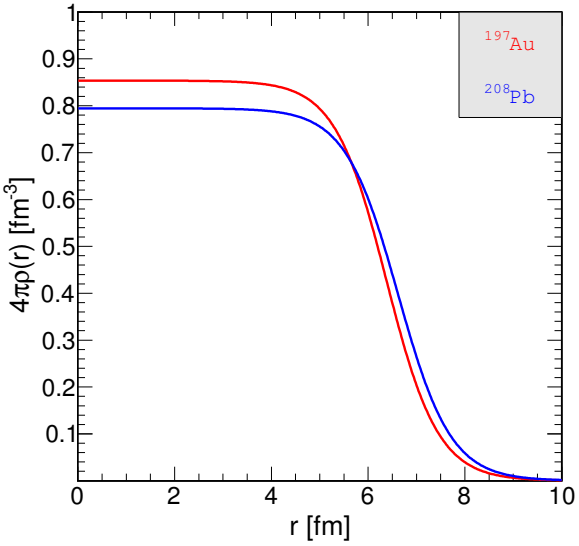

Figure 1.10: Charge densities as a function of nucleus radius for ^{197}Au and ^{208}Pb nucleus obtained using the two-parameter Fermi model.

- $\rho_0 = \frac{Z}{A} 0.1604$ fm^{-3} for ^{197}Au,
- $\rho_0 = \frac{Z}{A} 0.1572$ fm^{-3} for ^{208}Pb.

Knowing "the best" parameters for the description of the charge density for a given nucleus, one can use formula (1.4.75) to calculate the corresponding form

factor. This form factor will be used then in further calculation. In relativistic collisions, it is more comfortable to use the natural units (the velocity of light c and Plancks constant $\hbar = 1$). In this case Eq. (1.4.75) can be rewritten as

$$F\left(\mathbf{q}^2\right) = \frac{4\pi}{|\mathbf{q}|}\int \rho\left(r\right)\sin\left(|\mathbf{q}|\, r\right) r\mathrm{d}r \ . \tag{1.4.83}$$

In the literature often (see e.g. [49]) a monopole form factor is used

$$F_{\mathrm{mon}}\left(\mathbf{q}^2\right) = \frac{\Lambda^2}{\Lambda^2 + |\mathbf{q}|^2} \tag{1.4.84}$$

which corresponds to the Yukawa charge distribution

$$\rho\left(r\right) = \frac{1}{4\pi r}\Lambda^2 \exp\left(-\Lambda r\right) \ . \tag{1.4.85}$$

The value of the Λ parameter is determined so that the root mean square of the electric radius equals to the experimental values

$$\sqrt{\langle r^2\rangle} = \sqrt{\frac{6}{\Lambda^2}} = 1 \text{ fm } A^{1/3} \tag{1.4.86}$$

giving $\Lambda \simeq 83$ MeV (Ref. [49]). This form of the form factor has some practical advantage over the form factor with the realistic charge distribution because it can be easily used in analytical calculations. In the literature very often the same value of Λ for Au and Pb nuclei is used [49]. This is not quite correct, because the value of Λ depends on the mass number A or on the root mean square radius of the nucleus. The calculations presented in this dissertation are done for different values of Λ for ^{197}Au and ^{208}Pb. In the further calculations the following values of Λ will be used:

- for ^{197}Au: $\sqrt{\langle r^2\rangle} = 5.3$ fm $\Rightarrow \Lambda = 0.091$ GeV,
- for ^{208}Pb: $\sqrt{\langle r^2\rangle} = 5.5$ fm $\Rightarrow \Lambda = 0.088$ GeV.

The value of Λ is adjusted to reproduce the root mean square radius of a nucleus with the help of experimental data [42]. Actually, the above values of $\sqrt{\langle r^2\rangle}$ are the arithmetic means of the numbers from the literature, presented in Table 1.2 and 1.3.

Fig. 1.11 presents the modulus of the form factor as a function of the momentum transfer. The results for gold and lead are shown by the red and blue lines, respectively. The solid line shows the shape of the form factor for realistic charge

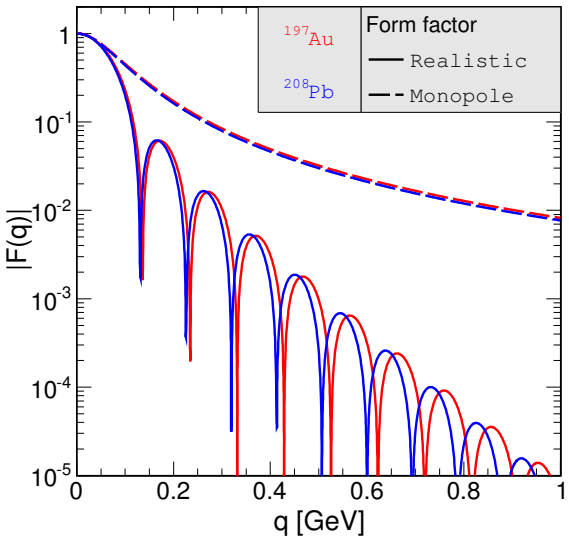

Figure 1.11: A comparison of the realistic and monopole form factor for gold and lead nuclei.

distribution. One can observe many oscillations that are characteristic for the relatively sharp edge of the nucleus. The distributions for ^{197}Au and ^{208}Pb are shifted relative to each other for larger values of q where the symbol q denotes the scalar quantity $q = |\mathbf{q}|$. The upper lines correspond to the monopole form factor. One can note that with larger value of q the difference between realistic and monopole form factors becomes larger. In general, the form factor reduces the scattering intensity for large momentum transfers.

Chapter 2

Elementary cross sections for different $\gamma\gamma$ fusion processes

Using the designation "elementary cross section" in the present dissertation we have in mind subprocess which "participates" in the production of particle pairs during UPC of heavy ions. Initially two-photon production in heavy-ion collisions was studied in fixed target experiments at the Bevalac, the BNL AGS and the CERN SPS. The feasibility of these photon-induced processes were demonstrated by experiments at Relativistic Heavy Ion Collider (RHIC). In general, the obtained cross sections agree with theoretical expectations but the statistics is rather poor. At the Large Hadron Collider (LHC) the situation seems to be better. Since the cross sections at the LHC are larger, this gives higher statistics for many interesting UPCs.

The correct form of the distribution in two-photon collision energy $W_{\gamma\gamma}$ is very important ingredient in the equivalent photon approximation. Below a generic process for the $\gamma\gamma \to X_1X_2$ reaction will be discussed. Different kinds of the particle pairs X_1X_2 will be studied in separate sections. First the energy dependence of the elementary cross section for the production of muon pairs will be presented. This is calculated within quantum electrodynamics. Next our fit to $\gamma\gamma \to \rho^0\rho^0$ experimental data will be shown and discussed. At larger energies vector-dominance-model and Regge (VDM-Regge) approach can be used. Then four different mechanisms for heavy quarks production will be discussed in detail and compared. Finally the neutral and charged pion pair production in very broad range of energy will be discussed.

We are the first and the only group which describes the experimental data both for the total cross section and for angular distributions for $\gamma\gamma \to \pi^+\pi^-$ and $\gamma\gamma \to \pi^0\pi^0$ reactions simultaneously at all experimentally available energies.

2.1 Dimuon production

The cross section for the elementary $\gamma\gamma \to e^+e^-$ or $\mu^+\mu^-$ processes are basic ingredients for the nuclear collisions. The elementary process $\gamma\gamma \to l^+l^-$ with on-shell photons could not yet be studied experimentally. Such internal Feynman diagrams appear, however, naturally in ep or e^+e^- collisions. For example in ep collisions the following reactions were studied [50]:

- Electroweak muon pair production: $ep \to ep\gamma^*\gamma^*$, $(\gamma^*\gamma^* \to \mu^+\mu^-)$,
  $ep \to ep\gamma^* Z^{0*}$, $(\gamma^* Z^{0*} \to \mu^+\mu^-)$,
  $ep \to epZ^{0*}Z^{0*}$, $(Z^{0*}Z^{0*} \to \mu^+\mu^-)$,
- Bremsstrahlung: $ep \to ep\gamma^* \to ep\mu^+\mu^-$,
- Z^0-production: $ep \to epZ^0 \to ep\mu^+\mu^-$.

Both ep and e^+e^- production can be well described in terms of quantum electrodynamics in leading order. Therefore we can safely assume that in nuclear collisions $\gamma\gamma \to \mu^+\mu^-$ can be calculated within quantum electrodynamics. The total cross section is known and the corresponding formula can be found e.g. in [23]:

$$\begin{aligned}\sigma_{\gamma\gamma\to\mu^+\mu^-}(W_{\gamma\gamma}) &= \frac{4\pi\alpha_{em}^2}{W_{\gamma\gamma}^2}\left\{2\ln\left[\frac{W_{\gamma\gamma}}{2m_\mu}\left(1+\sqrt{1-\frac{4m_\mu^2}{W_{\gamma\gamma}^2}}\right)\right]\left(1+\frac{4m_\mu^2 W_{\gamma\gamma}^2-8m_\mu^4}{W_{\gamma\gamma}^4}\right)\right. \\ &- \left.\sqrt{1-\frac{4m_\mu^2}{W_{\gamma\gamma}^2}}\left(1+\frac{4m_\mu^2}{W_{\gamma\gamma}^2}\right)\right\}. \qquad (2.1.1)\end{aligned}$$

The relevant calculation based on Feynman diagram technique can be found in many textbooks (see e.g. [23, 51–56]). Fig. 2.1 presents the elementary cross section for $\gamma\gamma \to \mu^+\mu^-$ process as a function of the $\gamma\gamma$ energy.

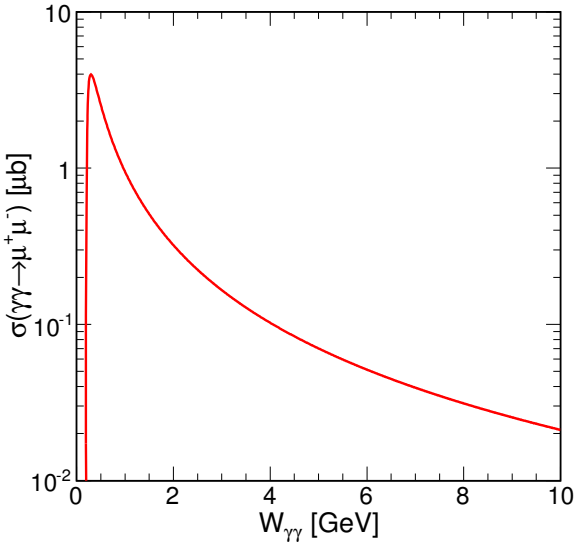

Figure 2.1: The elementary cross section for the $\gamma\gamma \to \mu^+\mu^-$ reaction.

2.2 $\rho^0\rho^0$ meson production

Experimental data for the $\gamma\gamma \to \rho^0\rho^0$ reaction were measured by several groups at e^+e^- colliders. Since its first observation in 1980 by the TASSO Collaboration [57], the reaction $\gamma\gamma \to \rho^0\rho^0$ has been extensively investigated. A next data set comes from the determination of the cross section for $\gamma\gamma \to \pi^+\pi^-\pi^+\pi^-$ in a way free of assumptions about the relative contributions from $\rho^0\rho^0$, $\rho^0 2\pi$ and 4π. The CELLO group found a rather high cross section of about 200 nb around $W_{\gamma\gamma} = 1.5$ GeV which consists of about 40% of the $\rho^0\rho^0$ production [58]. This experiment was performed using the CELLO detector at DESY-PETRA at the average beam energy of 17 GeV. Further results are presented for the exclusive production of four-prong final states in photon-photon collisions from the TPC/Two-Gamma detector at the SLAC e^+e^- storage ring PEP [59]. The $\rho^0\rho^0$ contribution dominates the four-pion cross section at low masses ($M_{\rho^0\rho^0} < 2$ GeV), but falls to nearly zero above 2 GeV. Next, the DESY-PETRA-PLUTO experiment presented the cross sections for four charged pions in photon-photon collisions [60]. The process is dominated by $2\rho^0$ production with rapid rise of cross section around $W_{\gamma\gamma} = 1.2$ GeV. Spin parity analysis of $2\rho^0$ system shows $J^P = 2^+$ to dominate, though 0^+ is also possible for

$W_{\gamma\gamma} < 1.4$ GeV. Negative parity states are excluded. Thereafter the DESY-DORIS-ARGUS experiment observed a partial waves $J^P = 2^+$ with helicity 2 dominance in the reaction $\gamma\gamma \to \rho^0(770)\rho^0(770)$ near threshold [61]. ARGUS experiment found a dominance of the $\rho^0\rho^0$ production in the region below $W_{\gamma\gamma} = 1.8$ GeV. At last the CERN-LEP-L3 experiment measured the cross sections for exclusive $\rho^0\rho^0$ production in the two-photon collisions involving a single highly virtual photon [62]. The data were collected at LEP in the centre-of-mass energy range 89 to 209 GeV. The cross section was determined as a function of Q^2 and $W_{\gamma\gamma}$ for $1.2 < Q^2 < 30$ GeV^2 and $1.1 < W_{\gamma\gamma} < 3$ GeV. The data taken into account in this consideration are for the range of photon virtuality $Q^2 = (1.2 - 8.5)$ GeV^2. The above experimental data are catalogued in Ref. [63].

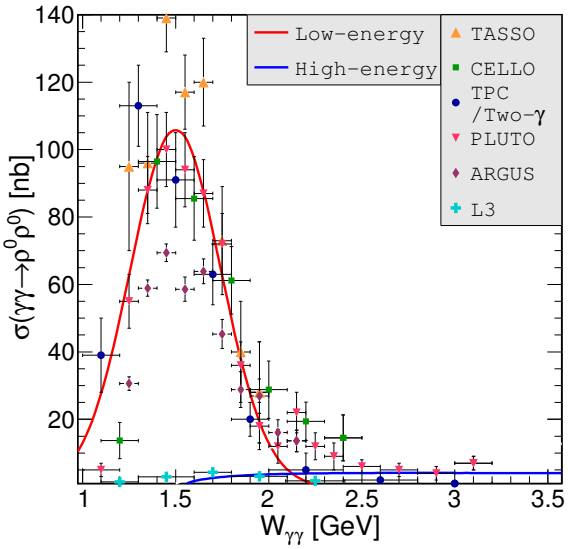

Figure 2.2: The elementary cross section for the $\gamma\gamma \to \rho^0\rho^0$ reaction.

Fig. 2.2 presents the collection of the e^+e^- experimental data (points) and our fit (solid lines). The experimental errors are calculated with the help of the relation

$$\Delta x = \sqrt{\Delta x^2_{\rm stat} + \Delta x^2_{\rm sys}}\,. \tag{2.2.2}$$

Experimentally one observes a huge enhancement close to the threshold. The origin of this enhancement was never understood. One can find some speculation on the issue in the literature. For example, in Refs. [64, 65] the authors proposed a view that this effect is due to a superposition of resonances with isospin zero. In the same

papers one can find explanation, that the presence of the threshold enhancement in $\gamma\gamma \to \rho^0\rho^0$ in the state of total angular momentum $J = 2$ and helicity $J_z = \pm 2$ can be obtained in resonance models by suitable choices of coupling constants. Another idea [66] is that each photon produces a ρ^0 and these vector mesons then interact through the repeated exchange of an $I = 0$ σ meson leading to an effective potential between the vector mesons. Another mechanism [67] which could account for the threshold enhancement with $J_z = \pm 2$ is the effect of Bose statistics in the final state. In Ref. [68] the huge cross section (at ≈ 1.5 GeV) was interpreted as a tensor resonance decaying into $\rho^0\rho^0$ channel. We leave the difficult problem of the microscopic origin of this threshold bump and take a pragmatic attitude of using directly experimental data instead of any model calculation results.

Fig. 2.2 presents the collection of experimental data and our fit

$$\sigma^{\text{low-energy}}_{\gamma\gamma\to\rho^0\rho^0}(W_{\gamma\gamma}) = 106 \exp\left(-4\ln 2 \cdot \left(\frac{W_{\gamma\gamma} - 1.5}{0.574}\right)^2\right) . \tag{2.2.3}$$

Above $W_{\gamma\gamma}$ is given in GeV and the cross section in nb. This formula describes the cross section in the range of energy $W_{\gamma\gamma} = (1 - 2)$ GeV (red line in Fig. 2.2). The low-energy component is a purely mathematical fit. The issue is a bit subtle as the peak appears close to the threshold. If this was a simple Breit-Wigner resonant shape the tails would be broader. The low-energy enhancement could be also some close-to-threshold mechanism. Our purely mathematical representation of the unknown effect may be therefore oversimplified. One can observe some disagreement of the data measured by different groups (Refs. [57–62]). All data sets (except those measured by the ARGUS experiment) are internally consistent thus we think that Eq. (2.2.3) gives sufficiently good representation of the world data. We do not have explanation why the ARGUS data are somewhat below the data obtained by other collaborations. Formula (2.2.3) effectively includes smearing of the masses of both ρ^0 mesons, and thus gives a strength below $W_{\gamma\gamma} < 2m_{\rho^0}$.

Very little is known for higher ($W_{\gamma\gamma} > 3$ GeV) energies. Several groups discussed about possible BFKL (Balitsky-Fadin-Kuraev-Lipatov) effects in the $\gamma\gamma \to \rho^0\rho^0$ reaction at high energies. First of all it is not clear how big the energies should be to observe such effects. Secondly it is not clear how realistic BFKL calculations are,

especially those in leading-logarithm approximation. On the other hand for many reactions with small-virtuality photons a description within vector-dominance-model (VDM) and Regge approach was confronted with the data and gave a reasonably good description. A good example is $\gamma p \to \rho^0 p$ reaction (also discussed in this dissertation in Appendix E) which was described e.g. in Refs. [69–71].

The $\gamma\gamma \to \rho^0\rho^0$ reaction was discussed long ago in Refs. [72, 73] where a simple Born amplitude for two-gluon exchange was considered. In recent decades BFKL effects for these reaction were studied (see [74, 75] and references therein). The BFKL approach applies when photon virtualities Q_1^2 and Q_2^2 are large [74] or momentum transfer is large [75]. The first case cannot be studied in ultrarelativistic heavy ion collisions where the photons are quasi real. The second case requires solution of so-called nonforward BFKL equation. In Ref. [75] it was done in leading-logarithm (LL) approximation. The LL approximation is known to lead to too fast (unrealistic) grow of the cross section with energy. The cross section with a lower cut on four-momentum transfer squared $|t| > 1$ GeV^2 is of the order of a few pb for $W_{\gamma\gamma} < 10$ GeV (Ref. [75]). This is much smaller than the cross sections for the soft nonperturbative region ($Q_1^2, Q_2^2, t \sim 0$) as will be discussed below. At RHIC and in the run 1 at the LHC the luminosity was too small to study the large-t region. It seems therefore that at present we can study only the soft processes and in the following we shall concentrate exclusively on the soft processes.

In our analysis, the high-energy part ($W_{\gamma\gamma} > 2$ GeV) is modelled in the VDM-Regge approach with rather standard parameters which are used to describe other hadronic processes. The total cross section is integrated over Mandelstam variable $\hat{t}$

$$\sigma^{\text{high-energy}}_{\gamma\gamma\to\rho^0\rho^0} = \int\limits_{\hat{t}_{min}(\hat{s})}^{\hat{t}_{max}(\hat{s})} \frac{\mathrm{d}\sigma^{\text{high-energy}}_{\gamma\gamma\to\rho^0\rho^0}}{\mathrm{d}\hat{t}} \mathrm{d}\hat{t} \,, \tag{2.2.4}$$

where t_{min} and t_{max} are $\hat{s}$-dependent kinematical limitations of $\hat{t}$. The differential cross section is given by the well-known relation

$$\frac{\mathrm{d}\sigma^{\text{high-energy}}_{\gamma\gamma\to\rho^0\rho^0}}{\mathrm{d}\hat{t}} = \frac{1}{16\pi\hat{s}^2} \overline{\left|\mathcal{M}_{\gamma\gamma\to\rho^0\rho^0}\left(\hat{s},\hat{t};q_1,q_2\right)\right|^2} \,. \tag{2.2.5}$$

The kinematics of this process is defined in Fig. 2.3.

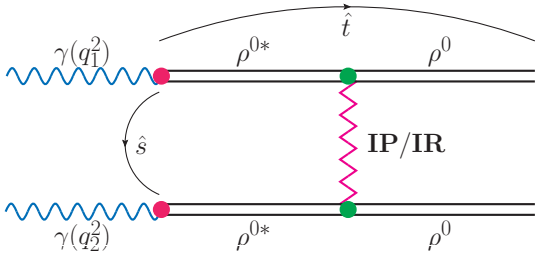

Figure 2.3: Feynman diagram for $\gamma\gamma \to \rho^{0*}\rho^{0*} \to \rho^0\rho^0$ process.

In the VDM-Regge approach the amplitude for the $\gamma\gamma \to \rho^0\rho^0$ can be written as

$$\mathcal{M}_{\gamma\gamma\to\rho^0\rho^0}\left(\hat{s},\hat{t};q_1,q_2\right) = C_{\gamma\to\rho^0}C_{\gamma\to\rho^0}\mathcal{M}_{\rho^{0*}\rho^{0*}\to\rho^0\rho^0}\left(\hat{s},\hat{t};q_1,q_2\right) \ . \tag{2.2.6}$$

Above $C_{\gamma\to\rho^0} = e/f_{\rho^0} = \sqrt{\alpha_{em}/2.54}$ factor describes transformation of photons to (virtual) vector mesons. A more detailed explanation of the vector meson coupling f_V is given in Appendix D.2. The amplitude for the $\rho^{0*}\rho^{0*} \to \rho^0\rho^0$ processes appearing in (2.2.6) is written in the Regge form

$$\begin{aligned}\mathcal{M}_{\rho^{0*}\rho^{0*}\to\rho^0\rho^0}\left(\hat{s},\hat{t};q_1,q_2\right) &= \left(\eta_{\mathbb{IP}}\left(\hat{s},\hat{t}\right)C_{\mathbb{IP}}\left(\frac{\hat{s}}{s_0}\right)^{\alpha_{\mathbb{IP}}\left(\hat{t}\right)-1}\right. \\ &+ \left.\eta_{\mathbb{IR}}\left(\hat{s},\hat{t}\right)C_{\mathbb{IR}}\left(\frac{\hat{s}}{s_0}\right)^{\alpha_{\mathbb{IR}}\left(\hat{t}\right)-1}\right) \\ &\times \hat{s}\,F\left(\hat{t};q_1^2\approx 0\right)F\left(\hat{t};q_2^2\approx 0\right) \ .\end{aligned} \tag{2.2.7}$$

Here we neglect helicity flip and assume helicity conservation in the whole process. $F\left(\hat{t};q_1^2\right)$ is a vertex form factor which, in general, is a function of exchanged Pomeron/Reggeon four-momentum squared and photon/ρ^0 meson virtualities. We parametrize them in the following factorized form

$$F\left(\hat{t};q_{1/2}^2\right) = \exp\left(\frac{B\hat{t}}{4}\right)\exp\left(\frac{q_{1/2}^2 - m_\rho^2}{2\Lambda^2}\right) \ . \tag{2.2.8}$$

The first component is for the case when ρ^0 meson is on-shell (green vertices in Fig. 2.3), and the second term takes into account the fact that ρ^0 meson can be off mass shell (red vertices in Fig. 2.3). This second term is normalized to unity when vector meson is on-mass-shell. We expect the slope parameter of the order $B \sim 4$ GeV^{-2} (typical for meson-meson interactions) and the parameter responsible

for off-shellness of the ρ^0 mesons $\Lambda \sim 1$ GeV. The difference between results for on/off-shellness form factor is presented in Appendix D.1.

The strength parameters of interaction are taken from the Donnachie-Landshoff fit [76] to the total NN and πN cross sections. Using the following parameters

$$C_{I\!P}^{NN} = 21.7 \text{ mb} , \qquad C_{I\!R}^{NN} = 75.4875 \text{ mb} , \tag{2.2.9}$$

$$C_{I\!P}^{\pi N} = 13.63 \text{ mb} , \qquad C_{I\!R}^{\pi N} = 31.79 \text{ mb} \tag{2.2.10}$$

and assuming Regge factorization and assuming $\sigma_{\rho^0\rho^0\to\rho^0\rho^0} = \sigma_{\pi^0\pi^0\to\pi^0\pi^0}$ one can calculate the value of $C_{I\!P}$ and $C_{I\!R} = C_{f_2}$ [77]:

$$C_{I\!P}^{\pi\pi} = 8.56 \text{ mb} , \qquad C_{I\!R}^{\pi\pi} = 13.39 \text{ mb} . \tag{2.2.11}$$

The Pomeron and Reggeon (linear) trajectories determined from elastic and total cross section given in the form $\alpha_i(t) = \alpha_i(0) + \alpha_i' t$ are (Ref. [76]):

$$\alpha_{I\!P}(t) = 1.008 + (0.25 \text{ GeV}^{-2})\, t , \quad \alpha_{I\!R}(t) = 0.5475 + (0.93 \text{ GeV}^{-2})\, t . \tag{2.2.12}$$

The signature factors η_i are complex functions. They are consistent with our choice of normalization,

$$\eta_{I\!P}\left(\hat{s}, \hat{t} = 0\right) \approx i , \qquad \eta_{I\!P}\left(\hat{s}, \hat{t} = 0\right) \approx i - 1 . \tag{2.2.13}$$

Standard signature functions [78] are normalized somewhat different. Ref. [79] includes very good treatment of Pomeron and Reggeon exchanges.

Fig. 2.2 shows that the cross section exceeds the VDM-Regge expectation (blue line) by more than one order of magnitude near the $\rho^0\rho^0$ threshold. The vanishing of the cross section below $W_{\gamma\gamma} = 2m_\rho$ is due to energy conservation and the assumption of sharp (delta-like) ρ^0 mesons. It is obvious that this model cannot explain the huge close-to-threshold enhancement. However, the VDM-Regge approach nicely describes the experimental data for $W_{\gamma\gamma} > 2.5$ GeV. The cross section above $W_{\gamma\gamma} = 3.1$ GeV was never measured but we expect that our Regge form well extrapolate to large subprocess energies. Using the VDM-Regge approach we do not use the smearing of ρ^0 meson masses (large decay width $\Gamma \approx 0.15$ GeV), because this mechanism gives only a small contributions at $W_{\gamma\gamma} = 2m_\rho$ (see Fig. 2.2).

At higher energies ($W_{\gamma\gamma} > 3$ GeV) the effect of the smearing is very small when looking at distributions related to ρ^0 mesons. It may be important only when looking at two-pion distributions. We shall return to the issue when discussing nuclear cross section.

The differential distributions in transverse momentum of meson p_t can be obtained by replacing total elementary cross section

$$\sigma_{\gamma\gamma\to\rho^0\rho^0} = \int \frac{\mathrm{d}\sigma_{\gamma\gamma\to\rho^0\rho^0}}{\mathrm{d}p_t}\mathrm{d}p_t \tag{2.2.14}$$

where

$$\frac{\mathrm{d}\sigma}{\mathrm{d}p_t} = \frac{\mathrm{d}\sigma}{\mathrm{d}p_t^2}\frac{\mathrm{d}p_t^2}{\mathrm{d}p_t} = \frac{\mathrm{d}\sigma}{\mathrm{d}p_t^2}2p_t = \frac{\mathrm{d}\sigma}{\mathrm{d}t}\left|\frac{\partial\hat{t}}{\partial p_t^2}\right|2p_t \ . \tag{2.2.15}$$

This transformation is useful for preparation of a grid which will be used in calculations of nuclear cross sections. This will allow to impose some cuts appropriate for experimental limitations.

2.3 Quark-antiquark production

Heavy quarks can be produced not only in gluon-gluon fusion processes in proton-proton scattering but also in $\gamma\gamma$ collisions at e^+e^- colliders. One can find many papers (Refs. [80–83]) about inclusive and exclusive quark production including direct, QCD radiative corrections for the leading subprocesses and one/two-resolved photon mechanisms.

In the current analysis, we use the following notation: $Q/\bar{Q}$ - heavy-quark/-antiquark (in our case: c or b), $q/\bar{q}$ - light-quark/-antiquark (u, d or s (anti)quarks). In contrast to dimuon production, the $Q\bar{Q}$ state cannot be directly observed because of the quark confinement. In practice, some experiments measure rather electrons or heavy mesons. Then, the hadronization process complicates the situation. Therefore taking into account the $\gamma\gamma \to Q\bar{Q}$ process is not enough and one has to include another partonic states such as $Q\bar{Q}g$ and $Q\bar{Q}q\bar{q}$. The contribution from a photon single-resolved components will be calculated too.

We take into account the mechanisms depicted in Fig. 2.4, 2.5, 2.6 and 2.7. The blue wavy lines represent the photons, the green curly lines denote the gluons,

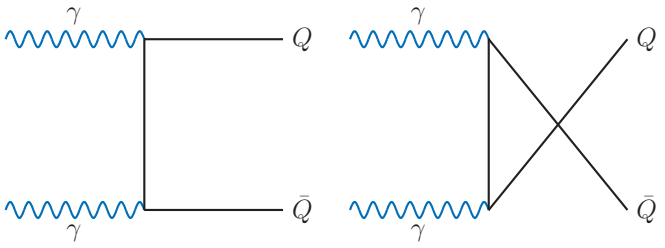

Figure 2.4: Feynman diagrams for the Born $2 \to 2$ amplitude.

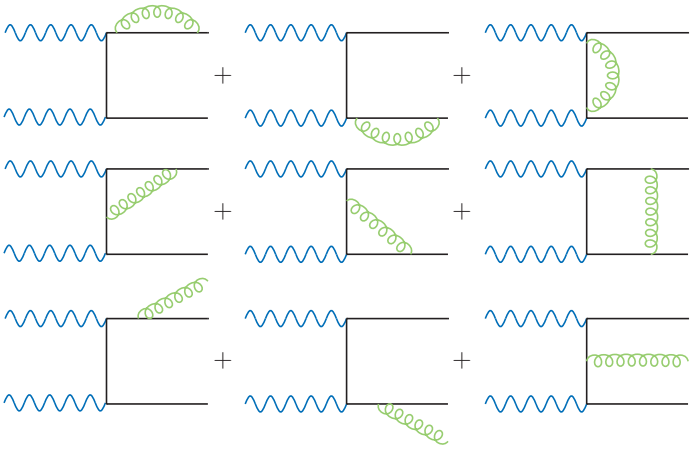

Figure 2.5: Feynman diagrams for the LO QCD corrections.

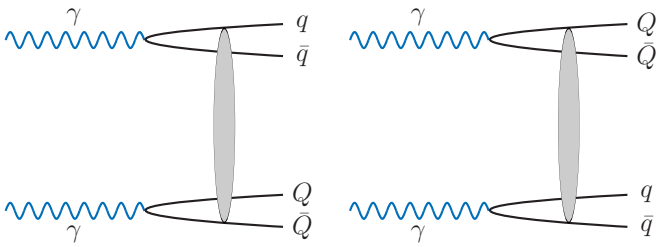

Figure 2.6: Feynman diagrams for the $Q\bar{Q}q\bar{q}$ production.

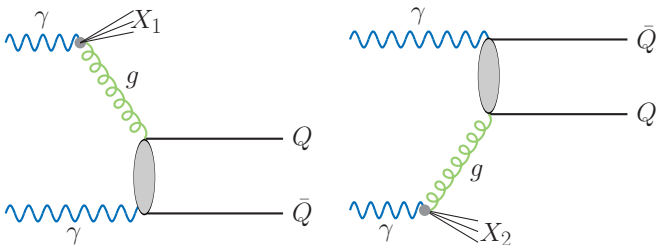

Figure 2.7: Feynman diagrams for the single-resolved mechanism.

and the black solid lines correspond to the heavy-quarks. The first of the figures represents the direct mechanism in the Born approximation. This is very similar

to the production of muon pairs in leading order. But in comparison to dilepton production, one has to include QCD corrections. Representative diagrams for a next-to-leading-order (NLO) approximation (leading-order corrections) are shown in Fig. 2.5. Fig. 2.6 depicts the production of heavy-quarks in association with light-quark-light-antiquark pair. The ovals in the figures mean a complicated interaction which is described in the present work in the saturation model framework. The diagrams presented in Fig. 2.7 represent single-resolved photon mechanism when only a small part of first photon interacts with the other one. All these processes were studied in details in Refs. [84–86].

Starting from the Born direct contribution (Fig. 2.4), it should be noted that the LO elementary cross section for $\gamma\gamma \to Q\bar{Q}$ at two-photon energy $W_{\gamma\gamma}$ takes a very similar form like the cross section for dimuon production (Eq. (2.1.1))

$$\begin{aligned}\sigma^{\rm Born}_{\gamma\gamma\to Q\bar{Q}}(W_{\gamma\gamma}) &= N_c e_Q^4 \frac{4\pi\alpha_{em}^2}{W_{\gamma\gamma}^2} \\ &\times \left\{ 2\ln\left[\frac{W_{\gamma\gamma}}{2m_Q}\left(1+\sqrt{1-\frac{4m_Q^2}{W_{\gamma\gamma}^2}}\right)\right]\left(1+\frac{4m_Q^2 W_{\gamma\gamma}^2 - 8m_Q^4}{W_{\gamma\gamma}^4}\right)\right. \\ &- \left.\sqrt{1-\frac{4m_Q^2}{W_{\gamma\gamma}^2}}\left(1+\frac{4m_Q^2}{W_{\gamma\gamma}^2}\right)\right\} . \qquad (2.3.16)\end{aligned}$$

One should only replace the quantities characteristic for muons by their counterparts for quarks: the number of quark color $N_c = 3$, the fractional charge e_Q of the c and b quark/antiquark. In the current analysis we take the following heavy-quark masses: $m_c = 1.5$ GeV, $m_b = 4.75$ GeV. The derivation of Eq. (2.3.16) was presented for the first time in Ref. [87]. It is obvious that the final $Q\bar{Q}$ state cannot be observed experimentally. Presence of additional few light mesons is rather natural. Thus one needs to include also more complicated final states.

In contrast to QED production of leptons in $\gamma\gamma$ collisions, in the case of quark-antiquark production one should include higher-order QCD processes which are known to be rather significant. Fig. 2.5 presents LO corrections only for the dominant, in heavy-ion collisions, direct contribution. The details of the higher-order corrections to heavy-quark-heavy-antiquark pairs production in $\gamma\gamma$ collisions can be found in Refs. [88–90]. In α_s order, Fig. 2.5 presents t-channel one-loop diagrams contributing to the photon fusion amplitude. In the current analysis, we follow

the approach presented in Ref. [89]. The LO QCD corrections can be written as

$$\sigma^{\text{QCD-corr.}}_{\gamma\gamma\to Q\bar{Q}}\left(W_{\gamma\gamma}\right) = N_c e_Q^4 \frac{2\pi\alpha_{em}^2}{W_{\gamma\gamma}^2} C_F \frac{\alpha_s}{\pi} f^{(1)} \; . \tag{2.3.17}$$

The function $f^{(1)}$ is calculated with the help of a code provided by the authors of Ref. [89] which uses the program package HPL [91]. In this analysis, the scale of α_s is fixed at $\mu^2 = 4m_Q^2$.

The $\gamma\gamma \to Q\bar{Q}q\bar{q}$ process is depicted in Fig. 2.6. The cross section for this mechanism can be calculated easily in the color dipole framework [84–86]. In general, the color dipole model makes use of virtual components of the photon in the plane transverse to the collision axis and their distribution is obtained in the perturbative framework.

In the present analysis, the dipole-dipole scattering approach [85] is used. Then the total cross section for the $\gamma\gamma \to Q\bar{Q}$ production can be expressed as

$$\begin{aligned}
\sigma^{\text{4q}}_{\gamma\gamma\to Q\bar{Q}} \;=\; & \left[\sum_{f_2\neq Q}\int \left|\Phi^{Q\bar{Q}}\left(\rho_1, z_1\right)\right|^2 \left|\Phi^{f_2\bar{f}_2}\left(\rho_2, z_2\right)\right|^2 \sigma_{dd}\left(\rho_1, \rho_2, x_{Qf}\right)\right. \\
& + \left.\sum_{f_1\neq Q}\int \left|\Phi^{f_1\bar{f}_1}\left(\rho_1, z_1\right)\right|^2 \left|\Phi^{Q\bar{Q}}\left(\rho_2, z_2\right)\right|^2 \sigma_{dd}\left(\rho_1, \rho_2, x_{fQ}\right)\right] \\
& \times \; \mathrm{d}^2\rho_1\,\mathrm{d}z_1\,\mathrm{d}^2\rho_2\,\mathrm{d}z_2 \; ,
\end{aligned} \tag{2.3.18}$$

where $\Phi^{Q\bar{Q}/f\bar{f}}(\rho, z)$ are the heavy/light quark-antiquark wave functions of the photon in the mixed representation. The parameters $\rho_{1/2}$ express the transverse separation of the quark and antiquark in a pair. This is often call the dipole size. The longitudinal momentum fraction of quark pair is denoted by z. Eq. (2.3.18) is correct at rather high energy $W_{\gamma\gamma} \gg 2m_Q$. At lower energies ($W_{\gamma\gamma} \leqslant 4m_Q$), the proximity of the kinematical threshold must be taken into account. In Ref. [84] a phenomenological saturation model inspired by the Golec-Biernat and Wüsthoff (GBW model) choice [92] for the dipole-dipole cross section was proposed

$$\sigma_{dd}\left(\rho_1, \rho_2, x_{ab}\right) = \sigma_0^{ab}\left[1 - \exp\left(-\frac{r_{eff}^2}{4R_0^2\left(x_{ab}\right)}\right)\right] \; , \tag{2.3.19}$$

where $\sigma_0^{ab} = \frac{2}{3}\sigma_0$. Different prescription of an effective radius have been considered in Ref. [84], but the best phenomenological choice is given by the prescription

$$r_{eff}^2 = \frac{\left(\rho_1\rho_2\right)^2}{\rho_1^2 + \rho_2^2} \; . \tag{2.3.20}$$

In Eq. (2.3.19) we use the same parametrization of the saturation radius as in [92]

$$R_0\left(x_{ab}\right) = \frac{1}{Q_0}\left(\frac{x_{ab}}{x_0}\right)^{-\frac{\lambda}{2}} , \tag{2.3.21}$$

where $Q_0 = 1$ GeV. The parameter x_{ab} controls the energy dependence

$$x_{ab} = \frac{4m_a^2 + 4m_b^2}{W_{\gamma\gamma}^2} . \tag{2.3.22}$$

The three parameters of the GBW model were fitted to all existing Deep Inelastic Scattering (DIS) data for $x < 0.01$: $\sigma_0 = 29.12$ mb, $x_0 = 0.41 \cdot 10^{-4}$, $\lambda = 0.277$. Some other parametrization of the dipole-dipole cross section were discussed for example in [93]. The cross section for the $\gamma\gamma \to Q\bar{Q}q\bar{q}$ is much bigger than the one corresponding to tree-level Feynman diagrams [82, 94], because it resumes higher-order QCD contributions.

In the standard collinear approach one usually includes so-called resolved contributions, when heavy quark-antiquark pairs are created either in the photon-gluon or gluon-photon fusion (see Fig. 2.7; the shaded oval means either t and u diagram shown in Fig. 2.4). This is known as the single-resolved process. Then only a small fraction of the first or the second photon longitudinal momentum fractions (x_1/x_2) enters into the production of heavy-quark or antiquark. As was discussed in Ref. [85] the $Q\bar{Q}q\bar{q}$ component has a very small overlap with the single-resolved component because of a quite different final state. Thus adding them together does not lead in practice to double counting. The cross section for the single-resolved contribution (Fig. 2.7) takes the form

$$\sigma^{\text{1-res}}_{\gamma\gamma\to Q\bar{Q}} = \int \mathrm{d}x_1\, g_1\left(x_1,\mu^2\right)\hat{\sigma}_{g\gamma}\left(\hat{s} = x_1 s\right) + \int \mathrm{d}x_2\, g_2\left(x_2,\mu^2\right)\hat{\sigma}_{\gamma g}\left(\hat{s} = x_2 s\right) , \tag{2.3.23}$$

where g_1 and g_2 are gluon distributions in photon 1 or photon 2. $\hat{\sigma}_{\gamma g}$ and $\hat{\sigma}_{g\gamma}$ denote the corresponding elementary cross sections. In the current analysis the gluon distributions is taken from Ref. [95].

Fig. 2.8 presents the elementary cross section for the production of $c\bar{c}$ (left panel) and $b\bar{b}$ (right panel) quark pairs separately. This is depicted as a function of the $\gamma\gamma$ c.m. energy. The lines refer to four mechanisms which are described above. The Born direct contribution is denoted by the green solid lines, LO QCD

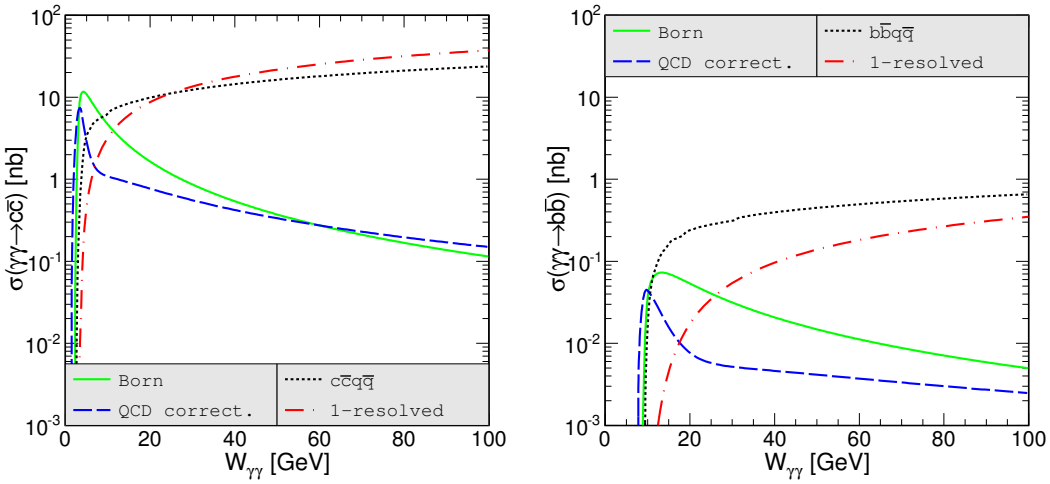

Figure 2.8: The elementary cross section for the $\gamma\gamma \to Q\bar{Q}X$ reaction.

corrections - blue dashed lines, $Q\bar{Q}q\bar{q}$ production - black dotted lines and single-resolved mechanism - red dashed-dotted lines. A huge contributions come from the production of charm and bottom quarks in association with light $q\bar{q}$ pairs. The LO $\gamma\gamma \to c\bar{c}$ elementary cross section dominates at low energies near the threshold ($W_{\gamma\gamma} < 10$ GeV).

We are the first group which tries to include all mechanisms for the production of heavy quarks in $\gamma\gamma \to Q\bar{Q}$ and then in nuclear UPCs. The corresponding results will be discussed in section 4.3.

2.4 Two-pion production

The elementary cross section for $\gamma\gamma \to \pi^+\pi^-$ and $\gamma\gamma \to \pi^0\pi^0$ reactions are interesting by themselves, because understanding of these mechanisms at low ($W_{\gamma\gamma} < 1$ GeV) and intermediate ($W_{\gamma\gamma} = (1 - 2.5)$ GeV) energies is very important for applications of chiral perturbation theory and pion-pion interaction [96–101]. At higher energies ($W_{\gamma\gamma} > 2.5$ GeV) the Brodsky-Lepage [102–105] and hand-bag [106, 107] mechanisms have been discussed in the literature.

The elementary cross section for $\gamma\gamma \to \pi^+\pi^-$ and $\gamma\gamma \to \pi^0\pi^0$ process will be discussed starting from the energy of two-pion threshold up to about $W_{\gamma\gamma} = 6$ GeV.

To obtain correct description of these reactions, one needs to include several mechanisms. Every of them will be studied in individual subsection. Then our results will be compared with experimental data for both total cross section and angular distributions.

2.4.1 $\gamma\gamma \to \pi^+\pi^-$ continuum

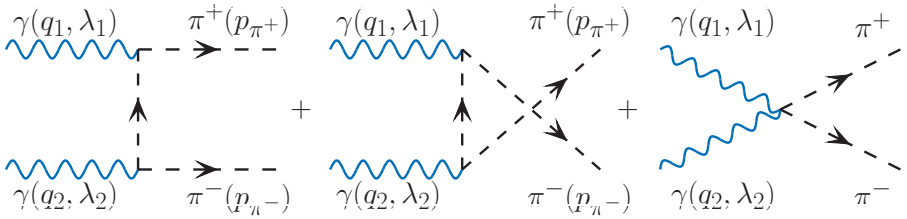

Figure 2.9: One-pion exchange Feynman diagrams for the t, u and contact amplitudes.

In the $\gamma\gamma \to \pi^+\pi^-$ a soft pion-exchange process is possible. The Feynman diagrams for the Born term matrix elements for charged pion pair production are depicted in Fig. 2.9. The helicity-dependent amplitude for point-like mesons

$$\mathcal{M}\left(\lambda_1,\lambda_2\right) = \mathcal{M}^t\left(\lambda_1,\lambda_2\right) + \mathcal{M}^u\left(\lambda_1,\lambda_2\right) + \mathcal{M}^c\left(\lambda_1,\lambda_2\right) \tag{2.4.24}$$

is a sum of the three terms [87]:

- t-channel pion-exchange amplitude (left diagram in Fig. 2.9)

$$\begin{aligned}\mathcal{M}^t\left(\lambda_1,\lambda_2;q_1,q_2,p_{\pi^+},p_{\pi^-}\right) &= e^2\sum\left(2p^\mu_{\pi^+}-q^\mu_1\right)\varepsilon_\mu\left(q_1,\lambda_1\right) \\ &\times \quad \left(2p^\nu_{\pi^-}-q^\nu_2\right)\varepsilon_\nu\left(q_2,\lambda_2\right)\frac{1}{t-m^2_\pi}\ ,\end{aligned} \tag{2.4.25}$$

- u-channel pion-exchange amplitude (middle diagram)

$$\begin{aligned}\mathcal{M}^u\left(\lambda_1,\lambda_2;q_1,q_2,p_{\pi^+},p_{\pi^-}\right) &= e^2\sum\left(2p^\mu_{\pi^-}-q^\mu_1\right)\varepsilon_\mu\left(q_1,\lambda_1\right) \\ &\times \quad \left(2p^\nu_{\pi^+}-q^\nu_2\right)\varepsilon_\nu\left(q_2,\lambda_2\right)\frac{1}{u-m^2_\pi}\ ,\end{aligned} \tag{2.4.26}$$

- contact amplitude (last diagram in Fig. 2.9)

$$\mathcal{M}^c\left(\lambda_1,\lambda_2;q_1,q_2,p_{\pi^+},p_{\pi^-}\right) = e^2\sum 2g^{\mu\nu}\varepsilon_\mu\left(\lambda_1\right)\varepsilon_\nu\left(\lambda_2\right)\ , \tag{2.4.27}$$

where $t = (p_{\pi^+} - q_1)^2 = (p_{\pi^-} - q_2)$, $u = (p_{\pi^+} - q_2)^2 = (p_{\pi^-} - q_1)$ and $\varepsilon_{\mu/\nu}$ are polarization vectors of the photons. The full helicity-dependent amplitude for the $\gamma\gamma \to \pi^+\pi^-$ continuum (2.4.24) can be written as

$$\mathcal{M}^c(\lambda_1, \lambda_2) = \varepsilon_\mu(q_1, \lambda_1)\,\varepsilon_\nu(q_2, \lambda_2)\,\mathcal{M}^{\mu\nu} . \tag{2.4.28}$$

It is easy to show that the total amplitude fulfills the gauge invariance conditions:

$$q_{1\mu}\mathcal{M}^{\mu\nu} = 0 , \tag{2.4.29}$$

$$q_{2\nu}\mathcal{M}^{\mu\nu} = 0 . \tag{2.4.30}$$

The QED Born amplitude for the production of charged (point-like) pions in the $\gamma\gamma$ fusion was known for a long time. In many calculations in the literature pions are treated as point-like particles. An interesting problem is to construct the QED amplitude for real, finite-size mesons. In 1986 Poppe proposed the form factor [108] which allows to include finite-size correction. In our calculations we use the idea proposed in Ref. [104]:

$$\Omega(s,t,u) = \frac{F^2(t) + F^2(u)}{1 + F^2(-s)} , \tag{2.4.31}$$

where $F(x) = \exp\left(\frac{B_{\gamma\pi}}{4}x\right)$ is the standard vertex function. One needs to multiply the full pion-exchange amplitude (2.4.24) by s-, t-, u-dependent form factor (2.4.31). The details of Eq. (2.4.31) and comparison with the Poppe form factor are presented in Appendix D.3.

2.4.2 s-channel $\gamma\gamma \to$ resonances

Exclusive resonance production in $\gamma\gamma$ reactions plays an important role in the studying substructure of resonances. The measurement of the decay widths into $\gamma\gamma$ allows to test for example the quark composition of the resonances and in this way provides a better understanding of the meson spectrum. Fig. 2.10 shows a list of all $\gamma\gamma \to \pi\pi$ resonances which are taken into account in the present studies:

- scalar resonances: $f_0(600) = \sigma(600)$, $f_0(980)$, $f_0(1500)$, $f_0(1710)$,

- tensor resonances: $f_2(1270)$, $f_2'(1525)$, $f_2(1565)$, $f_2(1950)$,

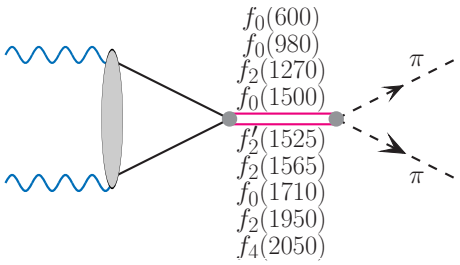

Figure 2.10: Feynman diagram for $\gamma\gamma$ $\rightarrow$resonances$\rightarrow$ $\pi^{+/0}\pi^{-/0}$ process.

- spin-4 resonance: $f_4(2050)$.

Only $\sigma(600)$ and $f_2(1270)$ resonances were discussed in this context in the literature.

Table 2.1: Parameters of resonances used in calculations.

No.	Resonance	m_R (MeV)	Γ_R (MeV)	$\Gamma_{\pi\pi}$ (MeV)	$\Gamma_{\gamma\gamma}$ (keV)	$\frac{\Gamma_{\gamma\gamma}\Gamma_{\pi\pi}}{\Gamma_R}$ (keV)
1	$f_0(600)$ [109]	600	400	400	0.5	
2	$f_0(980)$ [109]	980	50	51.3 [110]	0.29	
3	$f_2(1270)$ [109]	1 275	185	156.9	3.035	
4	$f_0(1500)$ [109]	1 505	109	38	-	0.033 [111]
5	$f_2'(1525)$ [109]	1 525	73	0.6	0.081	
6	$f_2(1565)$ [112]	1 570	160	25	0.7	
7	$f_0(1710)$ [109]	1 720	135	-	-	0.82
8	$f_2(1950)$ [109]	1 944	472	-	-	1.62
9	$f_4(2050)$ [109]	2 018	237	40.3	0.7	

Table 2.1 includes important characteristics of the resonances. Almost all parameters are known from Particle Data Group book [109]. While the $\pi\pi$ decay widths are usually well-known, the $\gamma\gamma$ decay widths are known only for some of the resonances. Therefore, studying the $\gamma\gamma \rightarrow \pi\pi$ data may help in extracting the latter quantities.

In most cases, PDG gives values of the resonance parameters: mass of mesons (resonance) m_R, width of resonance Γ_R, $\Gamma_{\pi\pi}$ and $\Gamma_{\gamma\gamma}$ decay widths. In our study somewhat smaller values of decay widths for $f_0(600)$ resonance are used than given in the PDG book. In the PDG book [109] a broad range of parameters is given:

$\Gamma_{f_0(600)} = (600 - 1000)$ MeV, $\Gamma_{\gamma\gamma} = (1.2 - 10)$ keV, but from our fit to experimental total cross sections and angular distributions, we found:

$$\Gamma_{f_0(600)} = 400 \text{ MeV}, \ \Gamma_{f_0(600)\to\gamma\gamma} = 0.5 \text{ keV} . \tag{2.4.32}$$

Additionally it is assumed here that the branching ratio: Br($f_0(600) \to \pi\pi$)= 100%. For $f_0(1500)$ scalar resonance which is a glueball candidate, PDG gives a number: $\frac{\Gamma_{\gamma\gamma}\Gamma_{\pi\pi}}{\Gamma_{f_0(1500)}} = 0.033$ keV which was obtained by the BELLE Collaboration [111]. Using this value, one can calculate: $\Gamma_{\gamma\gamma} = 0.1$ keV.
For $f_4(2050)$ the situation is even more complicated. Different values of the ratio $\frac{\Gamma_{\gamma\gamma}\Gamma_{\pi\pi}}{\Gamma_{f_4(2050)}}$ were given in the literature:

- Ref. [113]: 0.0231 keV,

- Ref. [114]: less than 1.1 keV.

Our fit to the BELLE experimental data (to be shown in the section 2.4.5) gives

$$\frac{\Gamma_{\gamma\gamma}\Gamma_{\pi\pi}}{\Gamma_{f_4(2050)}} = 0.12 \text{ keV}, \ \Gamma_{f_4(2050)\to\gamma\gamma} = 0.7 \text{ keV} . \tag{2.4.33}$$

The angular distribution for the s-channel resonances can be written in the standard (typical for Feynman diagrams) form:

$$\frac{d\sigma\left(\gamma\gamma \to \pi\pi\right)}{dz} = \sum_{\lambda_1,\lambda_2} \frac{\sqrt{\frac{W_{\gamma\gamma}^2}{4} - m_\pi^2}}{\frac{W_{\gamma\gamma}}{2}} \left|\mathcal{M}\left(\lambda_1, \lambda_2\right)\right|^2 \frac{4\pi}{4 \times 64\pi^2 W_{\gamma\gamma}^2} , \tag{2.4.34}$$

where the factor 4 in the denominator comes from averaging over initial photon helicities. The helicity-dependent resonant amplitudes in Eq. (2.4.34) must be modelled, as we do not have a priori microscopic models of the coupling of two photons to high-spin resonances. We parametrize the f_0, f_2 and f_4 resonances by the relativistic

Breit-Wigner resonance amplitude for a spin-J resonance R of mass m_R:

$$\begin{aligned}
\mathcal{M}(\lambda_1,\lambda_2) &= \frac{\sqrt{64\pi^2 W_{\gamma\gamma}^2 \times 8\pi\,(2J+1)\left(\frac{m_R}{W_{\gamma\gamma}}\right)^2 \Gamma_R \Gamma_R\,(W_{\gamma\gamma})}}{W_{\gamma\gamma}^2 - m_R^2 + i m_R \Gamma_R\,(W_{\gamma\gamma})} \\
&\times \sqrt{Br\,(R\to\gamma\gamma)\,Br\,(R\to\pi^{+/0}\pi^{-/0})}\; e^{i\varphi_R} \\
&\times \sqrt{2}\delta_{\lambda_1,\lambda_2} \left\{ \begin{array}{l} Y_0^0(\theta,\phi); \text{for } f_0 \\ Y_2^2(\theta,\phi); \text{for } f_2(1270), f_2'(1525), f_2(1950) \\ Y_2^0(\theta,\phi); \text{for } f_2(1565) \\ Y_4^0(\theta,\phi); \text{for } f_4(2050) \end{array} \right\} \\
&\times \exp\left(\frac{-\left(W_{\gamma\gamma}-m_R\right)^2}{\Lambda_R^2}\right) . \qquad (2.4.35)
\end{aligned}$$

The last form factor was introduced to correct the resonance form far from the actual resonance position where the simple resonance form is incorrect. One can expect Λ_R to be much larger than the resonance width Γ_R. In practice we will treat it as an extra free parameter to be adjusted to experimental world data. This is important only for broad resonances with $\Gamma > 0.1$ GeV.

The energy-dependent resonance width

$$\Gamma_R(W_{\gamma\gamma}) = \Gamma_R \frac{\sqrt{\frac{W_{\gamma\gamma}^2}{4} - m_\pi^2}}{\sqrt{\frac{m_R^2}{4} - m_\pi^2}} F^J\,(W_{\gamma\gamma}, R) \qquad (2.4.36)$$

is expressed through the spin-dependent Blatt-Weisskopf form factor [115]

$$\begin{aligned}
F^{J=0}\,(W_{\gamma\gamma},R) &= 1, \\
F^{J=2}\,(W_{\gamma\gamma},R) &= \frac{(Rp_R)^4 + 3\,(Rp_R)^2 + 9}{(Rp)^4 + 3\,(Rp)^2 + 9}, \qquad (2.4.37) \\
F^{J=4}\,(W,R) &= \frac{(Rp_R)^8 + 10\,(Rp_R)^6 + 135\,(Rp_R)^4 + 1575\,(Rp_R)^2 + 11025}{(Rp)^8 + 10\,(Rp)^6 + 135\,(Rp)^4 + 1575\,(Rp)^2 + 11025} .
\end{aligned}$$

In the equation above we have defined resonance momentum $p_R = \sqrt{\frac{m_R^2}{4} - m_\pi^2}$ and $\gamma\gamma \to \pi\pi$ system momentum $p = \sqrt{\frac{W_{\gamma\gamma}^2}{4} - m_\pi^2}$. The value of the barrier radius is taken to be $R = 1$ fm.

We consider two simple models of the amplitude for the tensor meson production:

$$\begin{aligned}
\mathcal{M}^{J=2}_{\lambda_1\lambda_2} &\propto Y_{2,\lambda_1-\lambda_2}(\theta,\phi)\cdot(\delta_{\lambda_1-\lambda_2,-2} + \delta_{\lambda_1-\lambda_2,2}) \text{ (type A)}, \\
\mathcal{M}^{J=2}_{\lambda_1\lambda_2} &\propto Y_{2,\lambda_1-\lambda_2}(\theta,\phi)\cdot\delta_{\lambda_1-\lambda_2,0} \text{ (type B)}. \qquad (2.4.38)
\end{aligned}$$

We shall call them model A and B, respectively. For $f_2(1270)$ production the amplitude is dominantly of the type A [108]. The same situation appears for the $f_2'(1525)$ and $f_2(1950)$ mesons since they are the same nonet partners of $f_2(1270)$.

For the first time the decay of $f_2(1565)$ into dipions was studied in Ref. [116], while its decay into two photons was analysed in Ref. [112]. The $f_2(1565)$ resonance is not well understood so far. The BELLE Collaboration found in this region both components (A, B) in their partial wave analysis [110,111,113]. We tried both models in order to describe the experimental data, taking the $\Gamma_{\pi\pi}$ decay width from [112] and fitting $\Gamma_{\gamma\gamma}$. A better description of the data was obtained using the relation:

$$\mathcal{M}^{f_2(1565)}_{\lambda_1\lambda_2} \propto Y_{2,\lambda_1-\lambda_2}(\theta,\phi)\cdot\delta_{\lambda_1-\lambda_2,0}\ . \tag{2.4.39}$$

This amplitude takes a different form than its counterpart for the $f_2(1270)$ meson. This is equivalent to the fact that the structure ($q\bar{q}$ state) of $f_2(1565)$ resonance may be completely different than that for $f_2(1270)$, $f_2'(1525)$ or $f_2(1950)$.

The $f_4(2050)$ resonance was not studied so far in the $\gamma\gamma \to \pi\pi$ reactions. For the spin-4 resonance again two simple possibilities come into the game:

$$\begin{aligned}
\mathcal{M}^{J=4}_{\lambda_1\lambda_2} &\propto Y_{4,\lambda_1-\lambda_2}(\theta,\phi)\cdot(\delta_{\lambda_1-\lambda_2,-2}+\delta_{\lambda_1-\lambda_2,2})\ \text{(type A)},\\
\mathcal{M}^{J=4}_{\lambda_1\lambda_2} &\propto Y_{4,\lambda_1-\lambda_2}(\theta,\phi)\cdot\delta_{\lambda_1-\lambda_2,0}\ \text{(type B)}.
\end{aligned} \tag{2.4.40}$$

While the BELLE partial wave analysis [110,111,113] suggests the dominance of the type A form, in our analysis we find that type B form fits better to the experimental data.

Fig. 2.11 shows a combination of all s-channel resonances which were discussed above. The biggest contribution comes from the $f_2(1270)$ meson production. Simultaneously this is one of the broadest resonances. At lower energies ($W_{\gamma\gamma} < 0.7$ GeV), the scalar $\sigma(600)$ meson dominates. Although the line shape of $f_2(1270)$ meson itself is crucial, the interference of the right wing of that resonance and other resonances which have peaks (resonance positions) at $W_{\gamma\gamma} > 1.5$ GeV play very important role.

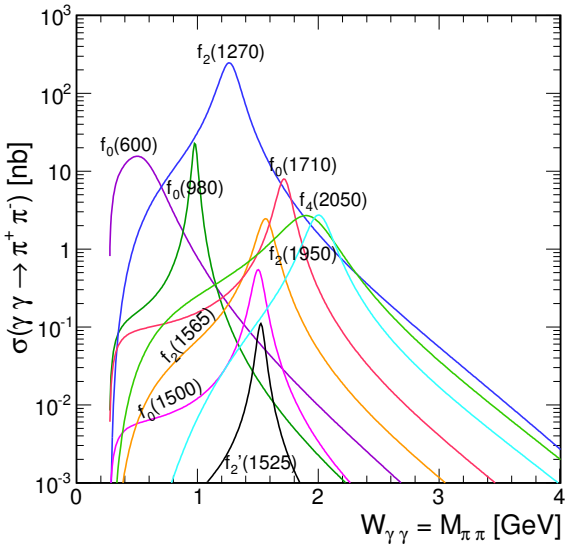

Figure 2.11: Contributions of the different s-channel $\gamma\gamma$ resonances for the $\pi^+\pi^-$ production as obtained based on PDG book [109] and our fit to be presented in the following.

2.4.3 $\gamma\gamma \to \pi^0\pi^0$ in a simple coupled-channel model with $\rho^\pm$ exchange

Due to vanishing charge of neutral pions the $\gamma\gamma \to \pi^0\pi^0$ amplitude vanishes at the Born-level. In this case a loop mechanism with $\rho^\pm$ exchange is possible (see Fig. 2.12). The amplitude for this mechanism is a combination of t-, u- amplitudes. An example of a process which leads to channel coupling is shown in Fig. 2.12. The left panel corresponds to contact amplitude and the right panel depicts the $\rho^\pm$ meson exchange in the t channel.

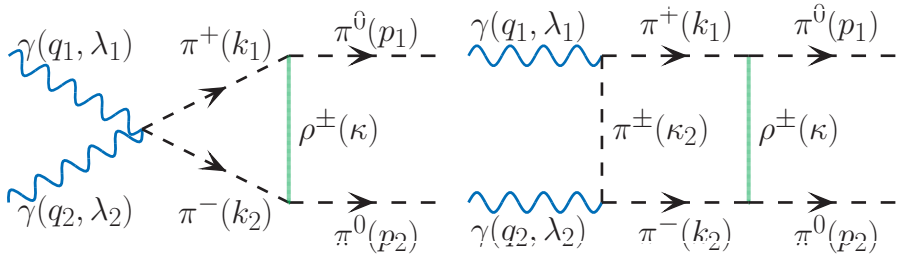

Figure 2.12: Feynman diagrams for $\gamma\gamma \to \pi^0\pi^0$ process with charged ρ meson exchange.

The contact amplitude can be written as:

$$\begin{aligned}\mathcal{M}^c(\lambda_1,\lambda_2) &= \int 2e^2 g^{\mu\nu}\epsilon_\mu(\lambda_1)\epsilon_\nu(\lambda_2)\frac{1}{k_1^2-m_\pi^2+i\epsilon}g_{\pi\pi\to\rho}\left(k_1^\alpha+p_1^\alpha\right)\\ &\times \frac{\left(-g_{\alpha\beta}+\frac{\kappa_\alpha\kappa_\beta}{m_\rho^2}\right)}{\kappa^2-m_\rho^2+i\Gamma_\rho m_\rho}g_{\pi\pi\to\rho}\left(k_2^\beta+p_2^\beta\right)\frac{1}{k_2^2-m_\pi^2+i\epsilon}\\ &\times F(\hat{s},\hat{t},\hat{u})F_{\rho^\pm}^2(\kappa)F_{\pi^+}^2(k_1)F_{\pi^-}^2(k_2)\frac{d^4\kappa}{(2\pi)^4} \qquad (2.4.41)\end{aligned}$$

and the corresponding t-channel amplitude as:

$$\begin{aligned}\mathcal{M}^t(\lambda_1,\lambda_2) &= \int \frac{e^2}{\kappa_2^2-m_\pi^2+i\epsilon}\frac{1}{k_1^2-m_\pi^2+i\epsilon}g_{\pi\pi\to\rho}\left(k_1^\alpha+p_1^\alpha\right)\\ &\times \frac{\left(-g_{\alpha\beta}+\frac{\kappa_\alpha\kappa_\beta}{m_\rho^2}\right)}{\kappa^2-m_\rho^2+i\Gamma_\rho m_\rho}g_{\pi\pi\to\rho}\left(k_2^\beta+p_2^\beta\right)\frac{1}{k_2^2-m_\pi^2+i\epsilon}\\ &\times \epsilon_\mu\left(\lambda_1\right)\left(\kappa_2^\mu+k_1^\mu\right)\epsilon_\nu\left(\lambda_2\right)\left(\kappa_2^\nu-k_2^\nu\right)\\ &\times F(\hat{s},\hat{t},\hat{u})F_{\rho^\pm}^2(\kappa)F_{\pi^+}^2(k_1)F_{\pi^-}^2(k_2)\frac{d^4\kappa}{(2\pi)^4}\ . \qquad (2.4.42)\end{aligned}$$

The amplitude for u-channel is obtained by a interchanging particle π^+ with particle π^- in Fig. 2.12. The coupling constant equals $g_{\pi\pi\to\rho}=\sqrt{4\pi\cdot 2.6}$.

The form factors that appear in the above formulae are parametrized here as:

- $F(\hat{s},\hat{t},\hat{u})=\frac{F^2(\hat{t})+F^2(\hat{u})}{1+F^2(\hat{s})}$
  where $F(\hat{s})=\exp\left(\frac{-\left(\hat{s}-4m_\pi^2\right)^2}{\Lambda_{BOX}^4}\right)$ and $F(x)=\exp\left(\frac{-\left(x^2-m_\pi^2\right)^2}{\Lambda_\pi^4}\right)$ for $x=\hat{t},\hat{u}$,

- $F_{\rho^\pm}(\kappa)=\exp\left(\frac{-\left(\kappa^2-m_\rho^2\right)^2}{\Lambda_\rho^4}\right)$,

- $F_{\pi^+/-}(x)=\exp\left(\frac{-\left(x^2-m_\pi^2\right)^2}{\Lambda_\pi^4}\right)$ for $x=k_1,k_2$,

where Λ_{BOX}, Λ_ρ and Λ_π are, in principle, free parameters. The resulting amplitude strongly depends on the value of the Λ parameters.

This coupled-channel model with charged ρ meson exchange is important for the $\gamma\gamma\to\pi^0\pi^0$ channel since the cross section for the $\gamma\gamma\to\pi^+\pi^-$ reaction is much bigger than that for the $\gamma\gamma\to\pi^0\pi^0$ reaction. Similar mechanism for the $\gamma\gamma\to\pi^+\pi^-$ can be, however, neglected.

2.4.4 pQCD mechanisms

At high dipion invariant masses ($W_{\gamma\gamma} > 2.5$ GeV) the mechanism of the reaction is not fully understood. Brodsky and Lepage made a first prediction of the leading-order perturbative quantum chromodynamics (pQCD) [102] which was further studied e.g. in [103, 117]. In general, the predictions of the pQCD calculation lay below the experimental data measured at The Large Electron-Positron Collider (LEP) in ALEPH detector [118] and recently by the BELLE Collaboration [119]. The next-to-leading-order calculations were presented only in Ref. [120] and these results are not able to describe the present experimental data.

Some time ago Diehl, Kroll and Vogt (DKV) suggested that a soft handbag mechanism may be the dominant mechanism [106] for the wide-angle scattering at intermediate energies. In this approach the normalization as well as energy dependence of the corresponding cross section are adjusted to the world data on the $\gamma\gamma \to \pi^+\pi^-$ production [106, 107].

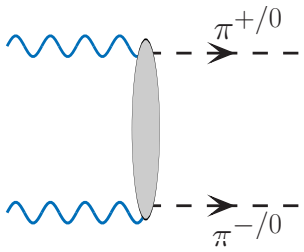

Figure 2.13: A generic Feynman diagram for dipion production in pQCD mechanisms.

Fig. 2.13 presents the general diagram for the pions production in LO pQCD. The oval in the figure means complicated interactions which are described in the Brodsky-Lepage (BL) or/and handbag mechanisms.

Brodsky-Lepage mechanism

The basic diagrams of the Brodsky and Lepage formalism are shown in Fig. 2.14 (Ref. [121]). In fact, the total number of LO diagrams contributing to the $\gamma\gamma \to (q\bar{q}) + (q\bar{q})$ amplitude is 20 (Ref. [120]). The invariant amplitude for the initial helicities of two photons is expressed through a parton distribution amplitudes ϕ_π

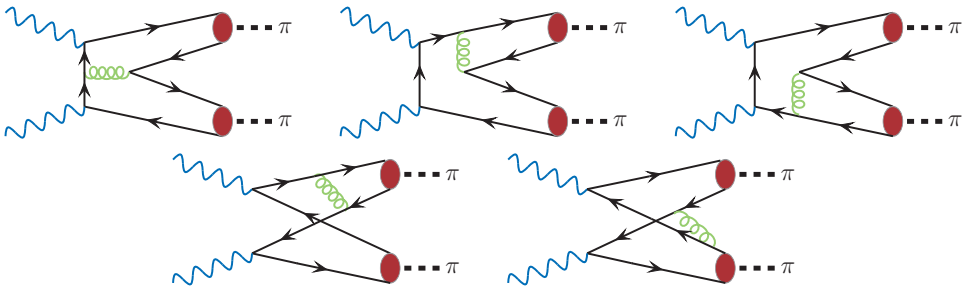

Figure 2.14: Some examples of Feynman diagrams for the Brodsky-Lepage perturbative mechanism for $\gamma\gamma \to \pi\pi$.

for each hadron and quark/antiquark carries some fractional x/y momentum of parent hadron and through a hard-scattering amplitude $T_H^{\lambda_1\lambda_2}$ for scattering the clusters of collinear valence partons from each hadron:

$$\begin{aligned}\mathcal{M}\left(\lambda_1,\lambda_2\right) &= \int_0^1 dx \int_0^1 dy\, \phi_\pi\left(x,\mu_x^2\right) T_H^{\lambda_1\lambda_2}\left(x,y,\mu^2\right) \phi_\pi\left(y,\mu_y^2\right) \\ &\times F^{pQCD}\left(s\right), \end{aligned} \tag{2.4.43}$$

where $\mu_{x_{/y}} = \min\left(x_{/y}, 1-x_{/y}\right)\sqrt{s(1-z^2)}$; $z = \cos\theta$ [102]. The details of the helicity-dependent hard scattering amplitudes are discussed in Appendix D.4.2. The extra form factor in Eq. 2.4.43 aims to separate the perturbative from non-perturbative processes. We use the following function which smoothly switches off the non-perturbative pQCD region at low energies ($W_{\gamma\gamma} < 2$ GeV):

$$F^{pQCD}(s) = 1 - \exp\left(\frac{-\left(s-4m_\pi^2\right)^4}{\Lambda_{pQCD}^8}\right). \tag{2.4.44}$$

The parameter Λ_{pQCD} is fitted to experimental data (in our calculation we find $\Lambda_{pQCD} = 2.5$ GeV). The other form of the form factor was proposed in Ref. [104]. A discussion about different forms of the form factor is given in Appendix D.4.1.

The distribution amplitudes are subjected to the (Efremov-Radyushkin-Brodsky-Lepage) ERBL pQCD evolution [122, 123]. The scale-dependent valence-quark distribution amplitude of the pion [124, 125] is expanded in terms of Gegenbauer polynomials $C_n^{3/2}$ [126]

$$\phi_\pi\left(x,\mu^2\right) = \frac{f_\pi}{2\sqrt{3}} 6x\left(1-x\right) \sum_{n=0}^{\infty'} C_n^{3/2}\left(2x-1\right) a_n\left(\mu^2\right), \tag{2.4.45}$$

where the expansion coefficient

$$a_n\left(\mu^2\right) = \frac{2}{3}\frac{2n+3}{(n+1)(n+2)}\left(\frac{\alpha_s\left(\mu^2\right)}{\alpha_s\left(\mu_0^2\right)}\right)^{-\frac{C_F}{\beta_0}\left[3+\frac{2}{(n+1)(n+2)}-4\sum_{k=1}^{n+1}\frac{1}{k}\right]} \times \int_0^1 \mathrm{d}x\, C_n^{3/2}(2x-1)\,\phi_\pi\left(x,\mu_0^2\right) \ , \tag{2.4.46}$$

depends on the form of the distribution amplitude $\phi_\pi\left(x,\mu_0^2\right)$. Above $C_F = \frac{4}{3}$, β_0 and α_s are explained in Appendix D.4.2.

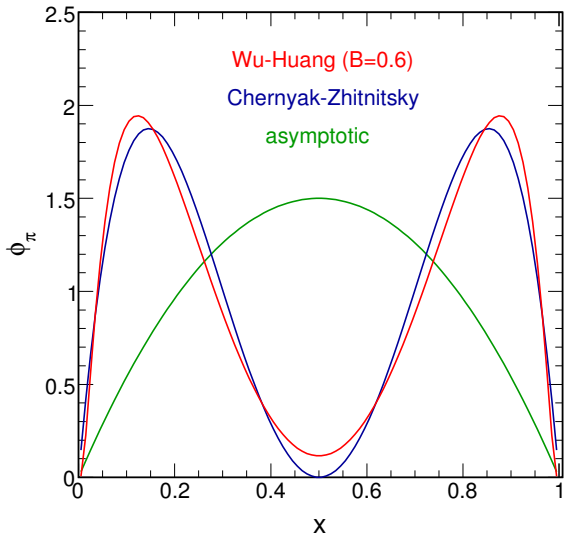

Figure 2.15: Quark distribution amplitudes of the pion.

Finally, the pQCD amplitude for the $\gamma\gamma \to \pi\pi$ reaction depends on the pion distribution amplitude. The letter has been, for long time, a subject of intensive discussion [102, 105, 125, 127]. The reference point is the asymptotic shape [128] (green line in Fig. 2.15)

$$\phi_{\pi\,\mathrm{asymp.}}(x) = 6x(1-x) \ . \tag{2.4.47}$$

This functional form turned out to be inconsistent with recent experimental data presented by the BaBar Collaboration for the pion transition form factor $F_{\gamma^*\gamma\pi}$ for large photon virtualities [129]. Wu and Huang [130] proposed recently a new form

of the distribution amplitude (red line in Fig. 2.15)

$$\phi_{\pi\,WH}\left(x,\mu_0^2\right) = \frac{\sqrt{3}A\,m_q\beta}{2\sqrt{2}\pi^{3/2}f_\pi}\sqrt{x\,(1-x)}\left(1+B\times C_2^{3/2}\,(2x-1)\right) \times \left(\mathrm{Erf}\left[\sqrt{\frac{m_q^2+\mu_0^2}{8\beta^2 x\,(1-x)}}\right] - \mathrm{Erf}\left[\sqrt{\frac{m_q^2}{8\beta^2 x\,(1-x)}}\right]\right)\,, \quad (2.4.48)$$

where the error function is defined as $\mathrm{Erf}(x) = \frac{2}{\sqrt{\pi}}\int_0^x \exp(-t^2)\mathrm{d}t$.
The authors take into account both the leading valence quark and the non-valence quark contribution. This pion distribution amplitude at the initial scale ($\mu_0^2 = 1$ GeV^2) is controlled by the parameter B, which defines the broadness of the pion distribution amplitude. This simple Wu-Huang (WH) model better describes (see Fig. 6 in Ref. [130]) recent BaBar data [129]. This pion distribution amplitude is rather close to the well-know Chernyak-Zhitnitsky [131] distribution amplitude (see the blue line in Fig. 2.15)

$$\phi_{\pi\,CZ}\,(x) = 30x(1-x)(2x-1)^2\,. \quad (2.4.49)$$

In the following we use quark distribution amplitude proposed by Wu & Huang (Eq. 2.4.48) and with parameters $B = 0.6$ and $m_q = 0.3$ GeV. Then a normalization constant $A = 16.62$ GeV^{-1} and a harmonic scale $\beta = 0.745$ GeV. $f_\pi = 93$ MeV above is the pion decay constant.

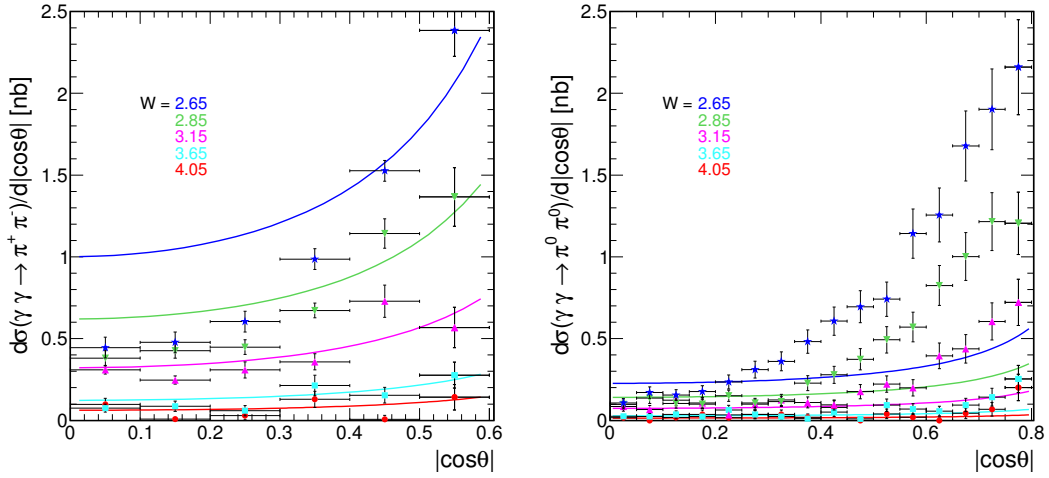

Figure 2.16: Comparison of the theoretical predictions of the Brodsky-Lepage pQCD angular distributions with the BELLE data.

Fig. 2.16 shows the comparison of the results for the BL approach with experimental data [113, 119] for five different values of energy. As can be seen from the figures the BL pQCD approach is not enough to describe the "high energy" data, especially for the $\gamma\gamma \to \pi^0\pi^0$ reaction. Thus one needs to take into account another mechanism which correctly describes the experimental data at higher-energies ($W_{\gamma\gamma} > 2.5$ GeV).

Handbag model

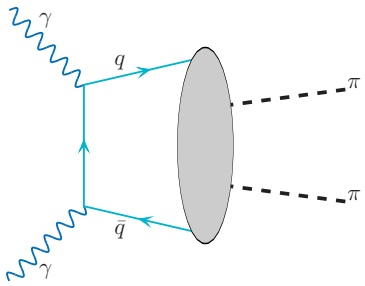

Figure 2.17: Feynman diagram for handbag mechanism.

The handbag approach was proposed in Ref. [106, 107]. Fig. 2.17 depicts the Feynman diagram for the handbag mechanism. There two photons interact with the same quark exchange and the intermediate state "active" $q\bar{q}$-quarks have almost the same momenta as meson, while the "passive" pair of other $q'\bar{q}'$-quarks is picked out from the vacuum by soft non-perturbative interactions. In this approach the only non-zero helicity-dependent amplitudes are

$$\mathcal{A}_{+-} = \mathcal{A}_{-+} = -4\pi\alpha_{em}\frac{s^2}{tu}R_{2\pi}(s) \ . \tag{2.4.50}$$

Handbag model predicts that the angular dependence of amplitude is $\propto 1/\sin^2\theta$, where θ is the c.m. scattering angle. The blob in Fig. 2.17 represents the two-pion distribution amplitude. The form factors $R_{2\pi}(s)$ are of non-perturbative nature and are in principle unknown. In practice they were fitted to the experimental total (integrated over experimentally measured region) cross section for $\gamma\gamma \to \pi^+\pi^-$ [106, 107], assuming that the mechanism exhausts the measured cross section at high energy ($W_{\gamma\gamma} > 2.5$ GeV). This is not a necessary condition. In our analysis

we relax this rather restrictive assumption and focus on the angular distributions. Following [106, 107] annihilation form factor is parametrized as follows:

$$\begin{aligned} R_{\pi^+\pi^-} = R_{\pi^0\pi^0} = R_{2\pi} &= \frac{5}{9}R^u_{2\pi} + \frac{1}{9}R^s_{2\pi} \\ &= \frac{5}{9s}a_u\left(\frac{s_0}{s}\right)^{n_u} + \frac{1}{9s}a_s\left(\frac{s_0}{s}\right)^{n_s} . \end{aligned} \tag{2.4.51}$$

Above equation is divided into two parts: a valence (u index) and a non-valence (s index) form factor. The values of a_u, n_u, a_s and n_s are taken from Ref. [106, 107]. We have averaged the values for different energies (see Table 1 in Ref. [107]): $a_u = 1.375$ GeV^2, $n_u = 0.4175$, $a_s = 0.5025$ GeV^2 and $n_s = 1.195$. The parameter $s_0 = 9$ GeV^2 is fitted to the experimental data for three channels: K^+K^-, $K^0\bar{K}^0$ and $\eta\pi^0$.

The cross section integrated over $\cos\theta$ from $-\cos\theta_0$ to $\cos\theta_0$ for pion pairs takes the form

$$\sigma\left(\gamma\gamma \to \pi\pi\right) = C\frac{4\pi\alpha^2_{em}}{s}\left(\frac{\cos\theta_0}{\sin^2\theta_0} + \frac{1}{2}\ln\frac{1+\cos\theta_0}{1-\cos\theta_0}\right)\left|R_{\pi\pi}\left(s\right)\right|^2 , \tag{2.4.52}$$

where $C = +1$ for charged pions and $C = -1$ for neutral mesons. The ratio of the cross section for the $\pi^0\pi^0$ process to the $\pi^+\pi^-$ process does not depend on θ and equals $\frac{1}{2}$. Usually the experimental data are presented with some limitation on $\cos\theta$, thus one can write the additional information coming from handbag approach:

$$\sigma\left(\gamma\gamma \to \pi^+\pi^-; \cos\theta_0 = 0.6\right) = 425 \text{ nb GeV}^2\left|R_{\pi\pi}\left(s\right)\right|^2\frac{1}{s} , \tag{2.4.53}$$

$$\sigma\left(\gamma\gamma \to \pi^+\pi^-; \cos\theta_0 = 0.8\right) = 866 \text{ nb GeV}^2\left|R_{\pi\pi}\left(s\right)\right|^2\frac{1}{s} . \tag{2.4.54}$$

A characteristic feature of the handbag mechanism is the fact that the differential cross section for charged and neutral pion pairs is the same, in striking contrast with what is found in the hard scattering approach.

Angular distributions calculated in the handbag approach together with the BELLE experimental data [113, 119] are shown in Fig. 2.18. Here one can see similar situation as in Fig. 2.16. Only at the highest energies ($W_{\gamma\gamma} > 3.5$ GeV) the handbag parametrization looks reasonable. It is very interesting whether the combination of the two QCD mechanisms can describe the experimental data. This will be shown in detail in the next subsection.

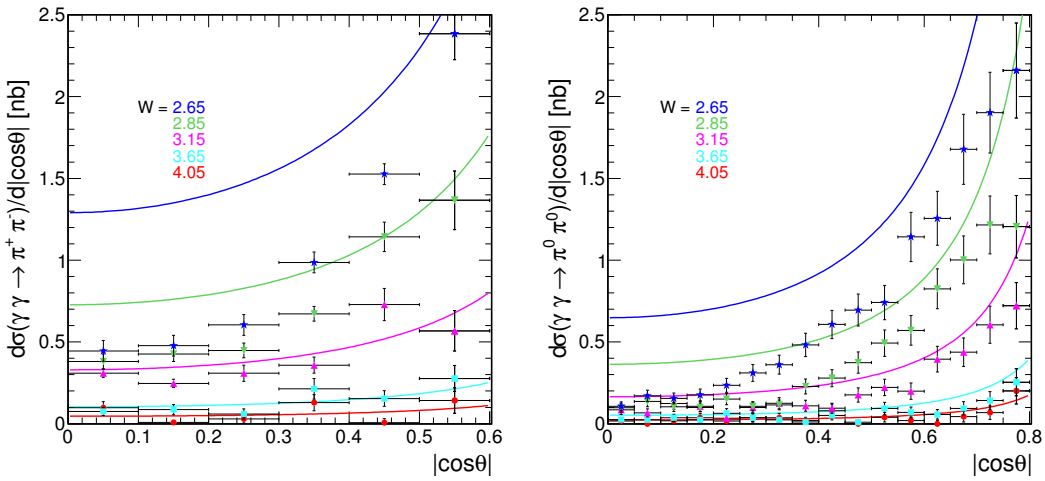

Figure 2.18: Comparison of the handbag model predictions with the BELLE angular data.

2.4.5 Results of the fit to experimental data

In chapters 2.4.1- 2.4.4 I have described all (potential) ingredients which, in our opinion, are necessary to describe experimental data for the $\gamma\gamma \to \pi\pi$ processes (total cross sections and angular distributions). The technical question is how to include all these ingredients together and how to fix free parameters of the combined model.

In our approach we shall make an educated (using our experience in hadronic physics) adjustment of the parameters essentially "by hand" in an iterative (several times repeated) procedure. We gave up from automatic fitting to the data in spite it leads to good χ^2 solution(s) as such automatic fit may lead to rather unphysical parameters.

In our adjustment to experimental data we shall include:

- Born soft pion exchange amplitude (see Fig. 2.9) for the $\gamma\gamma \to \pi^+\pi^-$ reaction with one free parameter (cut-off parameter of the form factor).

- soft loop $\rho^{\pm}$ exchange amplitude (see Fig. 2.12), where the form factor parameter is adjusted to describe the data for the $\gamma\gamma \to \pi^0\pi^0$ reaction.

- $\pi\pi$ resonances (see Fig. 2.10) with most of the parameters taken from particle data book, except of the parameters of rather poorly understood σ resonance.

In some cases we allow for modification of $\Gamma_{f_0(600)}$, $\Gamma_{f_0(600)\to\gamma\gamma}$, $\Gamma_{f_4(2050)\to\gamma\gamma}$. Since we add the resonances with other processes coherently we have to allow for a free phase factor in front of the resonance amplitudes.

- Brodsky-Lepage mechanism (see Fig. 2.14), calculated within pQCD. We start the ERBL evolution for $\mu_0^2 = 1$ GeV^2. The distributions at large angles ($|\cos\theta| \approx 1$), where the pQCD calculations does not apply, are corrected by the extra form factor (2.4.44) and the form factor parameter is treated as a free parameter to be adjusted to experimental data.

- Handbag mechanism (see Fig. 2.17) where we allow the magnitude of the process to be fitted (adjusted) to simultaneously describe the $\gamma\gamma \to \pi^+\pi^-$ and $\gamma\gamma \to \pi^0\pi^0$ data. As for the Brodsky-Lepage mechanism we allow for modifications of the cross section at large angles (one form factor parameter).

In the following we shall show one example of the most preferred by the data solution. As will be shown below, the agreement with the data is satisfactory and therefore the "educated fit" can be used for the predictions of the cross sections for nuclear collisions, which is our main aim.

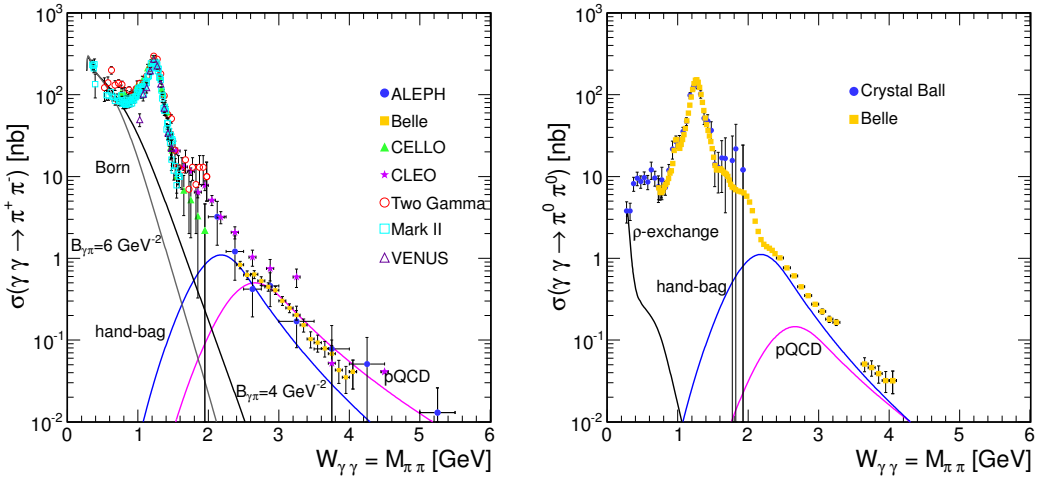

Figure 2.19: Contributions of the pQCD continua to the $\gamma\gamma \to \pi^+\pi^-$ and $\gamma\gamma \to \pi^0\pi^0$ reactions.

Fig. 2.19 presents the dipion continuum contributions as the function of incident photon-photon energy. One can see the results both for the $\gamma\gamma \to \pi^+\pi^-$ reaction

(left panel) and for production of neutral pions (right panel). Here we have depicted the prediction for pion exchange contribution (black lines) with two different values of the slope parameter $B_{\gamma\pi}$, pQCD BL mechanism (pink lines), handbag model (blue lines) and ρ meson exchange (black line for $\gamma\gamma \to \pi^0\pi^0$). One can observe that for larger values of energy, the QCD mechanisms reasonably well describe the data. Simultaneously, the low-energy continuum is not sufficient to describe the experimental data points. Thus the inclusion of the s-channel resonances is very important (see Fig. 2.10).

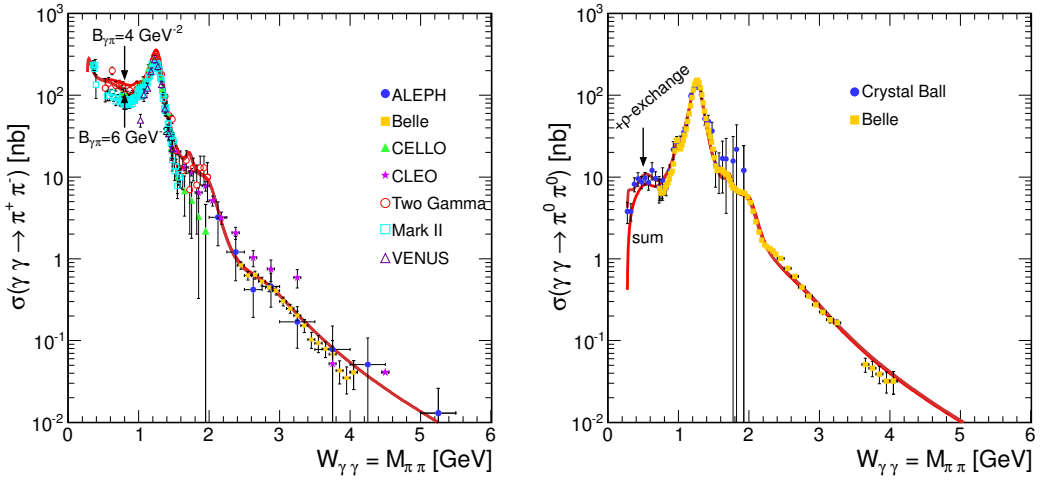

Figure 2.20: Theoretical fit of the $\gamma\gamma \to \pi^+\pi^-$ and $\gamma\gamma \to \pi^0\pi^0$ experimental data.

In the next figure one can see our full fit to the world experimental data as the function of the subprocess energy. Our predictions correspond to limited angular ranges of different experiments. The data for the $\gamma\gamma \to \pi^+\pi^-$ reaction are for the limit $|\cos\theta| < 0.6$ and they come from the ALEPH [118], BELLE [119], CELLO [132], CLEO [133], TPC/Two Gamma [134], Mark II [135] and VENUS [136] Collaborations. For the $\gamma\gamma \to \pi^0\pi^0$ reaction the data come from the BELLE [113] and Crystal Ball [137] groups and here the angular range is limited to $|\cos\theta| < 0.8$. Our approach rather nicely describes the experimental data simultaneously for the $\gamma\gamma \to \pi^+\pi^-$ (left panel) and for $\gamma\gamma \to \pi^0\pi^0$ (right panel) reactions. For the charged pions, one can see the two sums corresponding to two different values of $B_{\gamma\pi}$: 4 or 6 GeV^{-2}. Similarly, on the right panel of Fig. 2.20 one can observe the difference between the results with and without contribution with the $\rho^{\pm}$ meson exchange.

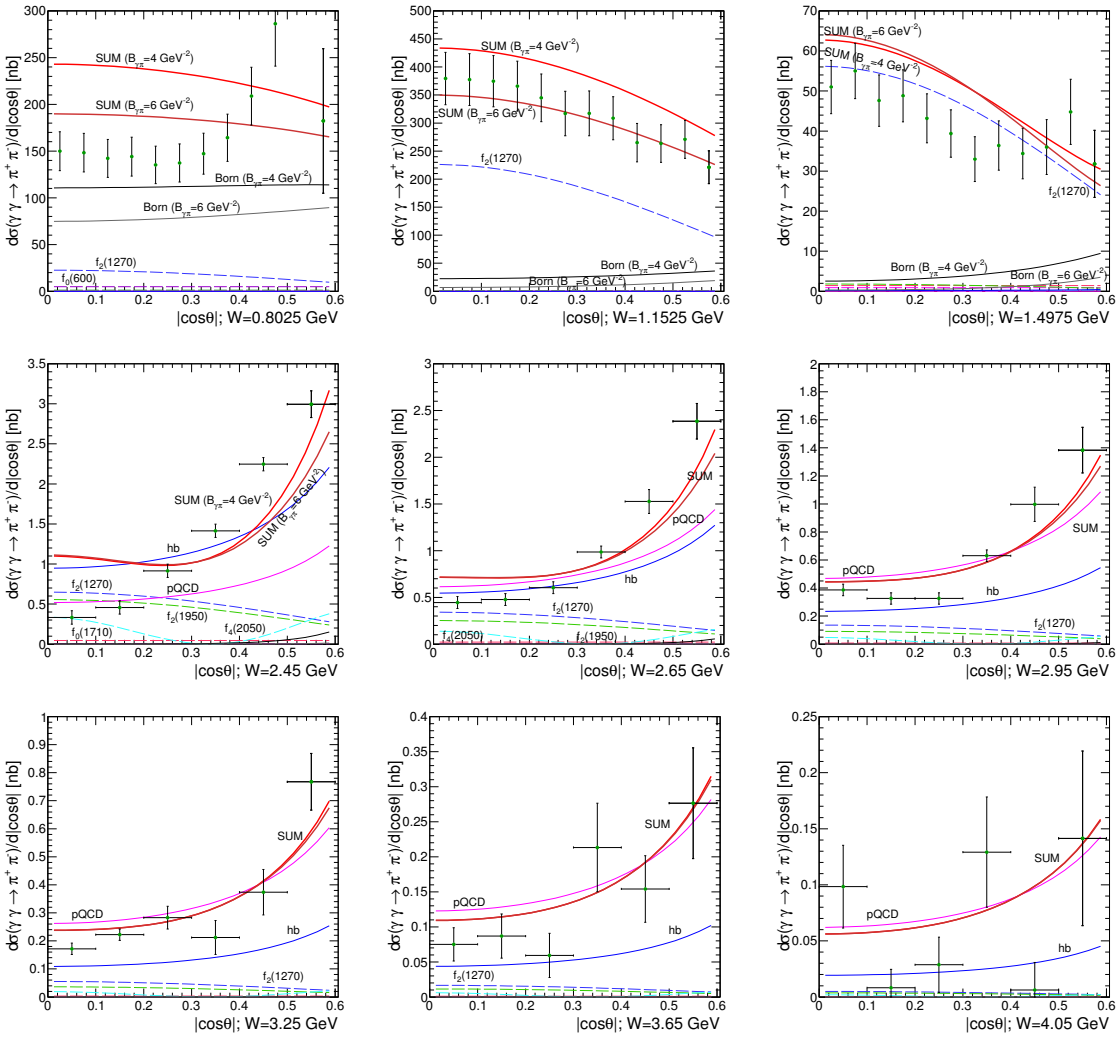

Figure 2.21: Angular distributions for the $\gamma\gamma \to \pi^+\pi^-$ reaction.

Fig. 2.21 and 2.22 show the comparison of our predictions with the angular experimental data measured by the BELLE Collaboration ([110,113,119]). The calculations are done for nine different energies ranging from 0.8025 GeV for $\gamma\gamma \to \pi^+\pi^-$ or 0.61 GeV for $\gamma\gamma \to \pi^0\pi^0$ to 4.05 GeV. The first four panels for the $\gamma\gamma \to \pi^+\pi^-$ reaction present the sum of contributions of many mechanisms for two different values of the slope parameter in the hadronic form factor. We obtain a better description of the experimental data points when we use the exponential form factor with $B_{\gamma\pi} = 6$ GeV^{-2}. The description for $W_{\gamma\gamma} = 1.4975$ GeV shows that one should include also D wave, but we have no theoretical guidance on how to do it. The contributions for the QCD mechanism start to dominate for larger values

of energy. The Brodsky-Lepage mechanism is the leading one in the high energy ($W_{\gamma\gamma} > 2.5$ GeV) domain. For the $\gamma\gamma \to \pi^0\pi^0$ reaction (Fig. 2.22), the first two figures present the cross section corresponding to the sum of processes with and without contribution from the charged ρ meson exchange. One can observe that the inclusion of this contribution is important only for $W_{\gamma\gamma} < 0.6$ GeV (see the right panel of Fig. 2.20).

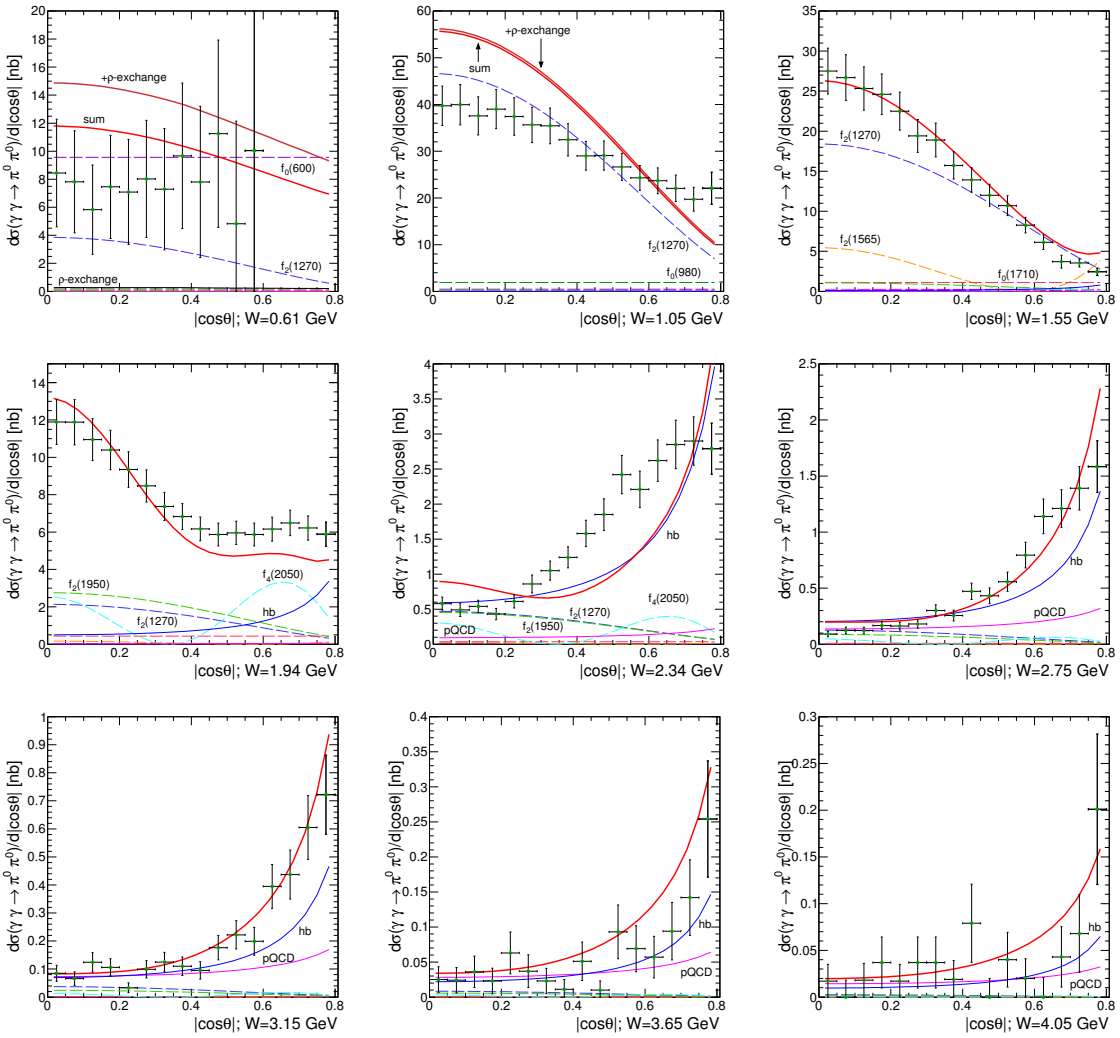

Figure 2.22: Angular distributions for the $\gamma\gamma \to \pi^0\pi^0$ reaction.

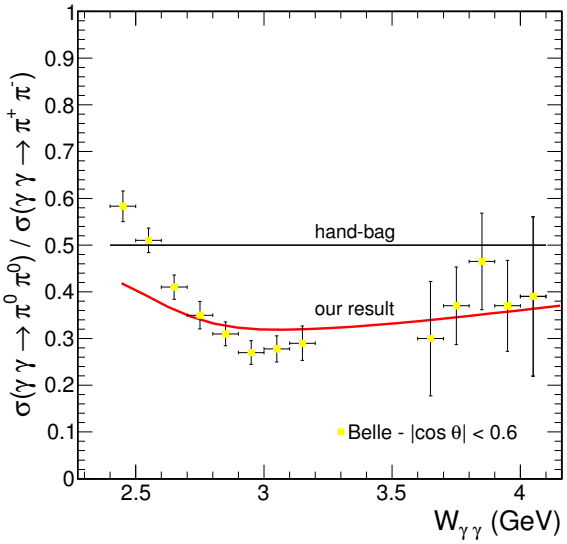

Figure 2.23: The ratio of the $\gamma\gamma \to \pi^0\pi^0$ and $\gamma\gamma \to \pi^+\pi^-$ cross sections as a function of $W_{\gamma\gamma}$ together with BELLE experimental data.

Very interesting seems to be the ratio of the neutral and charged pion pair production cross sections. This is shown in Fig. 2.23. Our result (red line) is confronted with BELLE experimental data [113, 119]. We have some problem with correct description of the data in the $(2.4-2.7)$ GeV range of the collision energy. This can be caused by not very good description of the angular data for the $\gamma\gamma \to \pi^0\pi^0$ reaction in this range of energy as discussed above. However, our results prove that the correct description of the high-energy cross section requires to take into account both the Brodsky-Lepage and handbag mechanisms simultaneously. The black solid line represents only the handbag model result, which is independent of θ and is constant $(= \frac{1}{2})$.

Finally we get good agreement of the total elementary cross section with all available experimental data for the first time in such a broad range of energies. Simultaneously we have obtained a reasonable description of the angular distributions. Presented above approach for $\gamma\gamma \to \pi\pi$ is well suited for the predictions of the cross sections for nucleus-nucleus collisions. It is worth to note that the corresponding nuclear cross section for both charged and neutral pion production is calculated for the same parameters of resonances and QCD mechanisms.

Chapter 3

Nuclear results for single and double vector meson photoproduction

In this chapter we will discuss first nuclear photoproduction of a single ρ^0 meson. We will show that a sequence of two single ρ^0 photoproductions in nuclear processes (explained below) leads to exclusive production of two ρ^0 mesons in nucleus-nucleus UPC. This process may compete with the $\gamma\gamma \to \rho^0\rho^0$ mechanism (in nucleus-nucleus) collisions discussed in the next chapter.

Nuclear photoproduction of a single ρ^0 can be understood as a photon fluctuation into hadronic or quark-antiquark component and its subsequent propagation through the second nucleus and transformation (fragmentation) into the ρ^0 meson.

3.1 Smearing of ρ^0 meson masses

The ρ^0 resonance is fairly broad, $\Gamma_{\rho^0} \approx 0.150$ GeV [109]. In further calculation of ρ^0 photoproduction two-different approximations will be considered: first one in which mass of ρ^0 meson is fixed (Dirac delta function) and second one in which mass is smeared as dictated by the decay width. Smearing of ρ^0 meson mass is included by using an amplitude which is a sum of the relativistic Breit-Wigner amplitude

and the amplitude $\mathcal{B}_{\pi\pi}$ for the direct $\pi^+\pi^-$ continuum production

$$\mathcal{A}(m) = \mathcal{A}_{\mathcal{BW}} \frac{\sqrt{m m_{\rho^0} \Gamma_{\rho^0}(m)}}{m^2 - m_{\rho^0}^2 + i m_{\rho^0} \Gamma_{\rho^0}(m)} + \mathcal{B}_{\pi\pi} \tag{3.1.1}$$

with

$$\Gamma_{\rho^0}(m) = \Gamma_{\rho^0} \frac{m_{\rho^0}}{m} \left(\frac{m^2 - 4m_\pi^2}{m_{\rho^0}^2 - 4m_\pi^2} \right)^{3/2}, \tag{3.1.2}$$

where m_{ρ^0} and Γ_{ρ^0} are the width and mass of the ρ^0 meson, m_π is the mass of the pion. The mass-dependent width (Ref. [138]) assures vanishing of the spectral shape below the two-pion threshold. The first amplitude in Eq. (3.1.1) has purely resonant character and the second one is added to describe a big asymmetry (enhancement of the left-hand side and damping of the right-hand side of the ρ^0 resonance). A physical interpretation of the constant term for proton-proton collisions can be found e.g. in Ref. [139]. It was explained there as due to the Deck (or Drell-Söding) two-pion continuum [140].

Table 3.1: Parameters for relativistic Breit-Wigner and continuum amplitudes for ρ^0.

Parameter	ZEUS [141]	STAR [138]	ALICE [142, 143]
m_{ρ^0} [GeV]	0.77 ± 0.002	0.775 ± 0.003	0.761 ± 0.0023
Γ_{ρ^0} [GeV]	0.146 ± 0.003	0.162 ± 0.007	0.1502 ± 5.5
$\left\lvert \frac{\mathcal{B}_{\pi\pi}}{\mathcal{A}_{\mathcal{BW}}} \right\rvert$ [GeV$^{-1/2}$]	0.669	0.89 ± 0.08	0.5 ± 0.04
m [GeV]	$(0.55 - 1.2)$	$(0.5 - 1.1)$	$(0.28 - 1.512)$

Table 3.1 collects parameters needed to calculate amplitude given by (3.1.1). The errors given in the table are of statistical origin. The systematic errors can be found in references given in the table. The last line in the table shows the range of invariant ρ^0 mass for which the parametrization was determined.

Fig. 3.1 presents the square of the amplitude (3.1.1) with (solid line) and without (dashed line) continuum component $\mathcal{B}_{\pi\pi}$. One can see results obtained with parametrizations of the ZEUS [141] (black lines), STAR [138] (blue lines) and ALICE [142,143] (red lines) Collaborations. The results obtained by each of the groups are very similar. The ALICE parametrization has a huge advantage: the ρ^0 mass smearing is done for larger range of center of mass energy ($m_{max} = 1.512$ GeV) than

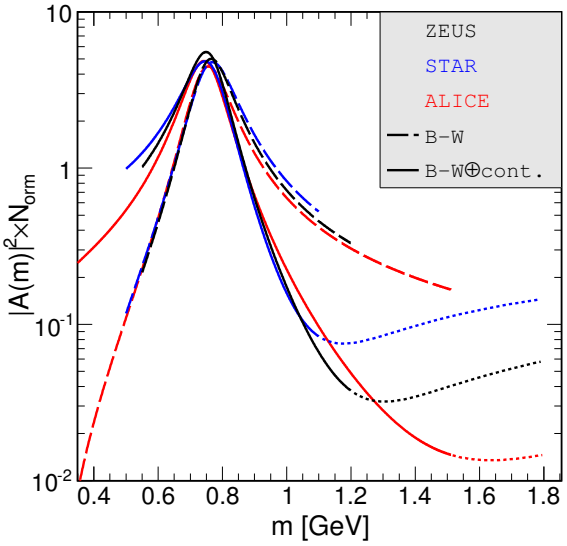

Figure 3.1: The invariant mass distribution for the "ρ^0" meson.

in other cases. This fact is very important in nuclear calculations if one wants to make predictions in a broad range of two-pion invariant mass. For comparison see the dotted lines in Fig. 3.1. At large m the shape of the distributions does not seem physical. This strange behaviour of the distributions for the large dipion masses happens beyond upper application limit (see the last row in Table. 3.1). This may be traced to a crude approximation of invariant dipion mass independence of the Deck mechanism.

Y-axis in Fig. 3.1 designates the magnitude of the resonance contribution which fulfills the condition

$$\int N_{orm} \, |\mathcal{A}(m)|^2 \, \mathrm{d}m \, = 1 \, . \tag{3.1.3}$$

As was mentioned above, the amplitude for the direct $\pi^+\pi^-$ production raises the left-hand side ($m < m_{\rho^0}$) of the resonance and simultaneously reduces the right-hand side ($m > m_{\rho^0}$) of the resonance. In further calculation, we will smear the mass of ρ^0 meson with the extra $\pi\pi$ continuum amplitude, because this way correctly describes the experimental data points for the invariant mass distribution.

The dominant decay channel of the ρ meson is a pair of pions with a branching rate of 99.9%. In the calculations performed in this dissertation the $\rho^0 \to \pi^+\pi^-$ decays are done in a separate Monte Carlo code. The distributions in the ρ^0 center

of mass are generated either isotropically or randomly with the decay function in the ρ^0 center of mass given by the distribution:

$$f(\theta^*) = \frac{3}{2}\sin^2(\theta^*) \; . \tag{3.1.4}$$

This distribution corresponds to the decay of transversely polarized ρ^0.

To calculate nuclear cross section for ρ^0 photoproduction we perform the following steps: first a map of the cross section for a dense grid in rapidity of meson(s) (y) or (y_1, y_2) is prepared in the case of single/double scattering with fixed ρ^0 meson masses (the corresponding ρ^0 mesons have negligibly small transverse momenta). One should include the smearing of the ρ^0 mass too. The cross section for single scattering (more details in section 3.2) can be written then as:

$$\frac{\mathrm{d}\sigma_{AA\to AA\rho_0}}{\mathrm{d}m\,\mathrm{d}y} = f(m)\frac{\mathrm{d}\sigma_{AA\to AA\rho_0}\,(y,m)}{\mathrm{d}y} \; . \tag{3.1.5}$$

Analogously for double scattering mechanism (see section 3.3):

$$\frac{\mathrm{d}\sigma_{AA\to AA\rho_0\rho_0}}{\mathrm{d}m_1\,\mathrm{d}m_2\,\mathrm{d}y_1\,\mathrm{d}y_2} = f(m_1)f(m_2)\frac{\mathrm{d}\sigma_{AA\to AA\rho_0\rho_0}\,(y_1y_2;m_1,m_2)}{\mathrm{d}y_1\mathrm{d}y_2} \; . \tag{3.1.6}$$

The smearing distribution $f(m)$ is called sometimes as spectral shape. It can be expressed formally through the relation

$$f(m) = \frac{|\mathcal{A}\,(m)|^2\,N_{orm}}{\int |\mathcal{A}\,(m)|^2\,N_{orm}\mathrm{d}m} \; . \tag{3.1.7}$$

Please note that the numerator of Eq. (3.1.7) is displayed in Fig. 3.1.

Next a Lorentz transformation to the overall ion-ion center of mass (laboratory system for both RHIC and LHC) is performed. Different kinematical variables related to charged pions are calculated and corresponding distributions are obtained by an appropriate binning. This way we have the full kinematics of the event thus any cut on kinematical variables can be easily imposed.

3.2 Single ρ^0 meson production

Fig. 3.2 illustrates a single vector meson production mechanism in ultraperipheral ultrarelativistic heavy-ion collisions. The cross section for this mechanism can be

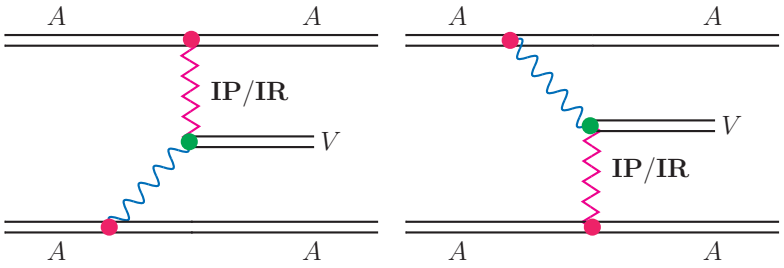

Figure 3.2: Feynman diagrams for the single vector meson production by photoproduction (photon-Pomeron or Pomeron-photon fusion).

written as a differential in the impact parameter b and in the vector meson rapidity y

$$\frac{\mathrm{d}\sigma_{A_1A_2\to A_1A_2V}}{\mathrm{d}^2b\mathrm{d}y} = \frac{\mathrm{d}P_{\gamma\mathbb{P}}\left(b,y\right)}{\mathrm{d}y} + \frac{\mathrm{d}P_{\mathbb{P}\gamma}\left(b,y\right)}{\mathrm{d}y} \,. \tag{3.2.8}$$

$P_{\gamma\mathbb{P}}(y,b)$ or $P_{\mathbb{P}\gamma}(y,b)$ is the probability density for producing a vector meson V at rapidity y for fixed impact parameter b of the heavy-ion collision. Only such cases when $b > 2R_A$ are included in the integration. Probability density expresses two-different possibilities of the production vector meson shown in Fig. 3.2. Each probability is the convolution of a energy of photon from first or second nucleus ($\omega_{1/2} = m_V/2\exp(\pm y)$) and a flux of equivalent photons:

$$P_{1/2}\left(y,b\right) = \omega_{1/2}\tilde{N}\left(\omega_{1/2},b\right)\sigma_{\gamma A_{2/1}\to VA_{2/1}}(W_{\gamma A_{2/1}}) \,, \tag{3.2.9}$$

where $\tilde{N}\left(\omega_{1/2},b\right)$ is in principle a function of heavy ion - heavy ion impact parameter b and not of photon-nucleus impact parameter. The effective impact factor can be formally expressed through the photon flux in one of the nuclei and effective strength for interaction of the photon with the second nucleus

$$\tilde{N}\left(\omega_1,b\right) = \int N\left(\omega_1,b_1\right)\frac{S^2(\mathbf{b_2})}{\pi R_A^2}\mathrm{d}^2b_1 \approx N\left(\omega_1,b\right) \,, \tag{3.2.10}$$

where $\mathbf{b_1} = \mathbf{b} + \mathbf{b_2}$. The extra $S^2(\mathbf{b_2}) \approx \theta(R_A - \mathbf{b_2})$ factor ensures collision when the photon hits the nucleus. For the photon flux in the second nucleus one needs to replace 1→2 (and 2→1). Here we use the photon flux in the form which was given in Eq. (1.2.29).

The $\gamma A \to \rho^0 A$ photonuclear cross section is discussed in some details in Appendix E. The cross section is calculated with the help of the Glauber model for ρ^0

meson photoproduction. Finally Eq. (E.0.10) expresses the total cross section for $\gamma A \to \rho^0 A$ reaction and can be written as

$$\sigma_{\gamma A\to\rho^0 A} = \frac{d\sigma_{\gamma A\to\rho^0 A}\left(t=0\right)}{dt} \int\limits_{-\infty}^{t_{max}} \mathrm{d}t \left|F_A\left(t\right)\right|^2 \ . \tag{3.2.11}$$

This cross section is actually a function of energy in the γA system, so in this case one can write: $W = W_{\gamma A}$. The factor $|F_A\left(t\right)|$ appears here due to coherent $q\bar{q}$ dipole rescattering off a nucleus. A good approximation is to use the realistic nuclear charge form factor which is defined in Eq. (1.4.83). The squared four-momentum transfer: $t = -q^2 = -(m^2_{\rho^0}/\left(2\omega_{lab}\right))^2$.

The cross section for the $\gamma A \to VA$ reaction could be also calculated e.g. in the QCD dipole picture in a so-called mixed representation (see e.g. [144,145]). Slightly more complicated momentum space formulation of the vector meson production was discussed in [146].

At high energy above resonances the imaginary part of the amplitude for the $\gamma A \to VA$ process can be written as in Refs. [147–150]:

$$\Im\left(A_{\gamma A\to VA}(W)\right) = \sum_{\lambda\bar{\lambda}} \int \mathrm{d}z\, \mathrm{d}^2\rho\ \Psi^V_{\lambda\bar{\lambda}}(z,\rho)\ \sigma_{dip-A}(W,\rho)\ \Psi^{\gamma}_{\lambda\bar{\lambda}}(z,\rho)\ . \tag{3.2.12}$$

In the equation above, λ and $\bar{\lambda}$ are quark and antiquark helicities. Helicity conservation at high energy rescattering of the dipole in the nucleus is explicitly assumed. The variable ρ is the transverse size of the quark-antiquark dipole, and z denotes the longitudinal momentum fraction carried by a quark. The longitudinal momentum fraction carried by antiquark is then $(1-z)$. Using explicit formulae for photon and vector meson wave functions, the generic formula (3.2.12) can be written in a convenient way (for calculation see [144]). The dipole-nucleus cross section can then be expressed in the Glauber-Gribov picture in terms of the nuclear thickness $T_A(b_\gamma)$, as seen be the $q\bar{q}$ dipole in its way through the nucleus, and the dipole-proton $\sigma_{dip-p}(\rho)$ cross section as given for instance in Ref. [151]:

$$\sigma_{dip-A}(\rho,W) = 2\int \mathrm{d}^2 b_\gamma \left\{1 - \exp\left(-\frac{1}{2}T_A(b_\gamma)\sigma_{dip-p}(\rho,W)\right)\right\}\ . \tag{3.2.13}$$

This simple formula allows for an easy and convenient way to include rather complex multiple scattering of the quark-antiquark dipole in the nucleus. Several parametrizations of the dipole-nucleon cross section have been proposed

in the literature. Most of them were obtained through fitting HERA deep-inelastic scattering data which, in principle, does not allow for unique extraction of its functional form. The saturation inspired parametrizations are the most popular and topical at present.

Returning to Eq. (3.2.11), the integral strongly depends on the running ρ^0 meson mass and not on the resonance position. In section 3.1 the idea of the smearing of ρ^0 mass was discussed. As was already mentioned in our calculations we use the ALICE parametrization [142, 143] which is the most appropriate for the LHC data. Firstly, the ALICE Collaboration showed data for the largest range of invariant mass. Secondly, their data for single ρ^0 production are for the same energy for which we wish to make predictions for the $\rho^0\rho^0$ double scattering production.

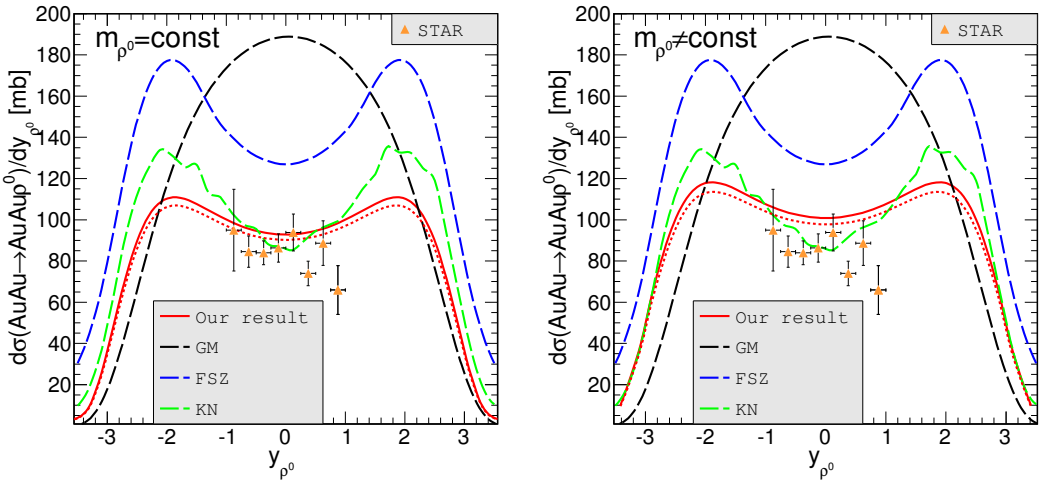

Figure 3.3: Rapidity distribution of ρ^0 meson with fixed mass (left panel) and with smeared mass of ρ^0 meson (right panel) for gold-gold collision at RHIC energy ($\sqrt{s_{NN}} = 200$ GeV) together with the STAR Collaboration data.

Figs. 3.3 show the comparison of cross section for coherent ρ^0 production measured by the STAR Collaboration [138] for different theoretical models. The left panel depicts the situation when our results are calculated for fixed ρ^0 mass (Ref. [109]) and the right panel includes the smearing of ρ^0 mass (convolution of Eq. (3.1.5) with (3.2.8)). One can observe that the calculation with fixed mass better describes the experimental points but we think it has no deep meaning. Furthermore I take into account two forms of B_{ρ^0}: the red solid line is calculated

for the case when the slope parameter appearing in the differential cross section for the $\gamma p \to \rho^0 p$ reaction (see Eq. (E.0.1)) is constant (like in Ref. [152]). The red dotted line corresponds to the slope parameters described by Eq. (E.0.13) which depend on the energy $W_{\gamma p}$ (see Eq. (E.0.2)). Other of the theoretical models were proposed by

- V.P. Gonçalves and M.V.T. Machado (Ref. [153]). GM model uses the description of the QCD color dipole picture with particular emphasis on the saturation model.

- L. Frankfurt, M. Strikman and M. Zhalov (Ref. [154, 155]). FSZ model is based on generalized vector dominance model and the Gribov (Ref. [156]) & Glauber (Ref. [157]) approach. The authors emphasize that the space-time evolution of high energy processes is different in quantum mechanical models and in quantum field theory.

- S. Klein and J. Nystrand (KN, Ref. [152]). In the KN approach the nuclear cross section is a convolution of the γp cross section with the photon spectrum in a classical model of multiple scattering to find the exclusive rates. The Klein and Nystrand calculations [152] are based on the STARLIGHT code [158] which is a C++ object-oriented Monte Carlo event generator for ultraperipheral collisions.

Fig. 3.4 shows our predictions in comparison to the ALICE experimental point [143]. In this case lead-lead collisions were studied at the center of mass energy equal to $\sqrt{s_{NN}} = 2.76$ TeV. The left panel represents the case when meson mass is fixed and the right panel corresponds to the situation when smearing of the ρ^0 mass described by the parametrization proposed by the ALICE Collaboration is included. In both situations our results are smaller than the experimental data point. Again one can see the distribution for different approaches to the slope parameter for the $\gamma p \to \rho^0 p$ reaction (solid line - $B_{\rho^0} = \text{const}$ (see Eq. (E.0.1)), dotted line is for the case when $B^{I\!P}_{\rho^0}(W_{\gamma p}) \oplus B^{I\!R}_{\rho^0}(W_{\gamma p})$ (like in Eq. (E.0.13))). It is worth to note that the $d\sigma/dy_{\rho^0}$ data point comes from the same analysis as the parametrization for the line shape of the ρ^0 meson mass.

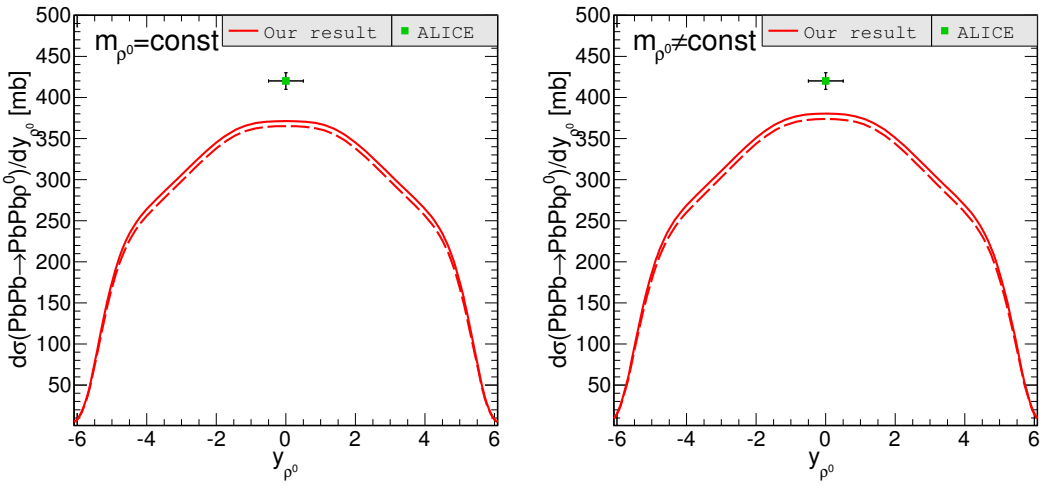

Figure 3.4: Rapidity distribution of ρ^0 meson photoproduction with fixed sharp ρ^0 mass (left panel) and with the smearing the mass of the ρ^0 meson (right panel) for lead-lead collision at the LHC energy ($\sqrt{s_{NN}} = 2.76$ TeV). The theoretical results are compared with the ALICE data point.

Table 3.2 presents the total nuclear cross section for ρ^0 photoproduction in UPCs at RHIC ($\sqrt{s_{NN}} = 130$ and 200 GeV) and LHC ($\sqrt{s_{NN}} = 2.76$ TeV) energies. Now I wish to accomplish a comparison of theoretical integrated cross section with experimental data. The numbers in the table were obtained with the same models as in Fig. 3.3. One can see the total coherent cross section for the full range of rapidity and with the cuts on y_{ρ^0}. This limitation is caused by experimental acceptance. The difference between results when the slope parameter B_{ρ^0} is constant or it depends on Pomeron and Reggeon characteristics (this was discussed in the context of Fig. 3.3) is only about 3%. The table contains a comparison of our results without ($m_{\rho^0} = \text{const}$) and with ($m_{\rho^0} \neq \text{const}$) smearing of the ρ^0 meson mass. The differences between these numbers are not negligible. At higher center of mass energy ($\sqrt{s_{NN}} = 200$ GeV) results obtained with both model exceeds the STAR cross section. The KN result and our number are much larger than the value extrapolated by experimentalists. For $\sqrt{s_{NN}} = 200$ GeV we obtain results similar as in Ref. [152]. But this is no surprising because our model is almost the same as the model proposed by Klein & Nystrand. The comparison of our numbers with the ALICE experimental

data shows that the relative difference ($= \frac{\text{theory}-\text{experiment}}{\text{experiment}} \cdot 100\%$) equals about -23% (for full range of ρ^0 rapidity) or -12% (for $|y_{\rho^0}| < 0.5$).

Table 3.2: Total (integrated over phase space) cross section in mb for the coherent photoproduction of ρ^0 meson in ultrarelativistic heavy ion collisions at RHIC and LHC energy.

GM [153]	FSZ [154]	KN [152]	Our result				Experimental data
			$B_{\rho^0} = \text{const}$		$B^{\mathbb{P}}_{\rho^0}(W_{\gamma p}) \oplus B^{\mathbb{R}}_{\rho^0}(W_{\gamma p})$		
			$m_{\rho^0} = \text{const}$	$m_{\rho^0} \neq \text{const}$	$m_{\rho^0} = \text{const}$	$m_{\rho^0} \neq \text{const}$	
$\sqrt{s_{NN}} = 130$ GeV; full $\lvert y_{\rho^0}\rvert$							STAR [138]
	490		359	407	346	392	$370 \pm 170 \pm 80$
$\sqrt{s_{NN}} = 130$ GeV; $\lvert y_{\rho^0}\rvert < 1$							STAR [138]
	140		130	143	126	139	$106 \pm 5 \pm 14$
$\sqrt{s_{NN}} = 200$ GeV; full $\lvert y_{\rho^0}\rvert$							STAR [138]
876	934	590	590	646	570	623	$391 \pm 18 \pm 55$
$\sqrt{s_{NN}} = 2.76$ TeV; full $\lvert y_{\rho^0}\rvert$							ALICE [143]
			3309	3405	3229		$4300 \pm 100^{+600}_{-500}$
$\sqrt{s_{NN}} = 2.76$ TeV; $\lvert y_{\rho^0}\rvert < 0.5$							ALICE [143]
			371	380	365	373	$420 \pm 10^{+39}_{-55}$

Finally, our result relatively well describes the STAR and ALICE experimental data. This fact is necessary for further calculations, i.e. for double-scattering mechanism which is discussed in the next section. We need a correct model for single ρ^0 meson production, because we will use this to calculate the cross sections for double-scattering mechanism. So far nobody, except of us, has presented a model or/and theoretical predictions for the AA$\to$AA$\pi^+\pi^-\pi^+\pi^-$ reaction.

3.3 Double-scattering mechanism

Large cross sections for single ρ^0 production were found in Ref. [152, 153, 155, 159]. This fact suggests that the cross section for double scattering process could be also rather large. The best example of a similar type of reaction is the production

of $c\bar{c}c\bar{c}$ final state in proton-proton collisions which was measured recently by the LHCb Collaboration [160] and which was predicted and explained as a double-parton scattering effect in Ref. [161]. The calculations show that the cross section for the $c\bar{c}c\bar{c}$ final state has the same order of magnitude as the cross section for single $c\bar{c}$ pair production. The situation for exclusive ρ^0 production is somewhat similar but the details will be discuss below. Due to easier control of absorption effect, the impact parameter formulation seems the best approach.

This section focuses on double ρ^0 production in ultraperipheral ultrarelativistic heavy ion collisions. In order to impose experimental cuts of existing experiments one should take into account explicitly the $\rho^0 \to \pi^+\pi^-$ decay. This is necessary step because so far the STAR and ALICE groups have got some distributions of kinematic variables for the AA$\to$AA$\pi^+\pi^-\pi^+\pi^-$ reaction, and not for the AA$\to$AA$\rho^0\rho^0$ reaction.

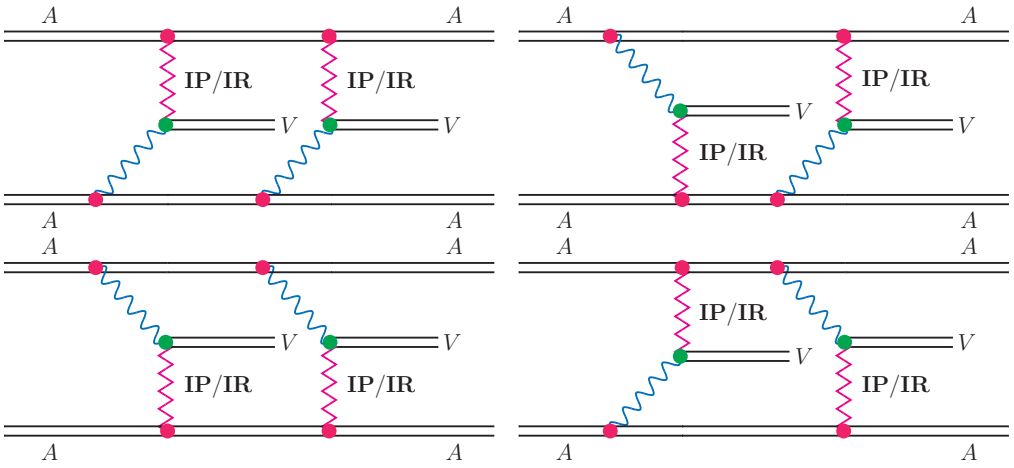

Figure 3.5: Schematic diagrams for the double-scattering mechanism of two vector meson production.

Fig. 3.5 shows the Feynman diagrams for the double-scattering mechanisms of two-vector-meson production in ultraperipheral ultrarelativistic heavy ion collisions. This mechanism is described with the help of single ρ^0 meson production mechanism. For example a two-dimensional distribution in rapidities of both ρ^0 mesons

is expressed through the equation

$$\frac{\mathrm{d}\sigma_{A_1A_2\to A_1A_2\rho^0\rho^0}}{\mathrm{d}y_1\mathrm{d}y_2} = \frac{1}{2}\int\left(\frac{\mathrm{d}P_{\gamma\mathbb{P}}\,(b,y_1)}{\mathrm{d}y_1} + \frac{\mathrm{d}P_{\mathbb{P}\gamma}\,(b,y_1)}{\mathrm{d}y_1}\right) \times \left(\frac{\mathrm{d}P_{\gamma\mathbb{P}}\,(b,y_2)}{\mathrm{d}y_2} + \frac{\mathrm{d}P_{\mathbb{P}\gamma}\,(b,y_2)}{\mathrm{d}y_2}\right)\mathrm{d}^2b\,. \tag{3.3.14}$$

The factor $\frac{1}{2}$ appears due to identity of mesons in the outgoing channel. Additionally, the smearing of ρ^0 meson mass is included as given by Eq. (3.1.6). In the following we consider a smearing of masses of both ρ^0 mesons as we intend to make distributions related to pions (in rapidity, transverse momentum and four-pion invariant mass). Having fixed the details of single vector meson production one can now proceed to the production of two vector mesons.

In the case of double ρ^0 production there are two mechanisms possible that we want to consider. The first one is the $\gamma\gamma$ fusion (section 2.2) where the elementary cross section is divided into two parts: low-energy component ($W_{\gamma\gamma} = (1-2)$ GeV) (Eq. (2.2.3)) and the VDM-Regge parametrization ($W_{\gamma\gamma} > 2$ GeV) (Eq. (2.2.4)). The second one is the double-scattering mechanism.

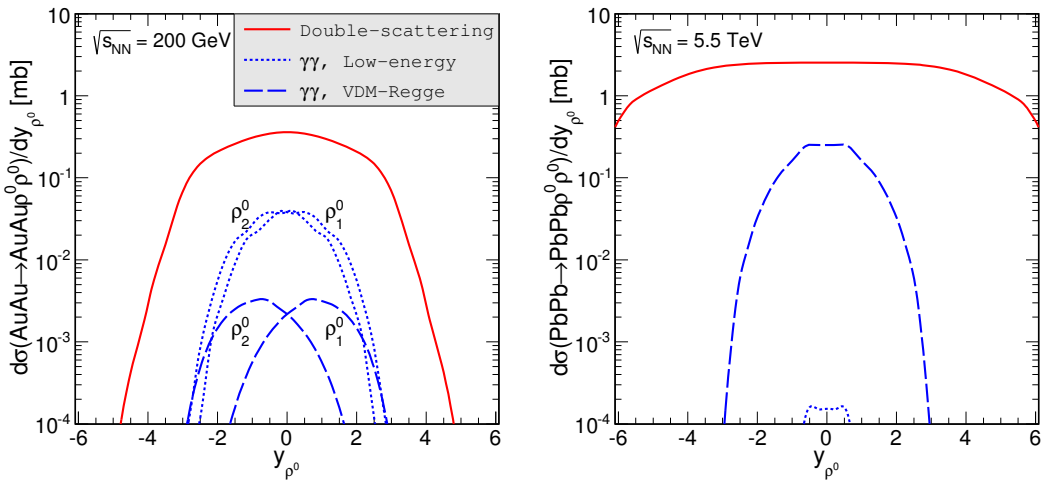

Figure 3.6: Rapidity distribution of one of the ρ^0 mesons produced in the double-scattering mechanism and in the $\gamma\gamma$ fusion.

The main results are shown in Fig. 3.6. The double-scattering contribution is shown by the red solid line, the blue dotted lines and the blue dashed lines represent distributions of forward and backward ρ^0 corresponding to the low-energy bump

and for high-energy VDM-Regge $\gamma\gamma$ fusion, respectively. One can observe a clear dominance of the double scattering component over the photon-photon component. This calculations are done for RHIC (left panel) and LHC energy (right panel). The distribution for center of mass energy $\sqrt{s_{NN}} = 5.5$ TeV is much broader than that for $\sqrt{s_{NN}} = 200$ GeV. At the LHC energy the higher values of two-meson invariant mass becomes more important which corresponds to larger values of particle rapidity. Thus the high-energy component of the elementary cross section starts to dominate at the LHC energy. Somewhat surprisingly at this energy, the VDM-Regge component is about three orders of magnitude larger than the low-energy (bump) component which is opposite to the case of RHIC energy. The left panel shows separate contributions for the forward and backward ρ^0 mesons. Both at the RHIC and LHC energy, the contributions coming from the $\gamma\gamma$ fusion is one order of magnitude smaller than that from the double-scattering mechanism.

Fig. 3.7 shows the contributions of individual diagrams from Fig. 3.5 to the $(y_{\rho_1^0}, y_{\rho_2^0})$ two-dimensional distribution. The distributions for different combinations are identical in shape but located in different corners in the $(y_{\rho_1^0}, y_{\rho_2^0})$ space. Obviously the total cross section for every case (diagram) is the same.

The left panel of Fig. 3.8 presents a full (including four diagrams of Fig. 3.5) two-dimensional distribution in rapidity of each of the mesons. This is approximately a sum of the individual contributions (Fig. 3.7). The distribution is rather flat in the entire $(y_{\rho_1^0}, y_{\rho_2^0})$ space. This is in contrast to the two-photon processes (right panel), where the cross section is concentrated almost along the $y_{\rho_1^0} = y_{\rho_2^0}$ diagonal. In principle, this clear difference can be used to distinguish the double photoproduction from the $\gamma\gamma$ fusion contributions. The asymmetry with respect to $y_{\rho_1^0} = y_{\rho_2^0}$ line for the photon-photon mechanism is due to our convention where $y_{\rho_1^0}$ denotes rapidity of the first meson which is emitted in forward direction and $y_{\rho_2^0}$ is rapidity of the second vector meson which is emitted in backward direction. This can be done only in model calculation.

In real experiment, charged pions are measured rather than ρ^0 mesons. Therefore, presentation of some observables related to charged pions might be useful.

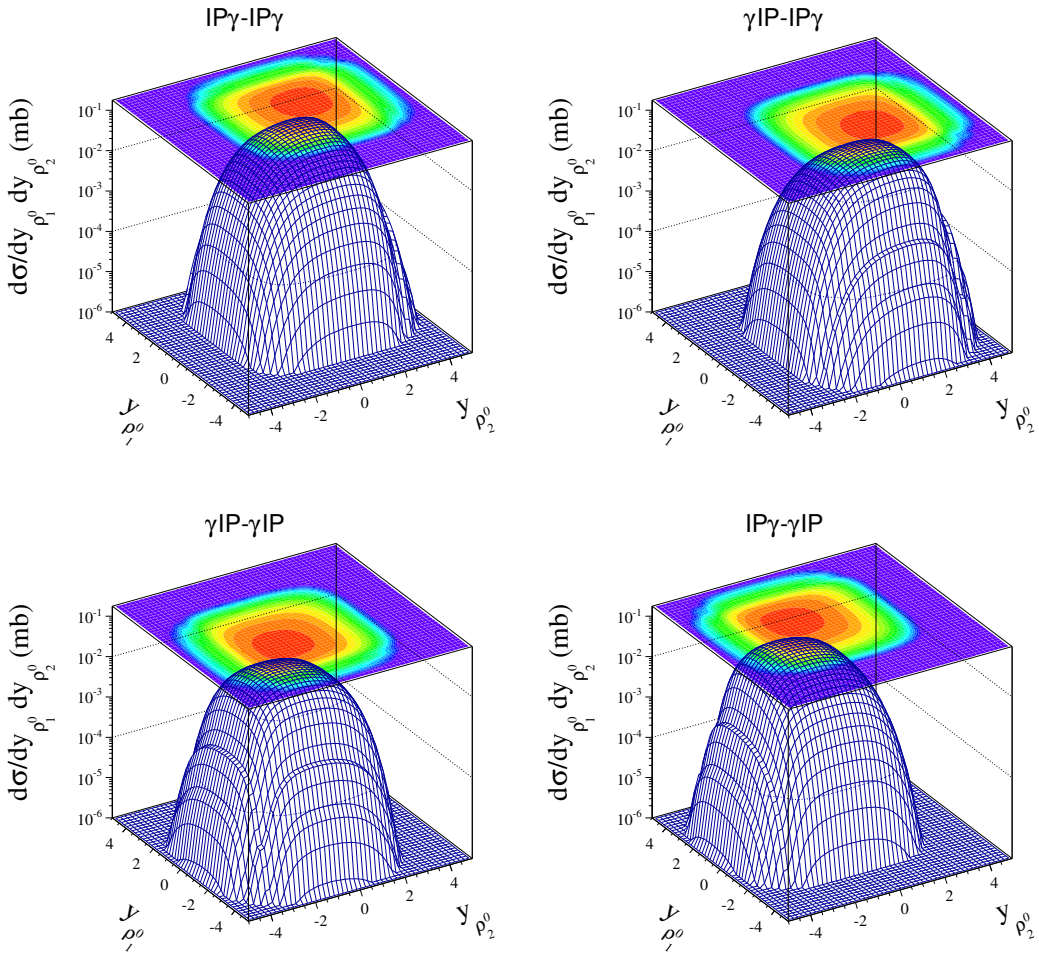

Figure 3.7: Contributions of individual diagrams of Fig. 3.5 to two-dimensional distribution in rapidities of both ρ^0 mesons for double scattering production at $\sqrt{s_{NN}} = 200$ GeV.

Fig. 3.9 depicts kinematic distributions for pions which comes from ρ^0 meson decay at the RHIC energy. The left panel shows the differential cross section as a function of pion transverse momenta (left panel). Of course transverse momentum distributions of each of the pions are the same. Again the red solid line denotes the double-scattering photoproduction mechanism, blue dotted line - the low-energy component for the $\gamma\gamma$ fusion and the blue dashed line corresponds to the VDM-Regge component. The peak (the maximum of the cross section) for all mechanisms appears at $\sim m_{\rho^0}/2$. Here we have taken into account the smearing of ρ^0 meson masses. The sharp upper limit is an artifact of our maximal value of ρ^0 meson mass

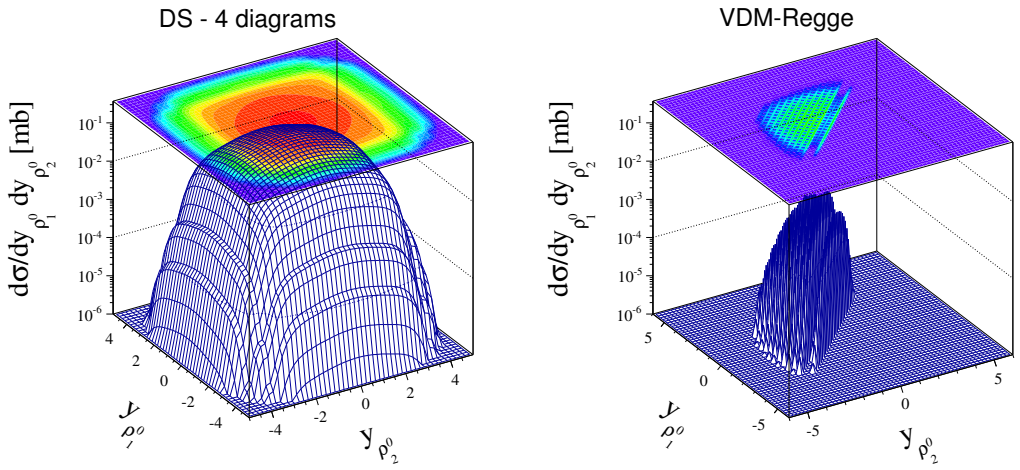

Figure 3.8: Two-dimensional distribution $(y_{\rho_1^0}, y_{\rho_2^0})$ in the ρ^0 meson rapidities for double scattering (left panel) and VDM-Regge photon-photon (right panel) production at $\sqrt{s_{NN}} = 200$ GeV.

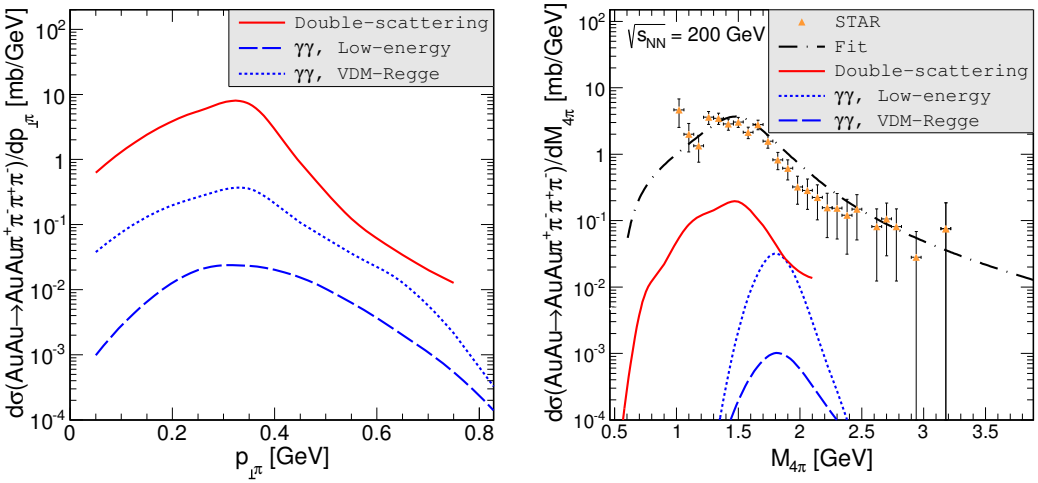

Figure 3.9: Transverse momentum distribution (left panel) and four-pion invariant mass distribution for the limited acceptance of the experiment (right panel) at $\sqrt{s_{NN}} = 200$ GeV.

$m_\rho^{max} = 1.5$ GeV taken in our calculations. However, we have imposed this upper limit because the spectral shape of "ρ^0 meson" above $m_\rho > 1.5$ GeV is not under good theoretical control. In principle, at larger $p_{\perp\pi}$, the contribution coming from the decay of a ρ^0 meson produced in the $\gamma\gamma$ fusion can be larger than that of double scattering mechanism, as the transverse momentum of ρ^0 mesons are not strictly

limited to small values. However, the cross section for such cases is expected to be rather small. The right panel of Fig. 3.9 shows four-pion invariant mass distribution for double-scattering, low-energy bump and high-energy VDM-Regge $\gamma\gamma$ fusion mechanism for the limited acceptance of the STAR experiment ($|\eta_\pi| < 1$) [162]. The double-scattering contribution accounts only for 20% of the cross section measured by the STAR Collaboration. The dash-dotted line represents a fit of the STAR Collaboration. The STAR experimental data [162] have been corrected by experimental acceptance function [162, 163]. Probably the production of the $\rho^0(1700)$ resonance and its subsequent decay into the four-pion final state (see e.g. [109]) is the dominant effect for the limited STAR acceptance. Both, the production mechanism of $\rho^0(1700)$ and its decay into four charged pions are not yet understood. In addition, there is another broad $\rho^0(1450)$ resonance [164], which also decays into four charged pions. A model production of the resonances and their decay is has to be work out in the future.

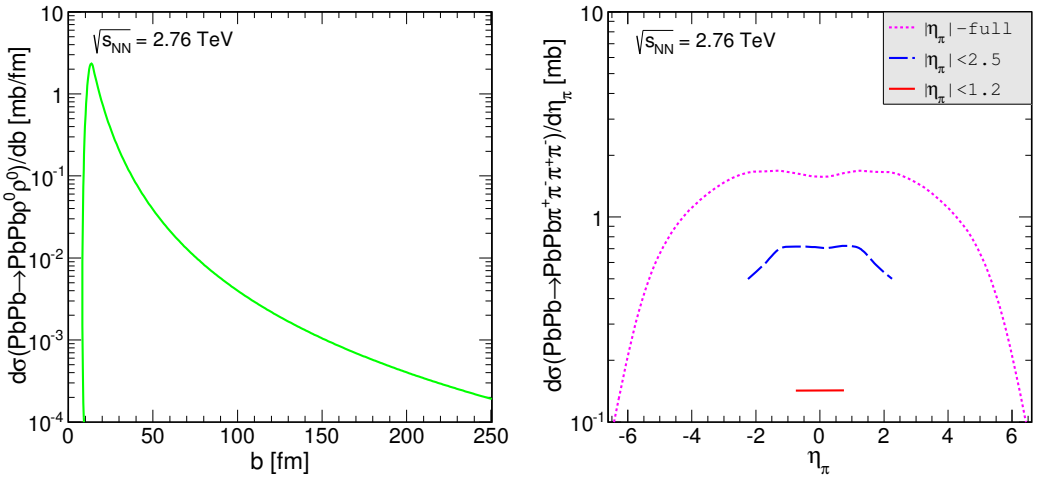

Figure 3.10: Impact parameter dependence of the cross section (left panel) and pion pseudorapidity distribution for limited range of pion pseudorapidity (right panel) at $\sqrt{s_{NN}} = 2.76$ TeV.

Fig. 3.10 shows the distribution in impact parameter b (left panel) for PbPb$\to$ PbPb$\rho^0\rho^0$ process. One can observe a peak at $b = 14$ fm which corresponds to minimum value of impact parameter corresponding to ultraperipheral heavy ion collision. The probability of the exclusive production of ρ^0 pairs very fast decreases

with increasing b. The right panel of Fig. 3.10 presents the differential cross section in mb as a function of charged pion pseudorapidity for three different limits on η_π (full range of $|\eta_\pi|$ - pink dotted line, $|\eta_\pi| < 2.5$ - blue dashed line and $|\eta_\pi| < 1.2$ - red solid line). We wish to emphasize that the STAR Collaboration at RHIC observes only a small fraction of pions (both for double-scattering and $\gamma\gamma$ fusion mechanisms) due to the rather limited angular (pseudorapidity) coverage $\eta_\pi \sim 0$. The ALICE Collaboration at the LHC can measure somewhat larger range of $|\eta_\pi| < 1.2$ [165].

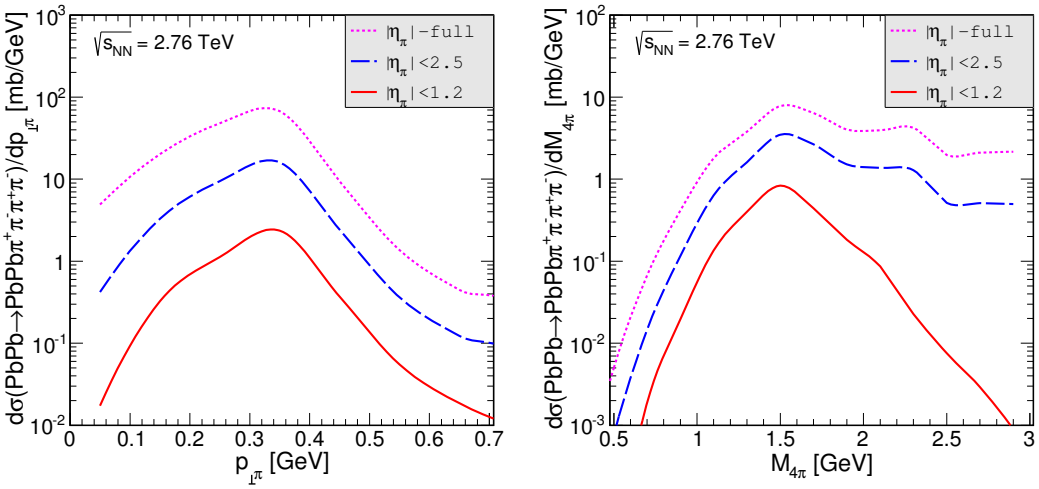

Figure 3.11: Pion transverse momentum distribution (left panel) and four-pion invariant mass distribution (right panel) for limited range of pion pseudorapidity at $\sqrt{s_{NN}} = 2.76$ TeV.

The last figures in this sections show the pion transverse momentum distribution (left panel) and four-pion invariant mass distribution (right panel) for limited range of pion pseudorapidity at the LHC energy. This is calculated with the smearing of ρ^0 masses using parametrization of the ALICE Collaboration [142, 143]. The distribution in $p_{\perp\pi}$ falls almost symmetrically around $p_{\perp\pi} \sim m_\rho/2$ independent of the limit on pseudorapidity. Both the STAR and ALICE experiments have a fairly good coverage in pion transverse momenta and could measure such distributions. Very useful seems to be the differential cross section as a function of four-pion invariant mass. The ALICE group collected the data for four-charged-pion production with the limitation $|\eta_\pi| < 1.2$. One can see that with larger cut on pseudorapidity, the tails

in $d\sigma/dM_{4\pi}$ fall quicker with growing $M_{\pi\pi}$. We cannot compare this distribution with the ALICE data [166], because those data are not absolutely normalized.

Chapter 4

Nuclear cross section for the exclusive production of particle pairs

Exclusive production of the Standard Model elementary particles or mesons in ultrarelativistic heavy ion collisions is an interesting field of theoretical investigation and a very good opportunity to study $\gamma\gamma$ processes (Refs. [23–26, 167]). On the experimental side the situation is slightly different. One can find only a small number of publications with results.

In this chapter I will present some predictions dedicated to the STAR experiment at Relativistic Heavy Ion Collider (^{197}Au+^{197}Au collisions at $\sqrt{s_{NN}} = 130$ or 200 GeV) and to the ALICE experiment at Large Hadron Collider (^{208}Pb+^{208}Pb collisions at $\sqrt{s_{NN}} = 2.76$, 3.5, 5.5 TeV).

In order to calculate the nuclear cross sections for different reactions we use the elementary cross sections which have been presented and described in Chapter 2.

4.1 Dimuon production

First I will focus on the nuclear cross section for muon-pair production. Fig. 4.1 shows the differential distribution as a function of the impact parameter. One can see

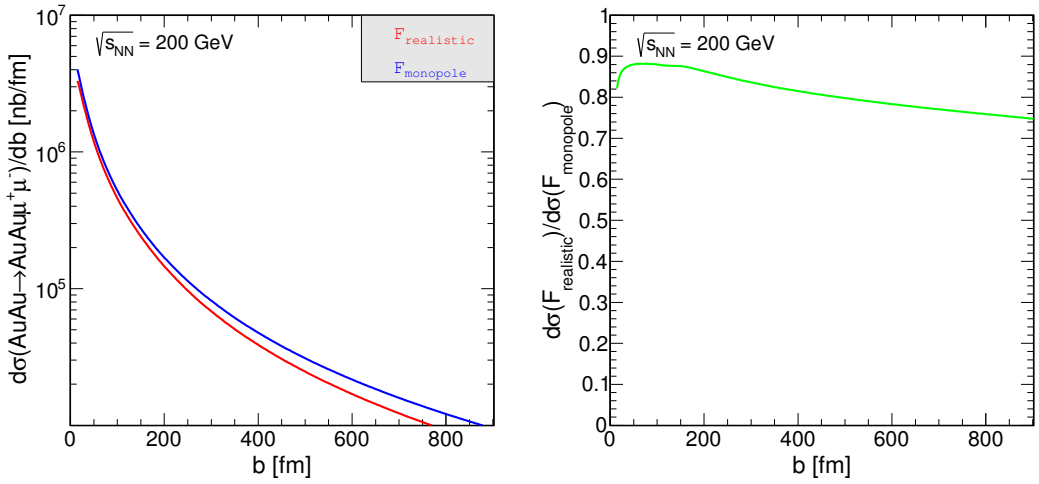

Figure 4.1: Impact parameter dependence of the cross section for AuAu→AuAu$\mu^+\mu^-$ reaction at RHIC energy (left panel) and the ratio of nuclear cross section for the realistic charge distribution to that for the monopole form factor (right panel).

the result for the exclusive muon-pair production for typical RHIC energy. The distribution with realistic charge density falls off somewhat quicker than that for the monopole form factor. This is better visualized in the right panel where the ratio of corresponding cross sections is shown: $\mathrm{d}\sigma\left(\mathrm{AuAu} \to \mathrm{AuAu}\mu^+\mu^-; F_{\mathrm{realistic}}\right) / \mathrm{d}\sigma\left(\mathrm{AuAu} \to \mathrm{AuAu}\mu^+\mu^-; F_{\mathrm{monopole}}\right)$. The both results agree within 88% at small b and with larger values of b the difference becomes larger.

In Fig. 4.2 I present the differential cross section for gold-gold scattering as a function of the $\gamma\gamma$ center of mass energy $W_{\gamma\gamma} = M_{\mu^+\mu^-}$ (left panel) and as a function of dimuon pair rapidity (right panel). The calculations are performed for the RHIC energy. Again one can see significant difference between cross sections for "realistic" and monopole form factor. The distribution in invariant mass of the $\mu^+\mu^-$ pair falls steeply off. We show the x-axis only up to 10 GeV to allow a comparison of the left panel of Fig. 4.2 with the $\gamma\gamma \to \mu^+\mu^-$ cross section shown in Fig. 2.1. The elementary cross section changes by about two orders of magnitude in the range of $W_{\gamma\gamma}$ $(= M_{\mu^+\mu^-})$ between 0 and 10 GeV. The nuclear cross section falls off about eight orders of magnitude in the same range of energy. This is caused by ω_1 or/and ω_2 dependence of the equivalent photon fluxes in formula (1.2.36).

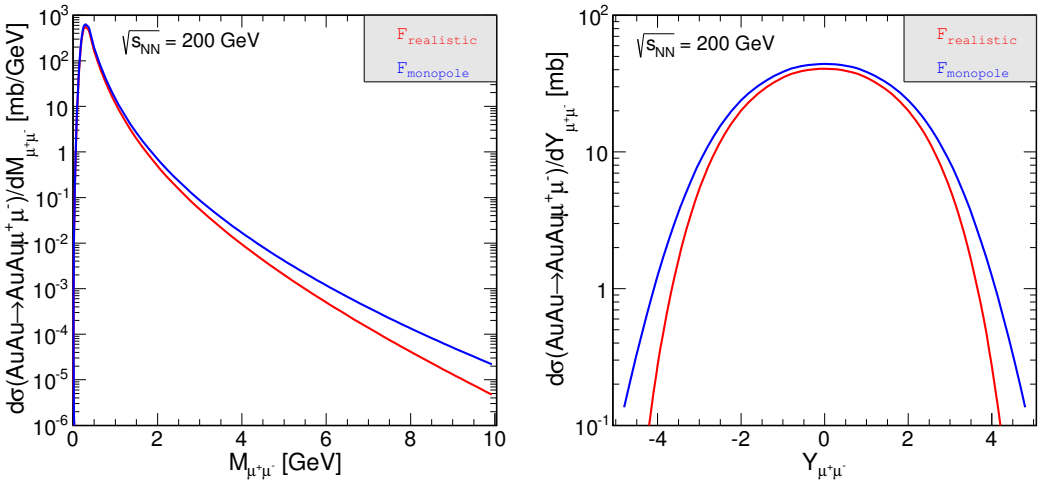

Figure 4.2: Invariant mass (left panel) and rapidity of $\mu^+\mu^-$ pair (right panel) distribution in AuAu→AuAu$\mu^+\mu^-$ process for $\sqrt{s_{NN}} = 200$ GeV.

We remind that $\omega_{1/2} = W_{\gamma\gamma}e^{\pm Y}$. The right panel of Fig. 4.2 shows the distribution in $Y_{\mu^+\mu^-} = \frac{1}{2}(y_{\mu^+} + y_{\mu^-})$. One can observe a huge difference between results for realistic and monopole form factors for large dilepton rapidities.

The distribution presented in Fig. 4.1 is purely theoretical as it cannot be easily measured. The distributions which could, at least in principle, be measured are presented in Fig. 4.2. However, every experiment is limited by some acceptance of its experimental apparatus. We have to include the experimental cuts on rapidity of outgoing particles or transferred momentum. This can be done relatively easy within the exact momentum space Quantum Electrodynamics framework. Some details of this approach are presented in Appendix F. By exact method we mean the correct inclusion of the $2 \to 4$ process with exact treatment of the phase-space. It is, however, rather difficult to include absorption effects in this approach.

Continuing the consideration of differential distributions for dimuon production in ultrarelativistic heavy-ion collisions, we will show predictions for some experiments. We will include also experimental limitations of the experiments. An interesting example are the predictions for the PHENIX experiment ($\sqrt{s_{NN}} = 200$ GeV). The PHENIX detector records many different particles emerging from the RHIC collisions, including photons, electrons, muons, and some charged hadrons. The PHENIX Collaboration can measure both forward ($\eta_\mu > 0$) and backward ($\eta_\mu < 0$)

muons with pseudorapidity coverage $1.2 < |\eta_\mu| < 2.4$ [168] and uses a relatively low cut on muon transverse momentum $p_{\perp\mu} > 2$ GeV. Due to the rather limited range of pseudorapidity coverage, we have given names to the four possible regions (squares) in Fig. 4.3.

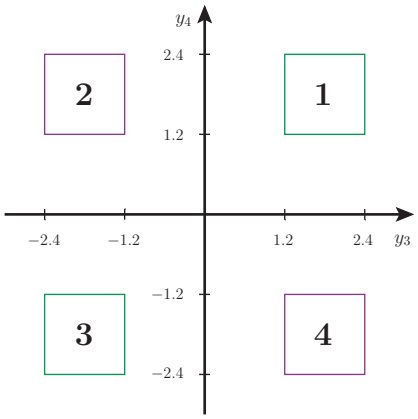

Figure 4.3: The μ^+ and μ^- rapidity regions available with the PHENIX detector.

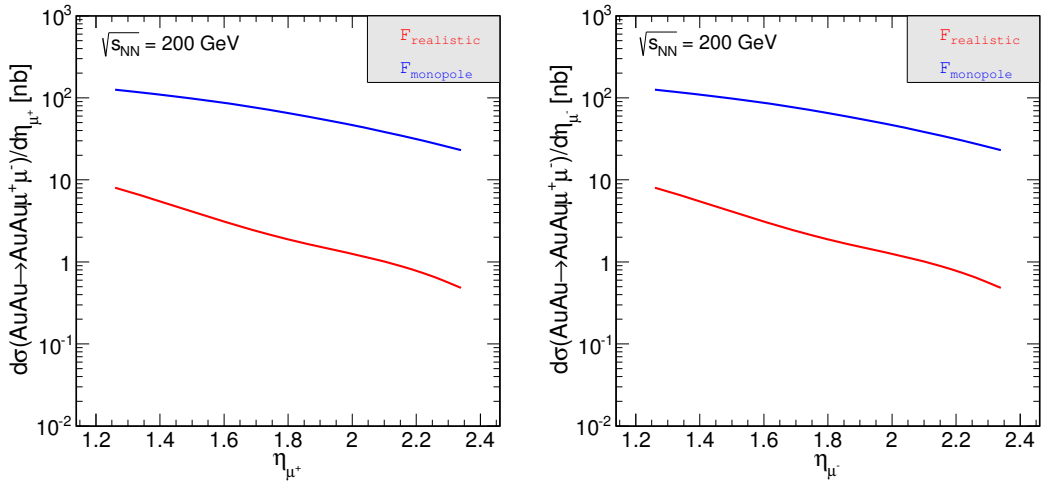

Figure 4.4: Differential cross section as a function of pseudorapidity of the first (left panel) and second (right panel) muon for square 1.

In spite of these limitations, interesting measurements can be done. As an example, in Fig. 4.4 and 4.5 one can see the results for the first and second square. Here the distributions such as the muon pseudorapidity function are shown. The left panels are for μ^+ and the right panels are for μ^-. The predictions for two other

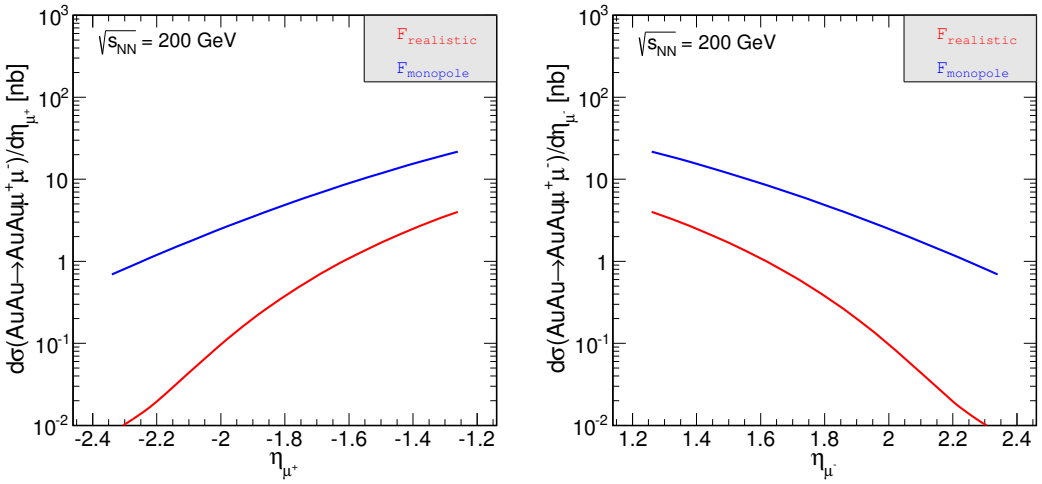

Figure 4.5: Differential cross section as a function of pseudorapidity of the first (left panel) and second (right panel) muon for square 2.

squares are the mirror images of the presented results ($1 \to 3$ and $2 \to 4$). The comparison of the red lines (form factor with realistic charge distribution) with the blue lines (monopole form factor) shows that the inclusion of "realistic" form factor is here very important. The difference between the results is larger than one order of magnitude. This can be caused by a cut on transverse momentum of each muon ($p_{\perp\mu} > 2$ GeV).

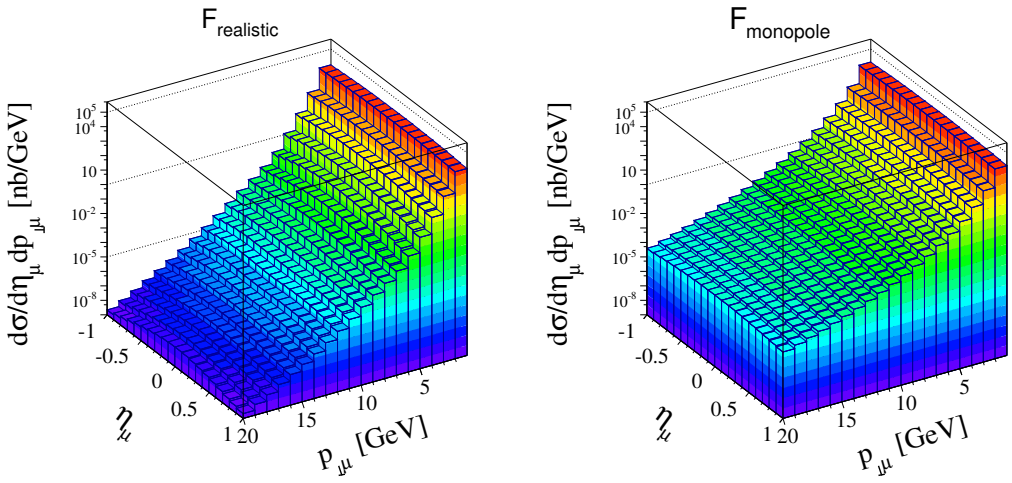

Figure 4.6: Two-dimensional distributions in pseudorapidity and transverse momentum of muon for the STAR experimental conditions for the realistic charge distribution (left panel) and for the monopole form factor (right panel).

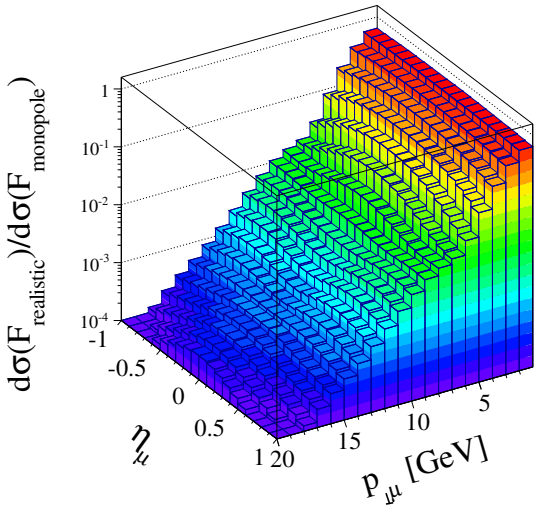

Figure 4.7: The ratio of the cross sections for the realistic charge distribution and for the monopole form factor in pseudorapidity and transverse momentum of muons for the STAR conditions.

Now I will present results for the STAR experiment at RHIC. There muons can be measured in the midrapidity region $|\eta| < 1$ and with limitation on $p_{\perp\mu} \geqslant 1$ GeV [169]. The two-dimensional distributions in muon pseudorapidity and muon transverse momentum are shown in Fig. 4.6 for realistic (left panel) and monopole (right panel) form factors. Their ratio is presented in Fig. 4.7. Big differences with respect to the monopole case can be seen for large $p_{\perp\mu}$. We can conclude that with larger cut on transverse momenta, we obtain a bigger difference between results with "realistic" and "monopole" form factors. So if we want to do more precise predictions for concrete experimental situation, we should include the more realistic approach which takes into account the realistic charge distribution in nucleus.

In our paper on exclusive muon-pair production (Ref. [3]), many more distributions are discussed and shown. There we present e.g. predictions for the ALICE and CMS detectors at the LHC. For every case one can observe that the cross sections obtained with realistic form factors are significantly smaller than those obtained with the monopole form factors. The effect is bigger for large muon (pseudo)rapidities and/or large muon transverse momenta.

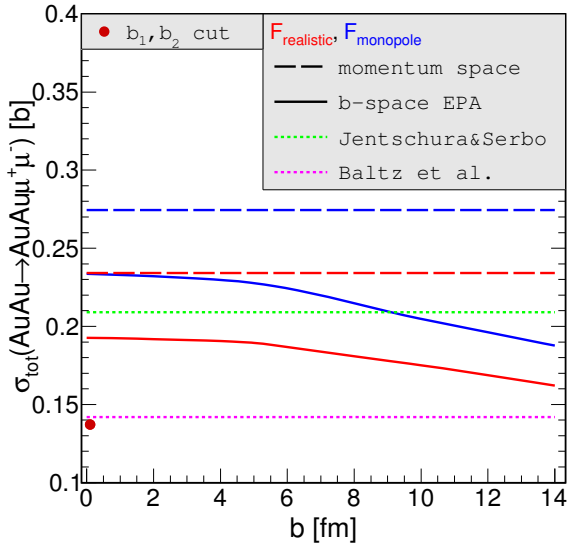

Figure 4.8: Total nuclear cross section for the AuAu→AuAu$\mu^+\mu^-$ reaction at $\sqrt{s_{NN}} = 200$ GeV as a function of the lower limit on impact parameter.

To close our presentation of results for $\mu^+\mu^-$ prediction we wish to compare results obtained in different approaches. The calculations in the literature usually concentrate on the total cross section and not on differential distributions. In Fig. 4.8 one can see the dependence of the total cross section on the lower limit of the impact parameter for different approaches. We present impact parameter space EPA results (solid curves) for realistic (red lines) and monopole (blue lines) form factors. The cross section without the cutoff on impact parameter is by about 15% larger than that for $b = 14$ fm. This result is smaller than the corresponding cross sections obtained within momentum space approach (dashed lines). The upper limit of the integration in b depends on the mass of produced particles. The muon mass is very small ($m_\mu = 106$ MeV) so the distributions in b should probably be calculated in larger range. But this implies the necessity of extension of the calculation time. Concurrently the numbers given by Jentschura and Serbo (Ref. [56]) up to $b \simeq R_A$ are between our results for the b space EPA. However, they have used monopole form factor. Similarly, Baltz et al. [170] calculated the total cross section in the EPA framework, but this number is much smaller than the other results. However, they have imposed extra cuts on b_1 and b_2 (see Fig. 1.7) instead on b as is usually done.

Comparing the numbers: $\sigma_{tot}^{\text{Baltz et al.}} = 0.142$ b and $\sigma_{tot}^{\text{our result}} = 0.137$ b (red point in Fig. 4.8), one can see that these results are very similar. The percentage difference equals to about 3.5%. It is very difficult to decide which approach is better.

The calculations for exclusive muon-pair production were restricted to lowest-order QED calculations with special attention to realistic form factors and absorption effects. Here higher-order correction were completely ignored. The importance of the QED higher-order correction was demonstrated in Refs. [56, 171]. While Jentschura and Serbo [56] suggest that the higher-order corrections are rather small, Baltz [171] obtains a huge reduction of the total nuclear cross section of the order of 20%. Predictions given in Ref. [56] are in agreement with the ALICE experimental data [172].

It would be also very interesting to calculate the higher-order corrections for differential distributions which will be measured by the LHC experiments. These calculations seems to us rather difficult technically.

4.2 $\rho^0\rho^0$ meson production

Now I will present results for the production of $\rho^0\rho^0$ pairs. No experiment showed such data. So far only the single ρ^0 meson exclusive cross section AA$\to$AAρ^0 was measured at RHIC (Ref. [138]) and recently at the LHC [143]. In this case the ρ^0 meson is produced accordingly in photoproduction (photon-Pomeron or Pomeron-photon fusion). For double-ρ^0 prediction one can find only some theoretical predictions in the literature. Usually the integrated cross section is estimated only.

In Fig. 4.9 we show distributions as a function of the impact parameter b calculated in the EPA. The left panel corresponds to the gold-gold collisions at the RHIC energy $\sqrt{s_{NN}} = 200$ GeV and the right panel presents the results for the lead-lead collisions at the LHC energy $\sqrt{s_{NN}} = 5.5$ TeV. The dash-dotted lines are for low-energy $\gamma\gamma$ fusion component ($W_{\gamma\gamma} = (1-2)$ GeV) and the dashed lines show the results for high-energy VDM-Regge component ($W_{\gamma\gamma} > 2$ GeV). By comparing the contribution of the low- and high-energy components one can

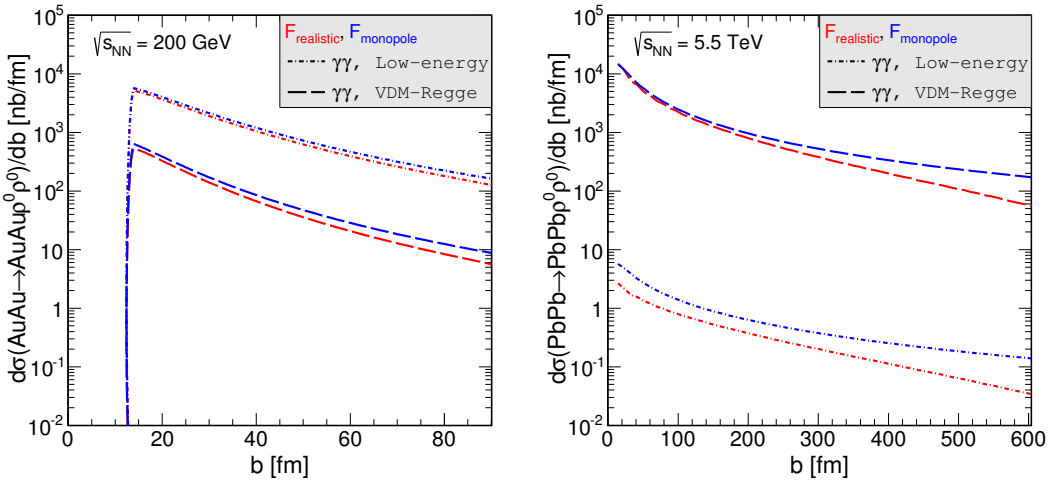

Figure 4.9: Impact parameter dependence of the cross section for AuAu→AuAu$\rho^0\rho^0$ reaction at RHIC energy (left panel) and for PbPb→PbPb$\rho^0\rho^0$ reaction at LHC energy (right panel).

observe that the low-energy bump dominates at smaller center of mass energy and the VDM-Regge component becomes important at larger values of $\sqrt{s_{NN}}$. The same conclusion can be drawn from the distribution in meson rapidity. This was presented in the previous section (3.3) when discussing results obtained in the $\gamma\gamma$ fusion and photoproduction. Next, in Fig. 4.9 I present the results calculated with realistic charge density (red lines) and monopole form factors (blue lines). One can clearly see different results for different approaches for calculating the flux factors of equivalent photons. The difference between these two approaches occurs in the whole range of impact parameter but is larger at larger values of b. Here the results with absorption effect ($b > 2R_A$) are presented. For larger values of the center of mass energy one should take a broader range of impact parameter as the corresponding distribution decreases rather slowly. For example at the LHC energy, the probability of the meson pairs production in ultraperipheral heavy-ion collisions is still huge even at $b = 140$ fm $\approx 10\times$ the nucleus diameter.

The comparison of the left panels of Figs. 4.9 and 4.1 seems very useful. The cross section for particle-pairs production at the same range of b is smaller for $\rho^0\rho^0$ production than for $\mu^+\mu^-$ production. This is caused mainly by the mass of particles. The muon is about seven times lighter than the $\rho^0(770)$ meson.

4.3 Quark-antiquark production

In Ref. [56] the authors developed a code which calculates the corresponding cross sections in the EPA in the momentum space. Thus it is possible to compare the results obtained with the help of the EPA in the impact parameter space with calculations done in the momentum space EPA including realistic charge distribution in the nucleus [4]. A comparison of the methods has sense only provided the integration over full range of b is performed in the b-space EPA. Interesting seems to be also a comparison of the EPA with the exact Quantum Electrodynamics method (Appendix F). This will be presented as an example for double-photon exclusive processes with heavy-quark-heavy-antiquark pair production.

Table 4.1: Total nuclear cross section for the direct component of the $Q\bar{Q}$ production at LHC energy ($\sqrt{s_{NN}} = 5.5$ TeV) for different cuts on the impact parameter.

Process	b-space EPA			p-space	p-space
	$b > 0$ fm	$b > 14$ fm	b_{max}	EPA	
PbPb→PbPb$c\bar{c}$	1.18 mb	1.05 mb	4000 fm	1.23 mb	1.36 mb
	1.13 mb	1.00 mb	1000 fm		
PbPb→PbPb$b\bar{b}$	2.53 μb	2.05 μb	1000 fm	2.54 μb	2.54 μb

In Table 4.1 I summarize the results for the total cross sections for the $Q\bar{Q}$ direct component calculated within the various models: EPA in the impact parameter space (second and third column), EPA in the momentum space (the next to last column) and exact momentum space (last column). The main assumptions of the momentum space EPA are described in Ref. [56]. To illustrate the absorption effect (breakup of nuclei), we show both the total cross section calculated from 0 to b_{max} and the integral cross section calculated from $R_1 + R_2 \simeq 14$ fm to b_{max}. The last row shows the total cross section for the PbPb→PbPb$b\bar{b}$ reaction. Two approaches (b-space and momentum space) give results which almost coincide. Additionally, the cross section for the momentum space approach has exactly the same value as the cross section for the others approaches. b quark has rather large mass ($m_b = 4.75$ GeV), therefore, the distribution in the impact parameter falls off very quickly

and a limit of $b_{max} = 1000$ fm seems sufficient. These numbers demonstrate that the EPA in impact parameter space ($b > 0$ fm), EPA in momentum space and the standard momentum space approach give the same results. Each of the models allows to consider the process in different kinematic variables. However, only b-space EPA has a possibility to control the peripheral character of the process. c quark is more then three times lighter than that for b quark. Thus the integration in the impact parameter b is also rather slowly convergent. Therefore we also show the upper limit dependence of the cross section for $b_{max} = 1000$ fm and for $b_{max} = 4000$ fm. The cross section grows very slowly with the upper limit of the impact parameter. The results obtained with the help of the momentum space EPA are very similar to those obtained with the help of the Feynman graph approach.

In contrast to dimuons, the $Q\bar{Q}$ state cannot be directly observed. This was briefly discussed when presenting elementary cross sections for the $\gamma\gamma \to Q\bar{Q}$ reaction (section 2.1). Finally, in practice one measures rather complicated final states. Thus one should include quite different processes: Born direct mechanism, LO QCD corrections, partonic states such $Q\bar{Q}q\bar{q}$ (4-quarks) and $Q\bar{Q}g$ (single-resolved).

Table 4.2: Total nuclear cross section for four different mechanisms of $Q\bar{Q}$ production at the LHC energy $\sqrt{s_{NN}} = 5.5$ TeV.

Component	b-space EPA		b-space EPA	
	$b > 0$ fm	$b > 14$ fm	$b > 0$ fm	$b > 14$ fm
	PbPb$\to$PbPb$c\bar{c}$		PbPb$\to$PbPb$b\bar{b}$	
Born	1.18 mb	1.05 mb	2.53 μb	2.05 μb
QCD corrections	0.41 mb	0.36 mb	1.00 μb	0.83 μb
4-quarks	0.82 mb	0.67 mb	9.40 μb	6.98 μb
Single-resolved	0.52 mb	0.39 mb	1.51 μb	0.97 μb
Total	2.93 mb	2.47 mb	14.44 μb	10.83 μb

Table 4.2 presents cross sections for the PbPb$\to$PbPb$Q\bar{Q}$ reaction at the LHC energy $\sqrt{s_{NN}} = 5.5$ TeV. Each row is assigned to another component. The last row shows the total cross section for the production of $c\bar{c}$ or $b\bar{b}$ quarks. Here we show the results for the b-space EPA without and with absorption effect. The difference

between the values of total cross section for $b_{min} = 0$ and $b_{min} = 14$ fm varies from 15% (for $c\bar{c}$ production) to 25% (for $b\bar{b}$ in the final channel). More interesting is percentage contribution of every component to the total cross section. Relative contribution of the Born mechanism to $c\bar{c}$ production equals about 43%. This large number is due to the dominance of this component near threshold as shown in Fig. 2.8. The production of $b\bar{b}$ pair is dominated by the $b\bar{b}q\bar{q}$ component (65%). The cross sections presented in the above table are larger than the estimations for the exclusive heavy-quark production in the double-Pomeron exchange (DPE) process. In Ref. [173] one can find: $\sigma^{DPE}_{PbPb\to PbPbc\bar{c}} = 4.2$ μb and $\sigma^{DPE}_{PbPb\to PbPbb\bar{b}} = 0.2$ μb. Since the QED process can be reliably calculated, it can be used as a background for much more involved diffractive processes.

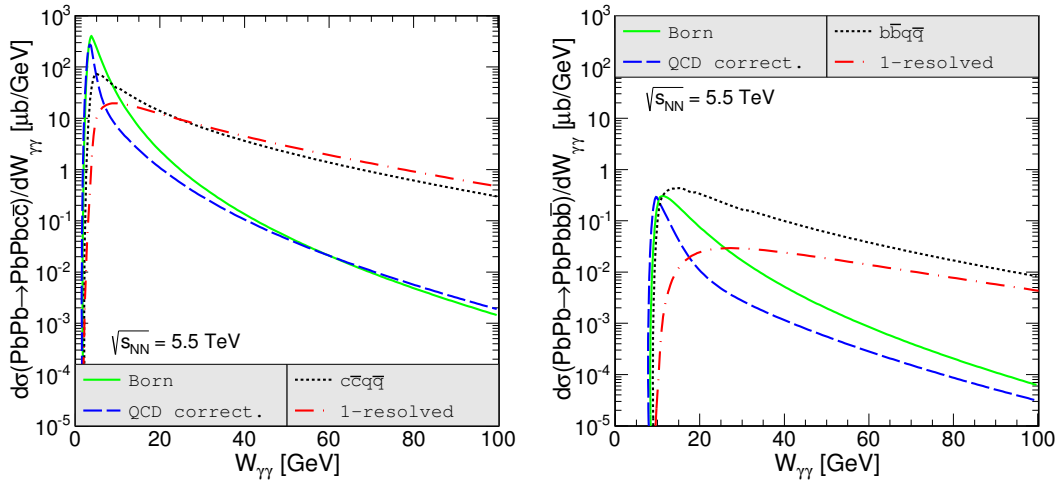

Figure 4.10: Differential nuclear cross section as a function of $\gamma\gamma$ subsystem energy for $c\bar{c}$ (left panel) and $b\bar{b}$ (right panel) production.

Fig. 4.10 depicts nuclear cross section as a function of $W_{\gamma\gamma}$ in the EPA (here $b_{min} = 0$ fm). For the Born direct production case it is identical as a distribution in quark-antiquark invariant mass ($M_{Q\bar{Q}}$). In the other cases the $\gamma\gamma$ subsystem energy is clearly different than the $Q\bar{Q}$ invariant mass. Therefore, this distribution is rather theoretical and would be difficult to measure experimentally. The presented distributions reflect the energy dependence of the elementary cross sections (see Fig. 2.8). Please note a sizeable contribution of the LO corrections close to the threshold and at large energies for the $c\bar{c}$ case. Since in this case $W_{\gamma\gamma} > M_{Q\bar{Q}}$, it becomes clear

that the $Q\bar{Q}q\bar{q}$ contributions must have much steeper dependence on the $Q\bar{Q}$ invariant mass than the direct one which means that large $Q\bar{Q}$ invariant masses are produced mostly in the direct process. In contrast, small invariant masses (close to the threshold) are populated dominantly by the four-quark contribution. Therefore, measuring the invariant mass distribution one can disentangle the different mechanisms. As far as this is clear for the $c\bar{c}$ it is less transparent and more complicated for the $b\bar{b}$ production. In the last case, the experimental decomposition may be in practice not possible.

In the present theoretical studies we have presented theoretical cross sections for quark/antiquark production. In experiments with heavy flavour production one measures rather charmed or bottom mesons or baryons. The formalism of the quark-to-meson conversion is rather well known and we could relatively easily calculate the cross section for a given type of mesons (Refs. [174, 175]). The corresponding integrated cross sections can be estimated easily by multiplying the present cross sections for quarks/antiquarks by a corresponding transition probabilities which are know for a given type of mesons [109, 176].

4.4 Two-pion production

Now I will concentrate on the dipion production in ultrarelativistic lead-lead UPCs. As in the whole dissertation the calculations for $\pi^+\pi^-$ and $\pi^0\pi^0$ pair production in $\gamma\gamma$ scattering are done for realistic charge distribution (form factor) in the colliding nuclei. The $\gamma\gamma$-induced dipion production in nuclear collision, interesting by itself, constitutes a background to another type of nucleus-nucleus reactions induced by photon-Pomeron (Pomeron-photon) exchanges [1], leading to a coherent production of ρ^0 meson [155, 177, 178] and its radial excitations. The interplay of the both processes was not discussed so far in the literature.

[1] We use the name photon-Pomeron or Pomeron-photon as an abbreviation of multiple scattering of hadron-like states in the nucleus. This can be better understood in the section about classical-mechanics Glauber model (Appendix E).

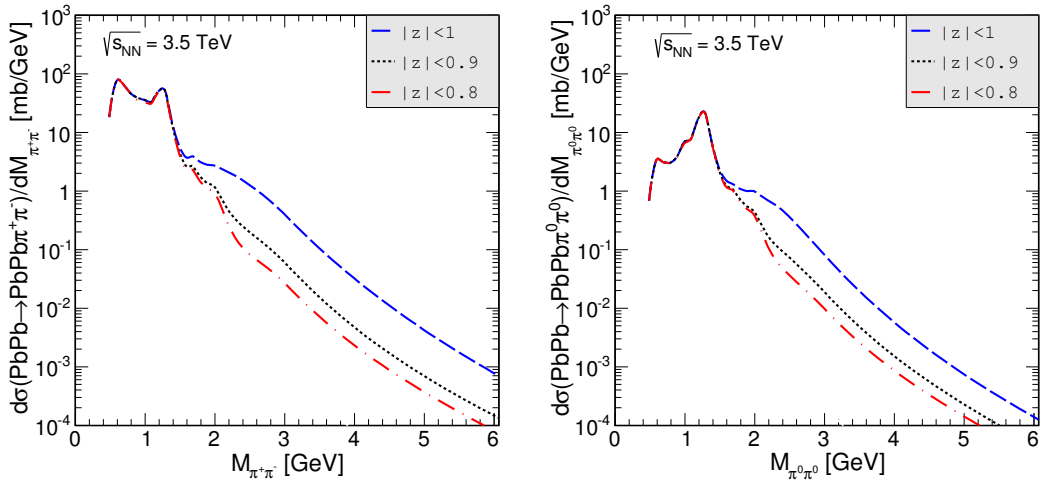

Figure 4.11: Differential nuclear cross section as a function of $\pi^+\pi^-$ (left panel) and $\pi^0\pi^0$ (right panel) invariant mass at $\sqrt{s_{NN}} = 3.5$ TeV and $p_{\perp\pi} > 0.2$ GeV.

Fig. 4.11 shows theoretical distributions for the full phase space (blue dashed lines) and for the angular range corresponding to the experimental limitations usually used for the $\pi\pi$ production in e^+e^- collisions ($|\cos\theta| < 0.8$ - red dash-dot lines) or for $|\cos\theta| < 0.9$ (black dotted lines). The results are presented for the PbPb→PbPb$\pi^+\pi^-$ (left panel) and for the PbPb→PbPb$\pi^0\pi^0$ (right panel) reactions. For both cases, the low-energy contribution ($W_{\gamma\gamma} < 1.5$ GeV) does not depend on the angular cuts. Large differences occurs in the region where the elementary cross section is described by the pQCD mechanisms (see Fig. 2.19).

Table 4.3: Total nuclear cross section for the dipion production at the LHC energy $\sqrt{s_{NN}} = 3.5$ TeV for different lower cuts on pion transverse momentum.

$p_{\perp\pi,\mathrm{min}}$	PbPb→PbPb$\pi^+\pi^-$	PbPb→PbPb$\pi^0\pi^0$
0.2	46.68	8.67
0.5	12.07	5.09
1.0	0.08	0.05

Usually every experimental set-up requires some minimal value of transverse momentum. The total cross section strongly depends on the cut in $p_\perp$. Table 4.3 shows the dependence between the value of nuclear cross section and different

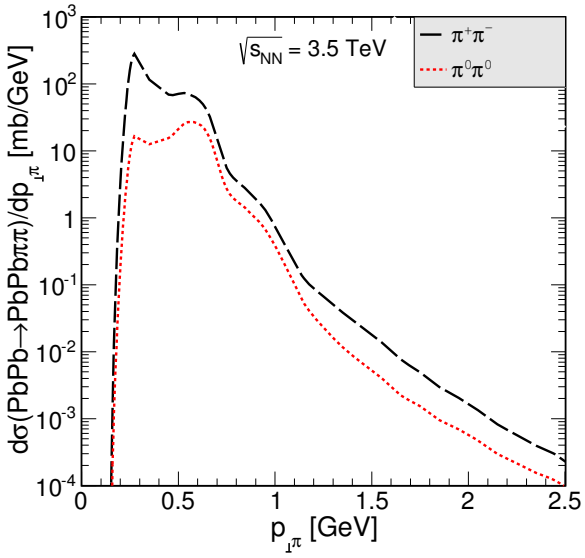

Figure 4.12: Differential nuclear cross section as a function of the transverse pion momentum at $\sqrt{s_{NN}} = 3.5$ TeV.

lower cuts on the pion transverse momentum at the LHC energy $\sqrt{s_{NN}} = 3.5$ TeV. The total cross sections are collected for both $\pi^+\pi^-$ and $\pi^0\pi^0$ channels. One can see that with larger cut on $p_{\perp\pi}$ the difference between cross section for charged and neutral pions starts to be much smaller. This can be better seen in Fig. 4.12. Here we show distribution in $p_{\perp\pi}$ for charged (black dashed line) and neutral (red dotted line) pions for PbPb→PbPb$\pi\pi$ reaction. The respective calculation was performed for the full phase space ($|\cos\theta| < 1$) and for the full range of particle (pseudo)rapidity.

The considered here mechanism of charged pion production constitutes a background for exclusive production of the ρ^0 mesons. In the next section I will present a more comprehensive analysis of the single and double production of the ρ mesons in nuclear collisions.

4.5 Single and double ρ meson production

Having fixed the details for single-vector-meson production (see Table 3.2), one can go to the discussion of double-vector-meson production. Table 4.4 collects total cross section for single- and double-ρ^0 scattering in ultrarelativistic heavy ion collisions.

A first part of Table 4.4 represents some extension of Table 3.2. Here we concentrate on the results with a fixed value of the parameter B_{ρ^0} and using the parametrization for the ρ^0 meson smearing which was proposed by the ALICE Collaboration [143]. The cross section for the smeared ρ^0 masses is somewhat larger than that for sharp resonance masses. The difference between the results without and with mass smearing is about 10% for the RHIC energy and 2% for three different LHC energies. For double-scattering mechanism this difference starts to disappear and equals only about 3% at the RHIC energy. The double scattering cross section for the $\rho^0\rho^0$ pair

Table 4.4: Total nuclear cross section for single ρ^0 meson photoproduction and for $\gamma\gamma$ fusion as well as for double-scattering production of $\rho^0\rho^0$ pairs in ultrarelativistic heavy ion UPCs.

Energy	$m_{\rho^0} = 0.77549$ GeV	Mass smearing
	single ρ^0 production	
RHIC ($\sqrt{s_{NN}} = 130$ GeV)	359	407
RHIC ($\sqrt{s_{NN}} = 200$ GeV)	590	646
LHC ($\sqrt{s_{NN}} = 2.76$ TeV)	3309	3405
LHC ($\sqrt{s_{NN}} = 3.5$ TeV)	4000	4089
LHC ($\sqrt{s_{NN}} = 5.5$ TeV)	4815	4944
	double scattering	
RHIC ($\sqrt{s_{NN}} = 200$ GeV)	1.50	1.55
LHC ($\sqrt{s_{NN}} = 3.5$ TeV)		15.25
	double scattering, $\lvert\eta_\pi\rvert < 1$	
RHIC ($\sqrt{s_{NN}} = 200$ GeV)		0.15
LHC ($\sqrt{s_{NN}} = 3.5$ TeV)		0.30
	$\gamma\gamma$ fusion	
RHIC ($\sqrt{s_{NN}} = 200$ GeV), VDM-Regge	$7.5\ 10^{-3}$	
RHIC ($\sqrt{s_{NN}} = 200$ GeV), low-energy bump	$95.0\ 10^{-3}$	
	$\gamma\gamma$ fusion, $\lvert\eta_\pi\rvert < 1$	
RHIC ($\sqrt{s_{NN}} = 200$ GeV), VDM-Regge	$0.5\ 10^{-3}$	
RHIC ($\sqrt{s_{NN}} = 200$ GeV), low-energy bump	$14.6\ 10^{-3}$	

production at the RHIC energy is about 1.5 mb. This is a rather large cross section (compared to the cross section for exclusive production of $\rho^0\rho^0$ via $\gamma\gamma$ fusion which is of the order of 0.1 mb at the RHIC energy $\sqrt{s_{NN}} = 200$ GeV). The cross section for the VDM-Regge component is rather small. Its relative contribution becomes larger at LHC energies where the $\gamma\gamma$ luminosities are much bigger.

Table 4.5: Total cross section for nuclear single and double $\rho^0(770)$ meson and two and four pion production in ultrarelativistic UPCs.

Energy	mechanism	σ_{tot} [mb]
RHIC ($\sqrt{s_{NN}} = 200$ GeV)	$\rho^0\rho^0$ in double-scattering	1.6
$-\|\|-$	$\rho^0\rho^0$ in $\gamma\gamma$ fusion	0.1
$-\|\|-$	$\pi^+\pi^-\pi^+\pi^-$ in $\gamma\gamma$ fusion	0.1
LHC ($\sqrt{s_{NN}} = 3.5$ TeV)	ρ^0 in photoproduction	4089.3
$-\|\|-$	$\pi^+\pi^-$ in $\gamma\gamma$ fusion	46.7

Table 4.5 collects predictions for double ρ^0 production in the double- γ-Pomeron exchanges and $\gamma\gamma$ fusion as well as results including the ρ^0 meson decays into four pions at RHIC energy. The last part of Table 4.5 shows results for single ρ^0 production and the cross section for pions in the final channel. The photon-photon production of $\pi^+\pi^-$ composes an irreducible background to the AA$\to$AAρ^0 reaction. At LHC energy, this background constitutes, however, only about 1% of the AA$\to$AAρ^0 cross section.

Theoretical calculations of the photonuclear ρ^0 production in the Pb-Pb collision for LHC energies give very large cross section of the order of a few barns. Table 4.6 contains total cross section predicted by several theoretical groups. The KN, FSZ ans GM models were discussed in section 3.2. Ivanov et al. [179] have presented results of calculations which were performed with two parametrizations of the dipole cross section, KST [180] and GBW [92] fitted their parameters to low and high Q^2 data from HERA experiments.

Fig. 4.13 shows the contribution of the $\rho^0(770)$ and $\rho' \equiv \rho^0(1450)$ meson integrated over the whole phase space (without any extra cuts). While the predictions for the ρ' meson production are rather uncertain, our prediction for the $\gamma\gamma$ process

Table 4.6: Total cross section in barns for the coherent $\rho^0(770)$ and $\rho^0(1450)$ meson production at the LHC energies.

Model	σ_{tot}(PbPb→PbPb$\rho^0(770)$)	σ_{tot}(PbPb→PbPb$\rho^0(1450)$)
$\sqrt{s_{NN}} \approx 5.5$ TeV		
KN [152]	5.200	
FSZ [154]	9.538	2.216
RSZ [181]	9.706	
IKS [179] /KST-R	4.900	
−||− /KST	4.360	
−||− /GBW	3.990	
−||− /VDM	10.030	
GM [144]	10.069	
our results	4.944	0.267
$\sqrt{s_{NN}} = 3.5$ TeV		
our results	4.089	0.221

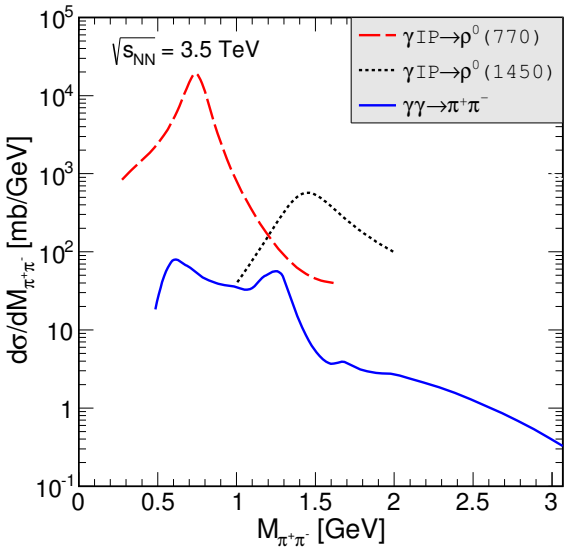

Figure 4.13: Invariant mass distributions of $\pi^+\pi^-$ from the decay of $\rho^0(770)$ and $\rho^0(1450)$ meson photoproduction and from the $\gamma\gamma$ fusion in Pb-Pb collisions at $\sqrt{s_{NN}} = 3.5$ TeV.

(blue solid line) should be fairly precise. Here we have taken into account a minimal experimental cut on transverse momentum $p_{\perp\pi} > 0.2$ GeV. The contribution from the $\rho^0(770)$ meson photoproduction dominates over the other contributions up to about $M_{\pi\pi} \simeq 1$ GeV. For larger values of the invariant dipion masses, the ρ' state is expected to appear. Because the continuum contribution (called Drell-Söding mechanism in $\gamma p \to \pi^+\pi^- p$ reactions) of single-photon photoproduction $\pi^+\pi^-$ background in this region was not studied, we have no information about its interference with the ρ' resonance. Therefore, at present it is possible to show only the resonance contribution and we leave the question of the background for future analyses, including perhaps the ALICE experimental data. The parametrization of the ρ' line shape used in our estimate is similar as that for $\rho^0(770)$ (see Eq. (3.1.1)). Below we have introduced an extra form factor which was already discussed (see Eq. (2.4.35)):

$$\frac{\mathrm{d}\sigma_{PbPb\to PbPb\rho'}}{\mathrm{d}M_{\pi\pi}} = \left| \mathcal{A}_{\rho'} \frac{\sqrt{M_{\pi\pi} m_{\rho'} \Gamma_{\rho'}(M_{\pi\pi})}}{M_{\pi\pi}^2 - m_{\rho'}^2 + i m_{\rho'} \Gamma_{\rho'}(M_{\pi\pi})} \times \exp\left(\frac{-\left(W - m_{\rho'}\right)^2}{\Lambda^2} \right) \right|^2 \tag{4.5.1}$$

and width:

$$\Gamma_{\rho'}(M_{\pi\pi}) = \Gamma_{\rho'} \frac{m_{\rho'}}{M_{\pi\pi}} \left(\frac{M_{\pi\pi}^2 - 4m_\pi^2}{m_{\rho'}^2 - 4m_\pi^2} \right)^{3/2} . \tag{4.5.2}$$

Here we use parameters from [109]: $m_{\rho'} = 1.465$ GeV and $\Gamma_{\rho'} = 0.4$ GeV. The width of the resonance is very large ($\Gamma_{\rho'} \gg 0.1$ GeV) and thus one should include extra (exponential) form factor to suppress the line strength far from the resonance position (this was already discussed in section 2.4.2).

The cross section for the photoproduction of $\rho' \equiv \rho^0(1450)$ was calculated only in Ref. [154]. This calculation finds that the ratio of total nuclear cross section for the production of $\rho^0(770)$ to the $\rho^0(1450)$ photoproduction is about 5. Here the signal in $\pi^+\pi^-$ channel is discussed and thus a corresponding branching fraction has to be included. Unfortunately, this value is not well known. The CRYSTAL BARREL Collaboration has measured only the ratio of the cross section for two- and four-pion channels [182]. They found

$$\frac{\mathrm{Br}\left(\rho^0(1450) \to 2\pi\right)}{\mathrm{Br}\left(\rho^0(1450) \to 4\pi\right)} = 0.37 \pm 0.10 . \tag{4.5.3}$$

In this situation we can only calculate an upper limit for the two-pion branching fraction:

$$\begin{aligned} \mathrm{Br}\left(\rho^0(1450) \to \pi^+\pi^-\right) &= \frac{\mathrm{Br}\,(2\pi)}{\mathrm{Br}\,(2\pi) + \mathrm{Br}\,(4\pi) + \mathrm{Br}\,(\mathrm{other})} \\ &< \frac{\mathrm{Br}\,(2\pi)}{\mathrm{Br}\,(2\pi) + \mathrm{Br}\,(4\pi)} = \frac{\mathrm{Br}\,(2\pi)\,/\mathrm{Br}\,(4\pi)}{\mathrm{Br}\,(2\pi)\,/\mathrm{Br}\,(4\pi) + 1} \\ &\simeq 0.27\,. \end{aligned} \tag{4.5.4}$$

We think that reasonable approximation at the moment is to multiply the resonance contribution for the $\rho^0(1450)$ by 0.27/5, as suggested by the calculation (Ref. [154]) and the above upper limit for the branching fraction into charged pions (Eq. (4.5.4)). It is clear that this will be only an upper estimate for the $\rho^0(1450)$ contribution in the $\pi^+\pi^-$ channel. The relative two-pion contribution from the $\rho^0(1450)$ photoproduction is still somewhat larger than observed, for example in the exclusive electroproduction of two pions with the ZEUS detector at HERA (Ref. [183]). Our prediction will of course change when we take into account experimental cuts for a concrete experiment.

In Fig. 4.13, the ρ^0 spectra are concentrated in pion-pion invariant mass around the ρ-resonance position. The ρ^0 photoproduction contribution cross sections there are much above our $\gamma\gamma \to \pi^+\pi^-$ contribution. It is not clear in the moment how the kinematic cuts may change the proportions of these two mechanisms. This should be studied in the future, because a comparison of these distributions with real data could be very interesting and should shed new light on the reaction mechanism.

In contrast, the PbPb→PbPb$\pi^0\pi^0$ reaction is free of the photoproduction mechanisms. However, it is not clear for us if, in this case, any measurement is possible.

Chapter 5

Electromagnetic excitation of nuclei

Production of particle pairs in heavy ion UPC at ultrarelativistic energies is associated with simultaneous production of huge fluxes of photons. The photon(s) may excite the nucleus (e.g. to a Giant Dipole resonance) and the de-excitation leads to breakup of the system and the emission of one or a few neutrons in the direction of the beam. Such neutrons can be registered by the so-called zero-degree-calorimeters (ZDC's), i.e., the Solenoidal Tracker (STAR) at RHIC [184] and A Large Ion Collider Experiment (ALICE) at LHC [185]. In this chapter a description of the photoexcitation of nuclei and the decay of excited nuclei in the framework of the Hauser-Feshbach theory will be presented. In addition, the results of our calculations for γAu$\rightarrow$Au*kn and γPb$\rightarrow$Pb*kn reactions will be confronted with existing experimental data. Then topological cross sections with a given number of neutrons in ion-ion collisions will be compared to RHIC and LHC data.

5.1 Photon-induced excitation of nuclei and neutron evaporation

5.1.1 Photoabsorption cross section

In the first step of the calculation of the electromagnetic excitation of nuclei one has to correctly describe photoabsorption cross section for gold and lead nucleus (Fig. 5.1).

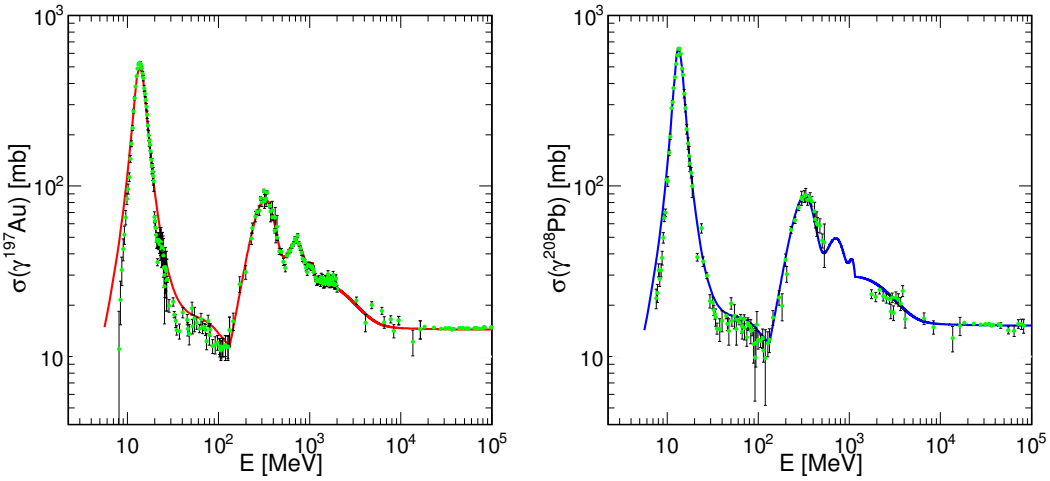

Figure 5.1: Photoabsorption cross section for the γ^{197}Au (left panel) and for the γ^{208}Pb reaction (right panel).

To evaluate the photoabsorption probabilities, in nucleus-nucleus collisions we need to parametrize the total photoabsorption cross section over a broad range of energies. Here we are not interested in a microscopic modelling of the different mechanisms which play an important role at different energies, but rather in a useful fit of empirical data.

At the lowest energies ($E_\gamma < 40$ MeV) of relevance, photoabsorption is dominated by giant resonances. The energy dependence of the cross section for the giant dipole resonance (GDR) component ($\sigma_{\rm GDR}$) is parametrized following Refs. [186, 187] as:

$$\sigma_{\rm GDR} = \frac{2}{\pi}\sigma_{TRK}\frac{E^2\Gamma_r}{\left(E^2-E_r^2\right)^2+\left(E\Gamma_r\right)^2}S_r \ . \qquad (5.1.1)$$

The parameters for the GDR component are presenten in Table 5.1. They are taken from Ref. [188] for gold and from Ref. [189] for lead nucleus. The value of

σ_{TRK} depends on the number of protons (Z), the number of neutrons (N) and the mass number (A) of the nucleus: $\sigma_{TRK} = 60\frac{NZ}{A}$ mb MeV.

Table 5.1: Parameters for the giant dipole resonance.

Parameter	^{197}Au	^{208}Pb
E_r	13.712 MeV	13.373 MeV
Γ_r	4.517 MeV	3.938 MeV
S_r	1.35416	1.33716

At somewhat larger energies a so-called quasi-deuteron contribution plays important role and this component is parametrized as in Ref. [190]:

$$\sigma_{\rm QD} = 6.5\frac{NZ}{A}\sigma_d f(E) \ , \tag{5.1.2}$$

where

$$\sigma_d = 61.2\frac{(E-2.224)^{3/2}}{E^3} \text{ mb} \ , \tag{5.1.3}$$

and

$$\begin{aligned} f(E<20MeV) &= \exp\left(\frac{-73.3}{E}\right), \\ f(20<E<140MeV) &= 8.3714\times10^{-2} \\ &- 9.8343\times10^{-3}E + 4.1222\times10^{-4}E^2 \\ &- 3.4762\times10^{-6}E^3 + 9.3537\times10^{-9}E^4 \ , \\ f(E>140MeV) &= \exp\left(\frac{-24.2}{E}\right) \ . \end{aligned} \tag{5.1.4}$$

Above photon energy $E_\gamma > 100$ MeV the nucleon resonances must be taken into account. The Δ resonance being the dominant feature of the excitation spectrum. We parametrize this region of the photoabsorption cross section as a sum of three ($i = 1, 2, 3$) Gaussian functions:

$$\sigma_{\text{nucleon res.}} = \sum_{i=1}^{3} \frac{C_G^i}{\sigma_G^i\sqrt{2\pi}} \exp\left(\frac{-\left(E-\mu_G^i\right)^2}{2\left(\sigma_G^i\right)^2}\right) \ , \tag{5.1.5}$$

where the parameters for gold nucleus found from our fit (see Fig. 5.1) are given in Table 5.2. For gold nucleus, the Gaussian function is scaled by 197/208.

Table 5.2: Parameters for the Gaussian (nucleon resonances, see Eq. (5.1.5)) and exponential components (low-energy continuum, see Eq. (5.1.6)) in parametrization of the total photoabsorption cross section for gold nucleus. The units of these parameters are the following: $[\sigma_{\mathrm{G/exp}}]$ = MeV, $[\mu_{\mathrm{G/exp}}]$ = MeV, $[C_{\mathrm{G}}]$ = b MeV, $[C_{\mathrm{exp}}]$ = mb/MeV.

Parameter	i=1	i=2	i=3
C_{G}	17	19	4
σ_{G}	90	200	90
μ_{G}	315	700	1
C_{exp}	$32 \cdot 10^{-3}$		
σ_{exp}	1050		
μ_{exp}	100		

Above $E_\gamma > 0.5$ GeV the resonant contributions disappear and the continuum related to breakup of nucleons starts to be important. The corresponding total cross section (forward amplitude of photon elastic scattering) is usually parametrized by exchange of Pomeron at very large energies and subleading Reggeons at intermediate energies. In our simple parametrization the Pomeron exchange contribution is parametrized as a constant and slightly phenomenological function is used to represent the Reggeon exchange contribution.

For energies between 1 GeV and 8 GeV we describe the data by using an exponential function:

$$\sigma^{\mathrm{low-energy}}_{\mathrm{nucleon\ continuum}} = C_{\mathrm{exp}}\,(E-\mu_{\mathrm{exp}})\exp\left(\frac{-\,(E-\mu_{\mathrm{exp}})}{\sigma_{\mathrm{exp}}}\right)\,, \tag{5.1.6}$$

where the parameters are given in Table 5.2.

For the high energy part ($E_\gamma > 8$ GeV) we use a simple functional form given in Ref. [191]:

$$\sigma^{\mathrm{high-energy}}_{\mathrm{nucleon\ continuum}} = \left(15.2 + 0.06\ln^2\left(\frac{E}{\omega_0}\right)\right)\mathrm{mb}, \tag{5.1.7}$$

For gold nucleus, this is scaled by 197/208 and $\omega_0 = 80$ GeV (Ref. [191])

Summarizing the nuclear photoproduction cross section can be written as

$$\sigma_{\gamma A} = \sigma_{\mathrm{GDR}} + \sigma_{\mathrm{QD}} + \sigma_{\mathrm{nucleon\ res.}} + \sigma_{\mathrm{nucleon\ cont.}} \tag{5.1.8}$$

This multicomponent parametrization is compared to the experimental data [192] for photoabsorption on gold and lead nuclei in Fig. 5.1. As can be seen from the figure the quality of the description of the data is fully sufficient for our purpose.

5.1.2 Decays of excited nuclear system

The calculation of probability of evaporating a given number of neutrons as a function of ^{197}Au and ^{208}Pb excitation energy was performed with the help of a Monte Carlo code GEMINI++ [193]. In this code the evaporation process is described by the Hauser-Feshbach formalism [194], in which the decay width for evaporation of a particle i from the compound nucleus with excitation energy E^* and spin S_{CN} is:

$$\Gamma_i = \frac{1}{2\pi\rho(E^*, S_{CN})} \int d\epsilon \sum_{S_d=0}^{\infty} \sum_{J=|S_{CN}-S_d|}^{S_{CN}+S_d} \sum_{\ell=|J-S_i|}^{J+S_i} T_\ell(\epsilon)\rho(E^* - B_i - \epsilon, S_d), \quad (5.1.9)$$

where S_d is the spin of the daughter nucleus, S_i, J and ℓ are spin, total and angular momentum of the evaporated particle, ϵ, B_i are kinetic and separation energies, T_ℓ is its transmission coefficient, ρ and ρ_{CN} are level densities of the daughter and compound nucleus, which can be calculated from the formula:

$$\rho(E^*, S) \propto (2S+1)\exp\left(2\sqrt{a(U,S)U}\right), \quad (5.1.10)$$

where $U = E^* - E_{rot}(S) - \delta P$ is thermal excitation energy calculated by taking into account pairing corrections to the empirical mass formula (δP) and rotational energy $E_{rot}(S)$. In the calculations the separation energies B_i, nuclear masses, shell and pairing corrections were used according to Ref. [195]. Level density parameter $a(U, S)$ was calculated as:

$$a(U,S) = \tilde{a}(U)\left(1 - h(U/\eta + S/S_\eta)\frac{\delta W}{U}\right), \quad (5.1.11)$$

where δW is the shell correction to the liquid-drop mass and $\tilde{a}$ is smoothed level-density parameter, the function specifying the rate of fadeout is $h(x) = \tanh x$, the fadeout parameter η was set to 18.52 MeV and the parameter S_η was set to 50 $\hbar$.

The smoothed level density parametrization depends on the excitation energy of nucleus as:

$$\tilde{a}(U) = \frac{A}{k_\infty - (k_\infty - k_0)\exp\left(-\frac{\kappa}{k_\infty - k_0}\frac{U}{A}\right)}, \quad (5.1.12)$$

where $k_0 = 7.3$, $k_\infty = 12$ and $\kappa = 0.00517\exp(0.0345A)$ [193].

We assume that in photoproduction excited nucleus is formed with angular momentum equal to 0 (which we believe is a good approximation for photoproduction) and full energy is used for excitation of the nucleus. The calculation of the decays is done with energy step of 1 MeV. For each excitation energy 10^5 events (decays) were generated. Finally, neutron emissions probabilities were obtained from the MC sample for each excitation energy (see histograms in Fig. 5.2). The sum of all probabilities obtained from GEMINI++ code (orange solid line = sum of all coloured lines) coincides with the sum off all probabilities from our fit (green dotted line = sum of all black solid lines).

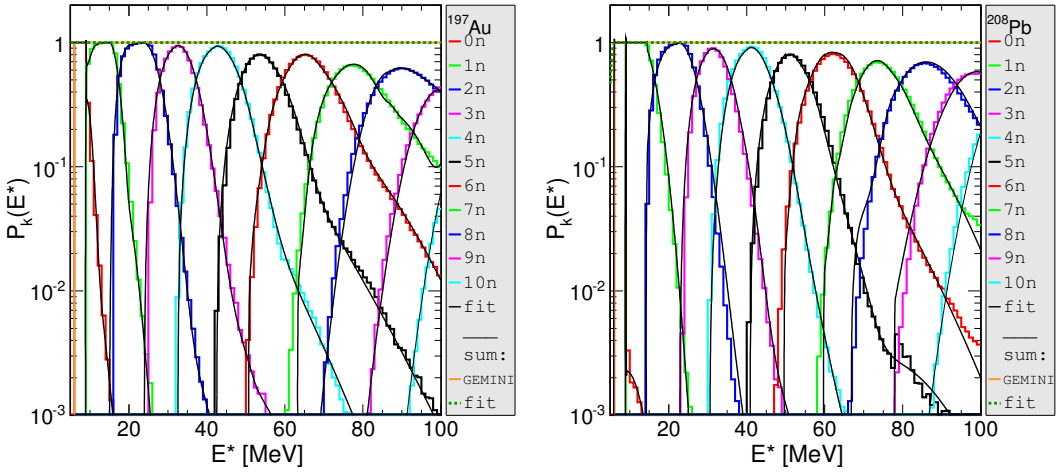

Figure 5.2: Probability of neutron multiplicity as a function of excitation energy of ^{197}Au nuclei (left panel) and of ^{208}Pb nuclei (right panel).

The fractions of events with a k-neutron final state (k is the neutron multiplicity) at excitation energy E^* can be well fitted by a sum of the following purely empirical functions:

$$f(E^*,k) \;=\; f_{\rm exp}(E^*,k) + f_{\rm Gauss}(E^*,k)\;, \tag{5.1.13}$$

where

$$f_{\rm exp}(E^*,k) \;=\; C_{\rm exp}\,(E^*-\mu_e)^2\exp\left(\frac{-\,(E^*-\mu_e)}{\sigma_e}\right)\;, \tag{5.1.14}$$

$$f_{\rm Gauss}(E^*,k) \;=\; \frac{C_G}{\sigma_G\sqrt{2\pi}}\exp\left(\frac{-\,(E^*-\mu_G)^2}{2\sigma_G^2}\right)\;. \tag{5.1.15}$$

5.1.3 Excitation functions for the γAu$\rightarrow$Au* $\rightarrow$kn and for the γPb$\rightarrow$Pb* $\rightarrow$kn reactions

Using photoabsorption cross sections which are shown in Fig. 5.1 and probabilities to emit a fixed number of neutrons (k) which are shown in Fig. 5.2, one can calculate photon-induced excitation function with a given number of associated neutrons. The results are presented in Figs. 5.3, 5.4, 5.5.

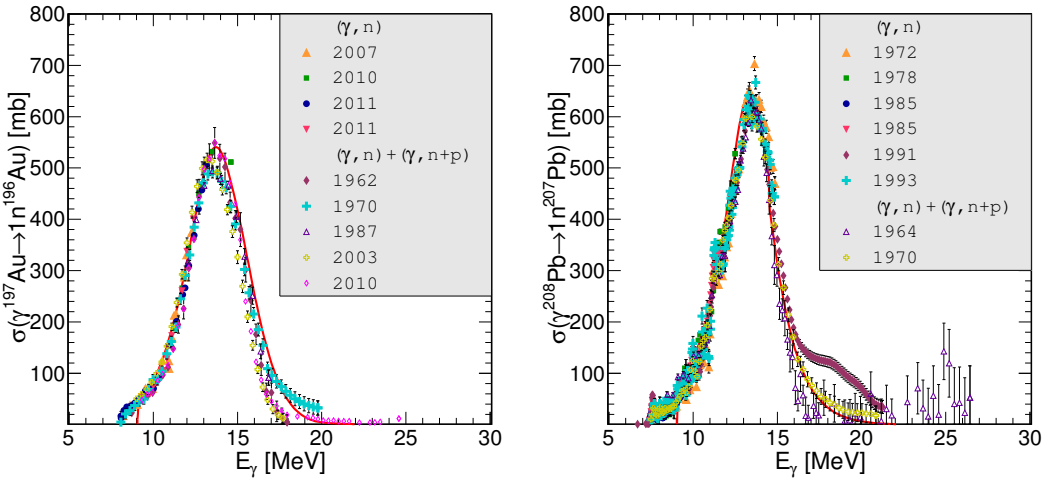

Figure 5.3: Excitation function for the γ^{197}Au $\rightarrow$ 1n^{196}Au reaction (left panel; experimental data are from Refs. [188, 189, 196–203]) and for the γ^{208}Pb $\rightarrow$ 1n^{207}Pb reaction (right panel; experimental data are from Refs. [188, 203–209]).

Experimental data are denoted by the coloured points and the description in the legend means the year when the paper was published where one can find the experimental data. References to these data are set in the figure caption. A relatively good agreement with the world data is obtained. This is rather surprising given that our calculation implicitly assumes equilibration of the nuclear system (Hauser-Feshbach formalism) formed after absorption of the photon. One can observe a small disagreement of experimental data sets obtained by different groups for production of two neutrons (Fig. 5.4). If we assumed that part of the energy of the photon would escape before equilibration of the nuclear system (due to pre-equilibrium processes) the agreement with the data would be much worse. Having proven usefulness of our

approach we can proceed to the excitation of nuclei in UPCs and related production of neutrons from the excited nuclear systems.

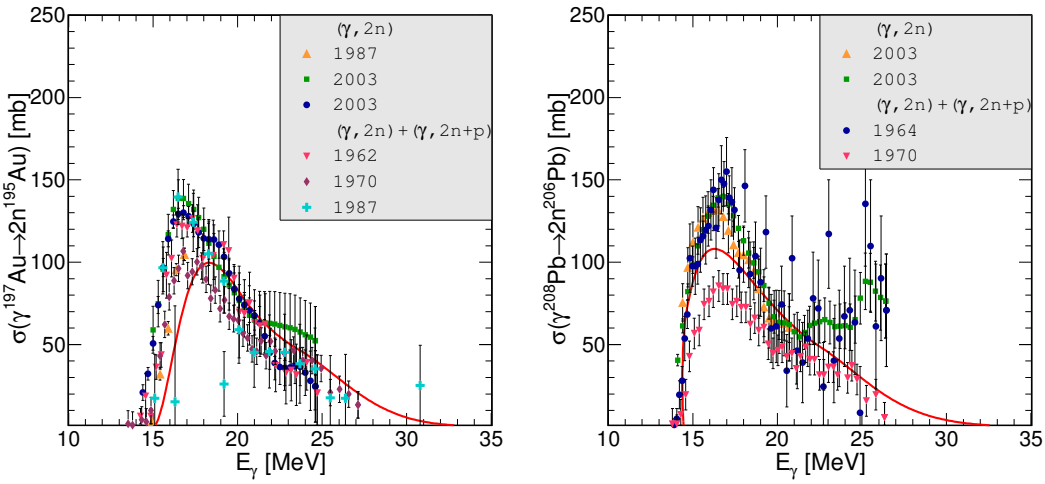

Figure 5.4: Excitation function for the $\gamma^{197}\mathrm{Au} \to 2\mathrm{n}^{195}\mathrm{Au}$ reaction (left panel; experimental data are from Refs. [188, 200–202, 210]) and for the $\gamma^{208}\mathrm{Pb} \to 2\mathrm{n}^{206}\mathrm{Pb}$ reaction (right panel; experimental data are from Refs. [188, 202, 209]).

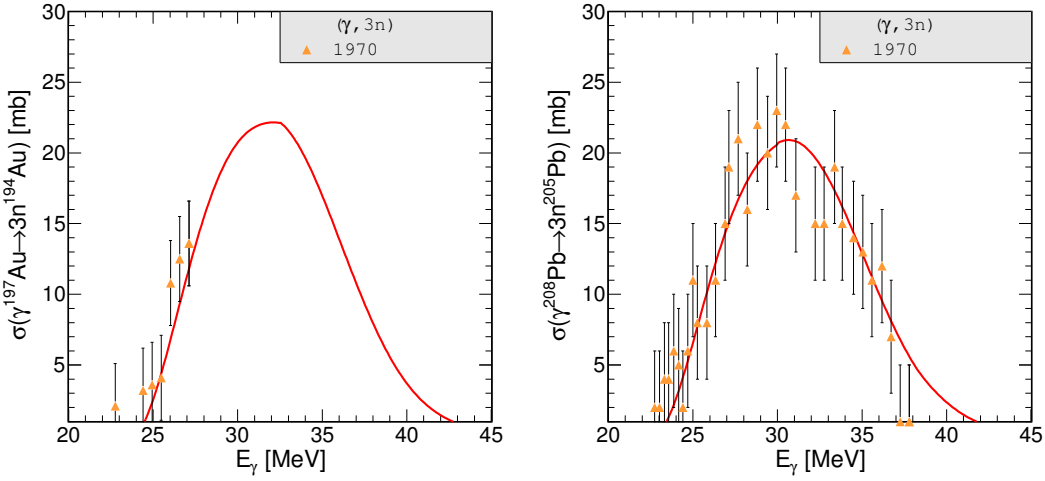

Figure 5.5: Excitation function for the $\gamma^{197}\mathrm{Au} \to 3\mathrm{n}^{194}\mathrm{Au}$ reaction (left panel; experimental data are from Ref. [188]) and for the $\gamma^{208}\mathrm{Pb} \to 3\mathrm{n}^{205}\mathrm{Pb}$ reaction (right panel; experimental data are from Ref. [188]).

5.2 Electromagnetic excitation in heavy ion UPCs

In this section we will use the classical probability methods [211–213] needed to describe the electromagnetic excitation of ions in UPCs due to multiple photon exchanges.

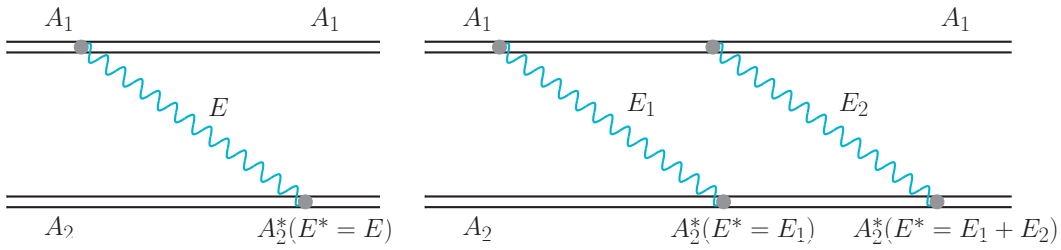

Figure 5.6: Feynman diagrams for single (left panel) and double (right panel) excitation in heavy ion UPCs.

One can identify single and double excitation in heavy ion UPCs (see Fig. 5.6). Because the coupling constant $Z\alpha_{em}$ is large (≈ 0.6 for gold and lead nuclei), single-photon and two-photon reactions may be accompanied by additional photonuclear reactions. These photonuclear reactions can lead to collective nuclear excitations (e.g. GDR).

The excitation cross section for the mechanism presented in the left panel of Fig. 5.6 can be expressed through the following equation

$$\sigma\left(A_1A_2 \to A_1A_2^*\right) = \int \mathrm{d}^2\mathbf{b}\, P_{surv}\left(\mathbf{b}\right) P_{A_2}^{exc}\left(\mathbf{b}\right) \ . \tag{5.2.16}$$

$P_{surv}\left(\mathbf{b}\right)$ here is the probability for the nuclei to survive the collision without additional strong interactions. This factor takes the form similar to the absorption factor (Eq. (B.0.2))

$$P_{surv}\left(\mathbf{b}\right) \approx \theta\left(|\mathbf{b}| - \left(R_1 - R_2\right)\right) \ , \tag{5.2.17}$$

where $R_{1/2}$ denotes a radius of the first and second nucleus and $\mathbf{b}$ is impact parameter vector. Now we should introduce the mean number of photons absorbed by a nucleus A_2 in the collision with nucleus A_1:

$$\overline{n}_{A_2}\left(\mathbf{b}\right) = \int\limits_{E_{min}}^{\infty} \mathrm{d}E\, N_{A_1}\left(E, \mathbf{b}\right) \sigma_{tot}\left(\gamma A_2; E\right) \ . \tag{5.2.18}$$

Here $\sigma_{tot}\left(\gamma A_2; E\right)$ is the photoabsorption cross section which was discussed in section 5.1.1. Here the nucleus photon flux is expressed through Eq. (1.2.37) (but one should replace the parameter $\omega \to E$ and now argument u (Eq. (1.2.25)) explicitly depends on the $\gamma_{lab} = 2\gamma_{cm}^2 - 1$ and not $\gamma_{cm} = \sqrt{s_{NN}}/(2m_N)$). Above E is the photon energy in the rest frame of nucleus A_2. The lower limit of integration in Eq. (5.2.18) is the threshold for photoexcitation. For statistically independent absorption, we can write the probability of absorption of n photons at impact parameter $\mathbf{b}$ in the Poissonian form

$$w_n\left(\mathbf{b}\right) = \frac{\left(\overline{n}_A\left(\mathbf{b}\right)\right)^n}{n!} \exp\left[-\overline{n}_A\left(\mathbf{b}\right)\right] \ . \tag{5.2.19}$$

In the next step, one should define the probability density for a single photon (left panel of Fig. 5.6) to excite nucleus A_2 in a collision at the impact parameter vector $\mathbf{b}$ of the A_1-A_2 collision:

$$p_{A_2}^{(1)}\left(E, \mathbf{b}\right) = \frac{N_{A_1}\left(E, \mathbf{b}\right) \sigma_{tot}\left(\gamma A_2; E\right)}{\overline{n}_{A_2}\left(\mathbf{b}\right)} \ . \tag{5.2.20}$$

Still under the assumption of statistical independence, n photons will excite the nucleus with the probability density

$$\begin{aligned} p_{A_2}^{(n)}\left(E, \mathbf{b}\right) &= \int \mathrm{d}E_1\, \mathrm{d}E_2 ... \mathrm{d}E_n \delta\left(E - \sum_{j=1}^{n} E_j\right) \\ &\times \ p_{A_2}^{(1)}\left(E_1, \mathbf{b}\right) p_{A_2}^{(1)}\left(E_2, \mathbf{b}\right) ... p_{A_2}^{(1)}\left(E_n, \mathbf{b}\right) \ . \end{aligned} \tag{5.2.21}$$

All the n-photon probability densities at each $\mathbf{b}$ are normalized as follows

$$\int\limits_{E_{min}}^{\infty} \mathrm{d}E\, p_{A_2}^{(n)}\left(E, \mathbf{b}\right) = 1 \ . \tag{5.2.22}$$

We shall show the results for $n = 1$ and $n = 2$, i.e., we will consider processes up to two photon exchanges (second diagram in Fig. 5.6). Generally, the probability for the excitation of nucleus A_2 in the n-photon process is given by

$$w_n\left(\mathbf{b}\right) p_{A_2}^{(n)}\left(E, \mathbf{b}\right) \ . \tag{5.2.23}$$

Summing over all numbers of photons

$$\frac{\mathrm{d}P_{A_2}^{exc}\left(\mathbf{b}\right)}{\mathrm{d}E} = \sum_n w_n\left(\mathbf{b}\right) p_{A_2}^{(n)}\left(E, \mathbf{b}\right) \tag{5.2.24}$$

and expecting the single-photon absorption to dominate one can rewrite

$$\frac{\mathrm{d}P_{A_2}^{exc}(\mathbf{b})}{\mathrm{d}E} \approx \exp\left[-\overline{n}_{A_2}(\mathbf{b})\right] N_{A_1}(E,\mathbf{b})\,\sigma_{tot}(\gamma A_2; E) \ . \tag{5.2.25}$$

It is worth to note that this may, in practice, depend on the impact parameter. Then the total probability for the nucleus to be excited is

$$\begin{aligned} P_{A_2}^{exc}(\mathbf{b}) &= \int \mathrm{d}E \frac{\mathrm{d}P_{A_2}^{exc}(\mathbf{b})}{\mathrm{d}E} \\ &= 1 - \exp\left[-\overline{n}_{A_2}(\mathbf{b})\right] \\ &= \exp\left[-\overline{n}_{A_2}(\mathbf{b})\right]\left(\exp\left[\overline{n}_{A_2}(\mathbf{b})\right] - 1\right) \\ &\approx \overline{n}_{A_2}(\mathbf{b}) \exp\left[-\overline{n}_{A_2}(\mathbf{b})\right] \ . \end{aligned} \tag{5.2.26}$$

Inserting the excitation probability to Eq. (5.2.16) one can calculate the single excitation cross section. Sometimes we are interested in the excitation cross section containing only excitations up to $E_{max} \leqslant 100$ MeV, then we can calculate the cross section from:

$$\begin{aligned} \sigma_{tot}(A_1A_2 \to A_1A_2^*; E_{max}) &\approx \int \mathrm{d}^2\mathbf{b}\, P_{surv}(\mathbf{b}) \exp\left[-\overline{n}_{A_2}(\mathbf{b})\right] \\ &\times \int_{E_{min}}^{E_{max}} \mathrm{d}E\, N_{A_1}(E,\mathbf{b})\,\sigma_{tot}(\gamma A_2; E) \ . \end{aligned} \tag{5.2.27}$$

As is apparent,

$$w_0(\mathbf{b}) = \exp\left[-\overline{n}_{A_2}(\mathbf{b})\right] \tag{5.2.28}$$

is the contribution to the survival probability from the electromagnetic dissociation channels.

The cross section for mutual electromagnetic dissociation can be written

$$\sigma_{tot}(A_1A_2 \to A_1^*A_2^*) = \int \mathrm{d}^2\mathbf{b}\, P_{surv}(\mathbf{b})\, P_{A_2}^{exc}(\mathbf{b})\, P_{A_1}^{exc}(\mathbf{b}) \ . \tag{5.2.29}$$

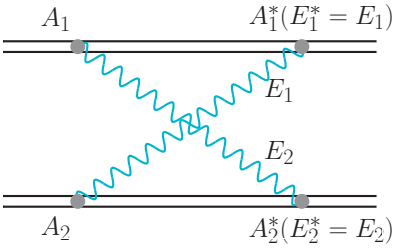

Figure 5.7: Feynman diagram for mutual excitation in heavy ion UPCs.

Fig. 5.7 shows the case when each of the nuclei emits a photon that then excites the collision partner. We shall call this case mutual excitations. the diagram shows the minimal mechanism needed to excite both nuclei simultaneously. Higher-order diagrams are possible as well.

In the next part of this section I will present our results for electromagnetic excitation of nuclei in UPCs.

Table 5.3 presents the dissociation cross section at the RHIC energy $\sqrt{s_{NN}} = 200$ GeV. We compare the results obtained by us to the results given in Ref. [214]. Our results extremely well agree with those obtained by Baltz et al. This is a very good check of our model.

Table 5.3: Cross section in barns for single-nucleus, single-photon excitation for different ranges of excitation energy for ^{197}Au+^{197}Au collisions at $\sqrt{s_{NN}} = 200$ GeV.

ω_{max} [MeV]	Our results	Baltz et al.
25	65.0	65
103	71.4	70
440	82.7	82
2000	89.9	90
17840	94.0	94

Table 5.4 shows the cross section in barns for one-nucleus single-photon excitation for different ranges of excitation energy and different collision energies represented by different $\gamma_{c.m.}$ adequate for RHIC and the LHC. The calculation was done for lead nuclei even at lower (RHIC) energy in order to compare with results published in Ref. [191]. Our results are compared with an earlier calculation by Vidović et al. [191]. Again very good agreement is observed. One can see that the largest difference between presented numbers is for the middle (second row) range of energy ($\approx 2\%$).

Now I will present results in the form of distributions. In Fig. 5.8 we have collected the cross section for neutron emission from only one Au nucleus relevant for Au-Au collisions at the RHIC energy $\sqrt{s_{NN}} = 130$ GeV (left panel of Fig. 5.8) and similar results but for Pb-Pb collisions at $\sqrt{s_{NN}} = 2.76$ TeV (right panel)

as a function of neutron multiplicities ($k = 0, 1, 2, 3, 4, 5, 6$). Our results for the LHC energy are confronted with the experimental data of the ALICE Collaboration [215]. One can observe some disagreement especially for three neutron final state. However, for the ratio $2n/1n$ we obtain within 21.6% which is in good agreement with the ALICE result of $(22.5 \pm 0.5$ stat ± 0.9 syst) %.

Table 5.4: Cross section in barns for single-nucleus, single-photon excitation for different ranges of excitation energy for ^{208}Pb+^{208}Pb collisions.

ω	Our results	Vidović et al.
	$\gamma_{c.m.} = 100$	
$(6 - 40)$	77.7	77.6
$(40 - 2000)$	26.1	25.7
$(2000 - 80000)$	5.6	5.6
	$\gamma_{c.m.} = 3100$	
$(6 - 40)$	133.4	133.6
$(40 - 2000)$	55.1	53.7
$(2000 - 80000)$	18.8	18.7

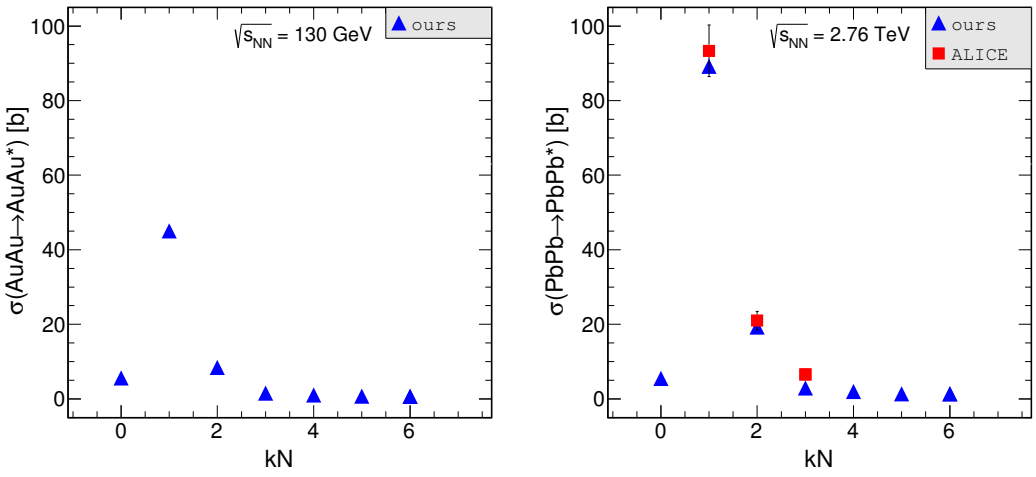

Figure 5.8: Cross section for a given multiplicity of neutrons in single-nucleus, single-photon excitation in ^{197}Au+^{197}Au collisions at $\sqrt{s_{NN}} = 130$ GeV (left panel) and in ^{208}Pb+^{208}Pb collisions at $\sqrt{s_{NN}} = 2.76$ TeV (right panel).

Table 5.5: Cross section (in barns) for mutual excitations with a given number of neutrons emitted from both nuclei in ^{197}Au+^{197}Au collisions at the RHIC energy $\sqrt{s_{NN}} = 130$ GeV.

	1n	2n	3n	4n	5n	6n
1n	0.5082	0.1002	0.0195	0.0137	0.0096	0.0091
2n	0.1002	0.0198	0.0038	0.0027	0.0019	0.0018
3n	0.0195	0.0038	0.0007	0.0005	0.0004	0.0003
4n	0.0137	0.0027	0.0005	0.0004	0.0003	0.0002
5n	0.0096	0.0019	0.0004	0.0003	0.0002	0.0002
6n	0.0091	0.0018	0.0003	0.0002	0.0002	0.0002
$\sum$	0.6603	0.1302	0.0252	0.0178	0.0126	0.0118
$\sum$			0.8579			

Table 5.6: Cross section (in barns) for mutual excitations with a given number of neutrons emitted from both nuclei in ^{208}Pb+^{208}Pb collisions at the LHC energy $\sqrt{s_{NN}} = 2.76$ TeV.

	1n	2n	3n	4n	5n	6n
1n	0.7043	0.1543	0.0248	0.0168	0.0121	0.0116
2n	0.1543	0.0339	0.0052	0.0037	0.0026	0.0025
3n	0.0248	0.0052	0.0009	0.0006	0.0004	0.0004
4n	0.0168	0.0037	0.0006	0.0004	0.0003	0.0003
5n	0.0121	0.0026	0.0004	0.0003	0.0002	0.0002
6n	0.0116	0.0025	0.0004	0.0003	0.0002	0.0002
$\sum$	0.9239	0.2022	0.0323	0.0221	0.0158	0.0152
$\sum$			1.2115			

Two-photon exchanges may also lead to simultaneous excitation of both nuclei (see Fig. 5.7). In Table 5.5 and 5.6 we have collected topological cross sections with a given number of neutrons emitted from first (k_1 neutrons) and second (k_2 neutrons) nucleus. We can compare our results with numbers given by Pshenichnov [213]. Our cross sections for neutron multiplicities $k_1 = 1$ and $k_2 = 1$ are smaller by about 17%

for RHIC and 5% for LHC energies than those in [213]. The differences quantify the uncertainties of theoretical calculations.

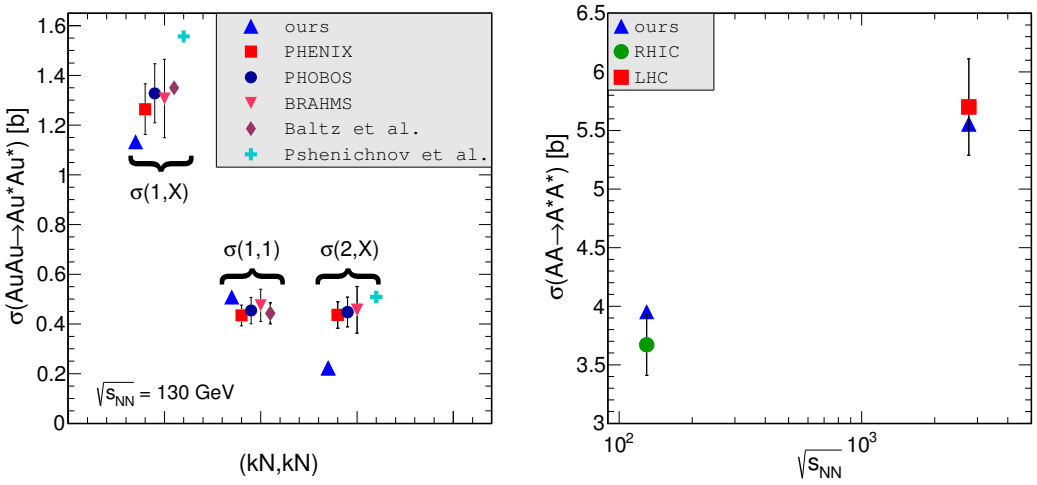

Figure 5.9: Cross section for one-neutron and two-neutron emissions in ^{197}Au+^{197}Au collisions at $\sqrt{s_{NN}} = 130$ GeV (left panel) and mutual cross section for RHIC and LHC energy (right panel).

The left panel of Fig. 5.9 depicts the summary of the cross section for one-neutron and two-neutron emissions at the RHIC energy. We refer to the data published in [216] from the PHENIX, PHOBOS and BRAHMS Collaborations, where the ratios: $\sigma(1,X)/\sigma_{tot}$, $\sigma(1,1)/\sigma_{tot}$, $\sigma(2,X)/\sigma(1,X)$ were collected. In our figure we have presented also corresponding values obtained by Baltz et al. [217] and Pshenichnov et al. [218]. In order to obtain our cross sections in barns we have multiplied the ratios given in Ref. [216] by the $\sigma_{tot} = 10.8$ b taken from the same reference. We have fairly good agreement with the experimental data for one neutron emissions and rather bad agreement for two neutron emission. In Ref. [15] we have shown contributions to mutual excitations from different regions of excitation energy of the first and second nucleus for RHIC and LHC. Quite large ranges of excitation energies ($E_1^*, E_2^* > 10$ GeV) contribute to the mutual excitation. The right panel of Fig. 5.9 presents the sum of the cross sections corresponding to the different regions. The sum adequately describes experimentally measured cross section at RHIC and LHC. We have confronted our numbers with the results obtained at RHIC [216] and by the ALICE Collaboration at the LHC [215]. We have obtained good agreement

with the experimental data. A percentage difference equals to 7.2% for RHIC and only 2.5% for LHC energy. This seems to be a rather satisfactory agreement.

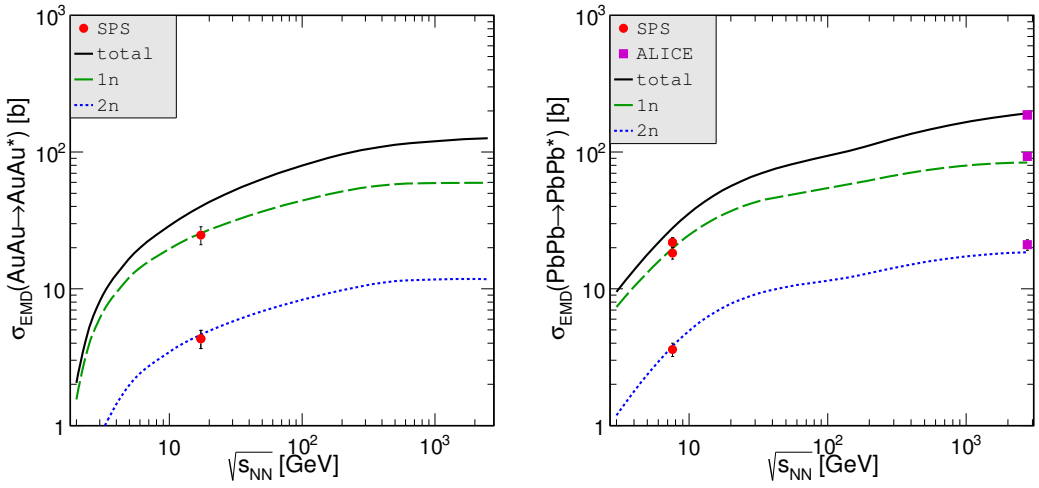

Figure 5.10: Single EMD cross sections as a function of $\sqrt{s_{NN}}$ for Au+Au (left panel) and Pb+Pb (right panel) collisions.

Excitation functions are particularly interesting. In Fig. 5.10 we show the total cross section (black solid lines) for electromagnetic excitation as a function of $\sqrt{s_{NN}}$ as well as the partial cross sections for one-neutron (green dashed lines) and two-neutron (blue dotted lines) final states. Our results are collected together with existing experimental data. The data for σ_{EMD}(AuAu→AuAu*) reaction are taken from SPS [219] where Au-Pb collision were measured. These data were rescaled to Au-Au case. The results for Pb-Pb collisions are taken from SPS [220] and from the LHC (ALICE) [215]. We get very good agreement with experimental data for both SPS and the LHC. It should be noted that we concentrate only on the neutrons evaporated from the electromagnetically excited nuclei. We do not account for neutrons from other hadronic processes, like the intranuclear cascading (see for example [213, 218]). We also neglect the mutual excitation of nuclei by strong interactions.

Fig. 5.11 presents purely theoretical results. Here we show our result for Au+Au→AuAu* reaction at the RHIC energy $\sqrt{s_{NN}} = 130$ GeV and for

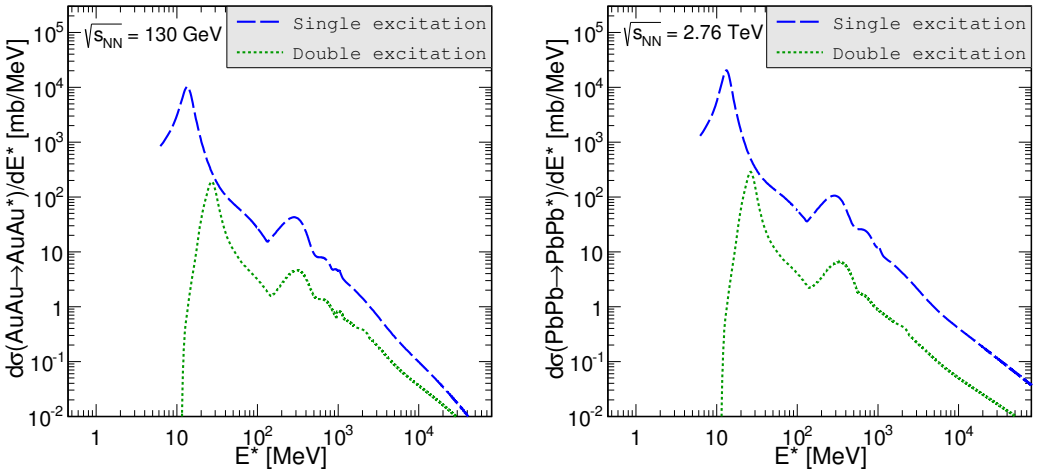

Figure 5.11: Differential cross section for a single and double excitation in UPCs of ^{197}Au+^{197}Au at $\sqrt{s_{NN}}$ = 130 GeV (left panel) and ^{208}Pb+^{208}Pb at $\sqrt{s_{NN}}$ = 2.76 TeV (right panel) as a function of nucleus excitation energy.

PbPb→PbPb* reaction at the LHC energy $\sqrt{s_{NN}} = 2.76$ TeV. The dashed line represents contribution of single-photon excitation (left diagram in Fig. 5.6) and the dotted line double-photon excitation (right diagram in Fig. 5.6). Both leading-order and next-to-leading order contributions reflect maxima present in the energy dependence of photoexcitation of Au or Pb nuclei. The double-photon contribution is rather small. Even at the very high nucleus-nucleus collision energy the low-energy ($E^* < 40$ MeV) nuclear excitations are still essential. The double-photon excitation contribution is much smaller than the single-photon one. In addition, the highest peak appears at the excitation energy twice larger than for single-photon excitation, which corresponds to excitation of giant dipole resonance excited on top of an already excited one. Such processes were already discussed in the literature (see [213] and the references therein).

So far we have applied the formalism to the calculation of the electromagnetic excitations of one or both nuclei. However, the formalism presented in this chapter may be easily applied to other exclusive ultraperipheral ultrarelativistic heavy ion processes such as: $AA \to AAJ/\Psi$, $AA \to AA\rho^0$, $AA \to AAe^+e^-$, $AA \to AA\mu^+\mu^-$. $AA \to AA\pi^+\pi^-$, $AA \to AA\pi^+\pi^-\pi^+\pi^-$.

Chapter 6

Summary

The main goal of the dissertation was a theoretical determination of the total and differential cross sections for the production of different particle pairs that are created in ultraperipheral ultrarelativistic heavy ion collisions. The Relativistic Heavy-Ion Collider (RHIC) at BNL and the Large Hadron Collider (LHC) at CERN produce Au+Au and Pb+Pb collisions at energies 200 GeV/nucleon and 2.76 or 5.5 TeV/nucleon, respectively. In this dissertation theoretical predictions for different ultraperipheral processes that could be studied experimentally at these energies have been presented.

In Chapter 1 we have discussed the Equivalent Photon Approximation which is a theoretical tool for calculation of the reaction mechanism in ultrarelativistic electromagnetic heavy ion collisions. In the literature this analysis is commonly referred to as the Weizsäcker-Williams method. The core of the Weizsäcker-Williams approach is to approximate the electric and magnetic fields of an ultrarelativistic charge as appropriate plane wave pulses of electromagnetic radiation. The first pulse is a transverse electromagnetic wave which moves along the fast moving particle direction and the second one is perpendicular to the first one. From the presentation of a frequency spectrum of these pulses, one can conclude that a significant contribution to further calculations comes from the perpendicular contribution of $N(\omega, b)$. For ultrarelativistic collisions of heavy ions, the second pulse can be neglected. We have derived the exact form of the equivalent photon fluxes for realistic charge distribution and for a point-like charge and we have compared the equivalent photon

fluxes as a function of the impact parameter for gold and lead nucleus for realistic (Fourier transform of the realistic charge distribution), monopole and point-like form factor. The biggest differences for these three cases appears for $b < 10$ fm. A typical analysis of the EPA leads to the total cross section which is factorized into an equivalent photon spectrum and the photon-ion interaction cross section. We consider ultraperipheral heavy ions UPCs, thus impact parameter plays a key role in this approach. The final form of the cross section in the b-space EPA is expressed through the five-fold integral over:

1. b - impact parameter,
2. $\overline{b}_x$ - x component of $\frac{\mathbf{b_1}+\mathbf{b_2}}{2}$,
3. $\overline{b}_y$ - y component of $\frac{\mathbf{b_1}+\mathbf{b_2}}{2}$,
4. $W_{\gamma\gamma}$ - energy in the $\gamma\gamma$ system,
5. $Y_{X_1X_2}$ - rapidity of the outgoing X_1X_2 system.

In our approach we have an opportunity to present differential cross sections as a function of the impact parameter and in other kinematic variables. The most important physical quantity for the production of particle pairs is the charge form factor of the nucleus which is hidden in the equivalent photon spectra.
In Chapter 1.4 we have presented the calculation which leads to our better understanding of the role of the nuclear form factor. First, we have reminded the differential cross section (Mott cross section) for elastic electron-nucleus scattering which is a modification of the relativistic Rutherford (for point-like and spinless particles) differential cross section. The change relies on the inclusion of the electron spin effects. In practice, the experimental cross section differs from the Rutherford cross section by a factor which depends on the momentum transfer. This quantity is so-called nucleus form factor. In the literature one can find several different forms of the form factor. We have focused on a comparison of results for the realistic and monopole form factor both for Au-Au and Pb-Pb collisions. The realistic charge distribution in a nucleus, which is used to calculate the Fourier transform, can be parametrized with the help of the two-parameter Fermi formula. The monopole

form factor depends on the root mean square radius of the nucleus. It was shown that the monopole and realistic form factors coincide at very limited range of momentum transfer. With larger value of q the difference becomes larger. In general, the form factor reduces the scattering cross section for large momentum transfer.

In Chapter 2 we have focussed on the discussion of the elementary cross sections for the $\gamma\gamma$ fusion. Each section in this chapter is devoted to another subprocess:

- dimuon production,
- ρ^0 mesons production,
- quark-antiquark production,
- two-pion production.

First we have presented the elementary cross section for dimuon production as a function of the $\gamma\gamma$ energy. The formula describing the $\gamma\gamma \to \mu^+\mu^-$ process is a text-book formula and is often called the Breit-Wheeler formula.
In the next section of Chapter 2 we have discussed the low- ($W_{\gamma\gamma} = (1-2)$ GeV) and high-energy ($W_{\gamma\gamma} > 2$ GeV) components of the $\gamma\gamma \to \rho^0\rho^0$ cross section. The low-energy part of the elementary process has been parametrized and the parameters have been fitted to the e^+e^- data while the high-energy part has been modelled in the vector-dominance Regge type model with parameters which were used to describe other hadronic processes. The model turned out to be consistent with the highest-energy data point ($W_{\gamma\gamma} > 2.5$ GeV) obtained from e^+e^- collisions. The cross section above $W_{\gamma\gamma} = 3.1$ GeV was never measured.
In the next section we have studied the elementary cross section for the $\gamma\gamma \to Q\bar{Q}X$ reaction. We have started with the Born direct contribution. The leading-order elementary cross section for the $\gamma\gamma \to Q\bar{Q}$ reaction as a function of $W_{\gamma\gamma}$ takes a simple form which differs from that for the $\gamma\gamma \to l^+l^-$ reaction by color factors and fractional charges of quarks. However, in contrast to the QED production of lepton pairs in $\gamma\gamma$ collisions, the situation for $\gamma\gamma \to Q\bar{Q}$ is much more complicated and we have included other partonic final states such as $Q\bar{Q}g$ and $Q\bar{Q}q\bar{q}$. The contribution from photon single-resolved components has been calculated too. The contributions

of each reaction to the elementary cross section have been compared to other mechanisms for the production of $c\bar{c}$ and $b\bar{b}$ quark pairs.
In the last section of this chapter we have discussed the $\gamma\gamma \to \pi\pi$ reactions, starting from the two-pion threshold up to about $W_{\gamma\gamma} = 6$ GeV. Several reaction mechanisms have been identified. We have included:

- the dipion continuum due to pion exchange (for the $\gamma\gamma \to \pi^+\pi^-$ reaction),
- $\rho^{\pm}$ exchange (for the $\gamma\gamma \to \pi^0\pi^0$ reaction),
- several dipion s-channel resonances:
    1. $f_0(600)$,
    2. $f_0(980)$,
    3. $f_2(1270)$,
    4. $f_0(1500)$,
    5. $f_2'(1525)$,
    6. $f_2(1565)$,
    7. $f_2(1950)$,
    8. $f_4(2050)$.
- QCD mechanisms:
    - Brodsky-Lepage mechanism,
    - handbag model mechanism.

This multicomponent model was then used to describe the world data for the $\gamma\gamma \to \pi\pi$ reactions. We have described the world data for $\gamma\gamma \to \pi\pi$ for the first time both for the total cross section and for angular distributions both for $\gamma\gamma \to \pi^+\pi^-$ and $\gamma\gamma \to \pi^0\pi^0$ reactions simultaneously for all experimentally available energies. We have adjusted some free parameters to get a reasonable description of the experimental data. We have obtained that the decay width of $f_0(600)$ is much smaller that that found in other partial wave analysis. Inclusion of the $f_4(2050)$ spin-4 resonance

improves angular distributions close the position of resonance peak. By fitting to the BELLE Collaboration data we have found $\Gamma_{f_4(2050)\to\gamma\gamma} = 0.7$ keV. At higher energies ($W_{\gamma\gamma} > 2.5$ GeV) the angular distributions for the $\gamma\gamma \to \pi^0\pi^0$ reaction show an enhancement at large $|\cos\theta|$. Such an enhancement was predicted before both by the Brodsky-Lepage and by the handbag model approaches separately. We have shown that a proper mixture of both processes provides a better description of the experimental data than each of them separately.

In Chapter 3 we have presented calculations for differential distributions for double-ρ^0-meson production as well as four-pion production in exclusive ultraperipheral ultrarelativistic heavy ion collisions via a double-scattering mechanisms of single ρ^0 photoproduction. The calculations have been done in the impact parameter space. We have included the smearing of ρ^0 meson masses and we have used the latest ALICE data to parametrize the Breit-Wigner amplitude and the Drell-Söding type continuum term to calculate distributions of the final state pions. The existence of these data allows to consider $\rho^0\rho^0$ or corresponding $\pi^+\pi^-\pi^+\pi^-$ double photoproduction in broad range of center of mass energy of the four pion system. Our results for single-ρ^0 production well agree with the STAR and ALICE experimental data. The produced ρ^0 mesons decay, with almost 100% probability, into charged pions, giving large contribution to exclusive production of the $\pi^+\pi^-\pi^+\pi^-$ final state. We have made a comparison of four-pion production via $\rho^0\rho^0$ production (nuclear photoproduction and $\gamma\gamma$ fusion) with experimental data measured by the STAR Collaboration for the AuAu$\to$AuAu$\pi^+\pi^-\pi^+\pi^-$ reaction. The theoretical predictions have similar shape in four-pion invariant mass as the distribution measured by the STAR Collaboration, but exhaust only about 20% of the measured cross section. The missing contribution can come from excited states of $\rho^0(770)$ (e.g. $\rho^0(1450)$ and $\rho^0(1700)$ resonances) and their decay into four charged pions. A separation of the double-scattering, $\gamma\gamma$, $\rho^0(1450)$ and $\rho^0(1700)$ mechanisms seems very important in a future. In general, transverse momentum of each of the produced ρ^0's in the double-scattering mechanism is smaller than in the other mechanisms. As a consequence, the pions from the decay of ρ^0's from the double-scattering mechanism are

produced dominantly back to back in azimuthal angle. This could be used to enhance the purity of the experimental sample as far as double-scattering mechanism is considered. Clearly further studies are needed. At large (pseudo)rapidity separations between two ρ^0's and/or large $\pi^+\pi^-\pi^+\pi^-$ (pseudo)rapidity separations, the double-scattering contribution should dominate over other contributions. The identification of the dominance region seems difficult, if not impossible, at RHIC. We plan a separate careful analysis devoted to the ALICE experimental conditions. It would be interesting if different mechanisms discussed in this dissertation could be separated and identified experimentally in the future. This requires, however, rather complicated correlation studies for four charged pions.

Chapter 4 includes collection of our theoretical results. The nuclear cross sections have been calculated with the help of EPA in impact parameter space. A part of results have been obtained with the help of EPA in momentum space and even using Feynman diagrammatic approach in the momentum space. This Chapter is divided into five sections and each section includes nuclear calculations corresponding one-to-one to the sections in Chapter 2 (elementary cross sections) plus additional section which sums up the results for single and double $\rho^0(770)$ meson and two and four pion production. We have presented predictions of a total and differential cross sections for the production of particle pairs which come from ultraperipheral ultrarelativistic heavy ion collisions. Calculations have been devoted to experiments at the RHIC and LHC accelerators. We have presented one and two-dimensional distributions in impact parameter (b), invariant mass ($M_{X_1X_2}$), rapidity of particle pairs ($Y_{X_1X_2}$), pseudorapidity of a particle in the final state ($\eta_{X_{1/2}}$) and transverse momentum of the produced particle ($p_{\perp X_{1/2}}$). In this dissertation we have presented a study of the role of charge density in nuclei or nuclear form factor for the exclusive production of particle pairs in heavy ion UPCs. Most of calculations in the literature use so-called monopole charge form factor, which allows to write several formulae analytically. While it may be reasonable for the total rate of the particle production it is certainly too crude for differential distributions and for the cross sections with extra cuts imposed on transverse momenta of the particles X_1 and X_2. Our calculations have shown that the results obtained with the realistic and the approximate form factors

may differ considerably. The effects related to the charge distribution in nuclei are particularly important at large invariant mass and rapidity of particle pairs or at large pseudorapidity and transverse momenta of particle. We have presented predictions for the PHENIX detector at RHIC. We have found significant deviations from the reference calculation obtained with the monopole form factor. It would be interesting to pin down the effects discussed here and verify the predictions in future studies at the LHC. In practice such studies may not be simple as an efficient trigger for the ultraperipheral collisions is required. The multi-photon exchanges leading to additional excitation of nuclei and subsequent emission of neutrons could be useful in this context. The neutrons could be then measured by the Zero Degree Calorimeters. First measurements of this type for e^+e^- pair emission have been already performed by the STAR and PHENIX Collaborations.

We have also discussed the role of absorption effects which can be easily estimated in the impact parameter space. We have done this e.g. following the example the exclusive production of charm-anticharm and bottom-antibottom pairs, for the $Q\bar{Q}g$ and $Q\bar{Q}q\bar{q}$ final state, as well as for the single-resolved components in lead-lead collisions for the LHC energy ($\sqrt{s_{NN}} = 5.5$ TeV). Large cross sections have been found in the case of charm quarks (antiquarks) production. In contrast to the exclusive dilepton production in the case of the heavy-quark-heavy-antiquark production, large QCD corrections appears. Their fractional contribution strongly depends on the $\gamma\gamma$ subsystem energy. The absorption effects turned about to be larger for bottom quarks (20%) than for charm quarks (10%). The calculations obtained with the help of EPA in the parameter space, EPA in the momentum space and exact momentum space are very similar. Since these methods lead to similar effects, one can use the momentum space approach to calculate, or at least to estimate, different observables which are not straightforward in the b-space EPA approach. We have found that the contributions of two- and four-quark and single-resolved final states are of similar size. We have found also that the large invariant masses of the $Q\bar{Q}$ system are populated predominantly by the direct $\gamma\gamma \to Q\bar{Q}$ subprocesses, while smaller invariant masses are dominated by the $\gamma\gamma \to Q\bar{Q}g$, $\gamma\gamma \to Q\bar{Q}q\bar{q}$, or photon single-resolved components. This could be potentially helpful

in experimental identification of the all components. There are known experimental methods for distinguishing large transverse momentum b ($\bar{b}$) jets; therefore, exclusive measurement of such jets should be possible in future LHC experiments.
Next we have calculated the cross section for the exclusive production of charged and neutral pions in heavy ion UPCs. The calculation of distributions for individual pions is slightly more complicated in the b-space EPA. The distributions in dipion invariant mass have been compared with the contribution of exclusive $\rho^0 \to \pi^+\pi^-$ production in $\gamma\mathbb{P}$ ($\mathbb{P}\gamma$) mechanism. Close to the ρ^0 resonance the $\gamma\gamma \to \pi^+\pi^-$ mechanism yields only a small contribution. The $\gamma\gamma$ contribution could be, perhaps, measured outside of the ρ^0 resonance window. A detailed comparison with the absolutely normalized ALICE experimental data should allow a quantitative test of our predictions. Imposing several experimental cuts may enhance the $\gamma\gamma \to \pi\pi$ contribution. We have analysed exclusive production of two and four pions. So far nobody, except of our group, has presented a model or/and predictions for four-pion production in nuclear reactions. In this dissertation we have concentrated on processes with final nuclei in the ground state. It is very difficult, if not impossible, to measure such very forward/backward nuclei. The multiple Coulomb excitations associated with $\rho^0\rho^0$ production may cause additional excitation of one or even both nuclei to the giant resonance region. We plan a detailed study of these processes in the future.

In Chapter 5 we have presented a new approach for calculating the excitation of Au and Pb nuclei in photoabsorption reactions as well as in ultraperipheral ultrarelativistic heavy ion collisions. The photoabsorption cross section on Au and Pb nuclei have been fitted using physics-motivated multicomponent parametrization. The giant resonances, quasi-deuteron, excitation of nucleon resonances, and breakup of the nucleon mechanisms have been included in the fit to the world data. The neutron emission from the excited nuclear system has been calculated within the Hauser-Feshbach formalism. Within our approach we have obtained a very good description of the excitation functions for $\gamma+^{197}$Au and $\gamma+^{208}$Pb reactions with a fixed number of neutrons. The excitation function has been used next to calculate several cross sections in UPCs. Both single-photon and double-photon excitation processes

have been included and discussed. We have calculated the corresponding excitation functions for single nucleus excitations. We have obtained a good agreement of the calculated total cross section for electromagnetic excitation as well as the cross section for one-neutron and two-neutron emissions with the recent experimental data of the PHENIX, PHOBOS, BRAHMS, and ALICE Collaborations. After small modifications the prepared package of programs can be used in future to exclusive production of particle pairs studied in this dissertation.

Appendix A

Frequency spectra of equivalent pulses

We start from rewriting equations defining electric field (1.2.11) in Gaussian units

$$E_x(\mathbf{r},t) = Ze\frac{b\gamma}{r^3}\left(1+mr\right)e^{-mr}\,, \tag{A.0.1}$$

$$E_z(\mathbf{r},t) = -Ze\frac{\gamma vt}{r^3}\left(1+mr\right)e^{-mr}\,. \tag{A.0.2}$$

Denoting a general field in the time domain as $\Psi(t)$, the corresponding Fourier transform $\Psi(\omega)$ is given as

$$\Psi(\omega) = \frac{1}{\sqrt{2\pi}}\int\limits_{-\infty}^{\infty}\mathrm{d}t\,\Psi(t)\exp\left(i\omega t\right) \tag{A.0.3}$$

for an even function of t, $\Psi(-t)=\Psi(t)$, the Fourier transform reduces to

$$\Psi(\omega) = \frac{2}{\sqrt{2\pi}}\int\limits_{0}^{\infty}\mathrm{d}t\,\Psi(t)\cos\left(\omega t\right)\,, \tag{A.0.4}$$

while for an odd function $\Psi(-t)=-\Psi(t)$, it can be calculated from

$$\Psi(\omega) = i\frac{2}{\sqrt{2\pi}}\int\limits_{0}^{\infty}\mathrm{d}t\,\Psi(t)\sin(\omega t)\,. \tag{A.0.5}$$

The derivation for the equivalent pulse 1:

$$E_x(\omega) = Ze\frac{2}{\sqrt{2\pi}}b\gamma\int\limits_{0}^{\infty}\mathrm{d}t\,\frac{1}{r^3}\left(1+mr\right)e^{-mr}\cos\left(\omega t\right) \tag{A.0.6}$$

$$= Ze\sqrt{\frac{2}{\pi}}b\gamma\left[\int\limits_{0}^{\infty}\mathrm{d}t\,\frac{1}{r^3}e^{-mr}\cos\left(\omega t\right)+\int\limits_{0}^{\infty}\mathrm{d}t\,\frac{m}{r^2}e^{-mr}\cos\left(\omega t\right)\right]\,,$$

$$
\begin{aligned}
X_1 &= \int_0^\infty \mathrm{d}t\, \frac{1}{r^3} e^{-mr} \cos(\omega t) \\
\Rightarrow \frac{\partial X_1}{\partial m} &= -\int_0^\infty \mathrm{d}t\, \frac{1}{r^2} e^{-mr} \cos(\omega t) \ , \qquad \text{(A.0.7)} \\
X_2 &= \int_0^\infty \mathrm{d}t\, \frac{m}{r^2} e^{-mr} \cos(\omega t) \\
\Rightarrow \frac{\partial X_2}{\partial m} &= \int_0^\infty \mathrm{d}t\, \frac{1}{r^2} e^{-mr} \cos(\omega t) - \int_0^\infty \mathrm{d}t\, \frac{m}{r} e^{-mr} \cos(\omega t) \ , \qquad \text{(A.0.8)}
\end{aligned}
$$

$$
\begin{aligned}
\frac{\partial E_x(\omega)}{\partial m} &= Ze\sqrt{\frac{2}{\pi}} b\gamma \left[\frac{\partial X_1}{\partial m} + \frac{\partial X_2}{\partial m} \right] \qquad \text{(A.0.9)} \\
&= -Zem\sqrt{\frac{2}{\pi}} b\gamma \int_0^\infty \mathrm{d}t\, \frac{1}{\sqrt{b^2 + (\gamma v t)^2}} e^{-m\sqrt{b^2+(\gamma v t)^2}} \cos(\omega t) \ .
\end{aligned}
$$

Using a mathematical handbook, such as Gradshteyn and Ryzhik's *Tables of Integrals* [126]:

$$
\int_0^\infty \frac{1}{\sqrt{\zeta^2 + u^2}} e^{-\beta\sqrt{\zeta^2+u^2}} \cos(\alpha u) \mathrm{d}u = K_0(\zeta\sqrt{\alpha^2+\beta^2}) \ , \qquad \text{(A.0.10)}
$$

where $K_0(z)$ is the modified Bessel function of the second kind with order zero. The integral in Eq. (A.0.9) one can solve as follows:

$$
\begin{aligned}
&\int_0^\infty \mathrm{d}t\, \frac{1}{\sqrt{b^2 + (\gamma v t)^2}} e^{-m\sqrt{b^2+(\gamma v t)^2}} \cos(\omega t) \\
&= \int_0^\infty \mathrm{d}t\, \frac{1}{\gamma v \sqrt{\frac{b^2}{\gamma^2 v^2} + t^2}} e^{-\gamma m v\sqrt{\frac{b^2}{\gamma^2 v^2}+t^2}} \cos(\omega t) \\
&= \frac{1}{\gamma v} K_0\left(\frac{b}{\gamma v} \sqrt{(\gamma m v)^2 + \omega^2} \right) \\
&= \frac{1}{\gamma v} K_0\left(b\sqrt{m^2 + \left(\frac{\omega}{\gamma v}\right)^2} \right) \ . \qquad \text{(A.0.11)}
\end{aligned}
$$

Finally, Eq. (A.0.9) takes the form

$$
\begin{aligned}
\frac{\partial E_x(\omega)}{\partial m} &= -Zem\sqrt{\frac{2}{\pi}} \frac{b}{v} K_0\left(b\sqrt{m^2 + \left(\frac{\omega}{\gamma v}\right)^2} \right) \\
&= -Zem\sqrt{\frac{2}{\pi}} \frac{b}{v} K_0(\xi) \ . \qquad \text{(A.0.12)}
\end{aligned}
$$

Here a new helpful quantity is defined as:

$$\xi = b\sqrt{m^2 + \left(\frac{\omega}{\gamma v}\right)^2} \,. \tag{A.0.13}$$

Using the Bessel function property:

$$\frac{\mathrm{d}}{\mathrm{d}x}\left[x^n K_n\left(x\right)\right] = -x^n K_{n-1}\left(x\right) \tag{A.0.14}$$

and

$$\frac{\partial \xi}{\partial m} = \frac{b^2 m}{\xi} \tag{A.0.15}$$

one can calculate

$$\begin{aligned} \frac{\partial E_x(\omega)}{\partial \xi} = \frac{\partial E_x(\omega)}{\partial m}\frac{\partial m}{\partial \xi} &= -Ze\sqrt{\frac{2}{\pi}}\frac{\xi}{bv}K_0(\xi) \\ &= Ze\sqrt{\frac{2}{\pi}}\frac{1}{bv}\frac{\partial\left[\xi K_1(\xi)\right]}{\partial \xi} \,. \end{aligned} \tag{A.0.16}$$

Finally, the solution of Eq. (A.0.6) has the form

$$E_x(\omega) = \text{const.} + Ze\sqrt{\frac{2}{\pi}}\frac{1}{bv}\xi K_1(\xi) \,. \tag{A.0.17}$$

In order to calculate the electric field in the z direction one has to use the following Fourier transform

$$\Psi(\omega) = i\frac{2}{\sqrt{2\pi}}\int_0^\infty \mathrm{d}t\, \Psi(t)\sin(\omega t) \,. \tag{A.0.18}$$

Transformation of Eq. (A.0.2)

$$\begin{aligned} E_z(\omega) &= i\sqrt{\frac{2}{\pi}}\int_0^\infty \mathrm{d}t\, \left[-Ze\frac{\gamma v t}{r^3}\left(1+mr\right)e^{-mr}\right]\sin(\omega t) \\ &= -iZe\sqrt{\frac{2}{\pi}}\gamma v\int_0^\infty \mathrm{d}t\, \left(\frac{1}{r^3}+\frac{m}{r^2}\right)e^{-mr}t\sin(\omega t) \,. \end{aligned} \tag{A.0.19}$$

Using the relation

$$t\sin(\omega t) = \frac{\mathrm{d}}{\mathrm{d}\omega}\left(-\cos\left(\omega t\right)\right) \tag{A.0.20}$$

one can continue and write

$$E_z(\omega) = iZe\sqrt{\frac{2}{\pi}}\gamma v\frac{\partial}{\partial \omega}\left[\int_0^\infty \mathrm{d}t\, \left(\frac{1}{r^3}+\frac{m}{r^2}\right)e^{-mr}\cos(\omega t)\right] \,. \tag{A.0.21}$$

The same form of the integral was calculated for $E_x(\omega)$ case, so automatically one can write

$$\begin{aligned} E_z(\omega) &= iZe\sqrt{\frac{2}{\pi}}\gamma v\frac{\partial}{\partial\omega}\left[\frac{1}{b^2\gamma v}\xi K_1(\xi)\right] \\ &= iZe\sqrt{\frac{2}{\pi}}\frac{1}{b^2}\frac{\partial\left[\xi K_1(\xi)\right]}{\partial\xi}\frac{\partial\xi}{\partial\omega}\ . \end{aligned} \tag{A.0.22}$$

Using the Bessel function property (A.0.14) and the relation

$$\frac{\partial\xi}{\partial\omega} = \frac{b^2\omega}{(\gamma v)^2\,\xi} \tag{A.0.23}$$

one can continue. Finally, the solution of Eq. (A.0.19) has the form

$$E_z(\omega) = -iZe\sqrt{\frac{2}{\pi}}\frac{\omega}{(\gamma v)^2}\left[K_0(\xi)\right]\ . \tag{A.0.24}$$

A.1 Realistic form factor

Let us start from a derivation of the realistic form factor argument in Eq. (1.2.35). The delta function $\delta(k\cdot u)$ in Eq. (1.2.35) enforces the dependence

$$\gamma\omega = \gamma\beta k_z\ . \tag{A.1.25}$$

Argument of the form factor fulfills the dependences [32]:

$$k^2 = -\left(\frac{\omega}{\gamma\beta}\right)^2 - k_\perp^2\ , \tag{A.1.26}$$

$$k^2 = \omega^2 - k_x^2 - k_y^2 - k_z^2\ , \tag{A.1.27}$$

where $k=(\omega,\mathbf{k})$. The transverse component is expressed through x and y components:

$$k_\perp^2 = k_x^2 + k_y^2\ . \tag{A.1.28}$$

Eq. (A.1.27) can be rewritten

$$k^2 = \omega^2 - k_z^2 - k_\perp^2\ . \tag{A.1.29}$$

In addition, using Eq. (A.1.25)

$$k_z = \frac{\omega}{\beta} \tag{A.1.30}$$

and the ultrarelativistic dependence

$$\gamma = \frac{1}{\sqrt{1-\beta^2}} \Rightarrow \beta^2 - 1 = -\frac{1}{\gamma^2} \tag{A.1.31}$$

one can continue to derive the argument of the elastic nuclear charge form factor

$$\begin{aligned} k^2 &= \omega^2 - \left(\frac{\omega}{\beta}\right)^2 - k_\perp^2 \\ &= \frac{\omega^2\left(\beta^2-1\right)}{\beta^2} - k_\perp^2 \\ &= -\left(\frac{\omega}{\gamma\beta}\right)^2 - k_\perp^2 \ . \end{aligned} \tag{A.1.32}$$

Now one can write:

$$\begin{aligned} \mathbf{E_x} = \mathbf{E}_\perp(k) &= -iA^0(k)\mathbf{k}_\perp \\ &= 2\pi i\gamma\delta\left(k\cdot u\right) Ze\frac{F\left(-k^2\right)}{k^2}\mathbf{k}_\perp \ . \end{aligned} \tag{A.1.33}$$

A partial Fourier transform of $\mathbf{E}(\mathbf{k}_\perp,\omega)$ in the z direction:

$$\begin{aligned} \mathbf{E}_\perp\left(z,\mathbf{k}_\perp,\omega\right) &= \int\limits_{-\infty}^{\infty}\frac{\mathrm{d}k_z}{2\pi}\mathbf{E}_\perp\left(k,\omega\right)e^{ik_z z} \\ &= iZe\gamma\mathbf{k}_\perp\int\limits_{-\infty}^{\infty}\mathrm{d}k_z e^{ik_z z}\frac{F\left(-k^2\right)}{k^2} \\ &= -iZe\gamma\mathbf{k}_\perp\frac{1}{v}\int\limits_{-\infty}^{\infty}\mathrm{d}\omega e^{i\frac{\omega}{v}z}\frac{F\left(\left(\frac{\omega}{\gamma\beta}\right)^2+k_\perp^2\right)}{\left(\frac{\omega}{\gamma\beta}\right)^2+k_\perp^2} \ . \end{aligned} \tag{A.1.34}$$

When Fourier transform of radially-symmetric functions are to be calculated, the one-dimensional Hankel transformation of order zero (the radial Fourier transform) is a useful alternative to the two-dimensional Fourier transform. The Fourier transform of the two-dimensional function $f(\mathbf{r})$ reads

$$f\left(\mathbf{k}\right) = \frac{1}{2\pi}\int \mathrm{d}^2 r f\left(\mathbf{r}\right)\exp\left(-i\mathbf{k}\cdot\mathbf{r}\right) \tag{A.1.35}$$

which, if f is radially symmetric, becomes

$$f\left(\mathbf{k}\right) = \frac{1}{2\pi}\int\limits_0^\infty \mathrm{d}r r f\left(r\right)\int\limits_0^{2\pi}\mathrm{d}\Phi\exp\left(-ikr\cos\Phi\right) \ , \tag{A.1.36}$$

where Φ is the angle between $\mathbf{k}$ and $\mathbf{r}$. A useful integral representation of the J_0 Bessel function is

$$J_0(z) = \frac{1}{\pi}\int_0^\pi \mathrm{d}\theta \cos(z\cos\theta) \tag{A.1.37}$$

Below we will also need the Bessel function $J_1(z)$:

$$J_1(z) = -\frac{\mathrm{d}J_0(z)}{\mathrm{d}z} \tag{A.1.38}$$

so that Eq. (A.1.36) can be rewritten in the radial Fourier transform form

$$f(\mathbf{k}) = \int_0^\infty \mathrm{d}r r J_0(kr) f(r) \ . \tag{A.1.39}$$

For the Fourier transform of the magnetic field we need to evaluate a Fourier integral of the type (where $k_\perp \equiv |\mathbf{k}_\perp|$):

$$\begin{aligned} I(\mathbf{x}_\perp) &= \int \frac{\mathrm{d}^2\mathbf{k}_\perp}{(2\pi)^2}\mathbf{k}_\perp f(k_\perp)\exp(i\mathbf{k}_\perp\mathbf{x}_\perp) \\ &= -i\nabla_\perp \int \frac{\mathrm{d}^2\mathbf{k}_\perp}{(2\pi)^2} f(k_\perp)\exp(i\mathbf{k}_\perp\mathbf{x}_\perp) \\ &= -i\nabla_\perp \int_0^\infty \frac{k_\perp \mathrm{d}k_\perp}{2\pi} f(k_\perp) J_0(x_\perp k_\perp) = -i\frac{\mathbf{x}_\perp}{x_\perp}\int_0^\infty \frac{k_\perp \mathrm{d}k_\perp}{2\pi} f(k_\perp)\frac{\partial}{\partial x_\perp}J_0(x_\perp k_\perp) \\ &= i\frac{\mathbf{x}_\perp}{x_\perp^2}\int_0^\infty \frac{k_\perp \mathrm{d}k_\perp}{2\pi} f(k_\perp)(x_\perp k_\perp)J_1(x_\perp k_\perp)\,. \end{aligned} \tag{A.1.40}$$

Using these steps, we obtain the expression for the electric field

$$\begin{aligned} \mathbf{E}(\omega,\mathbf{x}_\perp) &= \int \frac{\mathrm{d}^2\mathbf{k}_\perp}{(2\pi)^2}\mathbf{E}_\perp(\omega,\mathbf{k}_\perp)\, e^{i\mathbf{x}_\perp\mathbf{k}_\perp} \\ &= -\frac{\mathbf{x}_\perp}{x_\perp^2}\frac{Ze}{\beta}\int \frac{k_\perp \mathrm{d}k_\perp}{2\pi}(k_\perp x_\perp)J_1(x_\perp k_\perp)\frac{F\left(\left(\frac{\omega}{\beta\gamma}\right)^2 + k_\perp^2\right)}{\left(\left(\frac{\omega}{\beta\gamma}\right)^2 + k_\perp^2\right)} \end{aligned} \tag{A.1.41}$$

Finally, the equivalent photon flux for realistic charge distribution takes the form

$$\begin{aligned} N(\omega,b) &= \frac{1}{\pi\omega}|\mathbf{E}(\omega,\mathbf{x}_\perp)|^2 \\ &= \frac{Z^2\alpha_{em}}{\pi^2\beta^2\omega}\left|\int \mathrm{d}k_\perp\, k_\perp^2 \frac{F\left(\left(\frac{\omega}{\beta\gamma}\right)^2 + k_\perp^2\right)}{\left(\left(\frac{\omega}{\beta\gamma}\right)^2 + k_\perp^2\right)} J_1(x_\perp k_\perp)\right|^2 \\ &= \frac{Z^2\alpha_{em}}{\pi^2\beta^2\omega}\frac{1}{b^2}\left|\int \mathrm{d}\chi\, \chi^2 \frac{F\left(\frac{\chi^2+u^2}{b^2}\right)}{\chi^2+u^2} J_1(\chi)\right|^2 \ , \end{aligned} \tag{A.1.42}$$

where J_1 is the appropriate Bessel function and χ is a dimensionless auxiliary variable $\chi = k_\perp b$. In Eq. (A.1.42) we have used the scaling variable $u = \frac{\omega b}{\gamma\beta}$ which was defined in Eq. (1.2.25).

Appendix B

The cross section in EPA - the form used in the calculation

The basic equation for the calculation of the cross section for the exclusive production of pairs of particles in ultrarelativistic heavy ion collisions in the equivalent photon approach is Eq. (1.2.3). Starting from this notation and using the relation (1.2.1), one can write

$$\begin{aligned}\sigma_{A_1A_2\to A_1A_2X}\left(\sqrt{s_{A_1A_2}}\right) &= \int \sigma_{\gamma\gamma\to X_1X_2}\left(\omega_1,\omega_2\right) N\left(\omega_1,\mathbf{b_1}\right) N\left(\omega_2,\mathbf{b_2}\right) S^2_{abs}\left(\mathbf{b}\right) \\ &\times \ \mathrm{d}^2\mathbf{b_1}\,\mathrm{d}^2\mathbf{b_2}\,\mathrm{d}\omega_1\,\mathrm{d}\omega_2\ . \end{aligned} \tag{B.0.1}$$

The above equation is the convolution of the $\gamma\gamma \to X_1X_2$ subprocess cross section and the equivalent photon spectra $N\left(\omega, b\right)$. The factor related to the absorption is approximated in most of the calculations presented in this dissertation as (Refs. [221, 222])

$$S^2_{abs}\left(\mathbf{b}\right) = \theta\left(\mathbf{b} - 2R_A\right) = \theta\left(\left|\mathbf{b_1} - \mathbf{b_2}\right| - 2R_A\right)\ . \tag{B.0.2}$$

The main goal of the absorption factor is to exclude the situations when nuclei breakup. This is equivalent with taking into account only ultraperipheral collisions. This is possible when the colliding nuclei overlap. This factor can be calculated in different models. For example a model introduced in section E is a reasonable approach. On the other hand, the Glauber model is correct at not too high energies but Eq. (B.0.2) nicely describes the situation at higher energies too.

Performing the following change of integration variables: the energies of photons ($i = 1, 2$) are expressed in terms of $W_{\gamma\gamma}$ and rapidity of the pair $Y_{X_1X_2}$ as:

$$\omega_i = \frac{W_{\gamma\gamma}}{2} \exp\left(\pm Y_{X_1X_2}\right) \ . \tag{B.0.3}$$

Using some further transformation

$$\mathrm{d}\omega_1 \, \mathrm{d}\omega_2 = \frac{W_{\gamma\gamma}}{2} \mathrm{d}W_{\gamma\gamma} \, \mathrm{d}Y_{X_1X_2} \tag{B.0.4}$$

the cross section can be written equivalently

$$\begin{aligned} \sigma_{A_1A_2 \to A_1A_2X}\left(\sqrt{s_{A_1A_2}}\right) &= \int \sigma_{\gamma\gamma \to X_1X_2}\left(\sqrt{s_{A_1A_2}}\right) N\left(\omega_1, \mathbf{b_1}\right) N\left(\omega_2, \mathbf{b_2}\right) S^2_{abs}\left(\mathbf{b}\right) \\ &\times \ 2\pi b \mathrm{d}b \, \mathrm{d}\bar{b}_x \, \mathrm{d}\bar{b}_y \, \frac{W_{\gamma\gamma}}{2} \mathrm{d}W_{\gamma\gamma} \, \mathrm{d}Y_{X_1X_2} \ . \end{aligned} \tag{B.0.5}$$

Here the equivalent photon approximation is formulated in the impact parameter space. Thus it is the most comfortable to use the form of the cross section which explicitly depends on impact parameter. Then nuclear cross section for the $\gamma\gamma$ mechanism can be rewritten

$$\begin{aligned} \frac{\mathrm{d}\sigma_{A_1A_2 \to A_1A_2X}\left(\sqrt{s_{A_1A_2}}\right)}{\mathrm{d}^2 b} &= \int\limits_{b_{min}}^{\infty} \sigma_{\gamma\gamma \to X_1X_2}\left(\omega_1, \omega_2\right) N\left(\omega_1, b_1\right) N\left(\omega_2, b_2\right) \\ &\times \ \mathrm{d}^2\mathbf{b_1} \, \mathrm{d}^2\mathbf{b_2} \, \mathrm{d}\omega_1 \, \mathrm{d}\omega_2 \end{aligned} \tag{B.0.6}$$

Above equation can be derived using a new kinematic variable $x = \omega / E_A$, where $E_A = \gamma A m_{proton} = \gamma M_A$ is the energy of the nucleus. This approach is described in Ref. [3].

Appendix C

Form factors - details

In Table 1.2 and Table 1.3 the root mean square radii of the charge distributions are presented, so using Eq. (1.4.83) and (1.4.79), one can compare the shape of the form factors, which will be calculated with the help of the two equations.

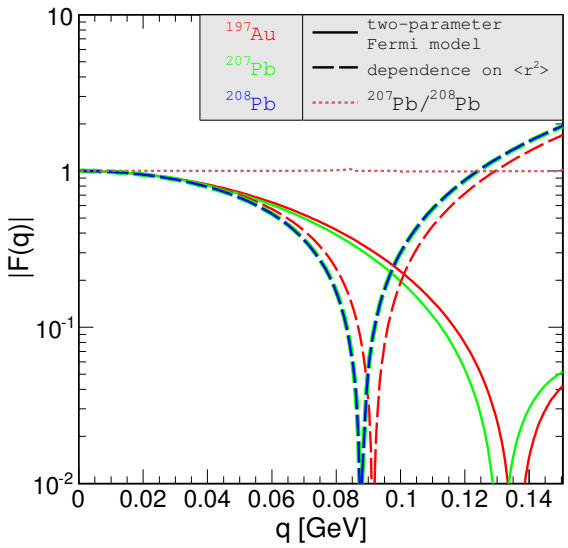

Figure C.1: A comparison of a shape of the form factor described by approximate (Eq. (1.4.79)) and exact (Eq. (1.4.83)) formula.

In Fig. C.1 we show the approximate and exact form factors for gold and lead nuclei. The solid lines correspond to two-parameter Fermi model (1.4.83) and the dashed lines represent form factor described with the help of the approximate formula which depends on the root mean square radius of the charge distribution

(1.4.79). The different nuclei are marked by red (^{197}Au), green (^{207}Pb) and blue (^{208}Pb) colors. The parameters for the charge density distribution are taken from Table 1.2 and 1.3, though Eq. (1.4.79). One can conclude that the expansion given by Eq. (1.4.79) is correct only in very limited range of momentum transfer. The consistency between the two methods appears only up to $q \approx 0.05$ GeV. One cannot believe in the result obtained by means of Eq. (1.4.79) for $q > 0.12$ GeV, because there the form factor is not physical ($F(q) > 1$). Secondly, the results described by Eq. (1.4.79) for two isotopes of lead are almost the same, which is shown by the dotted line. This line represents the ratio: $|F(q;^{207}\,\mathrm{Pb})/F(q;^{208}\,\mathrm{Pb})|$. This comparison shows that it is correct to use the same charge density distribution parameters for the ^{207}Pb and ^{208}Pb isotopes for the two-parameter Fermi model.

Appendix D

Some details for $\gamma\gamma \to X_1 X_2$ subprocesses

D.1 High-energy $\gamma\gamma \to \rho^0\rho^0$ cross section

The elementary cross section for high-energy part ($W_{\gamma\gamma} > 2$ GeV) of the $\gamma\gamma \to \rho^0\rho^0$ reaction is calculated with the help of the VDM-Regge approach. This model is described in section 2.2. This appendix focusses on the importance of the off-shell form factor which depends on virtuality of the meson involved. The second term of Eq. (2.2.8):

$$F\left(\hat{t}; q_{1/2}^2\right) = \exp\left(\frac{B\hat{t}}{4}\right) \exp\left(\frac{q_{1/2}^2 - m_\rho^2}{2\Lambda^2}\right)$$

is normalized at ρ meson mass shell.

Fig. D.1 shows the blow-up of Fig. 2.3 focussing on higher energies. The blue solid line is the correct description of the experimental data point from e^+e^- collisions. Fig. D.1 presents the elementary cross section i.e. for the case when we take into account only on-mass-shell vector meson (dashed green line). One can see the respective contribution from Reggeon (dashed-dotted lines) and Pomeron (dotted lines) exchanges. The green lines depict the cross section only for on mass shell form factor and the blue lines correspond to calculations which include form factors responsible for off-shell effects. We conclude that application of the correction for ρ^0 meson virtuality is necessary.

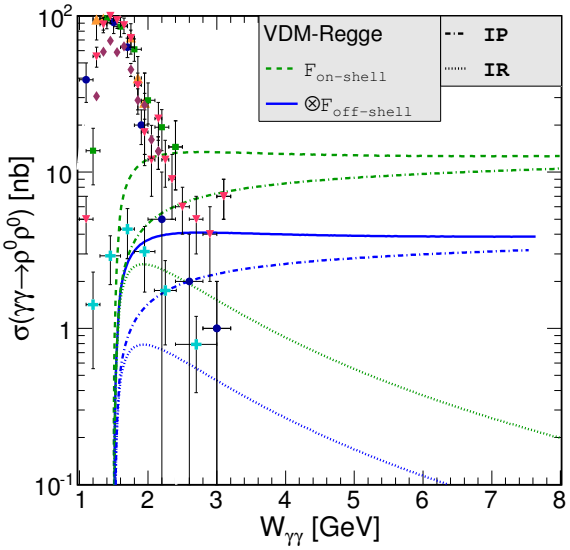

Figure D.1: The high-energy part of the $\gamma\gamma \to \rho^0\rho^0$ cross section obtained with the help of the VDM-Regge approach.

D.2 Vector meson coupling

The basic $V-\gamma$ coupling constants f_V can be measured in the annihilation processes. For example considering e^+e^- decay to hadronic final state F, the total cross section in the narrow-width approximation [223] takes the form

$$\sigma_{e^+e^-\to V\to F} = 4\pi\alpha_{em} \sum_V \left(\frac{e}{f_V}\right)^2 \delta\left(s - m_V^2\right) B_F^V \ , \tag{D.2.1}$$

where B_F^V is the branching ratio to the final state F. Summing over F and using experimental B_F^V, one can get the expression for the radiative decay width [224]

$$\Gamma_{V\to e^+e^-} = \left(\frac{m_V\alpha_{em}}{3}\right)\left(\frac{e}{f_V}\right)^2 = \frac{\alpha_{em}^2}{3}\frac{4\pi}{f_V^2} m_V \ . \tag{D.2.2}$$

Knowing the value of the leptonic decay partial width, one can calculate the exact value of the vector meson-photon coupling. We can say that in almost every paper a slightly different value of f_V is used. Different values of $\frac{f_\rho^2}{4\pi}$ for the $\rho^0 - \gamma$ coupling from the literature are collected in Table D.1.

In order to calculate the high-energy amplitude for the $\gamma\gamma \to \rho^0\rho^0$ reaction, we use the upper limit of the value calculated in Ref. [225]. The vector meson coupling is a dimensionless parameter.

Table D.1: Examples of the $\rho^0 - \gamma$ coupling constant from the literature.

$\frac{f_\rho^2}{4\pi}$	Ref.
2.25 ± 0.26	[225]
2.11 ± 0.29	[223]
2.06	[224]
2.02	[226]
1.96	[109]

D.3 Form factor for two-pion continuum

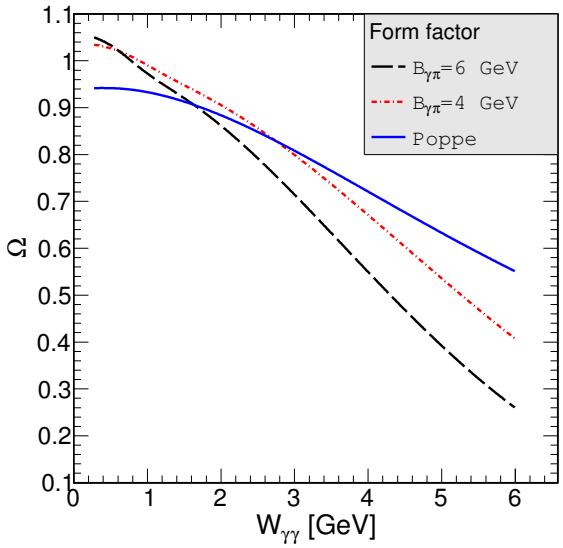

Figure D.2: A comparison of the form factors for the two-pion continuum.

Fig. D.2 shows a comparison of a few examples of form factors which include the finite-size pion corrections. Poppe proposed the following form of the form factor [108]

$$\Omega = \frac{1}{2}\left[\frac{1-\beta z}{1+\frac{s(1+\beta z)}{2m_\rho^2}} + \frac{1+\beta z}{1+\frac{s(1-\beta z)}{2m_\rho^2}}\right], \tag{D.3.3}$$

where $\beta = \sqrt{1-4m_\pi^2/s}$ is the velocity of the pion in the center-of-mass frame. The result obtained with the help of this formula is denoted by the blue solid line and it

is smaller than 1 in the whole range of the $\gamma\gamma$ energy. The dashed and dotted lines correspond to exponential form factor (Eq. (2.4.31))

$$\Omega\left(s,t,u\right)=\frac{F^{2}\left(t\right)+F^{2}\left(u\right)}{1+F^{2}\left(-s\right)}$$

This form with $B_{\gamma\pi}=4$ GeV^{-1} and $B_{\gamma\pi}=6$ GeV^{-1} is used in our further calculations.

In Eq. (2.4.31) the standard vertex function $F(x)$ is smaller than 1 and it provides the standard normalization $F(0)=1$. Additionally $F(t)\to 0$ when $t\to-\infty$. Eq. (2.4.31) has the feature that in the limit of large s

$$\begin{aligned}\Omega\left(s,t,u\right)&\xrightarrow{t\to0}F^{2}\left(t\right)\ ,\\ \Omega\left(s,t,u\right)&\xrightarrow{u\to0}F^{2}\left(u\right)\ .\end{aligned}\tag{D.3.4}$$

Then in the large s limit ($z=\cos\theta\approx0$) one can write $\Omega(s,t,u)\approx2F^{2}\left(\frac{-s}{2}\right)$, i.e.

$$\frac{\mathrm{d}\sigma}{\mathrm{d}z}\left(z=0,s\right)\propto F^{4}\left(\frac{-s}{2}\right)\ .\tag{D.3.5}$$

D.4 Some details for the $\gamma\gamma\to\pi\pi$ pQCD mechanisms

D.4.1 Form factors

Same extra form factor for the amplitude in the BL mechanism (2.4.43) was proposed in Ref. [104]

$$F_{reg}^{pQCD}\left(t,u\right)=\left[1-\exp\left(\frac{t-t_{m}}{\Lambda_{reg}^{2}}\right)\right]\left[1-\exp\left(\frac{u-u_{m}}{\Lambda_{reg}^{2}}\right)\right]\ ,\tag{D.4.1}$$

where $t_m=u_m$ are the maximal kinematically allowed values of t and u. Λ_{reg} is a cutoff parameter, which value is of course not completely well known. This form factor cuts the regions of the phase space where the Brodsky-Lepage formalism does not apply.

Fig. D.3 illustrates the role of the extra form factors described by Eq. (D.4.1) and Eq. (2.4.44): $F^{pQCD}(s)=1-\exp\left(\frac{-\left(s-4m_{\pi}^{2}\right)^{4}}{\Lambda_{pQCD}^{8}}\right)$. The main aim of the form factors

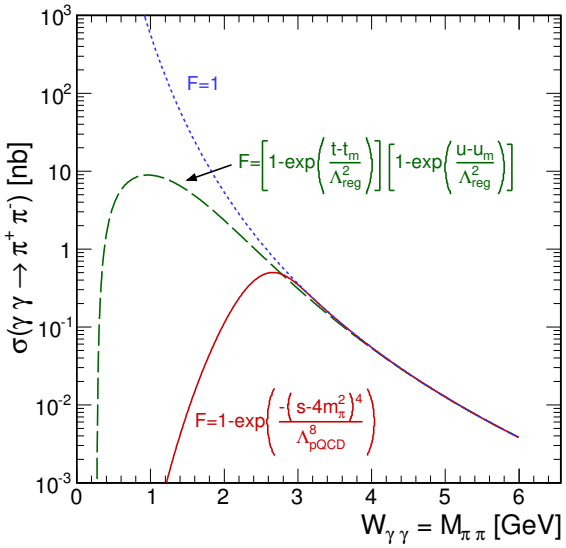

Figure D.3: Comparison of the cross section for $\gamma\gamma \to \pi^+\pi^-$ for different forms of the extra form factor in Brodsky-Lepage pQCD mechanism.

is the exclusion of the region of small Mandelstam t and u variables, i.e. the region which is clearly non-perturbative. The three lines presented in the figure are described in the figure caption. It is clear from the figure, that one cannot use the pQCD BL prediction without any form factor, because at low energy limit, this tends to infinity. The red line shows the BL pQCD cross section which we use in our further calculation. The green line corresponds to the form factor used in Ref. [8] ($\Lambda_{reg} = 1$ GeV).

D.4.2 Leading-order hard-scattering amplitude $T_H^{\lambda_1\lambda_2}$

The leading-log expression for analytic effective coupling in the QCD case takes the form

$$\alpha_s\left(Q^2\right) = \frac{4\pi}{\beta_0}\frac{1}{\ln\frac{Q^2}{\Lambda_\alpha^2}}\,, \tag{D.4.2}$$

where

$$\beta_0 = \frac{11}{3}C_A - \frac{2}{3}N_f \tag{D.4.3}$$

with $C_A = 3$ and the number of active quarks flavours $N_f = 3$. In our calculations the running coupling constant proposed in Ref. [227] is used. This includes a spectral

function in the one-loop approximation

$$\alpha_s\left(Q^2\right) = \frac{4\pi}{\beta_0}\left(\frac{1}{\ln\frac{Q^2}{\Lambda_\alpha^2}} + \frac{\Lambda_\alpha^2}{\Lambda_\alpha^2 - Q^2}\right) . \tag{D.4.4}$$

The Λ_α is the QCD scale parameter. In our numerical applications this equals to 200 MeV.

Ji and Amiri [103] presented the exact form of the LO hard-scattering amplitude including the running of α_s. The helicity-dependent amplitudes for the $\pi^+\pi^-$ production read:

$$\begin{aligned}
T_H^{++} \text{ or } T_H^{--} &= \frac{16\pi}{3s}\frac{32\pi\alpha_{em}}{x\left(1-x\right)y\left(1-y\right)}\frac{a}{1-z^2} \\
&\times \left[e_c^2\alpha_s\left(X_1\right) - e_c e_b\left(\alpha_s\left(X_2\right)+\alpha_s\left(X_3\right)\right) + e_b^2\alpha_s\left(X_4\right)\right] , \qquad \text{(D.4.5)} \\
T_H^{+-} \text{ or } T_H^{-+} &= \frac{16\pi}{3s}\frac{32\pi\alpha_{em}}{x\left(1-x\right)y\left(1-y\right)} \\
&\times \left[\frac{1-a}{1-z^2}\left\{e_c^2\alpha_s\left(X_1\right) - e_c e_b\left(\alpha_s\left(X_2\right)+\alpha_s\left(X_3\right)\right) + e_b^2\alpha_s\left(X_4\right)\right\}\right. \\
&+ e_c e_b\frac{x\left(1-x\right)+y\left(1-y\right)}{2}\left\{\frac{\alpha_s\left(X_2\right)}{a-bz}+\frac{\alpha_s\left(X_3\right)}{a+bz}\right\} \\
&+ \left.\left\{e_c^2\alpha_s\left(X_1\right) - e_b^2\alpha_s\left(X_4\right)\right\}\frac{x-y}{2}\right] , \qquad \text{(D.4.6)}
\end{aligned}$$

where arguments of α_s are denoted by

$$\begin{aligned}
X_1 &= \left|y\left(1-x\right)s\right| , \\
X_2 &= \left|\left(-a+bz\right)\frac{s}{2}\right| , \\
X_3 &= \left|\left(-a-bz\right)\frac{s}{2}\right| , \qquad \text{(D.4.7)} \\
X_4 &= \left|x\left(1-y\right)s\right| .
\end{aligned}$$

The auxiliary quantities:

$$\begin{aligned}
a &= (1-x)(1-y)+xy , \\
b &= (1-x)(1-y)-xy . \qquad \text{(D.4.8)}
\end{aligned}$$

The helicity-dependent amplitudes for the $\pi^0\pi^0$ production take the forms:

$$\begin{aligned}
T_H^{++} \text{ or } T_H^{--} &= \frac{16\pi}{3s}\frac{32\pi\alpha_{em}}{x\,(1-x)\,y\,(1-y)}\frac{a}{1-z^2}\frac{1}{\sqrt{2}} \\
&\times \left\{e_c^2\alpha_s\,(X_1) + e_c^2\alpha_s\,(X_4) - e_c^2\left[\alpha_s\,(X_2) + \alpha_s\,(X_3)\right]\right. \\
&- \left. e_b^2\alpha_s\,(X_1) - e_b^2\alpha_s\,(X_4) + e_b^2\left[\alpha_s\,(X_2) + \alpha_s\,(X_3)\right]\right\}\,, \qquad \text{(D.4.9)} \\
T_H^{+-} \text{ or } T_H^{-+} &= \frac{16\pi}{3s}\frac{32\pi\alpha_{em}}{x\,(1-x)\,y\,(1-y)}\frac{1}{\sqrt{2}} \\
&\times \left[\frac{1-a}{1-z^2}\left\{e_c^2\alpha_s\,(X_1) - e_c^2\left[\alpha_s\,(X_2) + \alpha_s\,(X_3)\right] + e_c^2\alpha_s\,(X_4)\right\}\right. \\
&+ e_c^2\frac{x\,(1-x) + y\,(1-y)}{2}\left[\frac{\alpha_s\,(X_2)}{a-bz} + \frac{\alpha_s\,(X_3)}{a+bz}\right] \\
&+ \left(e_c^2\alpha_s\,(X_1) - e_c^2\alpha_s\,(X_4)\right)\frac{x-y}{2} \\
&- \frac{1-a}{1-z^2}\left\{e_b^2\alpha_s\left(|X_1) - e_b^2\left[\alpha_s\,(X_2|) + \alpha_s\,(X_3)\right] + e_b^2\alpha_s\,(X_4)\right\}\right. \\
&- e_b^2\frac{x\,(1-x) + y\,(1-y)}{2}\left[\frac{\alpha_s\,(X_2)}{a-bz} + \frac{\alpha_s\,(X_3)}{a+bz}\right] \\
&- \left.\left(e_b^2\alpha_s\,(X_1) - e_b^2\alpha_s\,(X_4)\right)\frac{x-y}{2}\right]
\end{aligned}$$

where arguments of α_s are given in Eq. (D.4.8).

Neglecting the difference in the α_s argument, one can obtain simpler results presented by Brodsky and Lepage [102] and Nižić [117].

Appendix E

A semi-classical model for $\gamma A \to \rho^0 A$ reaction

A certain version of the classical mechanics (in our opinion wrongly called Glauber) model with application to $\gamma A \to \rho^0 A$ is described e.g. in Refs. [152,228–230]. There the authors present a short history, the essence of the model and a comparison of the model results with experimental results. Below I present a set of equations for description of the $\gamma A \to \rho^0 A$ reaction. In the multiple scattering model the $\gamma A \to \rho^0 A$ cross section needs the $\gamma p \to \rho^0 p$ cross section as input. The $\gamma p \to \rho^0 p$ data from HERA [231] can be described by the Regge inspired parametrization

$$\frac{\mathrm{d}\sigma_{\gamma p \to \rho^0 p}\,(t=0)}{\mathrm{d}t} = B_{\rho^0}\left(XW^{\epsilon} + YW^{-\eta}\right) \ , \tag{E.0.1}$$

where W is respective center of mass energy, $B_{\rho^0} = 11$ GeV^{-2}, $X = 5$ μb, $\epsilon = 0.22$, $Y = 26$ μb, $\eta = 1.23$. These parameters are taken from Ref. [152] where the parameters for four kinds of mesons (ρ^0, ω, Φ, J/Ψ) are given. The first term of Eq. (E.0.1) describes the Pomeron exchange and the second term corresponds to the Reggeon exchange. In the Regge theory the slope parameter is energy-dependent and is parametrized as:

$$B^i_{\rho^0} = B^i_0 + 2\alpha'_i \ln\left(\frac{W^2_{\gamma p}}{s_0}\right) \ , \tag{E.0.2}$$

where $B_0^{\mathbb{P}} = 5.5$ GeV^{-2}, $\alpha'_{\mathbb{P}} = 0.25$, $B_0^{\mathbb{R}} = 4.0$ GeV^{-2}, $\alpha'_{\mathbb{R}} = 0.93$, $s_0 = 1$ GeV^2. The values of the Pomeron $\mathbb{P}$ and Reggeon $\mathbb{R}$ slope parameters are taken from

Ref. [232]. Having the differential distribution of the $\gamma p \to \rho^0 p$ cross section (E.0.1) one can calculate the differential cross section for the $\rho^0 p \to \rho^0 p$ reaction

$$\frac{\mathrm{d}\sigma_{\rho^0 p\to\rho^0 p}\left(t=0\right)}{\mathrm{d}t} = \frac{f_{\rho^0}^2}{4\pi\alpha_{em}} \frac{\mathrm{d}\sigma_{\gamma p\to\rho^0 p}\left(t=0\right)}{\mathrm{d}t} \tag{E.0.3}$$

using standard VDM relation. The total cross section can be calculated as

$$\sigma_{tot}^2\left(\rho^0 p\right) = 16\pi \frac{\mathrm{d}\sigma_{\rho^0 p\to\rho^0 p}\left(t=0\right)}{\mathrm{d}t} \ . \tag{E.0.4}$$

Having the nuclear thickness function

$$T_A\left(\mathbf{r}\right) = \int \mathrm{d}z \rho_A\left(\sqrt{\left|\mathbf{r}\right|^2 + z^2}\right) \ , \tag{E.0.5}$$

where ρ_A is the charge distribution in nucleus A defined in Eq. (1.4.81) and writing the overlap function at a given impact parameter

$$T_{AA}\left(\left|\mathbf{b}\right|\right) = \int \mathrm{d}^2\mathbf{r}\, T_A\left(\mathbf{r}\right) T_A\left(\mathbf{r}-\mathbf{b}\right) \tag{E.0.6}$$

one writes the probability of having no hadronic interactions in the nuclear collision:

$$P\left(\left|\mathbf{b}\right|\right) = \exp\left(-T_{AA}\left(\left|\mathbf{b}\right|\right)\sigma_{NN}\right) \ . \tag{E.0.7}$$

Above $\mathbf{r}$ and $\mathbf{b}$ are vectors perpendicular to the direction of motion of ρ^0. The $T_{AA}\left(\left|\mathbf{b}\right|\right)$ is so-called overlap function. The cross section for the $\gamma A \to \rho^0 A$ (see e.g. [152]) takes the form

$$\sigma_{tot}\left(\rho^0 A\right) = \int \mathrm{d}^2\mathbf{r}\ \left(1 - \exp\left(-\sigma_{tot}\left(\rho^0 p\right) T_A\left(\mathbf{r}\right)\right)\right) \ . \tag{E.0.8}$$

The differential cross section can be written as

$$\frac{d\sigma_{\gamma A\to\rho^0 A}\left(t=0\right)}{dt} = \frac{\alpha_{em}\sigma_{tot}^2\left(\rho^0 A\right)}{4f_{\rho^0}^2} \tag{E.0.9}$$

and now the total cross section for the $\gamma A \to \rho^0 A$ reaction takes the form

$$\sigma_{\gamma A\to\rho^0 A} = \frac{d\sigma_{\gamma A\to\rho^0 A}\left(t=0\right)}{dt} \int\limits_{-\infty}^{t_{max}} \mathrm{d}t \left|F_A\left(t\right)\right|^2 \ , \tag{E.0.10}$$

where $F_A(t)$ is nucleus QCD-matter form factor. This form factor is approximated by charge form factor of the nucleus.

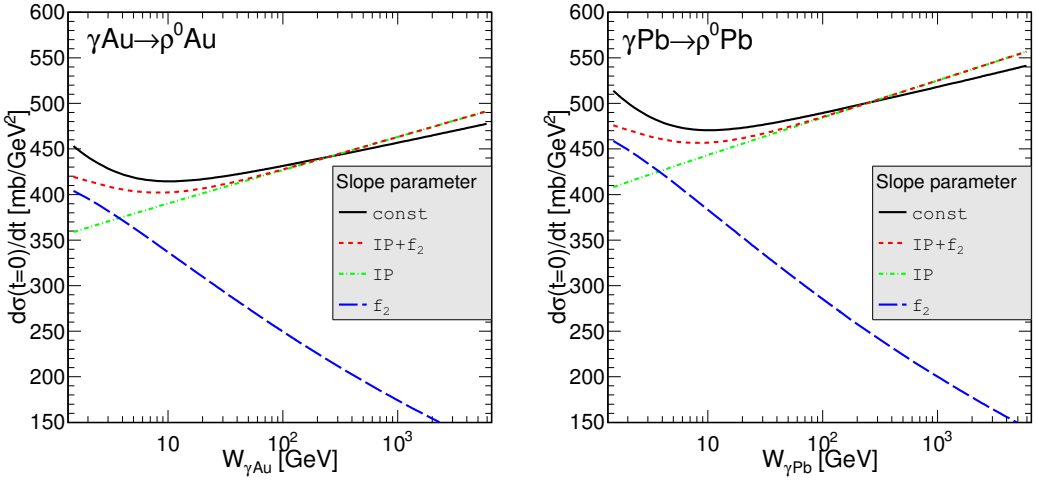

Figure E.1: The differential cross section for coherent ρ^0 photoproduction.

Fig. E.1 presents $\mathrm{d}\sigma/\mathrm{d}t_{|t=0}$ for coherent ρ^0 photoproduction on Au (left panel) and Pb (right panel) nucleus. The results are obtained with the help of the model discussed above. There are four lines in the figure. The first one (black line) corresponds to the slope parameter $B_{\rho^0} = 11$ GeV^{-2} which is taken from Ref. [152]. The other lines are calculated using Eq. (E.0.2) and parameters given below this equation. One can see separate contributions from Pomeron (green lines)

$$\frac{\mathrm{d}\sigma_{\gamma p\to\rho^0 p}\,(t=0)}{\mathrm{d}t} = B^{\mathbb{P}}_{\rho^0} X W^{\epsilon}\,, \tag{E.0.11}$$

f_2 Reggeon (blue lines)

$$\frac{\mathrm{d}\sigma_{\gamma p\to\rho^0 p}\,(t=0)}{\mathrm{d}t} = B^{\mathbb{R}}_{\rho^0} Y W^{-\eta}\,, \tag{E.0.12}$$

and the sum of these two contributions (red lines)

$$\frac{\mathrm{d}\sigma_{\gamma p\to\rho^0 p}\,(t=0)}{\mathrm{d}t} = B^{\mathbb{P}}_{\rho^0} X W^{\epsilon} + B^{\mathbb{R}}_{\rho^0} Y W^{-\eta}\,. \tag{E.0.13}$$

The shape of the distribution in $W_{\gamma A}$ for the approach with the Pomeron and Reggeon two-component-model (see Eq. (E.0.13)) is very similar as for the one with the slope parameter independent of $W_{\gamma p}$ (see Eq. (E.0.1)). At higher energy the largest contribution to Eq. (E.0.13) comes, of course, from the Pomeron exchange.

In our analysis we use the classical mechanics quasi-Glauber formula for calculating $\sigma_{tot}(\rho^0 A)$. As discussed in detail in Ref. [155] Eq. (E.0.8) implies that

in the black disk limit the total cross section becomes equal πR_A^2, which is a prediction of the classical mechanics. In contrast, a quantum mechanical approach implies that in that limit $\sigma_{tot}(\rho^0 A) = 2\pi R_A^2$. The quantum mechanics expression is given by the Glauber model [155, 233, 234]:

$$\sigma_{tot}^{qm}\left(\rho^0 A\right) = 2\int \mathrm{d}^2\mathbf{r}\left(1 - \exp\left(-\frac{1}{2}\sigma_{tot}\left(\rho^0 p\right) T_A\left(\mathbf{r}\right)\right)\right) . \tag{E.0.14}$$

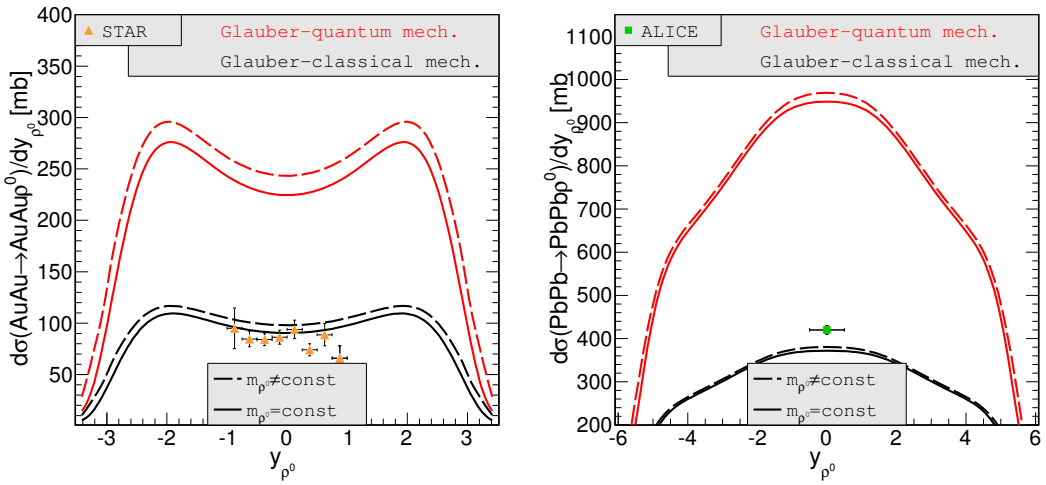

Figure E.2: Rapidity distribution of coherent ρ^0 production using the quasi-Glauber approach (black) and the quantum mechanical Glauber approach (red).

Now we proceed to the AA→AAρ^0 reaction. The authors of Refs. [154, 155] suggest that the classical mechanics formula leads to substantially smaller value of the total cross section than the quantum mechanical Glauber expression (a factor of two smaller for heavy nuclei). One can observe in Fig. E.2 that the difference between rapidity distribution of ρ^0 meson calculated in the classical (blue lines) and quantum Glauber approach (red lines) is really huge (a factor ≈ 2.5). The left panel corresponds to the results at RHIC energy $\sqrt{s_{NN}} = 200$ GeV and the right panel is dedicated for LHC energy $\sqrt{s_{NN}} = 2.76$ TeV. Both panels depict the situation when our results are calculated for sharp ρ^0 mass (solid lines) and including the smearing of ρ^0 mass (dashed lines). As is shown in Fig. E.2, the classical Glauber model surprisingly well describes the STAR data for $AA \to AA\rho^0$ whereas the quantal Glauber model substantially overestimates the experimental data of the STAR and ALICE Collaboration. The overestimation of the experimental data by the Glauber

model is not clear to us in the moment. The difference between the theoretical classical mechanics model and experimental results for the ALICE data is only about $10 - 15\%$. Therefore in this dissertation we shall use the classical mechanics model to estimate the double scattering effects (see section 3.3).

Appendix F

Momentum-space approach

The most of the results for nuclear production of fermion-antifermion pairs which are presented in this dissertation is calculated in the Equivalent Photon Approximation. Here I wish to concentrate on details of the calculations in the momentum space. However, this method has some shortcomings. Here we cannot easily exclude situations when the two ions collide with small impact parameter.

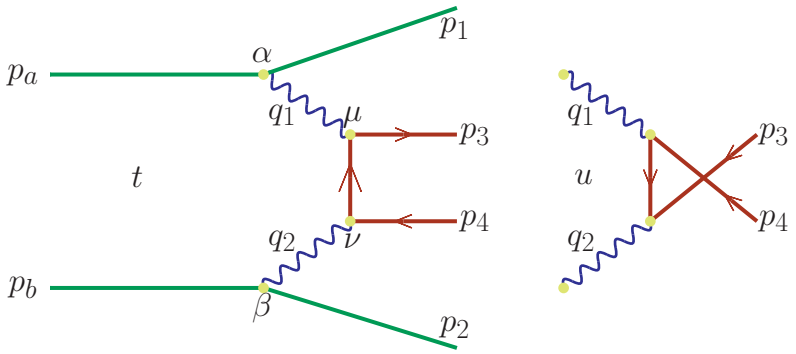

Figure F.1: t-channel (left panel) and u-channel (right panel) amplitudes of the $AA \to AAl^+l^-$ process in the momentum space.

In Fig. F.1 one can see Feynman diagrams for a genuine $2 \to 4$ reaction with four-momenta $p_a + p_b \to p_1 + p_2 + p_3 + p_4$. In the momentum space approach the cross section for the production of a pair of particles can be written as:

$$\begin{aligned} \sigma &= \int \frac{1}{2s} \overline{|\mathcal{M}|^2} \, (2\pi)^4 \, \delta^4 \left(p_a + p_b - p_1 - p_2 - p_3 - p_4\right) \\ &\times \frac{d^3p_1}{(2\pi)^3 \, 2E_1} \frac{d^3p_2}{(2\pi)^3 \, 2E_2} \frac{d^3p_3}{(2\pi)^3 \, 2E_3} \frac{d^3p_4}{(2\pi)^3 \, 2E_4} \, . \end{aligned} \tag{F.0.1}$$

Using a transformation

$$\frac{d^3p_i}{E_i} = dy_i\, d^2p_{i\perp} = dy_i p_{i\perp} dp_{i\perp} d\phi_i \tag{F.0.2}$$

Eq. (F.0.1) can be rewritten as:

$$\begin{aligned}\sigma &= \int \frac{1}{2s}\overline{|\mathcal{M}|^2}\delta^4\left(p_a + p_b - p_1 - p_2 - p_3 - p_4\right)\frac{1}{(2\pi)^8}\frac{1}{2^4} \\ &\times \left(dy_1 p_{1\perp} dp_{1\perp} d\phi_1\right)\left(dy_2 p_{2\perp} dp_{2\perp} d\phi_2\right)\left(dy_3 d^2p_{3\perp}\right)\left(dy_4 d^2p_{4\perp}\right) .\end{aligned} \tag{F.0.3}$$

In the above formula $p_{i\perp}$ are transverse momenta of outgoing nuclei and considered charged particles in the final state, ϕ_1, ϕ_2 are azimuthal angles of the outgoing nuclei. Additionally, we introduce a new auxiliary quantity

$$\mathbf{p}_m = \mathbf{p}_{3\perp} - \mathbf{p}_{4\perp} \tag{F.0.4}$$

and benefiting from 4-dimensional Dirac delta function properties, Eq. (F.0.3) can be written as:

$$\begin{aligned}\sigma &= \int \frac{1}{2s}\overline{|\mathcal{M}|^2}\delta\left(E_a + E_b - E_1 - E_2 - E_3 - E_4\right)\delta^3\left(p_{1z} + p_{2z} + p_{3z} + p_{4z}\right)\frac{1}{(2\pi)^8}\frac{1}{2^4} \\ &\times \left(dy_1 p_{1\perp} dp_{1\perp} d\phi_1\right)\left(dy_2 p_{2\perp} dp_{2\perp} d\phi_2\right) dy_3 dy_4 d^2p_m .\end{aligned} \tag{F.0.5}$$

The energy-momentum conservation gives the following system of equations that has to be solved for discrete solutions

$$\begin{cases} \sqrt{s} - E_3 - E_4 &= \sqrt{m_{1\perp}^2 + p_{1z}^2} + \sqrt{m_{2\perp}^2 + p_{2z}^2} , \\ -p_{3z} - p_{4z} &= p_{1z} + p_{2z} , \end{cases} \tag{F.0.6}$$

where $m_{1\perp}$, $m_{2\perp}$ are the so-called transverse masses of outgoing nuclei which are defined as:

$$m_{i\perp}^2 = p_{i\perp}^2 + m_i^2 . \tag{F.0.7}$$

We wish to make the transformation from $(y_1,\, y_2)$ to $(p_{1z},\, p_{2z})$. The transformation Jacobian takes the form:

$$\mathcal{J}_k = \left| \frac{p_{1z}(k)}{\sqrt{m_{1\perp}^2 + p_{1z}^2(k)}} - \frac{p_{2z}(k)}{\sqrt{m_{2\perp}^2 + p_{2z}^2(k)}} \right| , \tag{F.0.8}$$

where k numerates discrete solutions of Eq. (F.0.6). Thus the cross section for the $2 \to 4$ reaction reads:

$$\begin{aligned}\sigma &= \int \sum_k \mathcal{J}_k^{-1}\left(p_{1t},\, \phi_1,\, p_{2t},\, \phi_2,\, y_3,\, y_4,\, p_m,\, \phi_m\right)\frac{1}{2\sqrt{s\left(s - 4m^2\right)}}\overline{|\mathcal{M}|^2}\frac{1}{(2\pi)^8}\frac{1}{2^4} \\ &\times \left(p_{1\perp} dp_{1\perp} d\phi_1\right)\left(p_{2\perp} dp_{2\perp} d\phi_2\right)\frac{1}{4} dy_3 dy_4 d^2p_m .\end{aligned} \tag{F.0.9}$$

For photon-exchanges, considered here, it is convenient to change the variables $p_{1\perp} \to \xi_1 = \log_{10}(p_{1\perp})$, $p_{2\perp} \to \xi_2 = \log_{10}(p_{2\perp})$. The lepton helicity-dependent amplitudes of the process shown in Fig. F.1 can be written as:

$$\begin{aligned}\mathcal{M}_{\lambda_3,\lambda_4}(t\text{-channel}) &= e\,F_{ch}(q_1)\,(p_a+p_1)^{\alpha}\,\frac{-i\,g_{\alpha\mu}}{q_1^2+i\varepsilon}\bar{u}(p_3,\,\lambda_3)\,i\,\gamma^{\mu}\frac{i\,[(\not{p}_3-\not{q}_1)+m_{\mu}]}{(q_1-p_3)^2-m_{\mu}^2} \\ &\times\; i\,\gamma^{\nu}\,v(p_4,\,\lambda_4)\,\frac{-i\,g_{\nu\beta}}{q_2^2+i\varepsilon}\,(p_b+p_2)^{\beta}\,e\,F_{ch}(q_2) \qquad \text{(F.0.10)}\end{aligned}$$

and

$$\begin{aligned}\mathcal{M}_{\lambda_3,\lambda_4}(u\text{-channel}) &= e\,F_{ch}(q_1)\,(p_a+p_1)^{\alpha}\,\frac{-i\,g_{\alpha\mu}}{q_1^2+i\varepsilon}\bar{u}(p_3,\,\lambda_3)\,i\,\gamma^{\nu}\frac{i\,[(\not{p}_3-\not{q}_2)+m_{\mu}]}{(q_2-p_3)^2-m_{\mu}^2} \\ &\times\; i\,\gamma^{\mu}\,v(p_4,\,\lambda_4)\,\frac{-i\,g_{\nu\beta}}{q_2^2+i\varepsilon}\,(p_b+p_2)^{\beta}\,e\,F_{ch}(q_2)\;. \qquad \text{(F.0.11)}\end{aligned}$$

These amplitudes are calculated numerically. Finally, to calculate the total cross section one has to calculate 8-dimensional integral inserting

$$\mathcal{M}_{\lambda_3,\lambda_4} = \mathcal{M}_{\lambda_3,\lambda_4}(t\text{-channel}) + \mathcal{M}_{\lambda_3,\lambda_4}(u\text{-channel}) \qquad \text{(F.0.12)}$$

into Eq. (F.0.9).

List of Figures

List of Tables

Bibliography

[1] M. Kłusek, W. Schäfer, and A. Szczurek, "Exclusive production of $\rho^0\rho^0$ pairs in $\gamma\gamma$ collisions at RHIC," *Phys.Lett.* **B674** (2009) 92–97, arXiv:0902.1689 [hep-ph].

[2] M. Kłusek, A. Szczurek, and W. Schäfer, "Realistic cross sections for exclusive $\rho^0\rho^0$ production in ultrarelativistic heavy-ion collisions," *PoS* **EPS-HEP2009** (2009) 458.

[3] M. Kłusek-Gawenda and A. Szczurek, "Exclusive muon-pair productions in ultrarelativistic heavy-ion collisions – realistic nucleus charge form factor and differential distributions," *Phys.Rev.* **C82** (2010) 014904, arXiv:1004.5521 [nucl-th].

[4] M. Kłusek-Gawenda, A. Szczurek, M. Machado, and V. Serbo, "Double – photon exclusive processes with heavy quark – heavy antiquark pairs in high-energy Pb-Pb collisions at LHC," *Phys.Rev.* **C83** (2011) 024903, arXiv:1011.1191 [nucl-th].

[5] M. Kłusek-Gawenda and A. Szczurek, "Exclusive production of pion pairs with large invariant mass in nucleus-nucleus collisions," arXiv:1110.6378 [nucl-th].

[6] A. Szczurek and M. Kłusek-Gawenda, "Photon-photon production of lepton, quark and meson pairs in peripheral heavy ion collisions," arXiv:1110.4741 [nucl-th].

[7] M. Kłusek-Gawenda and A. Szczurek, "Exclusive production of $\rho^0\rho^0$ pairs in ultrarelativistic heavy ion collisions," *Int.J.Mod.Phys.* **A26** (2011) 741–743, arXiv:1008.3802 [nucl-th].

[8] M. Kłusek-Gawenda and A. Szczurek, "Exclusive production of large invariant mass pion pairs in ultraperipheral ultrarelativistic heavy ion collisions," *Phys.Lett.* **B700** (2011) 322–330, arXiv:1104.0571 [nucl-th].

[9] M. Kłusek-Gawenda and A. Szczurek, "Exclusive production of $\pi^+\pi^-$ and $\pi^0\pi^0$ pairs in photon-photon and in ultrarelativistic heavy ion collisions," *EPJ Web Conf.* **37** (2012) 06006, arXiv:1208.4623 [hep-ph].

[10] S. Baranov, A. Cisek, M. Kłusek-Gawenda, W. Schäfer, and A. Szczurek, "The $\gamma\gamma \to J/\psi J/\psi$ reaction and the $J/\psi J/\psi$ pair production in exclusive ultraperipheral ultrarelativistic heavy ion collisions," *Eur.Phys.J.* **C73** (2013) 2335, arXiv:1208.5917 [hep-ph].

[11] M. Kłusek-Gawenda and A. Szczurek, "$\pi^+\pi^-$ and $\pi^0\pi^0$ pair production in photon-photon and in ultraperipheral ultrarelativistic heavy ion collisions," *Phys.Rev.* **C87** no. 5, (2013) 054908, arXiv:1302.4204 [nucl-th].

[12] M. Kusek-Gawenda and A. Szczurek, "Exclusive production of two and four pions in ultraperipheral, ultrarelativistic collisions," *PoS* **EPS-HEP2013** (2013) 020.

[13] M. Kłusek-Gawenda, E. Kozik, A. Rybicki, I. Sputowska, and A. Szczurek, "Strong and Electromagnetic Forces in Heavy Ion Collisions," *Acta Phys.Polon.Supp.* **6** (2013) 451–456, arXiv:1303.6423 [nucl-ex].

[14] A. Rybicki, A. Szczurek, M. Kłusek-Gawenda, and I. Sputowska, "Studying the Interplay of Strong and Electromagnetic Forces in Heavy Ion Collisions with NICA," arXiv:1301.5210 [nucl-th].

[15] M. Kłusek-Gawenda, M. Ciemała, W. Schäfer, and A. Szczurek, "Electromagnetic excitation of nuclei and neutron evaporation in ultrarelativistic ultraperipheral heavy ion collisions," *Phys.Rev.* **C89** (2014) 054907.

[16] M. Kłusek-Gawenda and A. Szczurek, "Double-scattering mechanism in the exclusive $AA \to AA\rho^0\rho^0$ reaction in ultrarelativistic collisions," *Phys.Rev.* **C89** (2014) 024912.

[17] A. Szczurek and M. Kłusek-Gawenda, "Ultraperipheral production of very small number of particles in ultrarelativistic heavy ion collisions," *EPJ Web Conf.* **66** (2014) 04028.

[18] M. Kłusek-Gawenda and A. Szczurek, "Exclusive electromagnetic production of pion pairs in lead-lead collisions at LHC," *EPJ Web Conf.* **66** (2014) 04014.

[19] E. Williams, "Applications of the Method of Impact Parameter in Collisions," *Proc. R. Soc. Lond.* **A** (1933) 163–186.

[20] E. Fermi, "On the Theory of the impact between atoms and electrically charged particles," *Z.Phys.* **29** (1924) 315–327.

[21] C. von Weizsacker, "Radiation emitted in collisions of very fast electrons," *Z.Phys.* **88** (1934) 612–625.

[22] E. Williams, "Nature of the high-energy particles of penetrating radiation and status of ionization and radiation formulae," *Phys.Rev.* **45** (1934) 729–730.

[23] V. Budnev, I. Ginzburg, G. Meledin, and V. Serbo, "The Two photon particle production mechanism. Physical problems. Applications. Equivalent photon approximation," *Phys.Rept.* **15** (1975) 181–281.

[24] C. A. Bertulani and G. Baur, "Electromagnetic Processes in Relativistic Heavy Ion Collisions," *Phys.Rept.* **163** (1988) 299.

[25] G. Baur, K. Hencken, D. Trautmann, S. Sadovsky, and Y. Kharlov, "Coherent $\gamma\gamma$ and $\gamma - A$ interactions in very peripheral collisions at relativistic ion colliders," *Phys.Rept.* **364** (2002) 359–450, `arXiv:hep-ph/0112211 [hep-ph]`.

[26] A. Baltz, G. Baur, D. d'Enterria, L. Frankfurt, F. Gelis, *et al.*, "The Physics of Ultraperipheral Collisions at the LHC," *Phys.Rept.* **458** (2008) 1–171, `arXiv:0706.3356 [nucl-ex]`.

[27] J. D. Jackson, *Classical Electrodynamics*. John Wiley & Sons, Inc., New York, London, 1962.

[28] J. A. Heras and G. Baez, "The covariant formulation of Maxwell's equations expressed in a form independent of specific units," *Eur. J. Phys.* **30** (2009) 23–33.

[29] S. C. Ahern, "An Electroweak Weizsacker-Williams method," `arXiv:hep-ph/0211133 [hep-ph]`.

[30] S. C. Ahern and J. W. Norbury, "Semiclassical electroweak Weizsacker-Williams method," *Phys.Rev.* **D68** (2003) 113001.

[31] G. Baur and L. Ferreira, "Charge form-factor effects in gamma gamma production of nonstrongly interacting particles in relativistic heavy ion collisions," *Phys.Lett.* **B254** (1991) 30–34.

[32] F. Krauss, M. Greiner, and G. Soff, "Photon and gluon induced processes in relativistic heavy ion collisions," *Prog.Part.Nucl.Phys.* **39** (1997) 503–564.

[33] M. Abramowitz and I. Stegun, *Handbook of Mathematical Functions*. Dover, New York, fifth ed., 1964.

[34] M. Vidovic, M. Greiner, C. Best, and G. Soff, "Impact parameter dependence of the electromagnetic particle production in ultrarelativistic heavy ion collisions," *Phys.Rev.* **C47** (1993) 2308–2319.

[35] R. Hagedorn, *Relativistic Kinematics, High Energy Physics*. W. A. Benjamin, Reading, MA, 1963.

[36] B. Povh, K. Rith, C. Scholz, and F. Zetsche, *Particles and Nuclei: An Introduction to the Physical Concepts*. Springer, Verlag Berlin Heidelberg, 6th ed., 2008.

[37] J. D. Bjorken and S. D. Drell, *Relatywistyczna teoria kwantów*. Państwowe Wydawnictwo Naukowe (Warszawa), 1985.

[38] N. F. Mott, "The Scattering of Fast Electrons by Atomic Nuclei," *Proc. Roy. Soc.* **A124** (1929) 425442.

[39] N. F. Mott, "The Polarization of Electrons by Double Scattering," *Proc. Roy. Soc.* **A135** (1932) 429458.

[40] R. C. Barrett and D. F. Jackson, *Nuclear sizes and structure*. Clarendon Press (Oxford), 1977.

[41] O. Zimmer, "Introduction to nuclear and particle physics." https://www.e12.ph.tum.de/stud/vorlesungen/fabbietti/WS2007/script.pdf, 2005.

[42] H. De Vries, C. De Jager, and C. De Vries, "Nuclear charge and magnetization density distribution parameters from elastic electron scattering," *Atom.Data Nucl.Data Tabl.* **36** (1987) 495–536.

[43] L. C. Maximon and R. A. Schrack, "The Form Factor of the Fermi Model Spatial Distribution," *Journal of Research of the National Bureau of Standards* **70B** (1966) 85–94.

[44] B. Hahn, D. Ravenhall, and R. Hofstadter, "High-Energy Electron Scattering and the Charge Distributions of Selected Nuclei," *Phys.Rev.* **101** (1956) 1131–1142.

[45] J. Bellicard and P. Barreau, "Mesures de diffusion lastique d'lectrons de 28 MeV par les noyaux lourds," *Nucl.Phys.* **17** (1960) 141–152.

[46] C. de Jager. PhD thesis, University of Amsterdam, 1973. unpublished.

[47] A. Bernstein, ed., Massachusetts Institute of Technology. Friar,J.L. and Heisenberg,J. and Negele,J.W., Proceedings of the June Workshop in Intermediate Energy Electromagnetic Interaction, 1977. p. 152.

[48] H. Euteneuer, J. Friedrich, and N. Vogler, "The Charge Distribution Differences of Bi-209, Pb-208, Pb-207, Pb-206, Pb-204 and Tl-205, Tl-203 Investigated by Elastic electron Scattering and Muonic x-Ray Data," *Nucl.Phys.* **A298** (1978) 452–476.

[49] K. Hencken, D. Trautmann, and G. Baur, "Electromagnetic electron - positron pair production in heavy ion collisions with impact parameter zero," *Phys.Rev.* **A49** (1994) 1584–1596.

[50] B. Leissner, "Muon pair production in electron proton collisions,". DESY-THESIS-2002-049.

[51] G. Baur and C. Bertulani, "Electromagnetic Production of Heavy Leptons in Relativistic Heavy Ion Collisions," *Phys.Rev.* **C35** (1987) 836–837.

[52] K. Hencken, D. Trautmann, and G. Baur, "Calculation of higher order effects in electron positron pair production in relativistic heavy ion collisions," *Phys.Rev.* **C59** (1999) 841–844, `arXiv:nucl-th/9808035 [nucl-th]`.

[53] D. Y. Ivanov, A. Schiller, and V. Serbo, "Large Coulomb corrections to the e^+e^- pair production at relativistic heavy ion colliders," *Phys.Lett.* **B454** (1999) 155–160, `arXiv:hep-ph/9809449 [hep-ph]`.

[54] K. Hencken, E. Kuraev, and V. Serbo, "Exclusive and inclusive muon pair production in collisions of relativistic nuclei," *Phys.Rev.* **C75** (2007) 034903, arXiv:hep-ph/0606069 [hep-ph].

[55] U. Jentschura, K. Hencken, and V. Serbo, "Revisiting unitarity corrections for electromagnetic processes in collisions of relativistic nuclei," *Eur.Phys.J.* **C58** (2008) 281–289, arXiv:0808.1350 [hep-ph].

[56] U. Jentschura and V. Serbo, "Nuclear form factor, validity of the equivalent photon approximation and Coulomb corrections to muon pair production in photon-nucleus and nucleus-nucleus collisions," *Eur.Phys.J.* **C64** (2009) 309–317, arXiv:0908.3853 [hep-ph].

[57] **TASSO** Collaboration, M. Althoff *et al.*, "Angular Correlations in $\gamma\gamma \to \rho^0\rho^0$ Near Threshold," *Z.Phys.* **C16** (1982) 13.

[58] **CELLO** Collaboration, H. Behrend *et al.*, "Measurement of the Reaction $\gamma\gamma \to \pi^+\pi^+\pi^-\pi^-$ at PETRA," *Z.Phys.* **C21** (1984) 205.

[59] **TPC/Two Gamma** Collaboration, H. Aihara *et al.*, "Production of Four Prong Final States in Photon-photon Collisions," *Phys.Rev.* **D37** (1988) 28.

[60] **PLUTO** Collaboration, C. Berger *et al.*, "Measurement and Analysis of the Reaction $\gamma\gamma \to \pi^+\pi^-\pi^+\pi^-$," *Z.Phys.* **C38** (1988) 521.

[61] **ARGUS** Collaboration, H. Albrecht *et al.*, "Observation of Spin Parity 2+ Dominance in the Reaction $\gamma\gamma \to \rho^0\rho^0$ Near Threshold," *Z.Phys.* **C50** (1991) 1–10.

[62] **L3** Collaboration, P. Achard *et al.*, "Measurement of exclusive $\rho^0\rho^0$ production in two photon collisions at high Q^2 at LEP," *Phys.Lett.* **B568** (2003) 11–22, arXiv:hep-ex/0305082 [hep-ex].

[63] D. Morgan, M. Pennington, and M. Whalley, "A Compilation of data on two photon reactions leading to hadron final states,". DPDG-94-01, RAL-94-061.

[64] N. Achasov and G. Shestakov, "Summary of the search for four quark states in gamma gamma collisions," *Sov.Phys.Usp.* **34** (1991) 471–496.

[65] B. A. Li and K.-F. Liu, "$K^*\bar{K}^*$ Mesonium Production in $\gamma\gamma$ Reactions and Hadronic Collisions," *Phys.Rev.* **D40** (1989) 2856–2860.

[66] B. Bajc, S. Prelovsek, and M. Rosina, "The Controversy in the $\gamma\gamma \to \rho\rho$ process: Potential scattering or q q anti-q anti-q resonance?," *Z.Phys.* **A356** (1996) 187–191, arXiv:hep-ph/9606243 [hep-ph].

[67] G. Goldhaber, S. Goldhaber, W.-Y. Lee, and A. Pais, "Influence of Bose-Einstein statistics on the anti-proton proton annihilation process," *Phys.Rev.* **120** (1960) 300–312.

[68] I. Anikin, B. Pire, and O. Teryaev, "Search for isotensor exotic meson and twist 4 contribution to $\gamma * \gamma \to \rho\rho$," *Phys.Lett.* **B626** (2005) 86–94, arXiv:hep-ph/0506277 [hep-ph].

[69] A. Bolz, C. Ewerz, M. Maniatis, O. Nachtmann, M. Sauter, *et al.*, "Photoproduction of π^+ π^- pairs in a model with tensor-pomeron and vector-odderon exchange," *JHEP* **1501** (2015) 151, arXiv:1409.8483 [hep-ph].

[70] P. Lebiedowicz, O. Nachtmann, and A. Szczurek, "The ρ^0 and Drell-Söding contributions to central exclusive production of $\pi^+\pi^-$ pairs in proton-proton collisions at high energies," arXiv:1412.3677 [hep-ph].

[71] S. Fazio, R. Fiore, L. Jenkovszky, and A. Salii, "Unifying soft and hard diffractive exclusive vector meson production and deeply virtual Compton scattering," *Phys.Rev.* **D90** no. 1, (2014) 016007, arXiv:1312.5683 [hep-ph].

[72] I. Ginzburg, S. Panfil, and V. Serbo, "Possibility of the Experimental Investigation of the QCD Pomeron in Semihard Processes at the $\gamma\gamma$ Collisions," *Nucl.Phys.* **B284** (1987) 685–705.

[73] I. Ginzburg and D. Y. Ivanov, "Semihard production of neutral pseudoscalar and tensor mesons in photon-photon collisions," *Nucl.Phys.* **B388** (1992) 376–390.

[74] R. Enberg, B. Pire, L. Szymanowski, and S. Wallon, "BFKL resummation effects in $\gamma^*\gamma^* \to \rho\rho$," *Eur.Phys.J.* **C45** (2006) 759–769, arXiv:hep-ph/0508134 [hep-ph].

[75] V. Gonçalves and W. Sauter, "Double vector meson production from the BFKL equation," *Eur.Phys.J.* **C44** (2005) 515–522, arXiv:hep-ph/0506178 [hep-ph].

[76] A. Donnachie and P. Landshoff, "Total cross-sections," *Phys.Lett.* **B296** (1992) 227–232, arXiv:hep-ph/9209205 [hep-ph].

[77] A. Szczurek, N. N. Nikolaev, and J. Speth, "From soft to hard regime in elastic pion pion scattering above resonances," *Phys.Rev.* **C66** (2002) 055206, arXiv:hep-ph/0112331 [hep-ph].

[78] S. Donnachie, H. G. Dosch, O. Nachtmann, and P. Landshoff, "Pomeron physics and QCD," *Camb.Monogr.Part.Phys.Nucl.Phys.Cosmol.* **19** (2002) 1–347.

[79] P. Lebiedowicz and A. Szczurek, "Exclusive $pp \to nn\pi^+\pi^+$ reaction at LHC and RHIC," *Phys.Rev.* **D83** (2011) 076002, arXiv:1005.2309 [hep-ph].

[80] J. H. Kuhn, E. Mirkes, and J. Steegborn, "Heavy quark production at a photon linear collider," *Z.Phys.* **C57** (1993) 615–622.

[81] M. Drees, M. Kramer, J. Zunft, and P. Zerwas, "Heavy quark production in two photon collisions," *Phys.Lett.* **B306** (1993) 371–378.

[82] J. Chyla, "Towards understanding $b\bar{b}$ production in $\gamma\gamma$ collisions," *Phys.Rev.* **D70** (2004) 054001, arXiv:hep-ph/0311074 [hep-ph].

[83] M. Kramer and E. Laenen, "Heavy quark correlations in direct photon-photon collisions," *Phys.Lett.* **B371** (1996) 303–309, arXiv:hep-ph/9511358 [hep-ph].

[84] N. Timneanu, J. Kwieciński, and L. Motyka, "Saturation model for two photon interactions at high-energies," *Eur.Phys.J.* **C23** (2002) 513–526, arXiv:hep-ph/0110409 [hep-ph].

[85] A. Szczurek, "Heavy quark production in photon nucleon and photon photon collisions," *Eur.Phys.J.* **C26** (2002) 183–194, arXiv:hep-ph/0203050 [hep-ph].

[86] V. Gonçalves and M. Machado, "The QCD pomeron in ultraperipheral heavy ion collisions. 2. Heavy quark production," *Eur.Phys.J.* **C29** (2003) 37–44, arXiv:hep-ph/0301263 [hep-ph].

[87] S. J. Brodsky, T. Kinoshita, and H. Terazawa, "Two Photon Mechanism of Particle Production by High-Energy Colliding Beams," *Phys.Rev.* **D4** (1971) 1532–1557.

[88] J. Korner, Z. Merebashvili, and M. Rogal, "Next-to-next-to-leading order $O(\alpha^2\alpha^2(s))$ results for top quark pair production in photon-photon collisions: The One-loop squared contributions," *Phys.Rev.* **D74** (2006) 094006, arXiv:hep-ph/0608287 [hep-ph].

[89] B. Kniehl, A. Kotikov, Z. Merebashvili, and O. Veretin, "Heavy-quark pair production in polarized photon-photon collisions at next-to-leading order: Fully integrated total cross sections," *Phys.Rev.* **D79** (2009) 114032, arXiv:0905.1649 [hep-ph].

[90] S. Frixione, M. Kramer, and E. Laenen, "D* production in two photon collisions," *Nucl.Phys.* **B571** (2000) 169–184, arXiv:hep-ph/9908483 [hep-ph].

[91] D. Maitre, "HPL, a mathematica implementation of the harmonic polylogarithms," *Comput.Phys.Commun.* **174** (2006) 222–240, arXiv:hep-ph/0507152 [hep-ph].

[92] K. J. Golec-Biernat and M. Wusthoff, "Saturation effects in deep inelastic scattering at low Q^2 and its implications on diffraction," *Phys.Rev.* **D59** (1998) 014017, arXiv:hep-ph/9807513 [hep-ph].

[93] V. Gonçalves, M. Kugeratski, E. Cazaroto, F. Carvalho, and F. Navarra, "Non-linear QCD dynamics in two-photon interactions at high energies," *Eur.Phys.J.* **C71** (2011) 1779, arXiv:1009.1112 [hep-ph].

[94] E. Kuraev, A. Schiller, and V. Serbo, "The $\gamma\gamma \to \mu^+\mu^- e^+e^-$ and $\gamma\gamma \to e^+e^- e^+e^-$ reactions as main calibration processes for high-energy $\gamma\gamma$ colliding beams," *Nucl.Phys.* **B256** (1985) 189–210.

[95] M. Glück, E. Reya, and A. Vogt, "Photonic parton distributions," *Phys.Rev.* **D46** (1992) 1973–1979.

[96] N. Achasov and G. Shestakov, "Lightest Scalar Resonances and the Dynamics of the $\gamma\gamma \to \pi\pi$ Reactions," *JETP Lett.* **88** (2008) 295–301, arXiv:0810.2201 [hep-ph].

[97] N. Achasov and G. Shestakov, "Lightest scalar and tensor resonances in $\gamma\gamma \to \pi\pi$ after the BELLE experiment," *Phys.Rev.* **D77** (2008) 074020, arXiv:0712.0885 [hep-ph].

[98] P. Ko, "Vector Meson Contributions to the Processes $\gamma\gamma \to \pi^0\pi^0$, $\pi^+\pi^-$, $K_L \to \pi^0\gamma\gamma$, and $K^+ \to \pi^+\gamma\gamma$," *Phys.Rev.* **D41** (1990) 1531.

[99] G. Mennessier, S. Narison, and X.-G. Wang, "The σ and $f_0(980)$ from $K_{e4} \oplus \pi\pi$, $\gamma\gamma$ scatterings, J/ψ, $\phi \to \gamma\sigma_B$ and $D_s \to l\nu\sigma_B$," *Nucl.Phys.Proc.Suppl.* **207-208** (2010) 177–180, arXiv:1009.3590 [hep-ph].

[100] M. Pennington, T. Mori, S. Uehara, and Y. Watanabe, "Amplitude Analysis of High Statistics Results on $\gamma\gamma \to \pi^+\pi^-$ and the Two Photon Width of Isoscalar States," *Eur.Phys.J.* **C56** (2008) 1–16, arXiv:0803.3389 [hep-ph].

[101] M. Boglione and M. Pennington, "Determination of radiative widths of scalar mesons from experimental results on $\gamma\gamma \to \pi\pi$," *Eur.Phys.J.* **C9** (1999) 11–29, arXiv:hep-ph/9812258 [hep-ph].

[102] S. J. Brodsky and G. P. Lepage, "Large Angle Two Photon Exclusive Channels in Quantum Chromodynamics," *Phys.Rev.* **D24** (1981) 1808.

[103] C.-R. Ji and F. Amiri, "Perturbative QCD Analysis of the Pion Form-factor Using a Frozen Coupling Constant," *Phys.Rev.* **D42** (1990) 3764–3769.

[104] A. Szczurek and J. Speth, "Perturbative QCD versus pion exchange and hadronic FSI effects in the $\gamma\gamma \to \pi^+\pi^-$ reaction," *Nucl.Phys.* **A728** (2003) 182–202, arXiv:hep-ph/0207265 [hep-ph].

[105] V. L. Chernyak, "$\gamma\gamma \to \pi\pi$, KK: Leading term QCD versus handbag model," *Phys.Lett.* **B640** (2006) 246–251, arXiv:hep-ph/0605072 [hep-ph].

[106] M. Diehl, P. Kroll, and C. Vogt, "The Handbag contribution to $\gamma\gamma \to \pi\pi$ and KK," *Phys.Lett.* **B532** (2002) 99–110, arXiv:hep-ph/0112274 [hep-ph].

[107] M. Diehl and P. Kroll, "Two-photon annihilation into octet meson pairs: Symmetry relations in the handbag approach," *Phys.Lett.* **B683** (2010) 165–171, arXiv:0911.3317 [hep-ph].

[108] M. Poppe, "Exclusive Hadron Production in Two Photon Reactions," *Int.J.Mod.Phys.* **A1** (1986) 545–668.

[109] **Particle Data Group** Collaboration, J. Beringer *et al.*, "Review of Particle Physics (RPP)," *Phys.Rev.* **D86** (2012) 010001.

[110] **BELLE** Collaboration, T. Mori *et al.*, "High statistics measurement of the cross-sections of $\gamma\gamma \to \pi^+\pi^-$ production," *J.Phys.Soc.Jap.* **76** (2007) 074102, arXiv:0704.3538 [hep-ex].

[111] **BELLE** Collaboration, S. Uehara *et al.*, "High-statistics measurement of neutral pion-pair production in two-photon collisions," *Phys.Rev.* **D78** (2008) 052004, arXiv:0805.3387 [hep-ex].

[112] V. Shchegelsky, A. Sarantsev, V. Nikonov, and A. Anisovich, "The $K^0_S\ K^S_0$ final state in two-photon collisions and SU(3) tensor nonets," *Eur.Phys.J.* **A27** (2006) 207–212.

[113] **BELLE** Collaboration, S. Uehara *et al.*, "High-statistics study of neutral-pion pair production in two-photon collisions," *Phys.Rev.* **D79** (2009) 052009, arXiv:0903.3697 [hep-ex].

[114] **JADE** Collaboration, T. Oest *et al.*, "Measurement of Resonance Productions in the Reactions $\gamma\gamma \to \pi^0\pi^0$ and $\gamma\gamma \to \pi^0\eta$," *Z.Phys.* **C47** (1990) 343–352.

[115] J. M. Blatt and V. Weisskopf, *Theoretical Nuclear Physics*. Wiley, New York, 1952.

[116] C. Baker, B. Barnett, C. Batty, K. Braune, D. Bugg, *et al.*, "The $f_2(1565)$ in $\bar{p}p \to (\omega\omega)\pi^0$ interactions at rest," *Phys.Lett.* **B467** (1999) 147–155, arXiv:1109.2287 [hep-ex].

[117] B. Nižić, "Beyond leading order perturbative QCD coorections to $\gamma\gamma \to M^+M^-$ $(M = \pi, K)$," *Phys.Rev.* **D35** (1987) 80–101.

[118] **ALEPH** Collaboration, A. Heister *et al.*, "Exclusive production of pion and kaon meson pairs in two photon collisions at LEP," *Phys.Lett.* **B569** (2003) 140–150.

[119] **BELLE** Collaboration, H. Nakazawa *et al.*, "Measurement of the $\gamma\gamma \to \pi^+\pi^-$ and $\gamma\gamma \to K^+K^-$ processes at energies of 2.4 Gev to 4.1 GeV," *Phys.Lett.* **B615** (2005) 39–49, arXiv:hep-ex/0412058 [hep-ex].

[120] G. Duplančić and B. Nižić, "NLO perturbative QCD predictions for $\gamma\gamma \to M^+M^-$ $(M = \pi, K)$," *Phys.Rev.Lett.* **97** (2006) 142003, arXiv:hep-ph/0607069 [hep-ph].

[121] M. Diehl, T. Feldmann, P. Kroll, and C. Vogt, "The Perturbative limit of the two pion light cone distribution amplitude," *Phys.Rev.* **D61** (2000) 074029, arXiv:hep-ph/9912364 [hep-ph].

[122] A. Efremov and A. Radyushkin, "Factorization and Asymptotical Behavior of Pion Form-Factor in QCD," *Phys.Lett.* **B94** (1980) 245–250.

[123] G. P. Lepage and S. J. Brodsky, "Exclusive Processes in Quantum Chromodynamics: Evolution Equations for Hadronic Wave Functions and the Form-Factors of Mesons," *Phys.Lett.* **B87** (1979) 359–365.

[124] D. Mueller, "The Evolution of the pion distribution amplitude in next-to-leading-order," *Phys.Rev.* **D51** (1995) 3855–3864, `arXiv:hep-ph/9411338 [hep-ph]`.

[125] E. Ruiz Arriola and W. Broniowski, "Pion light cone wave function and pion distribution amplitude in the Nambu-Jona-Lasinio model," *Phys.Rev.* **D66** (2002) 094016, `arXiv:hep-ph/0207266 [hep-ph]`.

[126] I. S. Gradshteyn and I. M. Ryzhik, *Table of Integrals, Series, and Products*. Edited by A. Jeffrey and D. Zwillinger. Academic Press, New York, 2007.

[127] L. Harland-Lang, V. Khoze, M. Ryskin, and W. Stirling, "Central exclusive meson pair production in the perturbative regime at hadron colliders," *Eur.Phys.J.* **C71** (2011) 1714, `arXiv:1105.1626 [hep-ph]`.

[128] G. P. Lepage and S. J. Brodsky, "Exclusive Processes in Perturbative Quantum Chromodynamics," *Phys.Rev.* **D22** (1980) 2157.

[129] **BaBar** Collaboration, B. Aubert *et al.*, "Measurement of the $\gamma\gamma^* \to \pi^0$ transition form factor," *Phys.Rev.* **D80** (2009) 052002, `arXiv:0905.4778 [hep-ex]`.

[130] X.-G. Wu and T. Huang, "An Implication on the Pion Distribution Amplitude from the Pion-Photon Transition Form Factor with the New BABAR Data," *Phys.Rev.* **D82** (2010) 034024, `arXiv:1005.3359 [hep-ph]`.

[131] V. Chernyak and A. Zhitnitsky, "Exclusive Decays of Heavy Mesons," *Nucl.Phys.* **B201** (1982) 492.

[132] **CELLO** Collaboration, H. Behrend *et al.*, "An Experimental study of the process $\gamma\gamma \to \pi^+\pi^-$," *Z.Phys.* **C56** (1992) 381–390.

[133] **CLEO** Collaboration, J. Dominick *et al.*, "Two photon production of charged pion and kaon pairs," *Phys.Rev.* **D50** (1994) 3027–3037, arXiv:hep-ph/9403379 [hep-ph].

[134] **TPC/Two Gamma** Collaboration, H. Aihara *et al.*, "Pion and Kaon Pair Production in Photon-Photon Collisions," *Phys.Rev.Lett.* **57** (1986) 404.

[135] J. Boyer, F. Butler, G. Gidal, G. Abrams, D. Amidei, *et al.*, "Two photon production of pion pairs," *Phys.Rev.* **D42** (1990) 1350–1367.

[136] **VENUS** Collaboration, F. Yabuki *et al.*, "Study of $\pi^+\pi^-$ pair production in a two photon process at TRISTAN," *J.Phys.Soc.Jap.* **64** (1995) 435–447.

[137] **Crystal Ball** Collaboration, H. Marsiske *et al.*, "A Measurement of $\pi^0\pi^0$ Production in Two Photon Collisions," *Phys.Rev.* **D41** (1990) 3324.

[138] **STAR** Collaboration, B. Abelev *et al.*, "ρ^0 photoproduction in ultraperipheral relativistic heavy ion collisions at $s(NN)^{1/2}$," *Phys.Rev.* **C77** (2008) 034910, arXiv:0712.3320 [nucl-ex].

[139] A. Szczurek and A. P. Szczepaniak, "Diffractive photoproduction of opposite-charge pseudoscalar meson pairs at high energies," *Phys.Rev.* **D71** (2005) 054005, arXiv:hep-ph/0410083 [hep-ph].

[140] L. Jones, "A Remark on the Phase of the Deck Model," *Phys.Rev.* **D14** (1976) 3233.

[141] **ZEUS** Collaboration, J. Breitweg *et al.*, "Elastic and proton dissociative ρ^0 photoproduction at HERA," *Eur.Phys.J.* **C2** (1998) 247–267, arXiv:hep-ex/9712020 [hep-ex].

[142] **ALICE** Collaboration, J. Nystrand, "Photonuclear production of vector mesons in ultra-peripheral Pb-Pb collisions at the LHC," arXiv:1408.0811 [nucl-ex].

[143] C. Mayer, "Coherent photo-production of ρ^0 mesons in ultra-peripheral Pb+Pb collisions at the LHC, measured by ALICE.". 13^{th} International Workshop on Meson Production, Properties and Interaction KRAKÓW, POLAND, 28.05.2014.

[144] V. Gonçalves and M. Machado, "Vector meson production in ultraperipheral heavy ion collisions," *J.Phys.* **G32** (2006) 295–308, arXiv:hep-ph/0506331 [hep-ph].

[145] T. Lappi and H. Mantysaari, "J/ψ production in ultraperipheral Pb+Pb and p+Pb collisions at energies available at the CERN Large Hadron Collider," *Phys.Rev.* **C87** no. 3, (2013) 032201, arXiv:1301.4095 [hep-ph].

[146] A. Cisek, W. Schäfer, and A. Szczurek, "Exclusive coherent production of heavy vector mesons in nucleus-nucleus collisions at LHC," *Phys.Rev.* **C86** (2012) 014905, arXiv:1204.5381 [hep-ph].

[147] B. Kopeliovich, J. Nemchick, N. N. Nikolaev, and B. Zakharov, "Novel color transparency effect: Scanning the wave function of vector mesons," *Phys.Lett.* **B309** (1993) 179–186, arXiv:hep-ph/9305225 [hep-ph].

[148] B. Kopeliovich, J. Nemchick, N. N. Nikolaev, and B. Zakharov, "Decisive test of color transparency in exclusive electroproduction of vector mesons," *Phys.Lett.* **B324** (1994) 469–476, arXiv:hep-ph/9311237 [hep-ph].

[149] J. Nemchik, N. N. Nikolaev, and B. Zakharov, "Scanning the BFKL pomeron in elastic production of vector mesons at HERA," *Phys.Lett.* **B341** (1994) 228–237, arXiv:hep-ph/9405355 [hep-ph].

[150] J. Nemchik, N. N. Nikolaev, E. Predazzi, and B. Zakharov, "Color dipole phenomenology of diffractive electroproduction of light vector mesons at HERA," *Z.Phys.* **C75** (1997) 71–87, arXiv:hep-ph/9605231 [hep-ph].

[151] N. N. Nikolaev and B. Zakharov, "Color transparency and scaling properties of nuclear shadowing in deep inelastic scattering," *Z.Phys.* **C49** (1991) 607–618.

[152] S. Klein and J. Nystrand, "Exclusive vector meson production in relativistic heavy ion collisions," *Phys.Rev.* **C60** (1999) 014903, arXiv:hep-ph/9902259 [hep-ph].

[153] V. Gonçalves and M. Machado, "The QCD pomeron in ultraperipheral heavy ion collisions. IV. Photonuclear production of vector mesons," *Eur.Phys.J.* **C40** (2005) 519–529, arXiv:hep-ph/0501099 [hep-ph].

[154] L. Frankfurt, M. Strikman, and M. Zhalov, "Signals for black body limit in coherent ultraperipheral heavy ion collisions," *Phys.Lett.* **B537** (2002) 51–61, arXiv:hep-ph/0204175 [hep-ph].

[155] L. Frankfurt, M. Strikman, and M. Zhalov, "Predictions of the generalized Glauber model for the coherent ρ production at RHIC and the STAR data," *Phys.Rev.* **C67** (2003) 034901, arXiv:hep-ph/0210303 [hep-ph].

[156] V. Gribov, "Interaction of gamma quanta and electrons with nuclei at high-energies," *Sov.Phys.JETP* **30** (1970) 709–717.

[157] G. Bochmann, "Multiple-step production model for coherent reactions on nuclei," *Phys.Rev.* **D6** (1972) 1938–1942.

[158] STARLIGHT website, http://starlight.hepforge.org/.

[159] V. Gonçalves and M. Machado, "Photoproduction of ρ^0 meson in ultraperipheral heavy ion collisions at the BNL RHIC and CERN LHC," *Phys.Rev.* **C80** (2009) 054901, arXiv:0907.4123 [hep-ph].

[160] **LHCb** Collaboration, R. Aaij *et al.*, "Observation of double charm production involving open charm in pp collisions at $\sqrt{s} = 7$ TeV," *JHEP* **1206** (2012) 141, arXiv:1205.0975 [hep-ex].

[161] R. Maciuła and A. Szczurek, "Production of $c\bar{c}c\bar{c}$ in double-parton scattering within k_t-factorization approach – meson-meson correlations," *Phys.Rev.* **D87** no. 7, (2013) 074039, arXiv:1301.4469 [hep-ph].

[162] **STAR** Collaboration, B. Abelev *et al.*, "Observation of $\pi^+\pi^-\pi^+\pi^-$ Photoproduction in Ultra-Peripheral Heavy Ion Collisions at STAR," *Phys.Rev.* **C81** (2010) 044901, arXiv:0912.0604 [nucl-ex].

[163] Private communication with Xin Dong and Boris Grube.

[164] L. Frankfurt, M. Strikman, and M. Zhalov, "Coherent photoproduction from nuclei," *Acta Phys.Polon.* **B34** (2003) 3215–3254, arXiv:hep-ph/0304301 [hep-ph].

[165] Information received during my stay at CERN - financial support for M. K-G from the National Science Centre in the framework of a doctoral scholarship financing based on the decision no. 2013/08/T/ST/00669.

[166] G. Contreras, R. Cruz Albino, M. Rodriguez Cahuantzi, and D. Tapia Takaki, "$\pi^+\pi^-\pi^+\pi^-$ production in Ultra Peripheral Collisions (Pb+Pb & p+Pb).". UPC-PAG, PWG-UD session, ALICE's Physics Week - Padova, Italia, 25.05.2013.

[167] C. A. Bertulani, S. R. Klein, and J. Nystrand, "Physics of ultra-peripheral nuclear collisions," *Ann.Rev.Nucl.Part.Sci.* **55** (2005) 271–310, arXiv:nucl-ex/0502005 [nucl-ex].

[168] X. Wang, "Measurement of Open Heavy Flavor Production with Single Muons in $p+p$ and d+Au Collisions at RHIC," *J.Phys.* **G32** (2006) S511–S514, arXiv:nucl-ex/0609036 [nucl-ex].

[169] C. Yang, X. Huang, C. Du, B. Huang, Z. Ahammed, *et al.*, "Calibration and performance of the STAR Muon Telescope Detector using cosmic rays," arXiv:1402.1078 [physics.ins-det].

[170] A. J. Baltz, Y. Gorbunov, S. R. Klein, and J. Nystrand, "Two-Photon Interactions with Nuclear Breakup in Relativistic Heavy Ion Collisions," *Phys.Rev.* **C80** (2009) 044902, arXiv:0907.1214 [nucl-ex].

[171] A. Baltz, "Higher Order QED Calculation of Ultrarelativistic Heavy Ion Production of $\mu^+\mu^-$ Pairs," *Phys.Rev.* **C80** (2009) 034901, arXiv:0901.0891 [nucl-th].

[172] **ALICE** Collaboration, B. Abelev *et al.*, "Production of muons from heavy flavour decays at forward rapidity in pp and Pb-Pb collisions at $\sqrt{s_{NN}} = 2.76$ TeV," *Phys.Rev.Lett.* **109** (2012) 112301, arXiv:1205.6443 [hep-ex].

[173] M. Gay Ducati, M. Machado, and M. Machado, "Charm and bottom production in inclusive double Pomeron exchange in heavy ion collisions at the LHC," *Phys.Rev.* **C83** (2011) 014903, arXiv:1008.4807 [hep-ph].

[174] R. Maciuła and A. Szczurek, "Open charm production at the LHC - k_t-factorization approach," *Phys.Rev.* **D87** no. 9, (2013) 094022, arXiv:1301.3033 [hep-ph].

[175] M. Luszczak, R. Maciuła, and A. Szczurek, "Single- and central-diffractive production of open charm and bottom mesons at the LHC: theoretical predictions and experimental capabilities," arXiv:1412.3132 [hep-ph].

[176] E. Lohrmann, "A Summary of Charm Hadron Production Fractions," arXiv:1112.3757 [hep-ex].

[177] **STAR** Collaboration, B. Grube, "Photoproduction in Ultra-Peripheral Heavy Ion Collisions at STAR," *Nucl.Phys.Proc.Suppl.* **179** (2008) 117–124, arXiv:0808.3991 [nucl-ex].

[178] A. J. Baltz, S. R. Klein, and J. Nystrand, "Coherent vector meson photoproduction with nuclear breakup in relativistic heavy ion collisions," *Phys.Rev.Lett.* **89** (2002) 012301, arXiv:nucl-th/0205031 [nucl-th].

[179] Y. Ivanov, B. Kopeliovich, and I. Schmidt, "Vector meson production in ultra-peripheral collisions at LHC," arXiv:0706.1532 [hep-ph].

[180] B. Z. Kopeliovich, A. Schafer, and A. V. Tarasov, "Nonperturbative effects in gluon radiation and photoproduction of quark pairs," *Phys.Rev.* **D62** (2000) 054022, arXiv:hep-ph/9908245 [hep-ph].

[181] V. Rebyakova, M. Strikman, and M. Zhalov, "Coherent ρ and J/ψ photoproduction in ultraperipheral processes with electromagnetic dissociation of heavy ions at RHIC and LHC," *Phys.Lett.* **B710** (2012) 647–653, arXiv:1109.0737 [hep-ph].

[182] **CRYSTAL BARREL** Collaboration, A. Abele *et al.*, "4π decays of scalar and vector mesons," *Eur.Phys.J.* **C21** (2001) 261–269.

[183] **ZEUS** Collaboration, H. Abramowicz *et al.*, "Exclusive electroproduction of two pions at HERA," *Eur.Phys.J.* **C72** (2012) 1869, arXiv:1111.4905 [hep-ex].

[184] C. Adler, A. Denisov, E. Garcia, M. J. Murray, H. Strobele, *et al.*, "The RHIC zero degree calorimeter," *Nucl.Instrum.Meth.* **A470** (2001) 488–499, arXiv:nucl-ex/0008005 [nucl-ex].

[185] **ALICE** Collaboration, K. Aamodt *et al.*, "The ALICE experiment at the CERN LHC," *JINST* **3** (2008) S08002.

[186] J. Speth and A. van der Woude, "Giant resonances in nuclei," *Rep. Progr. Phys.* **44** (1981) 719.

[187] V. Plujko, R. Capote, and O. Gorbachenko, "Giant dipole resonance parameters with uncertainties from photonuclear cross sections," *At. Data and Nucl. Data Tables* **97** (2011) 567–585.

[188] A. Veyssiere, H. Beil, R. Bergere, P. Carlos, and A. Lepretre, "Photoneutron cross sections of ^{208}Pb and ^{197}Au," *Nucl. Phys.* **A159** (1970) 561–576.

[189] V. Varlamov, M. Stepanov, and V. Chesnokov *Izv. Ross. Akad. Nauk, Ser. Fiz.* **67** (2003) 656.

[190] M. Chadwick, P. Obloinsky, P. Hodgson, and G. Reffo, "Pauli-blocking in the quasideuteron model of photoabsorption," *Phys.Rev.* **C44** (1991) 814–823.

[191] M. Vidović, M. Greiner, and G. Soff, "Electromagnetic dissociation of Pb nuclei in peripheral ultrarelativistic heavy-ion collisions," *Phys. Rev.* **C48** (1993) 2011–2015.

[192] J. Ahrens, "The Total Absorption of Photons by Nuclei," *Nucl.Phys.* **A446** (1985) 229C–239C.

[193] R. J. Charity, "Systematic description of evaporation spectra for light and heavy compound nuclei," *Phys. Rev.* **C82** (2010) 014610.

[194] W. Hauser and H. Feshbach, "The inelastic scattering of neutrons," *Phys. Rev.* **87** (Jul, 1952) 366–373.

[195] P. Moller, J. Nix, W. Myers, and W. Swiątecki, "Nuclear ground state masses and deformations," *Atom.Data Nucl.Data Tabl.* **59** (1995) 185–381, `arXiv:nucl-th/9308022 [nucl-th]`.

[196] K. Hara, H. Harada, F. Kitatani, S. Goko, S. Hohara, T. Kaihori, A. Makinaga, H. Utsunomiya, T. H., and K. Yamada, "Measurements of the ^{152}Srn(γ, n) Cross Section with Laser-Compton Scattering γ Rays and the Photon Difference Method," *Journal of Nuclear Science and Technology* **44** (2007) 938–945.

[197] F. Kitatani, H. Harada, H. Utsunomiya, H. Akimune, T. Kaihori, T. H., and K. Yamada, "Measurement of the ^{80}Se(γ, n) Cross Section Using Laser-Compton Scattering γ-Rays," *Journal of Nuclear Science and Technology* **47** (2010) 367–375.

[198] O. Itoh, H. Utsunomiya, H. Akimune, T. Kondo, M. Kamata, T. Yamagata, T. H., H. Harada, F. Kitatani, S. Goko, C. Nair, and Y.-W. Lui, "Photoneutron Cross

Sections for Au Revisited: Measurements with Laser Compton Scattering γ-Rays and Data Reduction by a Least-Squares Method," *Journal of Nuclear Science and Technology* **48** (2011) 834–840.

[199] F. Kitatani, H. Harada, S. Goko, H. Utsunomiya, H. Akimune, T. H, and K. Yamada, "Measurement of ^{76}Se and ^{78}Se (γ, n) Cross Sections," *Journal of Nuclear Science and Technology* **48** (2011) 1017–1024.

[200] S. C. Fultz, R. L. Bramblett, J. T. Caldwell, and N. A. Kerr, "Photoneutron cross-section measurements on gold using nearly monochromatic photons," *Phys. Rev.* **127** (1962) 1273–1279.

[201] B. L. Berman, R. E. Pywell, S. S. Dietrich, M. N. Thompson, K. G. McNeill, and J. W. Jury, "Absolute photoneutron cross sections for Zr, I, Pr, Au, and Pb," *Phys. Rev. C* **36** (1987) 1286–1292.

[202] V. Varlamov, N. Peskov, D. Rudenko, and M. Stepanov, "Consistent evaluation of photoneutron reaction cross-sections using data obtained in experiments with quasimonoenergetic annihilation photon beams at Livermore (USA) and Saclay (France)," *Voprosy Atomnoj Nauki i Tekhniki. Seriya: Yadernye Konstanty (Nuclear Constants)(in Russian)* **1-2** (2003) 48–89.

[203] V. Varlamov, N. Efimkin, B. Ishkhanov, and V. Ishkhanov *Voprosy Atomnoj Nauki i Tekhniki. Seriya: Yadernye Konstanty (Nuclear Constants)(in Russian)* **1** (1993) 52.

[204] L. Young, *Photoneutron Cross Sections and Spectra from Monoenergetic Photons on Y, Pr, Pb, and Bi in the Giant Resonance.* PhD thesis, University of Illinois at Urbana-Champaign, 1972. unpublished.

[205] R. Van de Vyver, J. Devos, H. Ferdinande, R. Carchon, and E. Van Camp, "Fine structure in the ^{208}Pb(γ, n) cross section," *Zeitschrift für Physik A Atoms and Nuclei* **284** no. 1, (1978) 91–93.

[206] S. Belyaev, A. Kozin, A. Nechkin, V. Semenov, and S. Semenko *, Yad. Fiz.* **42** (1985) 1050.

[207] Belyaev, S.N. and Vasilev, O.V. and Kozin, A.B. and Nechkin, A.A. and Semenov, V.A. Program and Theses, Proc.35th Ann. Conf. Nucl. Spectrosc. Struct. At. Nuclei, Leningrad, 1985. p. 351.

[208] S. Belyaev, A. Nechkin, and V. Semenov *,Izv. Rossiiskoi Akademii Nauk, Ser. Fiz.* **55** (1991) 953.

[209] R. R. Harvey, J. T. Caldwell, R. L. Bramblett, and S. C. Fultz, "Photoneutron Cross Sections of Pb^{206}, Pb^{207}, Pb^{208}, and Bi^{209}," *Phys. Rev.* **136** (1964) B126–B131.

[210] V. Varlamov, B. Ishkhanov, V. Orlin, and S. Troshchiev, "New data for the $^{197}\mathrm{Au}(\gamma, nX)$ and $^{197}\mathrm{Au}(\gamma, 2nX)$ reaction cross sections," *Bulletin of the Russian Academy of Sciences: Physics* **74** (2010) 842–849.

[211] W. J. Llope and P. Braun-Munzinger, "Electromagnetic dissociation of relativistic heavy ions," *Phys. Rev.* **C41** (1990) 2644–2653.

[212] G. Baur, K. Hencken, A. Aste, D. Trautmann, and S. R. Klein, "Multiphoton exchange processes in ultraperipheral relativistic heavy ion collisions," *Nucl.Phys.* **A729** (2003) 787–808, `arXiv:nucl-th/0307031 [nucl-th]`.

[213] I. Pshenichnov, "Electromagnetic excitation and fragmentation of ultrarelativistic nuclei," *Phys.Part.Nucl.* **42** (2011) 215–250.

[214] A. Baltz, M. Rhoades-Brown, and J. Weneser, "Heavy ion partial beam lifetimes due to Coulomb induced processes," *Phys.Rev.* **E54** (1996) 4233–4239.

[215] **ALICE** Collaboration, B. Abelev *et al.*, "Measurement of the Cross Section for Electromagnetic Dissociation with Neutron Emission in Pb-Pb Collisions at $\sqrt{s_{NN}}$ = 2.76 TeV," *Phys.Rev.Lett.* **109** (2012) 252302, `arXiv:1203.2436 [nucl-ex]`.

[216] M. Chiu, A. Denisov, E. Garcia, J. Katzy, and S. N. White, "Measurement of Mutual Coulomb Dissociation in $\sqrt{s_{NN}} = 130$ GeV Au+Au collisions at RHIC," *Phys.Rev.Lett.* **89** (2002) 012302, `arXiv:nucl-ex/0109018 [nucl-ex]`.

[217] A. J. Baltz, C. Chasman, and S. N. White, "Correlated forward - backward dissociation and neutron spectra as luminosity monitor in heavy ion colliders," *Nucl.Instrum.Meth.* **A417** (1998) 1–8, `arXiv:nucl-ex/9801002 [nucl-ex]`.

[218] I. Pshenichnov, J. Bondorf, I. Mishustin, A. Ventura, and S. Masetti, "Mutual heavy ion dissociation in peripheral collisions at ultrarelativistic energies," *Phys.Rev.* **C64** (2001) 024903, arXiv:nucl-th/0101035 [nucl-th].

[219] J. Hill, A. Petridis, B. Fadem, and F. Wohn, "Electromagnetic dissociation of Au targets by relativistic Pb projectiles," *Nucl.Phys.* **A661** (1999) 313–316.

[220] M. Golubeva, F. Guber, T. Karavicheva, E. Karpechev, A. Kurepin, *et al.*, "Neutron emission in electromagnetic dissociation of ultrarelativistic Pb ions," *Phys.Rev.* **C71** (2005) 024905.

[221] G. Baur and L. Ferreira Filho, "Coherent particle production at relativistic heavy ion colliders inluding strong absorption effects," *Nucl.Phys.* **A518** (1990) 786–800.

[222] R. N. Cahn and J. D. Jackson, "Realistic equivalent photon yields in heavy ion collisions," *Phys.Rev.* **D42** (1990) 3690–3695.

[223] A. Donnachie and G. Shaw, eds., *Electromagnetic Interactions of Hadrons*, vol. 2. Plenum Press (NY), 1979.

[224] S. Donnachie, H. G. Dosch, O. Nachtmann, and P. Landshoff, "Pomeron physics and QCD," *Camb.Monogr.Part.Phys.Nucl.Phys.Cosmol.* **19** (2002) 1–347.

[225] D. Leith, *Electromagnetic interactions of hadrons*, vol. 1. Plenum Press (NY), 1978.

[226] N. Cartiglia, "Diffraction at HERA," arXiv:hep-ph/9703245 [hep-ph].

[227] D. Shirkov and I. Solovtsov, "Analytic model for the QCD running coupling with universal $\alpha_s(0)$ value," *Phys.Rev.Lett.* **79** (1997) 1209–1212, arXiv:hep-ph/9704333 [hep-ph].

[228] P. J. Karol, "Nucleus-nucleus reaction cross sections at high energies: Soft-spheres model," *Phys.Rev.* **C11** (1975) 1203–1209.

[229] J. Chauvin, D. Lebrun, A. Lounis, and M. Buenerd, "Low and intermediate energy nucleus-nucleus elastic scattering and the optical limit of Glauber theory," *Phys.Rev.* **C28** (1983) 1970–1974.

[230] M. L. Miller, K. Reygers, S. J. Sanders, and P. Steinberg, "Glauber modeling in high energy nuclear collisions," *Ann.Rev.Nucl.Part.Sci.* **57** (2007) 205–243, arXiv:nucl-ex/0701025 [nucl-ex].

[231] **H1 and ZEUS** Collaboration, N. Cartiglia, "Diffraction at HERA," arXiv:hep-ph/9703245 [hep-ph].

[232] P. Lebiedowicz and A. Szczurek, "Exclusive $pp \to pp\pi^+\pi^-$ reaction: From the threshold to LHC," *Phys.Rev.* **D81** (2010) 036003, arXiv:0912.0190 [hep-ph].

[233] V. Gribov, "Glauber corrections and the interaction between high-energy hadrons and nuclei," *Sov.Phys.JETP* **29** (1969) 483–487.

[234] A. Kaidalov, "Nucleus-nucleus interaction dynamics and the Glauber-Gribov approach," *Nucl.Phys.* **A525** (1991) 39–58.